

Recent Advances in Array Antenna and Array Signal Processing for Radar

Lead Guest Editor: Elisa Giusti

Guest Editors: Piotr Samczynski, Pilar Jarabo-Amores, and Amerigo Capria





Recent Advances in Array Antenna and Array Signal Processing for Radar

International Journal of Antennas and Propagation

Recent Advances in Array Antenna and Array Signal Processing for Radar

Lead Guest Editor: Elisa Giusti

Guest Editors: Piotr Samczynski, Pilar Jarabo-Amores,
and Amerigo Capria



Copyright © 2018 Hindawi. All rights reserved.

This is a special issue published in “International Journal of Antennas and Propagation.” All articles are open access articles distributed under the Creative Commons Attribution License, which permits unrestricted use, distribution, and reproduction in any medium, provided the original work is properly cited.

Editorial Board

- Ana Alejos, Spain
Mohammad Ali, USA
Jaume Anguera, Spain
Rodolfo Araneo, Italy
Alexei Ashikhmin, USA
Herve Aubert, France
Paolo Baccarelli, Italy
Xiulong Bao, Ireland
Toni Björninen, Finland
Stefania Bonafoni, Italy
Paolo Burghignoli, Italy
Shah Nawaz Burokur, France
Giuseppe Castaldi, Italy
Luca Catarinucci, Italy
Felipe Catedra, Spain
Marta Cavagnaro, Italy
Shih Yuan Chen, Taiwan
Yu Jian Cheng, China
Renato Cicchetti, Italy
Riccardo Colella, Italy
Laura Corchia, Italy
Lorenzo Crocco, Italy
Claudio Curcio, Italy
Francesco D'Agostino, Italy
María Elena de Cos Gómez, Spain
Tayeb A. Denidni, Canada
Giuseppe Di Massa, Italy
- Michele D'Urso, Italy
Francisco Falcone, Spain
Miguel Ferrando Bataller, Spain
Flaminio Ferrara, Italy
Vincenzo Galdi, Italy
Claudio Gennarelli, Italy
Farid Ghanem, Algeria
Sotirios K. Goudos, Greece
Rocco Guerriero, Italy
Kerim Guney, Turkey
Song Guo, Japan
Tamer S. Ibrahim, USA
M. Ramlee Kamarudin, UK
Slawomir Koziel, Iceland
Luis Landesa, Spain
Ding-Bing Lin, Taiwan
Angelo Liseno, Italy
Pierfrancesco Lombardo, Italy
Lorenzo Luini, Italy
Atsushi Mase, Japan
Diego Masotti, Italy
Ch. F. Mecklenbräuker, Austria
A. T. Mobashsher, Australia
Ananda S. Mohan, Australia
J.-M. Molina-Garcia-Pardo, Spain
Giuseppina Monti, Italy
Giorgio Montisci, Italy
- Andrea Francesco Morabito, Italy
N. Nasimuddin, Singapore
Mourad Nedil, Canada
Symeon Nikolaou, Cyprus
Giacomo Oliveri, Italy
Mauro Parise, Italy
Ikmo Park, Republic of Korea
Josep Parrón, Spain
Matteo Pastorino, Italy
Xianming Qing, Singapore
Ahmad Safaai-Jazi, USA
Safieddin Safavi-Naeini, Canada
Magdalena Salazar-Palma, Spain
Stefano Selleri, Italy
Raffaele Solimene, Italy
Gino Sorbello, Italy
Seong-Youp Suh, USA
Sheng Sun, Hong Kong
Larbi Talbi, Canada
Luciano Tarricone, Italy
Parveen Wahid, USA
Chien-Jen Wang, Taiwan
Wen-Qin Wang, China
Mustapha C E Yagoub, Canada
Shiwen Yang, China
Yuan Yao, China

Contents

Recent Advances in Array Antenna and Array Signal Processing for Radar

Elisa Giusti , Piotr Samczynski, Maria-Pilar Jarabo-Amores, and Amerigo Capria 
Editorial (2 pages), Article ID 6195704, Volume 2018 (2018)

Space-Time Adaptive Cancellation in Passive Radar Systems

Tamás Pető  and Rudolf Seller
Research Article (16 pages), Article ID 2467673, Volume 2018 (2018)

Reduced-Complexity Direction of Arrival Estimation Using Real-Valued Computation with Arbitrary Array Configurations

Feng-Gang Yan , Jun Wang , Shuai Liu , Yi Shen, and Ming Jin
Research Article (10 pages), Article ID 3284619, Volume 2018 (2018)

Joint DOA and DOD Estimation Based on Tensor Subspace with Partially Calibrated Bistatic MIMO Radar

Junxiang Wang , Ping Huang, and Dingjie Xu
Research Article (7 pages), Article ID 4370637, Volume 2018 (2018)

Enhanced 2D-DOA Estimation for Large Spacing Three-Parallel Uniform Linear Arrays

Dong Zhang , Yongshun Zhang, and Cunqian Feng
Research Article (7 pages), Article ID 3679494, Volume 2018 (2018)

Radio and Clutter Suppression Algorithm Based on Spatial Multiple Beams for Small-Aperture HFSWR

Di Yao , Xin Zhang, Qiang Yang , and Weibo Deng
Research Article (15 pages), Article ID 1574870, Volume 2018 (2018)

Joint-2D-SL0 Algorithm for Joint Sparse Matrix Reconstruction

Dong Zhang, Yongshun Zhang, and Cunqian Feng
Research Article (7 pages), Article ID 6862852, Volume 2017 (2018)

Ocean Surface Current Observation with a Dual Monopole-Cross-Loop Antenna Array

Yeping Lai, Hao Zhou, Yuming Zeng, and Biyang Wen
Research Article (8 pages), Article ID 2754831, Volume 2017 (2018)

Robust STAP for MIMO Radar Based on Direct Data Domain Approach

Cheng Chen, Junjie He, Zeshi Yuan, Xiaohua Zhu, and Hongtao Li
Research Article (9 pages), Article ID 6967130, Volume 2017 (2018)

Circularly Polarized Dielectric Resonator Antenna Arrays with Fractal Cross-Slot-Coupled DRA Elements

Jia-Hong Lin, Wen-Hui Shen, Zhi-Dong Shi, and Shun-Shi Zhong
Research Article (11 pages), Article ID 8160768, Volume 2017 (2018)

Estimating Direction of Arrival by Using Two-Dimensional State-Space Balance Method

Jun Wang, Hong Xiang, Shaoming Wei, and Zhongsheng Sun
Research Article (5 pages), Article ID 4890203, Volume 2017 (2018)

DOA Estimation of Noncircular Signals Using Quaternions

Tianzhen Meng, Minjie Wu, and Naichang Yuan
Research Article (6 pages), Article ID 9848169, Volume 2017 (2018)

Editorial

Recent Advances in Array Antenna and Array Signal Processing for Radar

Elisa Giusti ¹, Piotr Samczynski,² Maria-Pilar Jarabo-Amores,³ and Amerigo Capria ¹

¹CNIT-RaSS (National Interuniversity Consortium on Telecommunications-Radar and Surveillance Systems National Laboratory), Galleria Gerace No. 18, 56124 Pisa, Italy

²Institute of Electronic Systems, Warsaw University of Technology, Nowowiejska 15/19, 00-665 Warsaw, Poland

³Signal Theory and Communications Department, Polytechnic School, University of Alcalá, Campus Universitario, s/n, 28805 Alcalá de Henares, Madrid, Spain

Correspondence should be addressed to Elisa Giusti; elisa.giusti@cnit.it

Received 29 March 2018; Accepted 1 April 2018; Published 7 June 2018

Copyright © 2018 Elisa Giusti et al. This is an open access article distributed under the Creative Commons Attribution License, which permits unrestricted use, distribution, and reproduction in any medium, provided the original work is properly cited.

Beside the fact that array antenna design and array processing have experienced five decades of research, they are still an active and open topic in the field of radar. As a matter of fact, the recent technological advances have made the realization of array systems (ground/air/space borne) and real-time processing possible.

Riding on the wave of electronic hardware and computer system advances, the scientific interest in the realization of complex systems such as array antenna and real-time signal processing has grown enormously in the recent years.

So far, array antenna design as well as array signal processing has obtained fruitful achievements in theory, algorithm, and hardware. However, the need for faster and more accurate signal processing routines as well as the need for more efficient and miniaturized antenna and sensors still continues.

The purpose of this special issue is to publish high-quality contributions and reviews that investigate the most relevant research activities on array antenna subsystems and array signal processing for radar applications, as well as address challenges and opportunities ahead.

A substantial number of papers have been submitted, and after a thorough peer review process, eleven papers have been selected to be included in this special issue.

These papers cover important applications including antenna array design and array signal processing for direction of arrival (DoA), direction of departure (DoD)

estimation, and clutter mitigation through space-time adaptive processing (STAP) to cite a few.

We believe that the papers collected in this special issue well address the contemporary topics in research related to array antenna design and array signal processing for radar systems and well introduce the reader in recent advances in such a research field.

The paper by T. Meng et al. presents an algorithm for DoA estimation of noncircular signals which is based on the use of quaternions. In this paper, the authors show that the use of quaternions allows for a computation cost reduction and a fine enough estimation accuracy since the quaternions have stronger orthogonality with respect to complex numbers.

The paper by J. Wang et al. presents a method to estimate the DoA by means of a two-dimensional state space balance (2D-SSB) method and uniformly rectangular array (URA). The proposed approach is proven to perform well in case of nonstationary environment, and its performance is compared with other methods (matrix pencil and unitary matrix pencil methods).

The paper by J. Wang et al. proposes an algorithm for the joint estimation of the DoA and DoD for a partially calibrated bistatic MIMO radar. By exploiting the multidimensional nature of the received signal, the gain-phase uncertainties of the transmit and receive arrays are estimated in a closed-form solution. These gain-phase uncertainties are

used to calibrate the arrays, and the DoA and DoD of the sources can be estimated accurately.

The paper by D. Zhang et al. proposes a method for the source DoA and DoD estimation when using MIMO radars and makes use of compressive sensing approach. In particular, a “joint” sparse matrix reconstruction method is proposed and implemented through the 2D-SL0 algorithm. In this paper, the term “joint” refers to the estimates.

The paper by J.-H. Lin et al. considers the use of circular polarized (CP) dielectric resonator antenna (DRA) coupled by a fractal cross-slot. By adjusting the dimension of the fractal cross-slot property, the resonances of the fractal cross-slot, and the dielectric resonator, two different CP-DRA arrays are designed, specifically a wideband circularly polarized (CP) dielectric resonator antenna (DRA) array and a low-sidelobe-level DRA array. The designed CP DRA arrays have been also realized and measured.

The paper by F.-G. Yan et al. proposes a low-complexity algorithm for the estimation of the source DoA. The proposed algorithm aims at providing estimation accuracy comparable with that of standard MUSIC algorithm but a drastically lower complexity. The underpinning concept relies on an efficient real-valued computation of both the eigenvalue decomposition (EVD) and spectral search.

The paper by D. Zhang et al. proposes a method for the 2D DoA estimation. The idea behind the proposed approach is to exploit the relationship between three parallel uniform linear arrays (ULAs). An ambiguous estimate of the DoA at each array is obtained firstly by using the propagator method (PM). The ambiguity is due to the large spacing between the array elements. The ambiguity is then solved by triangulating the three DoA estimates. Proceeding in this way, there is no need to use subarrays or eigenspace to resolve ambiguity.

The paper by T. Petó and R. Sella proposes an algorithm for clutter cancellation in passive radar systems. The proposed algorithm jointly exploits spatial and temporal information of a receiving array in a passive radar system. The proposed approach differs however from STAP processing since the clutter is cancelled before applying any beamspace processing, and this allows to detect targets even in the direction of the direct signal, coming from the illuminator of opportunity (IO). The proposed approach is named space-time adaptive cancellation (STAC).

The paper by C. Chen et al. reports a modified STAP processing algorithm for colocated MIMO radars. The proposed method provides good detection performance even in low SNR (signal to noise ratio) level. The algorithm makes use of the worst-case performance optimization (WCPO) for avoiding target self-nulling effect. Moreover, in the proposed approach, a modified objective function (with respect to D^3 approach) is used to enhance the output signal to interference plus noise ratio (SINR) even in low SNR conditions. The analysis of the proposed method is performed by using simulated dataset.

The paper by D. Yao et al. presents an algorithm for efficient detection of a target embedded in strong radio and clutter interferences in high-frequency surface wave radar (HFSWR). In the proposed approach, the radio and clutter interferences in the main beam are estimated and suppressed

through the dataset collected from auxiliary beams. The robustness versus array amplitude-phase errors is also analyzed in details.

The paper by Y. Lai et al. proposes to use a dual monopole cross-loop (MCL) antenna array to improve the performance of sea clutter echo DoA estimation of a HFR system for sea current measures. An analysis on pointing errors with respect to the number of array elements has shown that a MLC antenna with 2 or 3 elements provides significant improvement in the sea clutter echo DoA estimation. Moreover, the examination of the interelement spacing against performance shows that a spacing greater than the theoretical limits of half a wavelength is allowed. The performance improvement has been validated through on-field trials.

*Elisa Giusti
Piotr Samczynski
Maria-Pilar Jarabo-Amores
Amerigo Capria*

Research Article

Space-Time Adaptive Cancellation in Passive Radar Systems

Tamás Pető  and Rudolf Seller

Broadband Infocommunication and Electromagnetic Theory, Budapest University of Technology and Economics, 1111 Egrý József St. 18 Building V1, Budapest, Hungary

Correspondence should be addressed to Tamás Pető; peto@hvt.bme.hu

Received 26 September 2017; Accepted 22 November 2017; Published 22 May 2018

Academic Editor: Amerigo Capria

Copyright © 2018 Tamás Pető and Rudolf Seller. This is an open access article distributed under the Creative Commons Attribution License, which permits unrestricted use, distribution, and reproduction in any medium, provided the original work is properly cited.

A critical issue in the realization of passive radar systems is the effective suppression of the zero Doppler interference (ZDI). The performance of the clutter cancellation relies much on the used algorithms. Several state-of-the-art approaches consist in the independent use of spatial and temporal algorithms for ZDI suppression. In this paper, a novel interference cancellation algorithm is proposed, which jointly exploits the available information from both space and time domains. We call this novel method Space-Time Adaptive Cancellation (STAC), and it differs from previous schemes included among the tools of Space-Time Adaptive Processing (STAP). The STAC algorithm is able to cancel out the high power direct and multipath signals on all the surveillance antenna channels prior to the beamforming and other space domain processing methods. The proposed preprocessing technique facilitates the detection of targets even in the direction of the illuminator or large static scatterers. Moreover, the interference rejection capability is also enhanced in the space domain. The performance of the presented algorithm is verified through simulations and field measurements. The experiments show improvement over the currently available filtering techniques.

1. Introduction

The detection performance of passive radars is strongly limited by the direct and zero Doppler multipath signals from the used illuminator of opportunity (IO). The ambiguity function of the typically available reference signals (e.g., Digital Video Broadcasting-Terrestrial (DVB-T)) often has limited dynamic range. Therefore, a target can only be detected when its corresponding correlation peak can rise above the side lobes of the reference signal components. This is the so-called masking effect that appears in the case when unwanted echoes exist in the received signal in addition to the useful target reflection [1]. In recent times, the ZDI suppression is an actively researched field of passive radars.

Recently published papers present the applicability and effectiveness of spatial filtering algorithms. One of the most commonly used adaptive beamformers is the minimum variance distortionless response (MVDR) algorithm. It performs the filtering based on the knowledge of the target direction of arrival (DOA). The beampattern is evolved by these kinds of

algorithms in a way that it places nulls in the direction of high power interferences that are uncorrelated with the desired signal. The operation of these algorithms is widely inspected in passive radar scenarios [2–9].

Besides the application of spatial filtering by means of digital beamforming, also the adaptive temporal cancellation methods have a significant role in ZDI suppression. These techniques in passive radar scenario utilize the available reference signal to cancel out the zero Doppler-shifted and time-delayed replicas of the transmitted illumination signal. These procedures are quite different in implementation but solve the Wiener filtering problem without exception. The resulting FIR filter produces the sum of the properly weighted and delayed replicas of the reference signal, which is then subtracted from the surveillance channel [9–16].

As the proper interference suppression has major importance in passive radar systems, the spatial and temporal filtering must be utilized simultaneously. The traditional procedure is to combine the antenna channels with the surveillance beamformer and in the second stage perform the

temporal filtering. This implementation is the straightforward way. In [9], the system performs the optimal MVDR beamforming in the first stage and then filters the residual direct path interference with the CLEAN algorithm. The same filtering schema can be seen in [6, 15, 17, 18].

The application of the filtering methods in this way may encounter some limitation as the beamforming in the first stage wastes system resources. The reference-correlated direct and multipath signals can be effectively suppressed in the time domain where the resources are quite cheap. In contrast, for the elimination of a signal component in the space domain, a full coherent antenna receiver channel is required (including antenna element, RF front-end, digitalization, and beam space processing stages, resp.). Moreover, the spatial degrees of freedom can be utilized much more favorably to the suppression of nonreference-correlated interferences. Another problem is that beamforming techniques for direct path suppression blind the passive radar systems in the direction of the IO [3, 12]. Avoiding blindness in the direction of high power interferences could be especially important where high azimuth coverage is required [17]. Villano et al. [3] proposed the application of principal eigenvalue beamformer to avoid blind zones. This method places nulls only in the direction of the most dominant clutter components. For this reason, the suppression performance degrades. It would be rather advantageous to filter the antenna channels in the time domain first; then, the adaptive beamformer would receive a cleaner input resulting in a better distribution of the system resources and more enhanced detection. A processing scheme that performs time domain filtering on the surveillance antenna channels and then applies beamforming in the range-Doppler domain is used by the SMARP system in [5].

The implementation of this preprocessing scheme is not straightforward as the direct and independent filtering of the antenna channels (as implemented in [5]) may worsen the situation due to the fact that spatial information is disregarded. Thus, research has been carried out in this field.

The proposed algorithm is a combination of spatial and temporal filtering, using the information available from both domains to effectively cancel out the direct and multipath signals. The most outstanding feature of the proposed filtering procedure is that targets can be detected also in the direction of the high power IO. As the direct path interferences are totally cancelled prior to the beamspace processing, the applied beamformer will not place nulls in the direction of the IOs; hence, the target reflection will not be suppressed unintentionally.

Let us definitely distinguish the proposed prefiltering algorithm from the widely used STAP as the latter is mainly applied on moving platforms and operates in the angular and Doppler domain. The STAP uses the so-called spatiotemporal steering vector to match the desired signal component to the received multichannel signal matrix. In contrast, we use the term cancellation to indicate that the removed clutter components are reconstructed and subtracted at the receiver side. In Section 2, the considered space-time signal model is introduced. In Section 3, the currently used clutter cancellation techniques and the proposed prefiltering method are

described. Its configuration and fast implementation techniques are also presented in detail. Finally, the presented method is validated through simulations (Section 5) and field trials (Section 6).

2. Space-Time Interference Model

A proper signal model is constructed at the first place. The signal propagation paths of a typical passive detection scenario are illustrated in Figure 1. The passive radar receives the emitted illuminator signal on a number of different signal paths. Besides the useful target reflection, direct and multipath signals also appear in the received signal on the surveillance antenna. In the case of Digital Video Broadcasting-Terrestrial (DVB-T) illumination, it is common to use the nearby transmitter stations in single-frequency network mode, where all the transmitter towers transmit the same signal on the same frequency with finely tuned delays. This effect complicates further the situation [7].

Let us assume that the sampled illuminator signal transmitted from one of the towers is $s[n]$, where n denotes the discrete time index. The k sample time delayed signal path has the α_k complex coefficient, which describes its propagation factor. In addition, we can assign DOA information to every incident signal component. For this extension, an antenna array is assumed on the receiving side. We must also distinguish the signal components in the received signal, which has the same time delay (k) but comes from a different DOA. $\mathbf{a}(\vartheta_{k,q})$ denotes the array response vector which belongs to the signal path that has k time delay and comes from the q th incident angle. Correspondingly, we need to introduce different propagation factors to the impinging signals that have different DOAs but have the same time delay. Thus, we use $\alpha_{k,q}$ instead of α_k . Figure 2 illustrates the introduced signal path notation in detail. The dashed lines show the constant bistatic range ellipsoids, while the solid lines represent the signal propagation paths. On the k th bistatic ellipsoid Q_k , a number of signal paths with different DOAs are considered. In Figure 2, $Q_0 = 3$ and $Q_1 = 2$, respectively.

For an M element equidistant linear antenna system, the array response vector has the following form:

$$\mathbf{a}(\vartheta_{k,q}) = \left[1 \quad e^{j\psi_{k,q}} \quad e^{2j\psi_{k,q}} \quad \dots \quad e^{(M-1)j\psi_{k,q}} \right]^T, \quad (1)$$

where $\psi_{k,q} = (2\pi/\lambda)d \cos(\vartheta_{k,q})$, λ is the wavelength of the center frequency of the source signal, d denotes the antenna element spacing, and the direction of arrival for the impinging signal is denoted by $\vartheta_{k,q}$. The antenna element index is denoted by m , where $0 < m \leq M - 1$ holds. Thus, $\mathbf{a}(\vartheta_{k,q}) \in \mathbb{C}^{M \times 1}$. Correspondingly, the m th channel of the received surveillance signal is described by

$$\begin{aligned} x_s^{(m)}[n] = & \sum_{k=0}^{K-1} \sum_{q=0}^{Q_k-1} \alpha_{k,q} s[n-k] e^{j2\pi(f_{k,q}/f_s)n} e^{j\psi_{k,q}m} \\ & + \sum_{d=0}^{D-1} \alpha_d^i[n] e^{j\psi_d m} + \xi_m[n]. \end{aligned} \quad (2)$$

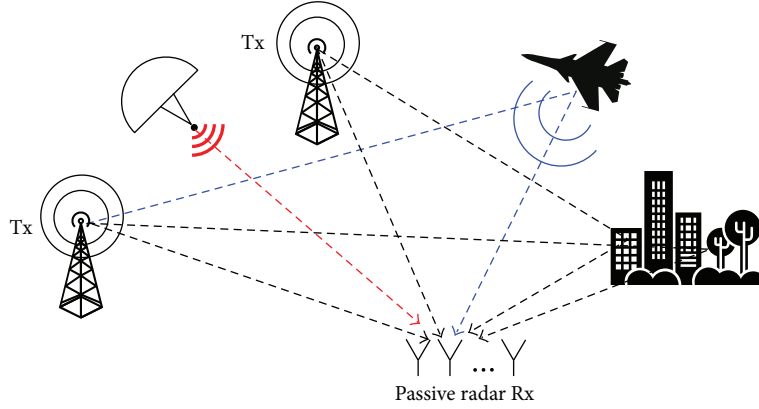


FIGURE 1: Signal model of the passive radar scenario.

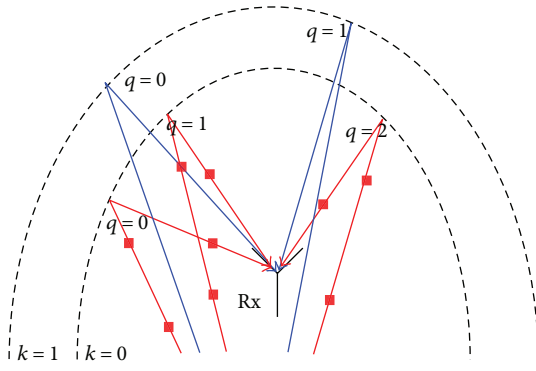


FIGURE 2: Signal path notation.

In (2), $f_{k,q}$ denotes the Doppler frequency of the current signal component, while f_s is the sampling frequency. For ZDI signal components, $f_{k,q} = 0$, and for the desired target reflection component, $f_{j,p} \neq 0$ is assumed. K is the number of considered time delays, which is absolutely determined by the environment. We also consider D interference sources that are statistically independent and uncorrelated with the illuminator signal $s[n]$. Thus, $\mathbf{E}\{s[n]i_d[n]\} = \mathbf{E}\{s[n]\}\mathbf{E}\{i_d[n]\}$, where $\mathbf{E}\{\cdot\}$ denotes the calculation of the expected value. $\psi_d = (2\pi/\lambda)d \cos(\theta_d)$ describes the phase shift of the d th interference component that is arriving to the array from the θ_d angle. α_d denotes the propagation factor of the d th interference component. The n th sample of signal-independent noise collected by the m th receiver channel is denoted by $\xi_m[n]$. A more compact form of the received signal array $\mathbf{x}_s[n] \in \mathbb{C}^{1 \times M}$ can be formulated using the array response vector $\mathbf{a}(\theta)$; thus,

$$\begin{aligned} \mathbf{x}_s[n]^T &= \sum_{k=0}^{K-1} \sum_{q=0}^{Q_k-1} \alpha_{k,q} s[n-k] e^{j2\pi(f_{k,q}/f_s)n} \mathbf{a}(\theta_{k,q}) \\ &+ \sum_{d=0}^{D-1} \alpha_d i_d[n] \mathbf{a}(\theta_d) + \boldsymbol{\xi}[n]. \end{aligned} \quad (3)$$

The multichannel noise vector at the n th time instant is denoted by $\boldsymbol{\xi}[n] \in \mathbb{C}^{M \times 1}$. In the following investigations, we

assume that the illuminator signal $s[n]$ and the interference signals $i_d[n]$, $d = 0, \dots, D-1$ are wide-sense stationary (WSS) processes with zero mean and unity variance.

$$\mathbf{E}\{s[n-k]\} = \mathbf{E}\{s[n-l]\} = 0, \quad k, l \in \mathbb{N}. \quad (4)$$

Besides this, we can safely consider the case when the received reference signal contains only the transmitted illuminator signal plus uncorrelated noise.

$$x_r[n] = s[n] + \mu[n]. \quad (5)$$

In real situations, it can be fairly guaranteed with the use of high gain antennas. Also for IOs, where digital modulations are applied such as DAB, DVB-T, DVB-S, UMTS, and LTE reference, signal reconstruction techniques are able to provide the clear reference signal [7, 19]. According to the described signal model, we can construct the corresponding adaptive filter.

3. Traditional Clutter Cancellation Algorithms

Let us first define the used reference and surveillance signal vector notations, which will be used in the outlined theoretical description of the filters.

- (i) $x_r[n]$ is the n th signal sample of the reference signal.
- (ii) $x_s^{(m)}[n]$ is the n th signal sample of the m th surveillance antenna channel.
- (iii) $x_f^{(m)}[n]$ is the n th signal sample of the m th filtered surveillance antenna channel.
- (iv) $\mathbf{x}_s[n]$ is a row vector that stores the signal samples of the surveillance antenna channels at the time instant n , $\mathbf{x}_s[n] \in \mathbb{C}^{1 \times M}$.
- (v) $\mathbf{x}_r[n]$ is the reference signal vector, which contains the last recorded K samples starting from the n th signal sample, $n = 0, \dots, N-1$.

$$\mathbf{x}_r[n] = [x_r[n] \quad x_r[n-1] \quad \dots \quad x_r[n-K+1]]^T, \quad \mathbf{x}_r[n] \in \mathbb{C}^{K \times 1}. \quad (6)$$

The signal samples that outlie the coherent processing interval are assumed to equal to zero.

$$x_r[n] = x_s^{(m)}[n] = x_f^{(m)}[n] = 0, \quad \forall n : n < 0, n > N - 1. \quad (7)$$

The used notations for linear algebra operators are the following:

- (i) \mathbf{a}^* is the complex conjugate of the \mathbf{a} vector.
- (ii) \mathbf{A}^H is the Hermitian transpose or the conjugate transpose of the \mathbf{A} matrix.
- (iii) $\mathbf{A} \odot \mathbf{B}$ is the Hadamard product of the two matrices.
- (iv) $\mathbf{A} \otimes \mathbf{B}$ is the Kronecker product of the two matrices.

According to the presented signal model, the main objective of the clutter cancellation is to suppress all the signal components in $x_s[n]$ expecting the target reflection $\alpha_{j,p} s[n-j] e^{j2\pi(f_{j,p}/f_s)n} \mathbf{a}(\theta_{j,p})$.

3.1. Adaptive Spatial Filtering. Adaptive beamformers combine the surveillance antenna channels using a coefficient vector in a way that the interference components are canceled and the desired signal is enhanced. The n th sample of the beam space processed surveillance signal is calculated as follows:

$$y_{sd}[n] = \sum_{m=0}^{M-1} w_m^{(s)*} x_s^{(m)}[n], \quad (8)$$

where $w_m^{(s)}$ is the m th coordinate of the beamformer coefficient vector. $\mathbf{w}^{(s)}$ is chosen in a way to minimize clutter power. The space adaptive processing (SAP) is often realized by the optimum MVDR beamformer. In this case, $\mathbf{w}^{(s)}$ is calculated using the spatial correlation matrix \mathbf{R}_s and the array response vector of the signal of interest $\mathbf{a}(\theta_{j,p})$.

$$\begin{aligned} \mathbf{w}^{(s)} &= \mathbf{R}_s^{-1} \mathbf{a}(\theta_{j,p}), \\ \mathbf{R}_s &= \mathbf{E} \left\{ \mathbf{x}_s[n]^T \mathbf{x}_s[n]^* \right\}. \end{aligned} \quad (9)$$

Other adaptive beamforming techniques may utilize information about the eigenstructure of the spatial autocorrelation matrix [2, 3]. Clearly, the degrees of freedom (DOFs) of the beamformer is equal with the number of antenna elements M ; hence, only $M - 1$ interference component can be dealt with. Also, it is important to note that no information is used regarding the illuminator signal $s[n]$.

3.2. Adaptive Temporal Filtering. Time domain filters subtract the weighted reference signal and its time delayed replicas from the surveillance signal. In systems where the number of receiver channels is limited only, time domain filter can be used $M = 1$, $x_s^{(0)}[n] \rightarrow x_s[n]$.

$$y_{td}[n] = x_s[n] - \sum_{j=0}^{J-1} w_j^{(t)*} x_r[n-j], \quad (10)$$

where $w_j^{(t)}$ is the j th coordinate of the temporal coefficient vector and J is the DOFs of the temporal adaptive filter. $\mathbf{w}^{(t)}$ is calculated using the following expression [20]:

$$\mathbf{w}^{(t)} = \mathbf{R}_t^{-1} \mathbf{r}_t, \quad (11)$$

where \mathbf{R}_t is the temporal autocorrelation matrix and \mathbf{r}_t is the temporal autocorrelation vector.

$$\begin{aligned} \mathbf{R}_t &= \mathbf{E} \left\{ x_r[n] x_r[n]^H \right\}, \\ \mathbf{r}_t &= \mathbf{E} \left\{ x_r[n] x_s[n]^* \right\}. \end{aligned} \quad (12)$$

The calculation of the optimal $\mathbf{w}^{(t)}$ is an active field of researches. According to the sample matrix inversion (SMI) technique, the temporal autocorrelation matrix and the cross-correlation vector are estimated with their sample average. Other techniques such as the variants of the extensive cancellation algorithm (ECA, ECA-B, and ECA-S) apply different time intervals to the coefficient estimation and filtering [10, 14]. Iterative algorithms like the least mean square, normalized least mean square, recursive least squares, and so on update the $\mathbf{w}^{(t)}$ vector from sample to sample [11, 16, 20]. Time domain filtering is a very effective method for the suppression of the time-delayed replicas of the reference signal; however, it is not able to deal with interferences that are non-reference correlated ($i_d[n]$, $d = 0, \dots, D - 1$) or lie outside the time delay range of the filter $s[n-k]$, $k > J$.

3.3. Temporal after Spatial Filtering. In multichannel systems, the combination of spatial and temporal domain filtering is used. The filtering process is preformed in two stages where the first stage beamformer suppresses the unwanted interference components in the space domain and in the second stage the temporal filter cancels the reference signal-correlated ZDI components. It is illustrated in Figure 3.

This filtering procedure is used in many systems [5, 15, 17, 18]. The filtered surveillance signal for this filter scheme can be calculated as follows:

$$y[n] = \sum_{m=0}^{M-1} w_m^{(s)*} x_s^{(m)}[n] - \sum_{j=0}^{J-1} w_j^{(t)*} x_r[n-j], \quad (13)$$

where the beamformer coefficient $w_m^{(s)*}$ is calculated according to Section 3.1 and the time domain filter coefficients are calculated using the algorithm described in Section 3.2 with replacing $x_s[n]$ to $y_{sd}[n]$.

4. Space-Time Prefiltering

The main point is to realize that utilizing the spatial filtering to suppress the time-delayed replicas of the illuminator signal may result in a waste of resources. Adaptive beamforming techniques such as the MVDR try to place nulls in the direction of the interferences. It can be proved without difficulty that the beamformer response in the direction of an interference is dependent on the power of the interferer.

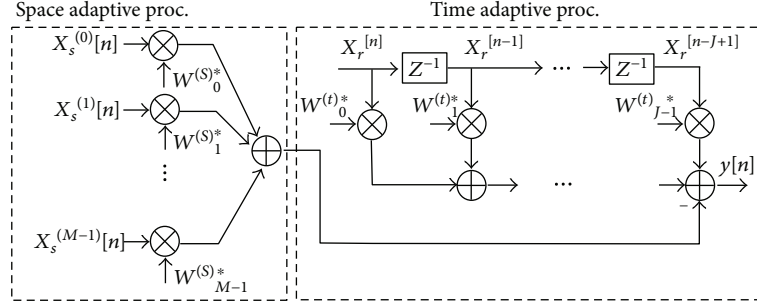


FIGURE 3: Temporal after spatial filter.

$$\mathbf{w}^{(s)H} \mathbf{a}(\theta_i) = \frac{\mathbf{a}(\theta_i)^H \mathbf{Q}^{-1} \mathbf{a}(\theta_i)}{1 + \sigma_i^2 \mathbf{a}(\theta_i)^H \mathbf{Q}^{-1} \mathbf{a}(\theta_i)}, \quad (14)$$

where $\mathbf{a}(\theta_i)$ is the array response vector of the particular interference, \mathbf{Q} is the spatial correlation matrix when the interference is not present, and σ_i^2 denotes the averaged power of the interference component. In most cases, the direct and multipath zero Doppler signals received from the used illuminator have very high power relative to the thermal noise floor and the target reflection $|\alpha_{k,q}^2| \gg \mathbf{E}\{|\xi_m[n]|^2\}$, $|a_{k,q}|^2 \gg |a_{j,p}|^2$, $k = 0, \dots, K-1$, $q = 0, \dots, Q_k-1$. Thus, the first stage spatial filter consumes the hardware resources to cancel out the high power ZDIs. At the same time, when the target direction is close to the incident angle of a clutter component $\theta_{j,p} \approx \theta_{k,q}$ or $\theta_{j,p} \approx \theta_d$, the target reflection will be suppressed by the null formed into the direction of the high power interference. This behaviour is also proved with simulations presented in Section 5.

However, these interference components can be eliminated with using purely signal processing resources in the time domain. The idea behind the following presented filtering technique is to apply time domain filtering prior to the adaptive beamformer to save resources.

4.1. Spatial Extension of the Transversal Filter. Before we introduce the optimal filter regarding the previously expressed signal model, we show a straightforward space-time filtering scheme, which is the simplest solution but unfortunately inadequate when adaptive beamformers are used after. One can say that the surveillance antenna channels can be prefiltered by M individual temporal filter. In this implementation, the filtered output of the antenna channels is described by (15).

$$x_f^{(m)}[n] = x_s^{(m)}[n] - \sum_{k=0}^{K-1} w_{k,m}^* x_r[n-k]. \quad (15)$$

We can rewrite this formula into a matrix equation

$$\mathbf{x}_f^T[n] = \mathbf{x}_s^T[n] - \mathbf{W}^H \mathbf{x}_r[n], \quad (16)$$

where \mathbf{W} is the filter coefficient matrix in which each column \mathbf{w}_m is assigned to an antenna channel. Thus, $w_{k,m}$ is the weight coefficient for the k time delay replica on the m th antenna channel. The maximum assumed time delay is K .

The optimal vector for the m th surveillance antenna channel is calculated using the following formula:

$$\mathbf{w}_m = \mathbf{R}_t^{-1} \mathbf{r}_t^{(m)}, \quad (17)$$

where $\mathbf{r}_t^{(m)} = \mathbf{E}\{x_r[n]x_s^{(m)*}[n]\}$ is the cross-correlation vector of the m th channel. As it is obvious from the formula, it does not use spatial information ($\mathbf{a}(\theta)$) in any sense to produce its output. Moreover, there is not any information coupling between the channels; thus, the signals are passed through the filter completely independently. In the optimal scenario, where there are not any undesirable RF effects on the antenna channels, this filtering scheme can work properly; however, in a real environment, it is likely to fail. This behaviour is supported by field measurement results in Section 6.3. Moscardini et al. [6] have made efforts to investigate a similar filter structure. They implemented the spatial adaptive processor in the range-Doppler domain where the individual range-Doppler matrices are obtained from the time domain filtered surveillance antenna channels. However, in their work, the spatial correlation matrix for the beamformer is estimated in a different way from the range-Doppler map. The same signal processing chain is addressed in [7].

4.2. Space-Time Adaptive Cancellation (STAC). Following the previously described signal model (3), one can construct the corresponding filter structure to cancel the ZDI components. It is illustrated in Figure 4. The filter first prepares the time-delayed replicas of the reference signal; then each replica is extended to the space domain by applying the associated steering vectors. Finally, the proper complex weight coefficient of the current signal path is adjusted, which sets the amplitude and the common phase shift. The temporal dimension of the filter is K ; thus, the clutter is expected on the first K range cells. Besides this, in each of the K ranges, Q_k , $k = 0, \dots, K-1$ interference directions are assumed.

Accordingly, the total number of considered interference components is $Q = \sum_{k=0}^{K-1} Q_k$. The output of the filter is described by

$$x_f^{(m)}[n] = x_s^{(m)}[n] - \sum_{k=0}^{K-1} \sum_{q=0}^{Q_k-1} w_{k,q}^* x_r[n-k] e^{j\psi_{k,q}m}. \quad (18)$$

In (18), the weight coefficient of the filter is denoted by $w_{k,q}$. The output of this filter can also be represented in a matrix form using

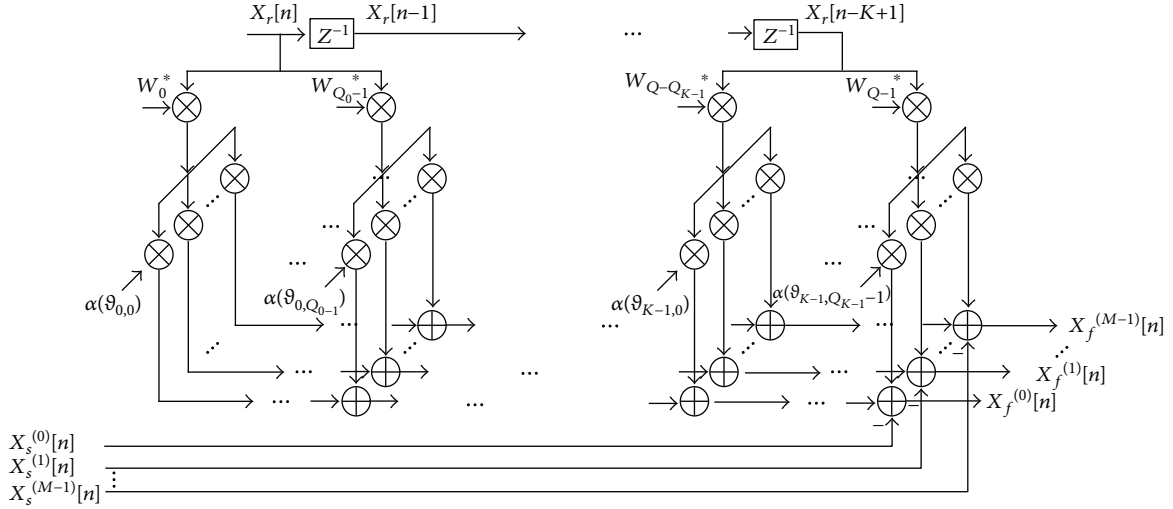


FIGURE 4: Structure of the proposed interference canceller filter block.

$$\mathbf{x}_f^{(m)}[n] = \mathbf{x}_s^{(m)}[n] - \mathbf{w}^H \mathbf{x}_{rQ}[n] \odot \Psi^{(m)}, \quad (19)$$

where $\Psi^{(m)}$ is a vector that contains the proper phase shift values corresponding to the direction of arrival on the m th channel and $\mathbf{x}_{rQ}[n]$ is the extension of the previously described $\mathbf{x}_r[n]$ reference signal vector

$$\mathbf{x}_{rQ}[n] = \begin{bmatrix} \mathbf{i}_{Q_0}^T \mathbf{x}_r[n] & \mathbf{i}_{Q_1}^T \mathbf{x}_r[n-1] & \dots & \mathbf{i}_{Q_{K-1}}^T \mathbf{x}_r[n-K+1] \end{bmatrix}, \quad (20)$$

where \mathbf{i}_{Q_k} is a vector, which has Q_k unity elements.

$$\mathbf{x}_{rQ}[n] = \begin{bmatrix} \mathbf{x}_r[n] \\ \vdots \\ \mathbf{x}_r[n] \\ \mathbf{x}_r[n-1] \\ \vdots \\ \mathbf{x}_r[n-1] \\ \vdots \\ \mathbf{x}_r[n-K+1] \\ \vdots \\ \mathbf{x}_r[n-K+1] \end{bmatrix} \left. \begin{array}{l} \left. \begin{array}{l} \vdots \\ \vdots \end{array} \right\} Q_0 \\ \left. \begin{array}{l} \vdots \\ \vdots \end{array} \right\} Q_1 \\ \left. \begin{array}{l} \vdots \\ \vdots \end{array} \right\} Q_{K-1} \end{array} \right\} (21)$$

$$\Psi^{(m)} = \begin{bmatrix} e^{j\psi_{0,0m}} \\ \vdots \\ e^{j\psi_{0,Q_0-1m}} \\ \vdots \\ e^{j\psi_{K-1,0m}} \\ \vdots \\ e^{j\psi_{K-1,Q_{K-1}-1m}} \end{bmatrix} \left. \begin{array}{l} \left. \begin{array}{l} \vdots \\ \vdots \end{array} \right\} Q_0 \\ \left. \begin{array}{l} \vdots \\ \vdots \end{array} \right\} Q_{K-1} \end{array} \right\} (21)$$

It must be emphasized that in (19) the \mathbf{w} weight coefficient vector is common to all channels and $\mathbf{w}, \mathbf{x}_{rQ}[n], \Psi^{(m)} \in \mathbb{C}^{Q \times 1}$. In this case, all the antenna channels use the same \mathbf{w} vector and the individual channels are linked together through the $\Psi^{(m)}$ vectors. In order to perform the filtering, the optimal coefficient vector for this model must be determined. Let us define the performance function $J[n]$ as the expected value of the squared power of the filter error. Our main goal is to find the optimal \mathbf{w} coefficient vector for this filter architecture that minimizes the performance function. We can follow the well-known steps of the derivation of the Wiener filter to obtain the final equation for the weight vector calculation [21].

$$\arg \min_{\mathbf{w}} \{J[n]\} = \arg \min_{\mathbf{w}} \{\mathbf{e}[n] \mathbf{e}[n]^H\}, \quad (22)$$

where $\mathbf{e}[n] = \mathbf{x}_f[n]$ is defined as the error vector. In this notation, $\mathbf{e}[n]$ is a row vector.

$$\mathbf{e}[n] = \mathbf{x}_f[n] = \begin{bmatrix} x_f^{(0)}[n] & x_f^{(1)}[n] & \dots & x_f^{(M-1)}[n] \end{bmatrix} \in \mathbb{C}^{1 \times M}. \quad (23)$$

The error vector and the vector of the filtered channel outputs are then calculated with the following matrix formula:

$$\mathbf{e}[n] = \mathbf{x}_f[n] = \mathbf{x}_s[n] - \mathbf{w}^H \mathbf{S}_Q \odot \Psi, \quad (24)$$

where the matrix \mathbf{S}_Q is the extension of the reference signal vector and the Ψ matrix contains the phase compensations for the associated reference signal time-delayed replicas. This phase compensation term is related to the phased array surveillance antenna.

$$\begin{aligned} \mathbf{S}_Q[n] &= [\mathbf{x}_{rQ}[n] \quad \mathbf{x}_{rQ}[n] \quad \dots \quad \mathbf{x}_{rQ}[n]] \in \mathbb{C}^{Q \times M}, \\ \Psi &= [\psi^{(0)} \quad \psi^{(1)} \quad \dots \quad \psi^{(M-1)}] \in \mathbb{C}^{Q \times M}. \end{aligned} \quad (25)$$

Let us note that the l th row of the Ψ matrix is the array response vector corresponding to the l th signal component $\Psi_{l,*} = \mathbf{a}(\theta_l)^T$. As Ψ contains information about the direction of arrival of the clutter components, we can call it as the clutter DOA matrix.

$$\Psi = [\mathbf{a}(\theta)_{0,0} \quad \mathbf{a}(\theta)_{0,1} \quad \dots \quad \mathbf{a}(\theta)_{0,Q_0-1} \quad \dots \quad \mathbf{a}(\theta)_{K-1,Q_{K-1}-1}]^T. \quad (26)$$

Using the above described notations, $J[n]$ can be written as follows:

$$\begin{aligned} J[n] &= \mathbf{E}\{|\mathbf{x}_s[n]|^2\} - \mathbf{E}\{\mathbf{x}_s[n](\mathbf{S}_Q \odot \Psi)^H\} \\ &\quad \cdot \mathbf{w} - \mathbf{w}^H \mathbf{E}\{(\mathbf{S}_Q \odot \Psi)\mathbf{x}_s[n]^H\} \\ &\quad + \mathbf{w}^H \mathbf{E}\{(\mathbf{S}_Q \odot \Psi)(\mathbf{S}_Q \odot \Psi)^H\}\mathbf{w}. \end{aligned} \quad (27)$$

Then, \mathbf{w} is found by solving (28) [21].

$$\frac{\partial}{\partial w_i} J[n] = 0, \quad \forall i \in \{0, \dots, Q-1\}. \quad (28)$$

We can write the solution in a matrix form as follows:

$$\mathbf{w} = \mathbf{R}_Q^{-1} \mathbf{r}_Q, \quad (29)$$

where \mathbf{R}_Q is known, respectively, as the autocorrelation matrix and \mathbf{r}_Q as the cross-correlation vector. These terms are defined as follows:

$$\begin{aligned} \mathbf{R}_Q &= \mathbf{E}\{(\mathbf{S}_Q[n] \odot \Psi)(\mathbf{S}_Q[n] \odot \Psi)^H\} \in \mathbb{C}^{Q \times Q}, \\ \mathbf{r}_Q &= \mathbf{E}\{(\mathbf{S}_Q \odot \Psi)\mathbf{x}_s[n]^H\} \in \mathbb{C}^{Q \times 1}. \end{aligned} \quad (30)$$

4.3. Coefficient Calculation Method. The autocorrelation matrix and the cross-correlation vector are often estimated using their sample average.

$$\begin{aligned} \hat{\mathbf{R}}_Q &= \frac{1}{N} \sum_{n=0}^{N-1} (\mathbf{S}_Q[n] \odot \Psi)(\mathbf{S}_Q[n] \odot \Psi)^H, \\ \hat{\mathbf{r}}_Q &= \frac{1}{N} \sum_{n=0}^{N-1} (\mathbf{S}_Q[n] \odot \Psi)\mathbf{x}_s^H[n]. \end{aligned} \quad (31)$$

It is often called the sample matrix inversion (SMI) technique. The calculation of these terms is a very computationally intensive task; thus, in the following, a fast calculation technique is introduced.

Let us assume that the number of considered clutter components is a constant value for all ranges $Q_k = c, k = 0, \dots, K-1$. Note that this assumption does not restrict the operation of the filter and the further theoretical investigations as the weight coefficient corresponding to a nonexisting clutter component will go to zero when N goes to infinity. It can be proved without difficulty that \mathbf{R}_Q can be decomposed to the

Hadamard product of a temporal autocorrelation matrix and a clutter DOA correlation matrix.

$$\mathbf{R}_Q = \mathbf{R}_Q^{(t)} \odot \mathbf{R}_Q^{(\Psi)}, \quad (32)$$

$$\mathbf{R}_Q^{(t)} = \mathbf{E}\{\mathbf{S}_Q[n]\mathbf{S}_Q[n]^H\}, \quad (33)$$

$$\mathbf{R}_Q^{(\Psi)} = \Psi\Psi^H. \quad (34)$$

In this form $\mathbf{R}_Q^{(t)}$ is a block matrix, where the elements in each block correspond to the elements of the traditional autocorrelation matrix used in many time domain least squares filter. In a consequence, $\mathbf{R}_Q^{(t)}$ can be obtained very fast by simply calculating the standard temporal autocorrelation matrix and extend it to a block matrix.

$$\mathbf{R}_Q^{(t)} = \mathbf{E}\{x_r[n]x_r[n]^H\} \otimes \mathbf{I}_c = \mathbf{R}_t \otimes \mathbf{I}_c, \quad (35)$$

where $\mathbf{I}_c \in \mathbb{R}^{c \times c}$ is an all-ones matrix.

Besides this, we can develop a closed form to calculate the $\mathbf{R}_Q^{(\Psi)}$ clutter DOA autocorrelation matrix in the knowledge of the clutter DOA incident angles $(\theta_{k,q}, k = 0, \dots, K-1, q = 0, \dots, Q_k-1)$. The i th and j th elements can be calculated as follows:

$$R_{Qij}^{(\Psi)} = \mathbf{a}(\theta_{k_1,q_1})^T \mathbf{a}(\theta_{k_2,q_2})^* = \frac{e^{j\beta d(\cos(\theta_{k_1,q_1}) - \cos(\theta_{k_2,q_2}))M} - 1}{e^{j\beta d(\cos(\theta_{k_1,q_1}) - \cos(\theta_{k_1,q_1}))} - 1}, \quad (36)$$

where the i th row selects the clutter component with (k_1, q_1) range and direction indexes, while the j th column selects the clutter component with (k_2, q_2) indexes.

A fast formula can also be developed for the calculation of the \mathbf{r}_Q cross-correlation vector. Using the same principle, we can define the cross-correlation vector of the m th channel:

$$\mathbf{r}_Q^{(m)} = \mathbf{E}\{\mathbf{x}_{rQ}[n]x_s^{(m)*}[n]\}, \quad (37)$$

that is, the block extension of the standard temporal cross-correlation vector of the m th channel.

$$\mathbf{r}_Q^{(m)} = \mathbf{E}\{\mathbf{x}_r[n]x_s^{(m)*}[n]\} \otimes \mathbf{i}_c = \mathbf{r}_t^{(m)} \otimes \mathbf{i}_c, \quad (38)$$

where $\mathbf{i}_c \in \mathbb{R}^{c \times 1}$ is an all-ones vector. Finally, the \mathbf{r}_Q vector can be calculated as the sum of the phase compensated cross-correlation vectors of the individual antenna channels.

$$\mathbf{r}_Q = \sum_{m=0}^{M-1} \Psi^{(m)} \odot \mathbf{r}_Q^{(m)}. \quad (39)$$

Using the presented method, we are able to reduce the computation costs by calculating only a $K \times K$ sized autocorrelation matrix and M piece of K dimensional cross-correlation vector instead of a $Q \times Q$ and M piece of $Q \times 1$ dimensional terms, respectively (we assumed $Q = K_c$ for simplicity).

Also note that however $\mathbf{R}_Q^{(t)-1} = \mathbf{R}_t^{-1} \otimes \mathbf{I}_c^{-1}$, the fast formula for $(\mathbf{A} \odot \mathbf{B})^{-1}$ is not known; thus, the inversion of the $Q \times Q$ dimensional \mathbf{R}_Q matrix can not be avoided.

4.4. Clutter DOA Estimation. One essential question remains in the implementation of the STAC filter that is the clutter DOA information. However, one can calculate the filter coefficient using (29); the Ψ clutter DOA matrix must be a known preliminary. In practical cases, this information is not an available preliminary; thus, we must obtain it from the received signal. One way to gain knowledge of the $\theta_{k,q}$, $k = 0, \dots, K-1$, $q = 0, \dots, Q_k-1$ angles is to perform several DOA estimations. It is vital to the operation of the STAC algorithm that the incident angles of the clutter components arriving from different ranges must be distinguished. It is essentially needed to prepare the \mathbf{S}_Q and Ψ matrices. We can manage to extract this information by performing DOA estimations for each range bin. In an ideal case, the surveillance signal array consists only of the following terms for the DOA estimation at the l th range.

$$\mathbf{u}_l[n] = \sum_{q=0}^{Q_l-1} \alpha_{l,q} s[n-k] \mathbf{a}(\theta_{l,q}). \quad (40)$$

According to the considered signal model in (3), the other unwanted signal components should not present $\alpha_{k,q} = 0, \forall k = 0, \dots, K-1, k \neq l, \forall q = 0, \dots, Q_k-1$ and $\alpha_d = 0, \forall d = 0, \dots, D-1$. A straightforward method to approximate \mathbf{u}_l is to apply coherent integration as the $s[n-k]$, $k = 0, \dots, K-1$ is known from the reference signal $x_r[n]$.

$$\begin{aligned} \hat{\mathbf{u}}_l[n] &= \sum_{n=0}^{N-1} \mathbf{x}_s[n]^T x_r[n-k]^*, \\ \mathbf{E}\{\hat{\mathbf{u}}_l[n]\} &= \sum_{q=0}^{Q_l-1} \alpha_{l,q} |s[n-k]|^2 \mathbf{a}(\theta_{l,q}). \end{aligned} \quad (41)$$

Without utilizing coherent integration at this stage, the estimated DOA angles may suffer from the effects of the low SNR condition and the cochannel interferences that result in inaccurate estimation. This behaviour of the DOA estimators is deeply investigated in the literature [22]. For the estimation of the DOA of the clutter components at the l th range, we can define the spatial correlation matrix as follows:

$$\mathbf{R}_s^{(l)} = \mathbf{E}\{\mathbf{u}_l[n] \mathbf{u}_l[n]^H\}. \quad (42)$$

It is often estimated by its sample average,

$$\hat{\mathbf{R}}_s^{(l)} = \sum_{n=0}^{N-1} \mathbf{u}_l[n] \mathbf{u}_l[n]^H. \quad (43)$$

After the spatial correlation matrix, $\mathbf{R}_s^{(l)} \in \mathbb{C}^{M \times M}$ has been obtained; the DOA of the desired signal components can be estimated using traditional DOA estimation methods like multiple signal classification (MUSIC), Capon's estimation or Burg's Maximum Entropy Method (MEM), and

so on. Nevertheless, problem may arise from the fact that zero Doppler signals with the same time delay are totally correlated.

$$\mathbf{E}\left\{s[n-k] \mathbf{a}(\theta_{k,q_i}) s[n-k]^* \mathbf{a}(\theta_{k,q_j})^H\right\} \neq 0. \quad (44)$$

The MEM shows higher resistance against the correlated sources than Capon's or the MUSIC method. It may correctly detect the number of correlated sources, but the results will suffer from inaccuracy. Despite this fact, it is feasible in all cases and could be a reasonable choice. The power angular density with the MEM can be calculated using [23]

$$P_{\text{MEM}}(\theta) = \frac{1}{\mathbf{s}(\theta)^H \mathbf{r}_j \mathbf{r}_j^H \mathbf{s}(\theta)}, \quad (45)$$

where $\mathbf{s}(\theta)$ denotes the steering vector and \mathbf{r}_j is the j th column of the inverse of the spatial correlation matrix. The MUSIC algorithm is often used in phased array systems due to its high angle resolution capability. It utilizes the eigenstructure of the spatial correlation matrix to find the direction of uncorrelated sources. The spatial spectrum can be estimated with the MUSIC using

$$P_{\text{MUSIC}}(\theta) = \frac{1}{\mathbf{s}(\theta)^H \mathbf{E} \mathbf{E}^H \mathbf{s}(\theta)}, \quad (46)$$

with \mathbf{E} being the noise subspace matrix, which is spanned by the eigenvectors corresponding to the smallest eigenvalues of the $\mathbf{R}_s^{(l)}$ matrix [24]. Since the basic algorithm (Schmidt—1977, Bienvenu—1979) fails to resolve correlated sources, a number of research have been carried out to resolve this weakness. Widespread preprocessing techniques for resolving the coherent source localization problem are the forward-backward averaging and the spatial smoothing [22, 23, 25]. The spatial correlation matrix lost from its rank and became nondiagonal and singular in a coherent environment. These methods are intended to restore the full rank of the spatial correlation matrix. They rely on the fact that the array response vector $\mathbf{a}(\theta)$ in uniform linear arrays is the same when its elements are reversed and conjugated. The forward-backward averaging is able to decorrelate two sources by replacing the standard spatial correlation matrix with its forward-backward smoothed version [24]. This matrix is given by

$$\mathbf{R}_{s-fb}^{(l)} = \frac{1}{2} \mathbf{R}_s^{(l)} + \mathbf{J} \mathbf{R}_s^{(l)*} \mathbf{J}, \quad (47)$$

where $\mathbf{J} \in \mathbb{C}^{M \times M}$ is the exchange matrix, which is defined as follows:

$$\mathbf{J} = \begin{bmatrix} 0 & \dots & 0 & 1 \\ 0 & \dots & 1 & 0 \\ \vdots & & \vdots & \vdots \\ 1 & \dots & 0 & 0 \end{bmatrix}. \quad (48)$$

The spatial smoothing technique can be applied to resolve even more coherent sources in the expense of

decreasing aperture. Using the forward-backward spatial smoothing technique, it is possible to detect up to $2M/3$ coherent sources. To achieve this improvement, the antenna array is divided into several subarrays. Let us denote the subarray size with L . Then from an M element antenna array, $P = M - L + 1$ subarray can be formed. The subarray formation is illustrated in Figure 5.

The signal vector of the p th forward subarray is made by the selection of the corresponding channels in the surveillance signal array. In this particular case, we use the coherent integrated $\mathbf{u}_l[n]$ channel vector instead of the raw surveillance channel vector $\mathbf{x}_s[n]$. Then, the forward subarray is denoted by $\mathbf{v}_p^f[n]$ and can be mathematically described by the following formula:

$$\mathbf{v}_p^f[n] = \begin{bmatrix} u_l^{(p)}[n] & u_l^{(p+1)}[n] & \dots & u_l^{(p+L-1)}[n] \end{bmatrix}^T, \quad (49)$$

where $p \in \mathbb{N}, p = 0, \dots, P - 1$. In contrast to the forward subarray selection, we can define the p th backward subarray as

$$\mathbf{v}_p^b[n] = \begin{bmatrix} u_l^{(M-1-p)}[n] & u_l^{(M-1-p-1)}[n] & \dots & u_l^{(M-1-p-L+1)}[n] \end{bmatrix}^H. \quad (50)$$

Note that in the backward subarray the elements are also complexly conjugated. Now the forward-backward spatially smoothed correlation matrix can be defined as

$$\mathbf{R}_{s-ss}^{(l)} = \sum_{n=0}^{N-1} \sum_{p=0}^{P-1} \mathbf{v}_p^f[n] \mathbf{v}_p^f[n]^H + \mathbf{v}_p^b[n] \mathbf{v}_p^b[n]^H. \quad (51)$$

It must be emphasized that using this technique the effective aperture of the antenna system is decreased to L from M antenna elements, $\mathbf{R}_{s-ss}^{(l)} \in \mathbb{C}^{L \times L}$ [23, 24]. Qing and Ruolun made efforts to determine the sufficient and necessary conditions to decorrelate the signal sources with spatial-smoothing. Their work can be very useful to understand the limitations of this technique [25].

After all, the proposed overall clutter DOA estimation procedure is illustrated in Figure 6. As it was described previously at the first step, the signal of interest is enhanced with coherent integration. After that, forward-backward averaging or spatial-smoothing is preformed in order to decorrelate the reference signal components that have the same time delay. After the spatial-correlation matrix is obtained, the DOA estimation method can be used to determine the power angular density information.

In the next step, the dominant peaks must be found from the DOA method output. The peak find process generates a list of peaks that may correspond to the DOA of the sought signal components. Antenna systems that have interelement spacing larger than half-wavelength suffer from the aliasing effect [3, 26, 27]. This results in multiple peaks corresponding to the same impinging signal. Of course, it is sufficient to select only one DOA for the filtering algorithm from among the overlapped peaks. Thus, to save resources, we may eliminate the peaks lying outside

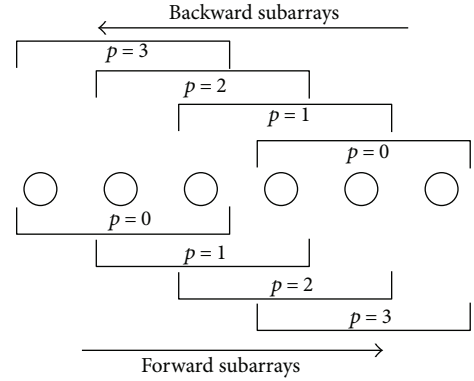


FIGURE 5: Illustration of the forward and backward subarray formation for a 6 element antenna array and subarray size 3. $M = 6$, $L = 3$, and $P = 4$.

the unambiguous region. The borders of this region can be determined using

$$\theta_{\min, \max} = a \cos\left(\pm \frac{\lambda}{2d}\right). \quad (52)$$

The last processing section in the clutter DOA estimation is the peak selection. In this stage, the available spatial DOFs must be taken into account. As it is well known, only $M - 1$ interference can be cancelled using an M element antenna system. Correspondingly, $M - 1$ direction must be selected for the filtering and the others must be discarded even when those correspond to dominant clutter components. Thus, we can declare the following:

$$Q_k \leq M - 1, \quad \forall k \in \{0, \dots, K - 1\}. \quad (53)$$

It is worthwhile to mention, when $Q_k = M$ the clutter DOA information is totally disregarded in the filter, because the filter has enough dimension to produce spatially independent weight coefficients. In this case, we return to the spatial extension of the transversal filter, which is described in Section 4.1. The determined clutter DOAs are then stored for every k time delay, and finally, the Ψ clutter DOA matrix can be prepared for the STAC filter.

4.5. Filter Summary. A filtering scheme that utilizes the STAC technique as a prefilter is illustrated in Figure 7. The main idea behind the presented filter is to cancel the ZDI prior to any space domain processing to save system resources. As it is highlighted in the previous section, the available degrees of freedom in the space domain limits the number of cancelled interferences $Q_k \leq M - 1, \forall k \in \{0, \dots, K - 1\}$. However, in such environments where the number of interferences at a given range is lower than $M - 1$, the filter is able to cancel all the disturbances and the time domain filter stage is not required.

A fast procedure for the STAC filtering can be summarized as follows:

- (1) Estimate the clutter DOA information and prepare the clutter DOA matrix Ψ according to the processing scheme illustrated in Figure 6.

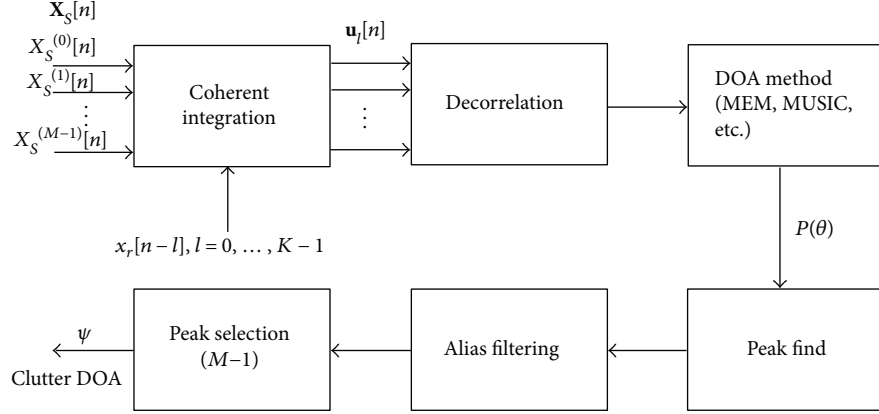


FIGURE 6: Signal processing chain for clutter DOA estimation.

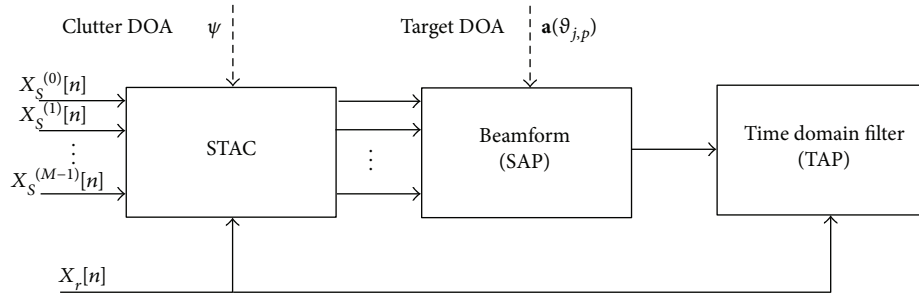


FIGURE 7: Application of STAC prefiltering technique.

- (2) Obtain the K dimensional temporal autocorrelation matrix \mathbf{R}_t and the cross-correlation vectors $\mathbf{r}_t^{(m)}$, $m = 0, \dots, M-1$ according to (35) and (36). These can also be used later by the time domain filter.
- (3) Extend the temporal autocorrelation matrix and cross-correlation vectors using (35) and (38) to calculate $\mathbf{R}_Q^{(t)}$ and $\mathbf{r}_Q^{(m)}$.
- (4) Calculate the clutter DOA correlation matrix $\mathbf{R}_Q^{(\psi)}$ using (21).
- (5) Calculate the Q dimensional autocorrelation matrix \mathbf{R}_Q and cross-correlation vector \mathbf{r}_Q using (32) and (39), respectively.
- (6) Obtain the optimal weight vector \mathbf{w} with (29).
- (7) Perform filtering using (18).

5. Simulation

The effectiveness of the proposed algorithm is investigated by comparing its performance with the available space, time, and space-time domain filters using simulated data. On the hardware side, a 6 element uniform linear array is assumed to receive the surveillance signal, while the reference signal is assumed to be received on a dedicated antenna and receiver channel. The samples of the illuminator signal are drawn from a normal distribution having zero mean and unity variance $s[n] \sim \mathcal{N}(0, 1)$. The simulated clutter and target

TABLE 1: Simulated signal parameters.

| k | q | $ \alpha_{k,q} ^2$ [dB] | $\theta_{k,q}$ [deg] | $f_{k,q}$ [Hz] |
|---------------------------|-----|-------------------------|----------------------|----------------|
| ZDI | | | | |
| 0 | 0 | 0 | 90 | 0 |
| 1 | 0 | -10 | 75 | 0 |
| 2 | 0 | -3 | 40 | 0 |
| 3 | 0 | -15 | 100 | 0 |
| 3 | 1 | -13 | 120 | 0 |
| 3 | 2 | -19 | 140 | 0 |
| 3 | 3 | -17 | 160 | 0 |
| 4 | 0 | -22 | 50 | 0 |
| 5 | 0 | -27 | 60 | 0 |
| Target | | | | |
| 25 | 0 | -50 | 41 | 125 |
| Uncorrelated interference | | | | |
| — | d | $ \alpha_d $ [dB] | θ_d [deg] | — |
| — | 0 | -35 | 130 | 0 |

parameters are summarized in Table 1. The first set of signal components describes the considered parameters of the ZDIs, while the next one corresponds to the target reflection. Accordingly, the clutter components have zero Doppler frequency $f_{k,q} = 0$ Hz. The final parameter set describes the considered jammer. The indicated $|\alpha_{k,q}|$ and $|\alpha_d|$ parameters give

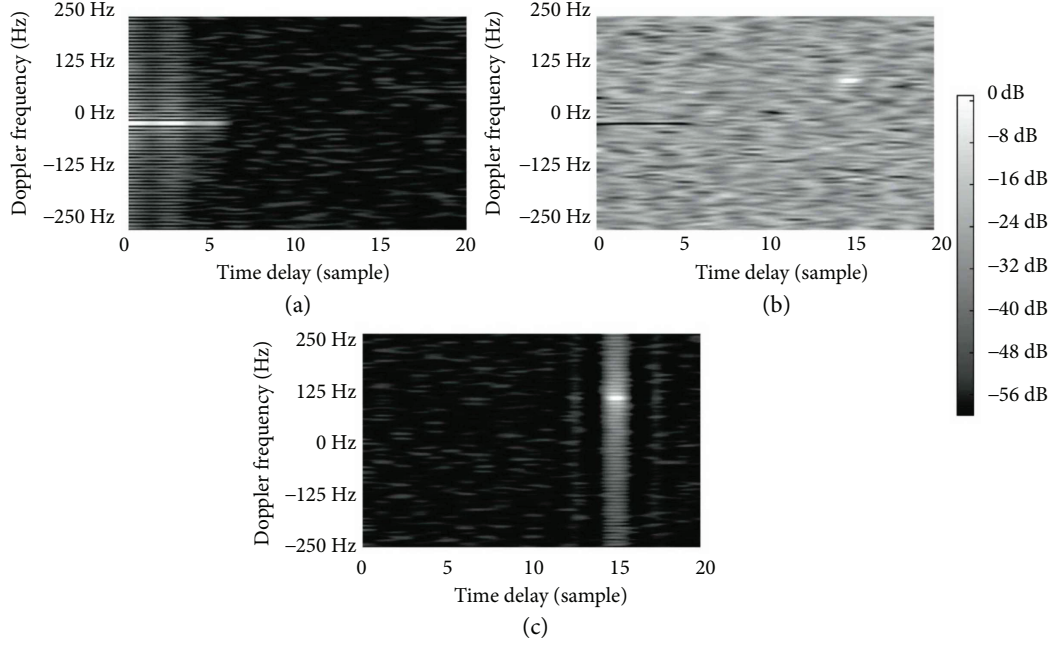


FIGURE 8: Calculated range-Doppler matrices with different interference cancellation schemes. The dynamic range is uniformly 60 dB.

the amplitude of the propagation factor of the current signal component. The values are expressed in decibels relative to the direct path signal amplitude ($k = 0$). The phases of the propagation factors $\alpha_{k,q}$ and α_d are generated randomly with uniform distribution for all components. The received signal is corrupted with white noise having -50 dB power relative to the direct path signal $E\{|\xi_m(n)|^2\}/|\alpha_{0,0}|^2 = -50$ dB. The coherent processing interval in the simulation is $N = 2^{20}$ sample.

The simulated signal is generated according to formula (2). Using the previously described signal composition, a number of different effects can be investigated at the same time. The incident angle of the clutter at the 2nd range cell is 40° which is very close to the target DOA that may result in unintentional target echo suppression. At the 3rd range, cell clutter is received from multiple directions; thus, coherent signals must be resolved by the clutter DOA estimator. At the same time, 4 directions are assumed, which is the theoretical maximum of the number of resolvable coherent signals by the spatial smoothing technique (51).

5.1. Performance Metrics. The performance is measured with the clutter attenuation (CA) previously introduced by Cardinali et al. [16] and with the estimated target signal to interference plus noise ratio (SINR). Clutter attenuation measures the averaged power of the cancelled signal. Let us denote the processed surveillance channel with $y[n]$. Then, the clutter attenuation is defined as

$$CA = \frac{\sum_{m=0}^{M-1} \sum_{n=0}^{N-1} |x_s^{(m)}[n]|^2}{\sum_{n=0}^{N-1} |y[n]|^2}. \quad (54)$$

We also calculated the estimated target SINR, which is defined by the following term:

$$\text{SINR}_{\text{target}} = \frac{|\chi(k, f_{k,q})|^2}{(1/L) \sum_{k' \in \mathcal{K}} \sum_{f' \in \mathcal{F}} |\chi(k', f')|^2}, \quad (55)$$

where $\chi(k, f)$ is the cross-correlation of the filtered surveillance channel and the time and Doppler shifted replica of the reference signal.

$$\chi(k, f) = \sum_{n=0}^{N-1} y[n] x_r[n-k] * e^{-j2\pi(f/f_s)n}. \quad (56)$$

Besides that, the \mathcal{K} and \mathcal{F} sets have the indices of the neighbouring range-Doppler cells leaving out the closest 2 cells as the guard cells. L denotes the number of considered cells in the calculation. That is, the clutter power around the target peak is estimated.

5.2. Processing Setups and Results. The simulated passive radar signals $x_r[n]$, $x_s[n]^{(m)}$, $m = 0, \dots, M-1$ are processed with different filter setups in order to demonstrate and highlight the STAC filter relevance.

- (i) In the first case, no filtering is applied. In Figure 8(a), the calculated range-Doppler matrix can be seen. As it is obvious from the figure, the desired target reflection at $k = 25$ and $f = 125$ Hz is totally masked by the clutter components.
- (ii) In the second processing scenario, both space and time domain filterings are utilized. This method is described in Section 3.3. The steering vector

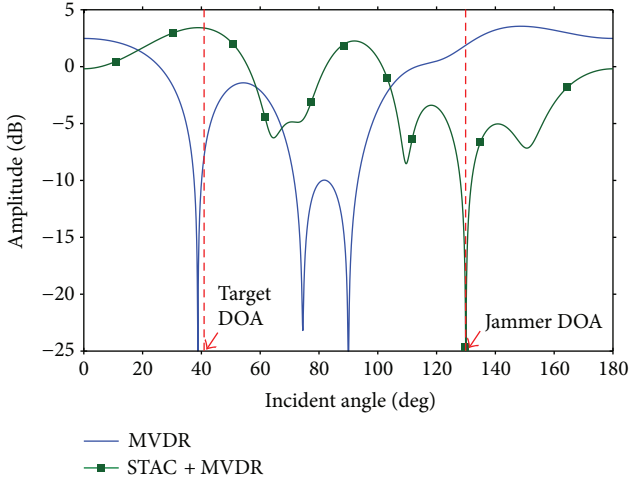


FIGURE 9: Beampatterns obtained from the simulated signal.

of the MVDR beamformer is set to the target DOA $\mathbf{a}(\theta_{j,p}) = \mathbf{a}(41^\circ)$. The calculated beampattern is shown in Figure 9 with the solid line. We can observe that the spatial filter was not able to effectively deal with all interferences as the number of clutter components is higher than the DOF of the digital beamformer. The jamming source at 130° also could not be suppressed. The beamformer also placed a deep null in the direction of the strong clutter at 40° , and thus, it suppresses unintentionally the target reflection at 41° . In the second stage, the time domain filter is configured to $J = 6$. The calculated range-Doppler map in Figure 8(b) shows that all the ZDI components are successfully cancelled and the target can be also identified. However, the jammer is not filtered, and the clutter is filtered in the space domain in the expense of the suppression of the useful target echo.

- (iii) In the third filter setup, the STAC is performed prior to the beamforming and the time domain filtering. The filtering scheme is illustrated in Figure 7. The STAC-filtered channels $x_f[n]^{(m)}$, $m = 0, \dots, M - 1$ are calculated using the method described in Section 4.2. In Figure 10, the results of the clutter DOA estimation can be seen. We can observe that using the proposed technique in Section 4.4 the clutter components at different ranges could be measured and separated successfully. In the next stage, the beamformer output is calculated using (8) with replacing the raw surveillance antenna channels $x_s[n]^{(m)}$ to its filtered versions $x_f[n]^{(m)}$. The calculated beampattern for the filtered surveillance channels is shown in Figure 9 with the squared line. As it can be seen, no nulls are placed in the direction of reference-correlated clutter sources as they are cancelled prior to the beamformer. This results in proper main beam formation in the direction of the target. Besides this, the freed DOFs could be used to filter the

uncorrelated jamming source at 130° . The output of the beamformer is filtered in the time domain at the last stage. The time domain-filtered signal is obtained with using (10) and setting $J = 6$. In Figure 8(c), the calculated range-Doppler map can be seen. We can conclude from the figure that all the clutter components are suppressed successfully.

As it is obvious from the simulation results, the traditional filter approach fails in several ways in the considered scenario. However, these problems can be resolved by the application of the STAC method. Table 2 summarizes the obtained simulation results by applied filtering techniques. The improvements can be clearly seen from the table both in the sense of the target SINR and the clutter attenuation. The table shows results for the cases also where only the spatial filtering or the temporal filtering has been applied according to Sections 3.1 and 3.2.

6. Field Trials

Besides simulations, the signal processing gain of the STAC algorithm is verified with field measurements. The proposed algorithm assumes statistically independent illuminator signal samples. For this reason, samples drawn from uncorrelated normal distribution are used through the simulations. In a real environment, the DVB-T signal is very close to uniform power spectral density and thus suitable for demonstration purposes in this case.

6.1. Demonstrator Hardware. The receiver hardware used for the demonstration is a quad channel UHF band receiver especially designed for passive radar application. The detailed description of the used demonstrator system structure and its capabilities can be found in [26]. One receiver channel from the four is dedicated to receive the reference signal. The remaining three channels are connected to a quad element linear antenna array with interelement spacing of $d = 0.528\lambda$, where λ is the center wavelength of the illumination signal. Leaving the third channel unconnected in the surveillance antenna system, it can be used in minimal redundancy alignment (MRA). This arrangement is applied to have maximum aperture size for DOA estimation. The antenna channel connection and the receiver build up are illustrated in Figure 11.

6.2. Scenario and Evaluation. The field measurement was taken near to the Ferenc Liszt International Airport at Budapest, where the receiver system has recorded several landing airplanes. The utilized illuminators were three DVB-T transmitters operating in single-frequency network mode at 634 MHz with horizontal polarization. The recorded samples were processed offline. In the first step, the landing airplane is detected and its range-Doppler track is extracted. Using the target track, the SINR is calculated with the different filtering algorithms to gain knowledge on their behaviour. The estimated SINR of the target is then used as the performance metric. The STAC algorithm is implemented in the way as it is illustrated in Figure 6 except the MRA modifications. After the spatial correlation, the matrix

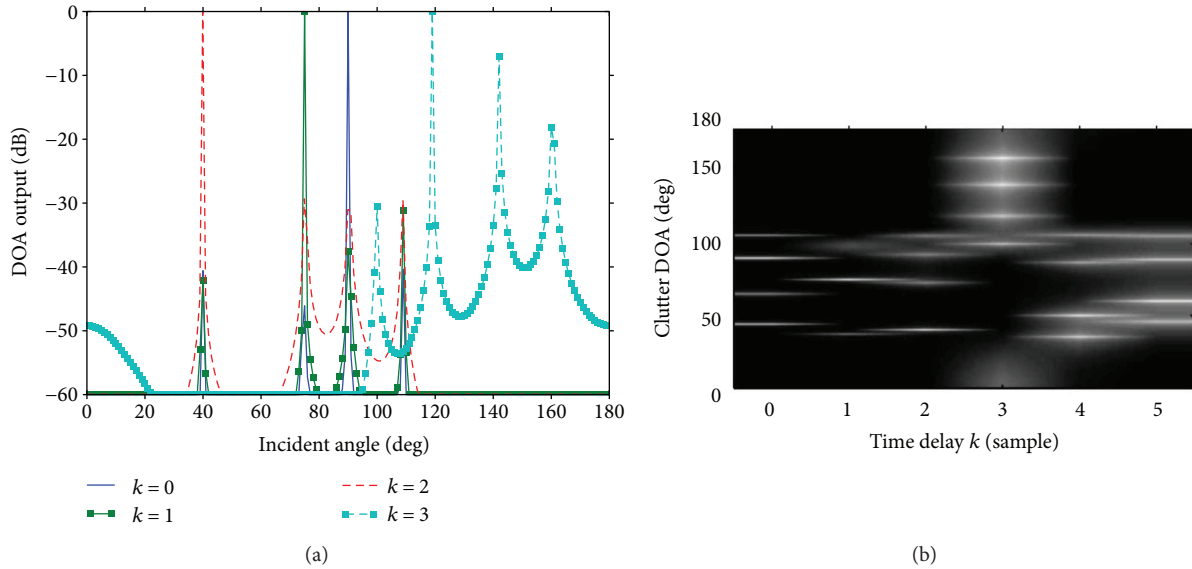


FIGURE 10: Clutter DOA estimation results for the simulated signal. The dynamic range is 60 dB. (a) Clutter DOA estimation on the first 4 range cells. (b) 2D map of the clutter DOA for the first 6 range cells.

TABLE 2: Measured filter performances.

| Filtering method | Target SINR [dB] | CA [dB] |
|--|------------------|---------|
| Spatial (MVDR) | 10.37 | 22.7 |
| Temporal (Wiener-SMI) | 43.6 | 36.9 |
| Spatial and temporal (MVDR & Wiener-SMI) | 26.37 | 34.1 |
| STAC before spatial and temporal (MVDR & Wiener-SMI) | 51.8 | 44.6 |

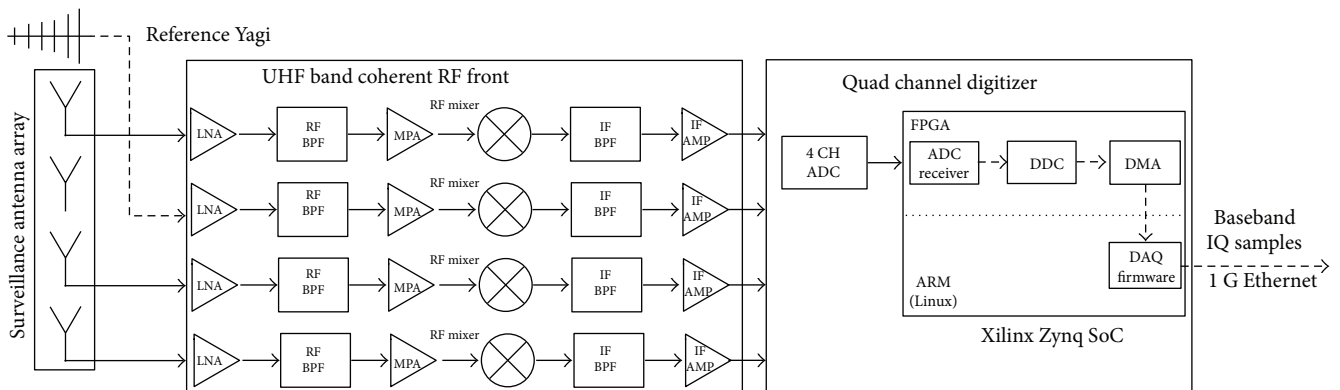


FIGURE 11: Block diagram of the demonstrator hardware and its antenna channel connections.

has found that its deficient elements ($R_{i,3}, R_{3,i}, i = 1, \dots, 4$) are completed utilizing the correlation matrix Hermitian property $\mathbf{R}_s^H = \mathbf{R}_s$.

6.3. Measurements in Real Environment. It must be strictly emphasized, with using three antenna channels, only two coherent sources can be resolved and thus $Q_k \leq 2$, $\forall k \in \{0, \dots, K-1\}$ in this particular measurement. The hardware resources of the used demonstrator system are

extremely limited, but the interference cancellation improvement over the currently available techniques is still evincible.

Figure 12 shows the extracted SINRs of the captured landing airplanes. The different curves correspond to different domain processing techniques. In Figure 12(a), each of the SINR curves is relative to the processing case when no filtering is applied. The gain of the different algorithms is summarized in Table 3. The investigated filtering setups are the same as described in Section 5.2. In addition, the

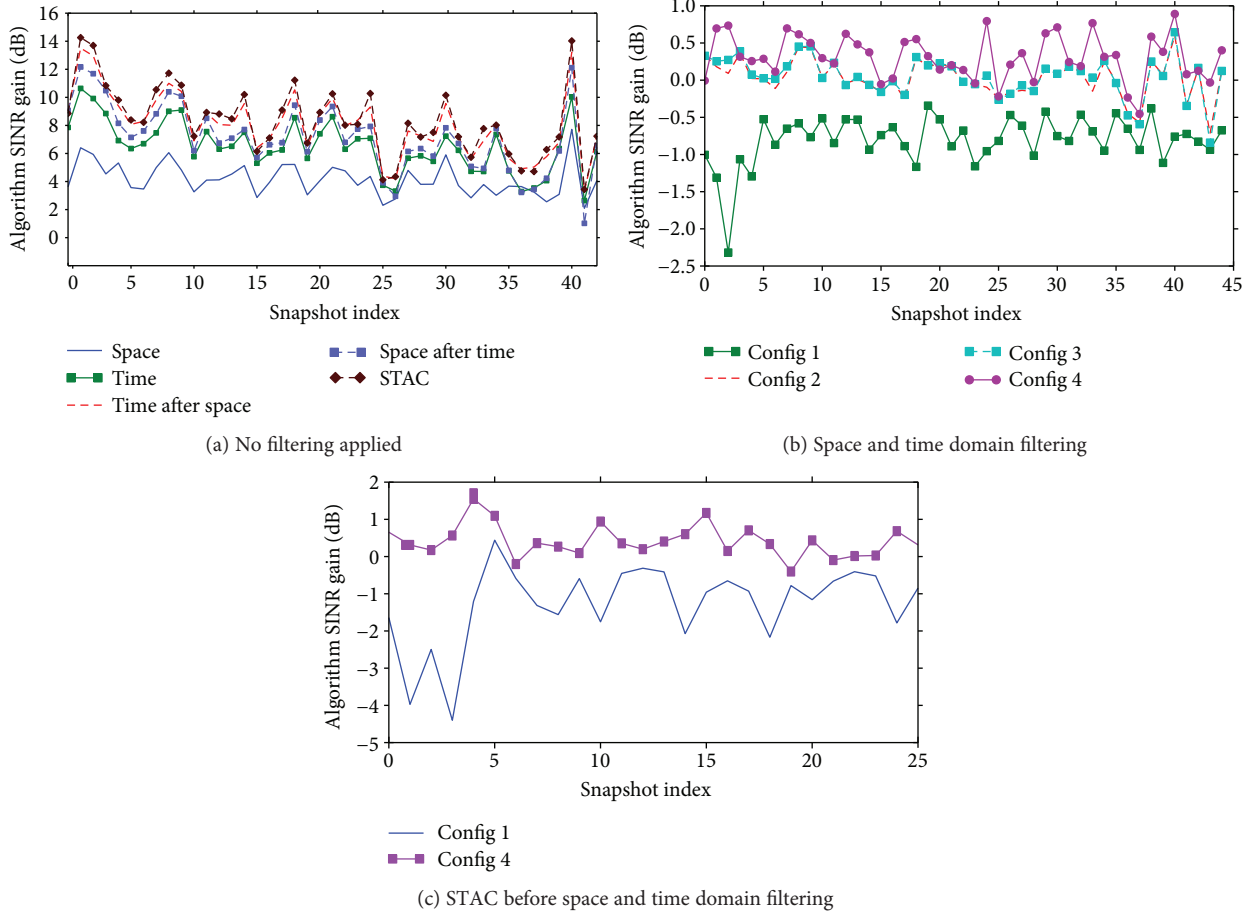


FIGURE 12: SINR improvements obtained from real measurements. (a) Improvements from the different domains (target number 1). (b) STAC improvement with different clutter DOA estimation techniques (target number 1). (c) STAC improvement with different clutter DOA estimation techniques (target number 2).

TABLE 3: SINR improvements.

| Method | Max gain [dB] |
|--------------------------------------|---------------|
| Space (MVDR) | 7.5 dB |
| Time (Wiener-SMI) | 10 dB |
| Time after space (MVDR & Wiener-SMI) | 13.5 |
| Space after time (Wiener-SMI & MVDR) | 12 |
| STAC & MVDR & Wiener-SMI | 14.5 |

TABLE 4: Algorithm configurations.

| Config | Method | Clutter DOA | Alias filt | Spatial decorr. |
|--------|--------------------|-------------|------------|-----------------|
| 1 | Wiener-SMI prefilt | — | — | — |
| 2 | STAC prefilt | MEM | No | No |
| 3 | STAC prefilt | MEM | Yes | No |
| 4 | STAC prefilt | MUSIC | Yes | F-B avg |

filtering setup that is described in Section 4.1 is also listed. In this processing setup, the standard temporal filter precedes the beamformer. Thus, the surveillance antenna channels $x_s[n]^{(m)}$, $m = 0, \dots, M - 1$ are filtered individually according to (15); then, the filtered output is calculated with beamforming of the prefiltered antenna channels using (8), where $x_s[n]^{(m)}$ is replaced by $x_f[n]^{(m)}$. The temporal dimension is uniformly $J = K = 128$ in all cases, and the MVDR beamformer uses $\mathbf{a}(83^\circ)$ as the steering vector to receive the target reflection.

In Figures 12(b) and 12(c), the results achieved with the two different prefiltering algorithms can be seen. The

SINR curves are relative to the standard space-time filter when no prefiltering is used (Section 3.3). The processing configurations are summarized in Table 4. Configurations 2, 3, and 4 belong to the STAC prefilter. These curves also illustrate the effect of the different configurations of the clutter DOA estimator. We can conclude from the measured curves that both the alias filtering and the spatial decorrelation have improvement on the clutter DOA estimation and thus on the STAC algorithm.

As it can be seen from the figures, the method described in Section 4.1 shows no improvement (configuration 1). This is due to the fact that spatial coherence is violated and the adaptive beamformer can no longer operate properly.

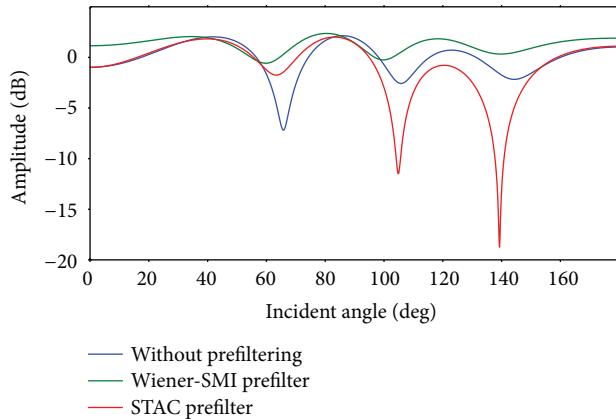


FIGURE 13: Calculated beampatterns from the measured data with different prefiltering techniques.

The obtained beampatterns for a snapshot with the different prefiltering techniques are visible in Figure 13. It can be clearly seen that using the STAC prefilter the MVDR beamformer could realize a deep null to cancel the interference at 140°; thus, it successfully contributed to the appropriate utilization of the system resources.

6.4. Results and Discussion. The field trial results presented in this paper are obtained from records of landing airplanes, in order to ensure a well-controlled measurement environment. This configuration can grant the small variation of the grazing angle of the approaching targets and also a fairly consistent SINR intensity increase. These considerations can emphasize the efficiency of the SINR-based performance improvement evaluation. At the same time, the receiver system was only able to record and transfer the samples with roughly 60 percent of duty cycle due to the large amount of generated data. As a result, the analysed radially approaching targets are observed only in a limited number of snapshots (less than 50). This could yield a poor estimation and hence a larger uncertainty on the expected value of target SINR improvement. However, as it is visible on the obtained results, the SINR curves belong to the differently processed surveillance records which follow the same tendency (see Figure 12(a)) and the improvements appear as an offset. This can lead us to the conclusion that the improvement is clearly visible and can be applied to a trustworthy validation of the proposed algorithm.

The realized processing gain over the currently available algorithms with this system is roughly 1 dB, while the overall gain from the clutter cancellation is 14.5 dB maximum. The STAC algorithm is mainly intended to make the space domain processing methods more effective by performing early spatially coherent clutter mitigation. The achievable improvement relies much on the manageable clutter components that are directly proportional to the DOF of the surveillance antenna system. It can be concluded that the proposed algorithm could realize improvement in a real environment even with strongly limited hardware resources. In this particular field measurement, the demonstrator system was only capable to cancel two clutter components at any given range

cell due to the extremely low antenna element count. According to the obtained results, the clutter had even more components that means only a fraction of the disturbances could be cancelled prior to the beamformer. This leads to a reduced overall improvement. In a more complex system, the achievable improvement increases with the extension of the surveillance antenna array with more elements until all the clutter components are totally cancelled in the space-time domain. The better distribution of the system resources that is the main contribution of the proposed algorithm could also be observed on the measurement results (see Figure 13).

7. Further Research Directions

The proposed filter is derived for idealized conditions. We preliminary assumed a stationary environment and statistically independent signal samples. In real cases, the illuminator signal samples may be partially correlated. Thus, to improve the filter performance, we must deal with these problems in clutter DOA estimation and filter coefficient calculation.

Besides this, the nonstationary behaviour of the environment could also decrease the performance. Using shorter time intervals than the coherent processing interval for the estimation of the clutter DOA and the filter coefficient could deal with the problem. Moreover, the clutter DOA estimation could be quite difficult, inaccurate, and computationally intensive to calculate for all coherent processing intervals; thus, it would be beneficial to learn more about its statistical behaviour.

Extension of the filter in the Doppler dimension [14] is not studied in this paper. Further works may investigate its performance.

8. Conclusion

In this paper, a novel interference cancellation algorithm is proposed for passive radar application. The introduced STAC algorithm jointly utilizes the available spatial and temporal information to perform filtering. Filtering of the antenna channels prior to any spatial processing helps the system to use its resources in a more favorable way. The performance of the algorithm is demonstrated and proved through simulations and measurements carried out in real environments.

Conflicts of Interest

The authors declare that they have no conflicts of interest.

Acknowledgments

This work has been supported in the frame of the project “Multichannel passive ISAR imaging for military applications (MAPIS) no. B-1359 IAP2 GP” of the European Defence Agency. The authors would like to express their gratitude to Levente Dudas for his generous support on the development of the demonstrator system and the preparation of the experimental measurements.

References

- [1] K. Kulpa, *Signal Processing in Noise Waveform Radar*, Artech House, Norwood, MA, USA, 1st edition, 2013.
- [2] R. Tao, H. Z. Wu, and T. Shan, "Direct-path suppression by spatial filtering in digital television terrestrial broadcasting-based passive radar," *IET Radar, Sonar & Navigation*, vol. 4, no. 6, pp. 791–805, 2010.
- [3] M. Villano, F. Colone, and P. Lombardo, "Antenna array for passive radar: configuration design and adaptive approaches to disturbance cancellation," *International Journal of Antennas and Propagation*, vol. 2013, Article ID 920639, 16 pages, 2013.
- [4] T. Peto and R. Seller, "Quad channel DVB-T based passive radar," in *2016 17th International Radar Symposium (IRS)*, p. 4, Cracow, Poland, May 2016.
- [5] A. Capria, D. Petri, C. Moscardini et al., *Software-Defined Multiband Array Passive Radar (SMARP) Demonstrator: A Test and Evaluation Perspective*, OCEANS, Genove, Italy, 2015.
- [6] C. Moscardini, M. Conti, F. Berizzi, M. Martorella, and A. Capria, "Spatial adaptive processing for passive bistatic radar," in *2014 IEEE Radar Conference*, pp. 1061–1066, Cincinnati, OH, USA, May 2014.
- [7] D. Petri, C. Moscardini, M. Conti, A. Capria, J. E. Palmer, and S. J. Searle, "The effects of DVB-T SFN data on passive radar signal processing," in *2013 International Conference on Radar*, pp. 280–285, Ottawa, ON, Canada, September 2013.
- [8] A. Di Lallo, R. Fulcoli, and L. Timmoneri, "Adaptive spatial processing applied to a prototype passive covert radar: test with real data," in *2008 International Conference on Radar*, pp. 139–143, Adelaide, Australia, September 2008.
- [9] M. Kubica, V. Kubica, X. Neyt, J. Raout, S. Roques, and M. Acheroy, "Optimum target detection using illuminators of opportunity," in *2006 IEEE Conference on Radar*, pp. 417–424, Verona, USA, April 2006.
- [10] F. Colone, C. Palmardini, T. Martelli, and E. Tilli, "Sliding extensive cancellation algorithm for disturbance removal in passive radar," *IEEE Transactions on Aerospace and Electronic Systems*, vol. 52, no. 3, pp. 1309–1326, 2016.
- [11] Y. Ma, T. Shan, Y. D. Zhang, M. G. Amin, R. Tao, and Y. Feng, "A novel two-dimensional sparse-weight NLMS filtering scheme for passive bistatic radar," *IEEE Geoscience and Remote Sensing Letters*, vol. 13, no. 5, pp. 676–680, 2016.
- [12] B. Demissie, "Clutter cancellation in passive radar using GSM broadcast channels," *IET Radar, Sonar & Navigation*, vol. 8, no. 7, pp. 787–796, 2014.
- [13] Z. Zhao, X. Wan, F. Cheng, Z. Gong, and Q. Shao, "Multipath clutter rejection for digital radio mondiale-based HF passive bistatic radar with OFDM waveform," *IET Radar, Sonar & Navigation*, vol. 6, no. 9, pp. 867–872, 2012.
- [14] F. Colone, D. W. O'Hagan, P. Lombardo, and C. J. Baker, "A multistage processing algorithm for disturbance removal and target detection in passive bistatic radar," *IEEE Transactions on Aerospace and Electronic Systems*, vol. 45, no. 2, pp. 698–722, 2009.
- [15] A. Baruzzi, C. Schwark, G. Bournaka, D. Cristallini, and H. Kuschel, "Multipath clutter cancellation and tracking algorithms for passive radars," in *2016 17th International Radar Symposium (IRS)*, p. 4, Cracow, Poland, May 2016.
- [16] R. Cardinali, F. Colone, C. Ferretti, and P. Lombardo, "Comparison of clutter and multipath cancellation techniques for passive radar," in *2007 IEEE Radar Conference*, pp. 469–474, Waltham, USA, April 2007.
- [17] M. Edrich, A. Schroeder, and F. Meyer, "Design and performance evaluation of a mature FM/DAB/DVB-T multi-illuminator passive radar system," *IET Radar, Sonar & Navigation*, vol. 8, no. 2, pp. 114–122, 2014.
- [18] V. Navratil, A. O'Brien, J. Landon Garry, and G. E. Smith, "Demonstration of space-time adaptive processing for DSI suppression in a passive radar," in *2017 18th International Radar Symposium (IRS)*, p. 10, Prague, Czech Republic, June 2017.
- [19] M. K. Baczyk and M. Malanowski, "Reconstruction of the reference signal in DVB-T based passive radar," *International Journal of Electronics and Telecommunications*, vol. 57, no. 1, pp. 43–48, 2011.
- [20] T. Peto and R. Seller, "Time domain filter comparison in passive radar systems," in *2017 18th International Radar Symposium (IRS)*, pp. 1–10, Prague, Czech Republic, June 2017.
- [21] S. Haykin, *Adaptive Filter Theory*, Prentice Hall, Upper Saddle River, NJ, USA, 3rd edition, 1996.
- [22] T. Engin Tuncer and B. Friedlander, *Classical and Modern Direction-of-Arrival Estimation*, Academic Press, Burlington, MA, USA, 1st edition, 2009.
- [23] L. C. Godara, *Smart Antennas*, CRC Press, Boca Raton, FL, USA, 1st edition, 2004.
- [24] Z. Chen, G. Gokeda, and Y. Yu, *Introduction to Direction-of-Arrival Estimation*, Artech House, Norwood, MA, USA, 1st edition, 2010.
- [25] Q. Chen and R. Liu, "On the explanation of spatial smoothing in MUSIC algorithm for coherent sources," in *International Conference on Information Science and Technology*, pp. 699–702, Nanjing, China, March 2011.
- [26] T. Peto and R. Seller, "Quad channel software defined receiver for passive radar application," *Archives of Electrical Engineering*, vol. 66, no. 1, p. 12, 2017.
- [27] D. W. O'Hagan, V. Basavarajappa, P. Knott et al., "A wideband antenna array for DVB-T based passive bistatic radar applications," in *IET International Conference on Radar Systems (Radar 2012)*, p. 6, Glasgow, UK, May 2012.

Research Article

Reduced-Complexity Direction of Arrival Estimation Using Real-Valued Computation with Arbitrary Array Configurations

Feng-Gang Yan ¹, Jun Wang ¹, Shuai Liu ¹, Yi Shen,² and Ming Jin¹

¹Harbin Institute of Technology at Weihai, Weihai 264209, China

²Harbin Institute of Technology, Harbin 150001, China

Correspondence should be addressed to Shuai Liu; lius_hit@163.com

Received 31 August 2017; Revised 14 December 2017; Accepted 4 March 2018; Published 29 April 2018

Academic Editor: Elisa Giusti

Copyright © 2018 Feng-Gang Yan et al. This is an open access article distributed under the Creative Commons Attribution License, which permits unrestricted use, distribution, and reproduction in any medium, provided the original work is properly cited.

A low-complexity algorithm is presented to dramatically reduce the complexity of the multiple signal classification (MUSIC) algorithm for direction of arrival (DOA) estimation, in which both tasks of eigenvalue decomposition (EVD) and spectral search are implemented with efficient real-valued computations, leading to about 75% complexity reduction as compared to the standard MUSIC. Furthermore, the proposed technique has no dependence on array configurations and is hence suitable for arbitrary array geometries, which shows a significant implementation advantage over most state-of-the-art unitary estimators including unitary MUSIC (U-MUSIC). Numerical simulations over a wide range of scenarios are conducted to show the performance of the new technique, which demonstrates that with a significantly reduced computational complexity, the new approach is able to provide a close accuracy to the standard MUSIC.

1. Introduction

Direction-of-arrival (DOA) estimation is a fundamental array processing problem with many applications, for example, radar, sonar, wireless communication, and smart antenna design [1, 2]. This topic has been extensively studied during the past four decades, resulting in many efficient and accurate algorithms including multiple signal classification (MUSIC) [3], maximum likelihood (ML) [4], subspace fitting (SF) [5], minimum norm (MN) [6], and their derivations. Among those methods, the MUSIC algorithm is able to provide super resolution DOA estimation for closely spaced sources and has an easy implementation with arbitrary array configuration [7]. However, such advantages are archived at the expense of huge complexity which is mainly caused by an involved eigenvalue decomposition (EVD) step and a tremendous spectral search step, both are generally implemented with complex-valued computations. Therefore, the standard MUSIC is prohibitively expensive in scenarios where real-time processing is required [8].

It is well known that the problem of DOA estimation can be simplified with some specified array structures, based on which a variety of low-complexity methods has been proposed for high computational efficiency. For example, when the array geometry satisfies the rotational invariant property, DOA can be immediately computed without spectral search by using the estimation of signal parameters via rotational invariance technique (ESPRIT) [9]. Exploiting the special geometry of a uniform linear array (ULA), one can also find source DOA by polynomial rooting with search-free computations using the well-known root-MUSIC algorithm [10]. Besides, numerous useful modifications of ESPRIT and root-MUSIC have been proposed with circular and other kinds of arrays [11, 12]. As the array structures used in these techniques are still rather specific, many promising attempts such as array interpolation (AI) [13], manifold separation technique (MST) [14], and Fourier-domain (FD) root-MUSIC [15] have been proposed recently to extend ESPRIT and root-MUSIC to more general classes of array configurations. Unfortunately, those approaches usually use a polynomial

with a sufficiently high order to warrant that the truncation errors are small, and hence, the complexity for finding the roots of this polynomial may be higher than expected [16].

Considering one multiplication between two complex variables generally require four times that between two real ones, algorithms with real-valued computation can reduce about 75% complexity as compared to their complex versions. Following this idea, Huarng and Yeh [17] introduced an outstanding unitary transformation for low-complexity DOA estimation with real-valued computation. Whereafter, Linebarger et al. [18] proposed a forward/backward (FB) averaging method which obtains real-valued arithmetic for fast DOA estimation as well. These techniques are firstly exploited by the unitary MUSIC (U-MUSIC) algorithm [19] and then extended to many other derivations including unitary root MUSIC (U-root-MUSIC) [20], unitary ESPRIT (U-ESPRIT) [21], unitary method of direction-of-arrival estimation (U-MODE) [22], and unitary matrix pencil (U-MP) [23]. Based on the special structure of a centrosymmetrical array (CSA), those algorithms transform the complex array covariance matrix into a real one. It has been proven that this real matrix is symmetrical, and hence, both matrix decomposition and spectral search can be implemented with real-valued computation. Besides, it has been found that real-valued algorithms also show improved accuracy as compared to complex-valued approaches. Despite their increased estimation accuracies with reduced costs, almost all of the state-of-the-art real-valued methods are only suitable for CSAs [24], which severely limits their applications [25, 26].

As a further development of our previous work in [27], the objective of the present paper is to propose a new real-valued subspace-based algorithm for fast DOA estimation. However, unlike the abovementioned methods that attempted to overcome the high-complexity problem using special array structures or array mapping techniques [28], we show that exploiting only the real part of the array covariance matrix can lead to a real-valued version of the MUSIC algorithm, which has implementation advantages over most state-of-the-art real-valued techniques since it can be used with arbitrary arrays. Furthermore, we prove that the real part of the array covariance matrix can be equivalently reformulated as an entire array covariance matrix received by a virtual array with an extended array manifold which is real. Because the virtual array covariance matrix and the virtual array manifold are real, both tasks of matrix decomposition and spectral search can be implemented with efficient real-valued computations instead of complex-valued ones. Thanks to these merits, the new algorithm is able to reduce about 75% computational complexity as compared to the standard MUSIC. Finally, we provide in-depth insights into the new approach including the EVD of the real part of the array covariance matrix as well as performance simulation over a wide range of application scenarios, which demonstrate that with significantly reduced complexity, the proposed approach can still provide acceptable accuracy close to the standard MUSIC.

1.1. Mathematical Notations. Throughout the paper, matrices and vectors are denoted by upper and lower boldface

letters, respectively. Complex and real vectors and matrices are denoted by single-bar- and double-bar upper boldface letters, respectively, and detailed mathematical notations are defined in Table 1.

2. Signal Model and Standard MUSIC

2.1. Signal Model and Basic Assumptions. Without loss of generality, let us consider an arbitrary linear array (as to be shown that the proposed method has no dependence on array geometries, and it can be easily extended to arbitrary plane array for two-dimensional DOA estimate) with M omnidirectional sensors labeled by $1, 2, \dots, M$, where the coordinate of the m th sensor is denoted by $x_m, m = 1, 2, \dots, M$. Suppose that there are L uncorrelated narrow-band plane waves with unknown DOAs $\Theta \triangleq \{\theta_1, \theta_2, \dots, \theta_L\}$ impinging on the array from far field, the array received data can be written as [1–28]

$$\mathbf{x}(t) = \mathbf{A}(\Theta)\mathbf{s}(t) + \mathbf{n}(t) \in \mathbb{C}^{M \times 1}, \quad t = 1, 2, \dots, N, \quad (1)$$

where N is the number of snapshots, $\mathbf{s}(t) = [\mathbf{s}_1(t), \mathbf{s}_2(t), \dots, \mathbf{s}_L(t)]^T \in \mathbb{C}^{L \times 1}$ is the signal waveform, $\mathbf{n}(t) = [\mathbf{n}_1(t), \mathbf{n}_2(t), \dots, \mathbf{n}_M(t)]^T \in \mathbb{C}^{M \times 1}$ is the additive white Gaussian noise (AWGN), and

$$\mathbf{A}(\Theta) \triangleq [\mathbf{a}(\theta_1), \mathbf{a}(\theta_2), \dots, \mathbf{a}(\theta_L)] \in \mathbb{C}^{M \times L} \quad (2)$$

is the steering vector matrix (also known as array manifold), and each column of $\mathbf{A}(\Theta)$ is defined as a so-called steering vector, which can be expressed as

$$\mathbf{a}(\theta) \triangleq \left[e^{j2\pi/\lambda \cdot x_1 \cdot \sin \theta}, e^{j2\pi/\lambda \cdot x_2 \cdot \sin \theta}, \dots, e^{j2\pi/\lambda \cdot x_M \cdot \sin \theta} \right]^T \in \mathbb{C}^{M \times 1}, \quad (3)$$

where $j = \sqrt{-1}$ and λ are the center wavelength. The goal of the DOA estimation is to find the DOA set Θ , based on N snapshots of array received data $\{\mathbf{x}(t)\}_{t=1}^N$.

Throughout the paper, it is assumed that the number of sources is known [29] and is smaller than half that of sensors such that $L \leq \lceil (M-1)/2 \rceil$. It is also assumed that positions and displacements of array elements do not need to be uniform or follow regular patterns, provided that they satisfy the rank $(M-1)$ ambiguity restriction [30]. The AWGN $\mathbf{n}(t)$ is assumed to satisfy the following statistical performances [31–33].

$$\begin{aligned} E[\mathbf{n}(t_i)\mathbf{n}^T(t_j)] &= \mathbf{0}, \\ E[\mathbf{n}(t_i)\mathbf{n}^T(t_j)] &= \delta(i-j)\sigma_n^2 \mathbf{I}_M, \end{aligned} \quad (4)$$

and the incident signal $\mathbf{s}(t)$ is uncorrelated and satisfies [34, 35]

$$\begin{aligned} E[\mathbf{s}(t)\mathbf{s}^T(t)] &= \mathbf{0}, \\ E[\mathbf{s}(t)\mathbf{s}^H(t)] &= \mathbb{R}_s, \end{aligned} \quad (5)$$

where \mathbb{R}_s is the $L \times L$ source covariance matrix and is a real diagonal matrix.

TABLE 1: Mathematical notations.

| | |
|-------------------------|---|
| σ_n^2 | Noise power |
| $(\cdot)^T$ | Transpose |
| $(\cdot)^*$ | Conjugation |
| $(\cdot)^H$ | Hermitian transpose |
| $\lfloor \cdot \rfloor$ | Round down to integer |
| $\ \cdot \ $ | Frobenius norm |
| $E[\cdot]$ | Mathematical expectation |
| $\text{Re}(\cdot)$ | Real part of the embraced element |
| $\text{Im}(\cdot)$ | Imaginary part of the embraced element |
| 0 | Zero matrix (vector) |
| I_M | $M \times M$ identity matrix |
| $\delta(\cdot)$ | Dirac delta function |
| $\text{rank}(\cdot)$ | Rank of the embraced matrix |
| $\text{span}(\cdot)$ | Column space of the embraced matrix |
| $\text{diag}\{\cdot\}$ | Diagonal matrix composed of the embraced elements |

2.2. *Standard MUSIC*. With N snapshots of array received data $\{\mathbf{x}(t)\}_{t=1}^N$, one can compute the $M \times M$ array output covariance matrix.

$$\begin{aligned} \mathbf{R} &= E[\mathbf{x}(t)\mathbf{x}^H(t)] \\ &= E\{[\mathbf{A}(\Theta)\mathbf{s}(t) + \mathbf{n}(t)] \times [\mathbf{A}(\Theta)\mathbf{s}(t) + \mathbf{n}(t)]^H\} \\ &= \mathbf{A}(\Theta)\mathbb{R}_s\mathbf{A}^H(\Theta) + \sigma_n^2\mathbb{I}_M, \end{aligned} \quad (6)$$

and further obtained the EVD of \mathbf{R} as follows:

$$\mathbf{R} = \mathbf{S}\mathbf{\Lambda}_s\mathbf{S}^H + \mathbf{G}\mathbf{\Lambda}_n\mathbf{G}^H, \quad (7)$$

where $\text{span}(\mathbf{S})$ and $\text{span}(\mathbf{G})$ are the signal and noise subspaces, respectively. In practical situations, the theoretical \mathbf{R} is estimated by

$$\hat{\mathbf{R}} = \frac{1}{N} \sum_{t=1}^N \mathbf{x}(t)\mathbf{x}^H(t). \quad (8)$$

Hence, the EVD of the array output covariance matrix is in fact given by

$$\hat{\mathbf{R}} = \hat{\mathbf{S}}\hat{\mathbf{\Lambda}}_s\hat{\mathbf{S}}^H + \hat{\mathbf{G}}\hat{\mathbf{\Lambda}}_n\hat{\mathbf{G}}^H. \quad (9)$$

Based on some facts $\text{span}(\mathbf{S}) \perp \text{span}(\mathbf{G})$ and $\text{span}(\mathbf{S}) = \text{span}(\mathbf{A})$, the standard MUSIC suggests to search the L peaks of the following function over $[-\pi/2, \pi/2]$ to find source DOAs.

$$f_{\text{MUSIC}}(\theta) \triangleq 10 \log_{10} \frac{1}{\|\mathbf{a}^H(\theta)\hat{\mathbf{G}}\|^2} [\text{dB}]. \quad (10)$$

The primary advantage of the MUSIC algorithm is its easy implementation with arbitrary array configurations,

which is archived at the expense of huge complexity caused by an involved tremendous spectral search step with expensive complex-valued computation.

3. The Proposed Algorithm

We begin our algorithm by considering the $M \times M$ real part of the array output covariance. Using (6), we have

$$\begin{aligned} \mathbb{R} &\triangleq \text{Re}(\mathbf{R}) = \frac{(\mathbf{R} + \mathbf{R}^*)}{2} \\ &= \frac{[\mathbf{A}(\Theta)\mathbb{R}_s\mathbf{A}^H(\Theta) + \mathbf{A}^*(\Theta)\mathbb{R}_s\mathbf{A}^T(\Theta)]}{2} + \sigma_n^2\mathbb{I} \\ &= \text{Re}[\mathbf{B}(\Theta)] + \sigma_n^2\mathbb{I}, \end{aligned} \quad (11)$$

where $\mathbf{B}(\Theta)$ is defined as

$$\mathbf{B}(\Theta) \triangleq \mathbf{A}(\Theta)\mathbb{R}_s\mathbf{A}^H(\Theta). \quad (12)$$

Using $\mathbf{A}(\Theta) = \text{Re}[\mathbf{A}(\Theta)] + j \text{Im}[\mathbf{A}(\Theta)]$, $\mathbf{B}(\Theta)$ can be expressed as

$$\begin{aligned} \mathbf{B}(\Theta) &= \{\text{Re}[\mathbf{A}(\Theta)] + j \text{Im}[\mathbf{A}(\Theta)]\} \cdot \mathbb{R}_s \\ &\quad \cdot \{\text{Re}^T[\mathbf{A}(\Theta)] - j \text{Im}^T[\mathbf{A}(\Theta)]\} \\ &= \{\text{Re}[\mathbf{A}(\Theta)]\mathbb{R}_s \text{Re}^T[\mathbf{A}(\Theta)] + \text{Im}[\mathbf{A}(\Theta)]\mathbb{R}_s \text{Im}^T[\mathbf{A}(\Theta)]\} \\ &\quad + j\{\text{Im}[\mathbf{A}(\Theta)]\mathbb{R}_s \text{Re}^T[\mathbf{A}(\Theta)] - \text{Re}[\mathbf{A}(\Theta)]\mathbb{R}_s \text{Im}^T[\mathbf{A}(\Theta)]\}. \end{aligned} \quad (13)$$

Therefore, we have

$$\begin{aligned} \text{Re}[\mathbf{B}(\Theta)] &= \text{Re}[\mathbf{A}(\Theta)]\mathbb{R}_s \text{Re}^T[\mathbf{A}(\Theta)] + \text{Im}[\mathbf{A}(\Theta)]\mathbb{R}_s \text{Im}^T[\mathbf{A}(\Theta)] \\ &= [\text{Re}[\mathbf{A}(\Theta)]\text{Im}[\mathbf{A}(\Theta)]] \times \begin{bmatrix} \mathbb{R}_s & 0 \\ 0 & \mathbb{R}_s \end{bmatrix} \times \begin{bmatrix} \text{Re}^T[\mathbf{A}(\Theta)] \\ \text{Im}^T[\mathbf{A}(\Theta)] \end{bmatrix} \\ &\triangleq \mathbb{A}(\Theta)\widetilde{\mathbb{R}}_s\mathbf{A}^T(\Theta), \end{aligned} \quad (14)$$

where $\mathbb{A}(\Theta)$ and $\widetilde{\mathbb{R}}_s$ are given by

$$\begin{aligned} \mathbb{A}(\Theta) &\triangleq [\text{Re}[\mathbf{A}(\Theta)]\text{Im}[\mathbf{A}(\Theta)]] \in \mathbb{R}^{M \times 2L}, \\ \widetilde{\mathbb{R}}_s &\triangleq \begin{bmatrix} \mathbb{R}_s & 0 \\ 0 & \mathbb{R}_s \end{bmatrix} \in \mathbb{R}^{2L \times 2L}. \end{aligned} \quad (15)$$

Using (5) and noting that $\mathbb{R}_s = \mathbb{R}_s^*$, we have

$$\widetilde{\mathbb{R}}_s = \begin{bmatrix} E[\mathbf{s}(t)\mathbf{s}^H(t)] & E[\mathbf{s}(t)\mathbf{s}^T(t)] \\ E[\mathbf{s}^*(t)\mathbf{s}^H(t)] & E[\mathbf{s}^*(t)\mathbf{s}^T(t)] \end{bmatrix} \triangleq E[\widetilde{\mathbf{s}}(t)\widetilde{\mathbf{s}}(t)^H], \quad (16)$$

where $\widetilde{\mathbf{s}}(t)$ is given by

$$\widetilde{\mathbf{s}}(t) \triangleq \begin{bmatrix} \mathbf{s}(t) \\ \mathbf{s}^*(t) \end{bmatrix} \in \mathbb{C}^{2L \times 1}. \quad (17)$$

Inserting (14) as well as (16) into (11), we obtain

$$\begin{aligned}
\mathbb{R} &= \mathbb{A}(\Theta) \widetilde{\mathbb{R}}_s \mathbb{A}^T(\Theta) + \sigma_n^2 \mathbb{I}_M \\
&= \mathbb{A}(\Theta) E \left[\widetilde{\mathbf{s}}(t) \widetilde{\mathbf{s}}(t)^H \right] \mathbb{A}^T(\Theta) + \sigma_n^2 \mathbb{I}_M \\
&= E \left\{ \left[\mathbb{A}(\Theta) \widetilde{\mathbf{s}}(t) + \mathbf{n}(t) \right] \times \left[\mathbb{A}(\Theta) \widetilde{\mathbf{s}}(t) + \mathbf{n}(t) \right]^H \right\} \quad (18) \\
&\triangleq E \left[\widetilde{\mathbf{x}}(t) \widetilde{\mathbf{x}}(t)^H \right],
\end{aligned}$$

where $\widetilde{\mathbf{x}}(t)$ is given by

$$\widetilde{\mathbf{x}}(t) \triangleq \mathbb{A}(\Theta) \widetilde{\mathbf{s}}(t) + \mathbf{n}(t) \in \mathbb{C}^{M \times 1}. \quad (19)$$

Comparing (18) and (19) with (1) and (6), the real part of the array covariance matrix can be regarded as an entire array covariance matrix of a virtual array with a manifold $\mathbb{A}(\Theta)$. The output sensor vector of this virtual array is $\widetilde{\mathbf{x}}(t)$ and the incident signal on this virtual array is $\widetilde{\mathbf{s}}(t)$ with its covariance matrix given by $\widetilde{\mathbb{R}}_s$. Therefore, (19) provides a virtual signal model for DOA estimation, which is similar to the conventional one given by (1).

Because DOA information is also contained in $\mathbb{A}(\Theta)$, one can exploit the idea of eigenvalue analysis to perform the EVD of the virtual array covariance matrix \mathbb{R} and construct a MUSIC-like spectral for DOA estimate. Noting that $\mathbb{R}^T = \mathbb{R}$, which implies that \mathbb{R} is a symmetrical real matrix. Therefore, the EVD computation

$$\mathbb{R} = \mathbb{U} \mathbb{Q} \mathbb{U}^T \quad (20)$$

requires only real-valued flops [36]. Using (6), it is shown in the appendix that the eigenvalues of \mathbb{R} are given by

$$\xi_i = \begin{cases} \beta_i + \sigma_n^2, & i = 1, 2, \dots, 2L - K, \\ \sigma_n^2, & i = 2L - K + 1, 2, \dots, M, \end{cases} \quad (21)$$

where $K (K \leq \lceil L/2 \rceil)$ is the number of pairs of symmetrical sources in Θ , $\beta_1, \beta_2, \dots, \beta_{2L-K}$ are the $2L - K$ eigenvalues of matrix

$$\mathbb{D}(\Theta) \triangleq \mathbb{H}(\Theta) \widetilde{\mathbb{R}}_s \mathbb{H}^H(\Theta) \in \mathbb{C}^{M \times M}, \quad (22)$$

and $\mathbb{H}(\Theta)$ is defined as

$$\mathbb{H}(\Theta) \triangleq \frac{1}{\sqrt{2}} [\mathbf{A}(\Theta) \mathbf{A}^*(\Theta)] \in \mathbb{C}^{M \times 2L}. \quad (23)$$

According to (21), \mathbb{R} has $2L - K$ significant and $M - 2L + K$ smallest eigenvalues. Therefore, (20) can be further written as

$$\mathbb{R} = \sum_{i=1}^{2L-K} \xi_i \mathbb{w}_i \mathbb{w}_i^H + \sum_{j=2L-K+1}^M \xi_j \mathbb{w}_j \mathbb{w}_j^H = \mathbb{S} \mathbb{Q}_s \mathbb{S}^T + \mathbb{G} \mathbb{Q}_n \mathbb{G}^T, \quad (24)$$

where \mathbb{Q}_s contains the $2L - K$ significant eigenvalues ξ_i , $i = 1, 2, \dots, 2L - K$, \mathbb{Q}_n contains the $M - 2L + K$ smallest

eigenvalues ξ_j , $j = 1, 2, \dots, M - 2L + K$, and \mathbb{S} and \mathbb{G} are the signal and noise matrices such that

$$\begin{aligned}
\mathbb{Q}_s &= \text{diag}\{\xi_1, \xi_2, \dots, \xi_{2L-K}\} \in \mathbb{R}^{(2L-K) \times (2L-K)}, \\
\mathbb{Q}_n &= \text{diag}\{\xi_{2L-K+1}, \xi_{2L-K+2}, \dots, \xi_M\} \in \mathbb{R}^{(M-2L+K) \times (M-2L+K)}, \\
\mathbb{S} &= [\mathbb{w}_1, \mathbb{w}_2, \dots, \mathbb{w}_{2L-K}] \in \mathbb{R}^{M \times (2L-K)}, \\
\mathbb{G} &= [\mathbb{w}_{2L-K+1}, \mathbb{w}_{2L-K+2}, \dots, \mathbb{w}_M] \in \mathbb{R}^{M \times (M-2L+K)}. \quad (25)
\end{aligned}$$

Since $\mathbb{A}(\Theta)$ is the virtual manifold matrix associated with \mathbb{R} , by using the orthogonality between the signal and the noise subspaces, we obtain

$$\begin{aligned}
\text{span}(\mathbb{S}) &\perp \text{span}(\mathbb{G}), \\
\text{span}(\mathbb{S}) &= \text{span}[\mathbb{A}(\Theta)]. \quad (26)
\end{aligned}$$

Because $\mathbb{A}(\Theta) = [\text{Re}[\mathbf{A}(\Theta)] \text{Im}[\mathbf{A}(\Theta)]]$ is in fact a combined manifold matrix covering both $\text{Re}[\mathbf{A}(\Theta)]$ and $\text{Im}[\mathbf{A}(\Theta)]$, we have

$$\text{span}[\mathbf{A}(\Theta)] = \text{span}\{\mathbf{a}_{\text{re}}(\theta_1), \mathbf{a}_{\text{re}}(\theta_2), \dots, \mathbf{a}_{\text{re}}(\theta_L), \mathbf{a}_{\text{im}}(\theta_1), \mathbf{a}_{\text{im}}(\theta_2), \dots, \mathbf{a}_{\text{im}}(\theta_L)\}, \quad (27)$$

where $\mathbf{a}_{\text{re}}(\theta) \triangleq \text{Re}[\mathbf{a}(\theta)] \in \mathbb{R}^{M \times 1}$ and $\mathbf{a}_{\text{im}}(\theta) \triangleq \text{Im}[\mathbf{a}(\theta)] \in \mathbb{R}^{M \times 1}$ are two real vectors, given by

$$\begin{aligned}
\mathbf{a}_{\text{re}}(\theta) \triangleq \text{Re}[\mathbf{a}(\theta)] &= \begin{bmatrix} \cos\left(\frac{2\pi}{\lambda} \cdot x_1 \cdot \sin \theta\right) \\ \cos\left(\frac{2\pi}{\lambda} \cdot x_2 \cdot \sin \theta\right) \\ \vdots \\ \cos\left(\frac{2\pi}{\lambda} \cdot x_M \cdot \sin \theta\right) \end{bmatrix} \in \mathbb{R}^{M \times 1}, \\
\mathbf{a}_{\text{im}}(\theta) \triangleq \text{Im}[\mathbf{a}(\theta)] &= \begin{bmatrix} \sin\left(\frac{2\pi}{\lambda} \cdot x_1 \cdot \sin \theta\right) \\ \sin\left(\frac{2\pi}{\lambda} \cdot x_2 \cdot \sin \theta\right) \\ \vdots \\ \sin\left(\frac{2\pi}{\lambda} \cdot x_M \cdot \sin \theta\right) \end{bmatrix} \in \mathbb{R}^{M \times 1}. \quad (28)
\end{aligned}$$

Based on (26) and (27), we can define a MUSIC-like spectral for DOA estimation as follows

$$f_{\text{Proposed}}(\theta) = 10 \log_{10} \frac{1}{\|\mathbf{a}_{\text{re}}^T(\theta) \widehat{\mathbb{G}}\|^2 + \|\mathbf{a}_{\text{im}}^T(\theta) \widehat{\mathbb{G}}\|^2}. \quad (29)$$

Since $\mathbf{a}_{\text{re}}(\theta)$, $\mathbf{a}_{\text{im}}(\theta)$, and \mathbb{G} are all real, we must have

$$f_{\text{Proposed}}(\theta) = f_{\text{Proposed}}(-\theta) = 0, \quad (30)$$

which means that the minima of $f_{\text{Proposed}}(\theta)$ over half of the angular field of view, that is, $[-\pi/2, 0]$ or $[0, \pi/2]$, is either true

DOAs or their images. Thus, we can search over half of the angular field of view $[0, \pi/2]$ to obtain T candidate angles

$$\Theta^+ \triangleq \{\hat{\theta}_1, \hat{\theta}_2, \dots, \hat{\theta}_T\} \quad (31)$$

and select the L true DOAs from Θ^+ and its mirror

$$\Theta^- \triangleq -\Theta^+ = \{-\hat{\theta}_1, -\hat{\theta}_2, \dots, -\hat{\theta}_T\}, \quad (32)$$

by a further step to solve the ambiguity problem. Because for one true DOA θ_k , $f_{\text{Proposed}}(\theta)$ shows two symmetrical peaks at angles θ_k and $-\theta_k$ simultaneously. Therefore, for L true DOAs, $f_{\text{Proposed}}(\theta)$ gives at most L peaks over half of the angular field of view. This happens if and only if any two of the L true DOAs are not symmetrical. Oppositely, $f_{\text{Proposed}}(\theta)$ generates at least $\lfloor L/2 \rfloor$ peaks over half of the angular field of view, and this happens if and only if all the L true DOAs are paired symmetrical themselves. In other words, the number of candidate angles T satisfies

$$\left\lfloor \frac{L}{2} \right\rfloor \leq T \leq L. \quad (33)$$

The conventional beamformer (CBF) [37] is exploited to select the L true DOAs among Θ^+ and Θ^- . As the CBF takes its maxima only at the true DOAs, the CBF spectral amplitudes responding to the true DOAs must be much larger than those associated with their symmetrical mirrors. On the other hand, as the number of the true DOAs is known in advance, the L true DOAs can be easily selected among the candidate angles by

$$\hat{\Theta} = \{\hat{\theta}_1, \hat{\theta}_2, \dots, \hat{\theta}_L\} = \arg \min_{\theta \in \{\Theta^+, \Theta^-\}} f_{\text{CBF}}(\theta), \quad (34)$$

where

$$f_{\text{CBF}}(\theta) \triangleq 10 \log_{10} \|\mathbf{a}^H(\theta) \hat{\mathbf{R}} \mathbf{a}(\theta)\| [\text{dB}]. \quad (35)$$

Although using CBF to exclude the symmetrical mirror DOAs means that there is an additional step involved in the proposed estimator, the complexity of this further step is substantially lower since we only need to compute the product $\|\mathbf{a}^H(\theta) \hat{\mathbf{R}} \mathbf{a}(\theta)\|$ for at most $2L$ spectral points. Detailed steps for implementing the proposed algorithm are summarized in Algorithm 1.

We end up this section by a comparison of primary real-valued computational flops required by MUSIC [3], U-MUSIC [19], and the proposed method, which is shown in Table 2. In the table, J stands for the total number of search points over $[-\pi/2, \pi/2]$. Because EVD and spectral search dominate the total complexity, the common flops required by the three algorithms for the estimation of \mathbf{R} and the slight flops required by the proposed method for solving the ambiguity problem are omitted.

Using the fast subspace decomposition (FSD) technique [38], the EVD computation on a $M \times M$ real matrix for a signal subspace of dimension L costs $M^2(L+2)$ real-valued flops. As the proposed method has $2L - K$ equivalent signals, this term for the proposed method is given by $M^2(2L -$

$K+2)$. Since the standard MUSIC needs to compute the EVD of the complex matrix \mathbf{R} , this term for MUSIC is given by $4 \times M^2(L+2)$. Because $\mathbf{a}(\theta) \in \mathbb{C}^{M \times 1}$ and $\mathbf{G} \in \mathbb{C}^{M \times (M-L)}$, computing the MUSIC spectral for J sample points over $[-\pi/2, \pi/2]$ costs $4 \times J(M+1)(M-L)$ real-valued flops [39]. Since the proposed method involves a compressed search over $[0, \pi/2]$ (or $[-\pi/2, 0]$), it only needs to compute $J/2$ sample points. Taking into account that $\mathbf{a}(\theta) \in \mathbb{R}^{M \times 1}$, $\mathbf{a}_{\text{im}}(\theta) \in \mathbb{R}^{M \times 1}$ and $\mathbf{G} \in \mathbb{R}^{M \times (M-2L+K)}$, the complexity of spectral search for the proposed method is significantly reduced to $J(M+1)(M-2L+K)$.

It can be concluded from Table 2 that our method has the lowest complexity among the three algorithms. Moreover, because we generally have $J \gg M$ [8, 15], about 3/4 = 75% complexities are reduced by the new method as compared to the standard MUSIC.

4. Simulation Results

Numerical simulations with 500 Monte Carlo trials are conducted to demonstrate the performance of the proposed method on a linear array composed of $M = 10$ sensors, where $L = 2$ sources are considered throughout the simulations. For the root mean square error (RMSE) comparison, the Cramer-Rao lower bound (CRLB) given in [40] is also applied for reference and the RMSE is defined as

$$\text{RMSE} \triangleq 10 \log_{10} \sqrt{\frac{1}{1000} \sum_{i=1}^{500} \sum_{l=1}^2 (\hat{\theta}_i^l - \theta_i^l)^2} [\text{dB}], \quad (36)$$

where $\hat{\theta}_i^l$ is the i th estimated value of the l th signal incident angle θ^l . For L sources, the signal-to-noise ratio (SNR) is defined as

$$\text{SNR} \triangleq 10 \log_{10} \left[\frac{P_{\text{avg}}}{\sigma_n^2} \right] [\text{dB}], \quad (37)$$

where $P_{\text{avg}} = 1/L \sum_{l=1}^L P_l$ denotes the average power of all sources, and $P_l = E[s_l^2(t)]$ is the power of the l th, $l = 1, 2, \dots, L$ source.

In the first simulation, we use a ULA to estimate the DOAs of two sources located at $\theta_1 = 30^\circ$ and $\theta_2 = 40^\circ$. Five algorithms including the standard MUSIC [3], ESPRIT [9], U-MUSIC [19], RV-MUSIC [39], and the proposed method are applied in the simulation.

Figure 1 compares the RMSEs of different algorithms against the SNR, where the number of snapshots is set as $N = 200$. It is seen from Figure 1 that U-MUSIC is the most accurate one among the four methods as expected, although it can be only used with CSAs. It is also seen from the figure that with a significantly reduced complexity, our method can still provide a close accuracy to the standard MUSIC and the RV-MUSIC algorithms, especially with $\text{SNR} > 0$ dB. In addition, the proposed has a much better accuracy than ESPRIT.

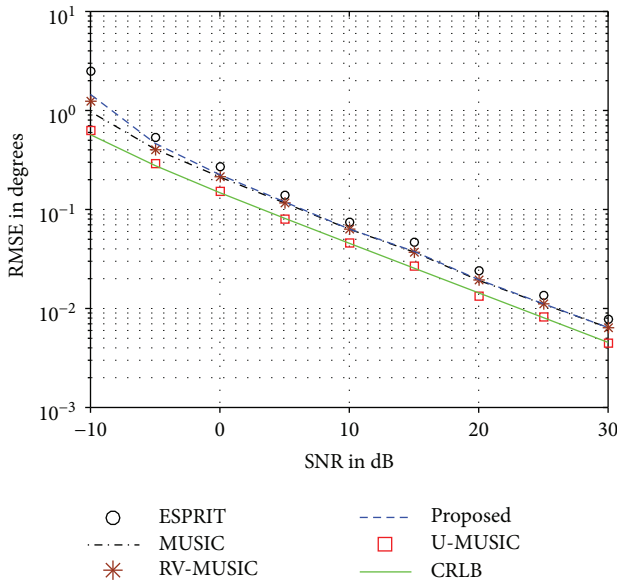
To see more clearly the performance of the new method with a ULA, Figure 2 plots the RMSEs of different algorithms as functions of the number of snapshots, where the SNR is

Require: $\{x(t)\}_{t=1}^N \rightarrow N$ snapshots of the array output vectors.
Return: $\hat{\Theta} = \{\hat{\theta}_l\}_{l=1}^L \rightarrow$ a set of L estimated source DOAs.
 1. Estimate $\hat{\mathbf{R}} = \mathbf{1}/N \sum_{t=1}^N x(t)x^H(t)$ and obtain its real part $\text{Re}(\hat{\mathbf{R}})$;
 2. Compute $\text{Re}(\hat{\mathbf{R}}) = \hat{\mathbf{S}}\hat{\mathbf{Q}}\hat{\mathbf{S}}^T + \hat{\mathbf{G}}\hat{\mathbf{Q}}_n\hat{\mathbf{G}}^T$ to get the noise matrix $\hat{\mathbf{G}}$;
 3. Construct $f_{\text{Proposed}}(\theta) = 10 \log_{10}(1/\|\mathbf{a}_{\text{re}}^T(\theta)\hat{\mathbf{G}}\|^2 + \|\mathbf{a}_{\text{im}}^T(\theta)\hat{\mathbf{G}}\|^2)$;
 4. Search $f_{\text{Proposed}}(\theta)$ over only $[0, \pi/2]$ to get T peak angles $\Theta^+ = \{\hat{\theta}_1, \hat{\theta}_2, \dots, \hat{\theta}_T\}$;
 5. Obtain $2T$ candidate angles Θ^+ and $\Theta^- = -\Theta^+$;
 6. Select the L true DOAs by $\hat{\Theta} = \arg \min_{\theta \in \{\Theta^+, \Theta^-\}} \|\mathbf{a}^H(\theta)\hat{\mathbf{R}}\mathbf{a}(\theta)\|$.

ALGORITHM 1: The Proposed Algorithm.

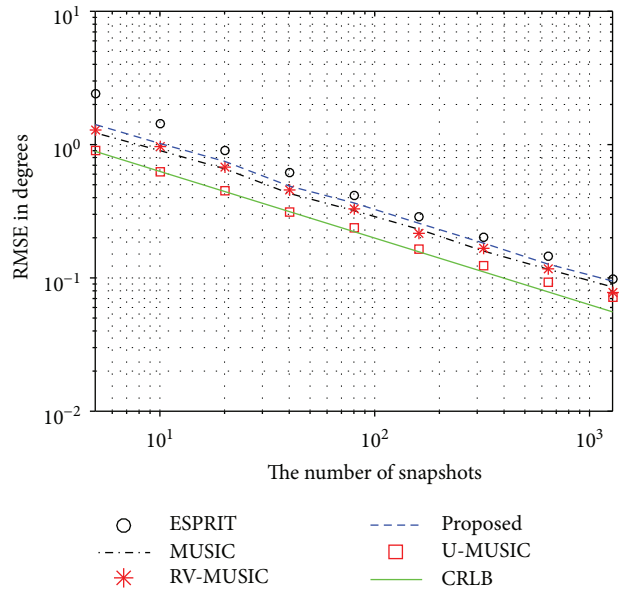
TABLE 2: Comparison of real-valued computational flops.

| Algorithms | Real-valued computational flops |
|------------|--|
| MUSIC | $4 \times M^2(L+2) + 4 \times J(M+1)(M-L)$ |
| U-MUSIC | $M^2(L+2) + J(L+1)(M-L)$ |
| Proposed | $M^2(2L-K+2) + J(M+1)(M-2L+K)$ |

FIGURE 1: RMSE versus the SNR, ULA, $N = 200$, $\theta_1 = 30^\circ$, $\theta_2 = 40^\circ$, and $M = 10$.

fixed as $\text{SNR} = 5$ dB. It can be concluded again from Figure 2 that the proposed method can provide acceptable estimation accuracy which is very close to MUSIC and RV-MUSIC and is much better than ESPRIT.

In the second simulation, we examine fast DOA estimation with nonuniform linear arrays (NULAs), where two closely spaced sources located at $\theta_1 = 25^\circ$ and $\theta_2 = 28^\circ$ are considered. We use a minimum redundancy linear array (MRLA) [41] to assess the performance of the proposed method and compare it to that of the standard MUSIC. Note that neither the shift invariant geometry or the centrosymmetrical structure exists in a MRLA, and hence ESPRIT [9] and most state-of-the-art real-valued methods [19–23]

FIGURE 2: RMSE versus the number of snapshots, ULA, $\text{SNR} = 5$ dB, $\theta_1 = 30^\circ$, $\theta_2 = 40^\circ$, and $M = 10$.

including U-MUSIC cannot be used in such an array directly without array mapping techniques [28].

In Figure 3, we set again the number of snapshots as $N = 200$ and compare the RMSEs of different algorithms against the SNR. In Figure 4, we fix $\text{SNR} = 5$ dB and plot RMSEs as functions of the number of snapshots, where the amounts of snapshots vary from a wide range over $N = 20$ to $N = 5120$.

It can be seen clearly from Figure 3 and Figure 4 that the three methods perform closely to each other. More specifically, the standard MUSIC slightly outperforms RV-MUSIC and the proposed technique, especially with low SNRs and small numbers of snapshots. However, as the proposed method is a real-valued DOA estimator which reduces about 75% complexities, it makes an efficient trade-off between complexity and accuracy as compared to the standard MUSIC.

In the third simulation, we examine the performance of the proposed method with different numbers of signals in Figure 5 and Figure 6, where the simulation parameters are given in the captions. As can be seen clearly from the two figures that our method provides very close RMSEs to

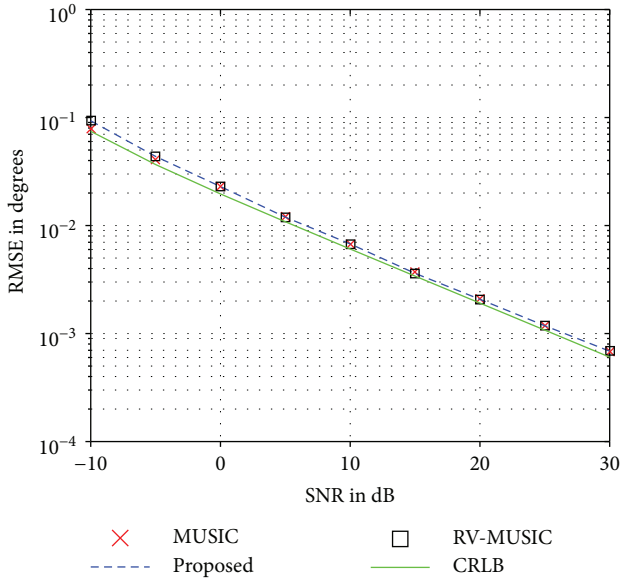


FIGURE 3: RMSE versus SNR, MRLA, $N = 200$, $\theta_1 = 25^\circ$, $\theta_2 = 28^\circ$, and $M = 10$.

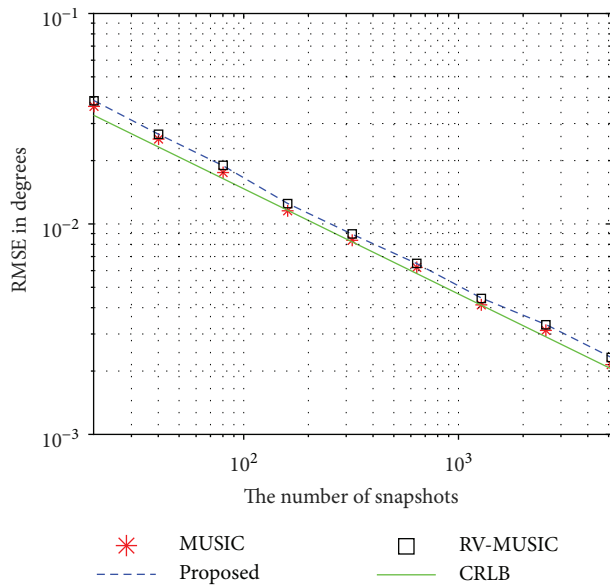


FIGURE 4: RMSE versus the number of snapshots, SNR = 5dB, MRLA, $\theta_1 = 25^\circ$, $\theta_2 = 28^\circ$, and $M = 10$.

the standard MUSIC with different numbers of signals. It is also seen from the two figures that the performances of both the two method decreases slightly when L increases. This is because when L increases, the dimensions of noise subspaces decreases oppositely.

In the last simulation, we use a ULA to plot the simulation times of DOA estimation by MUSIC [3], U-MUSIC [19], RV-MUSIC [39] and the proposed method as functions of the number of sensors in Figure 7, where we set SNR = 10 dB, $N = 200$, and two sources located at $\theta_1 = 10^\circ$ and $\theta_2 = 20^\circ$ are considered. The simulated results are given by a PC with Intel(R) Core(TM) Duo T5870 2.0 GHz CPU and 1 GB RAM by running the Matlab codes in the same

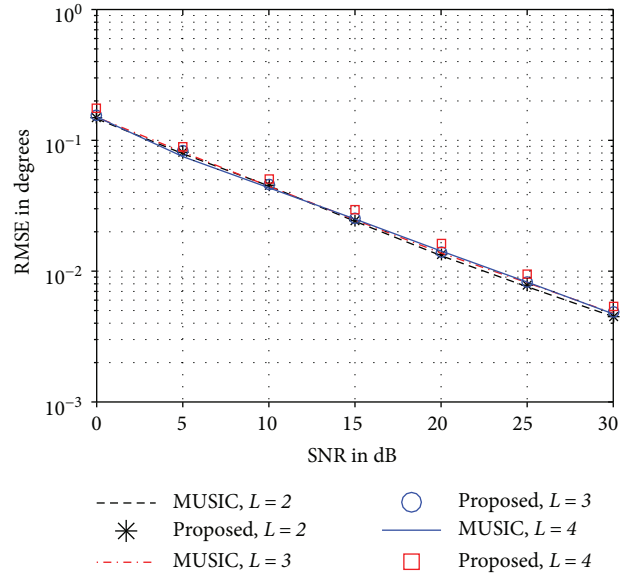


FIGURE 5: RMSE versus SNR respect to different numbers of signals, ULA, $N = 100$, and $M = 14$.

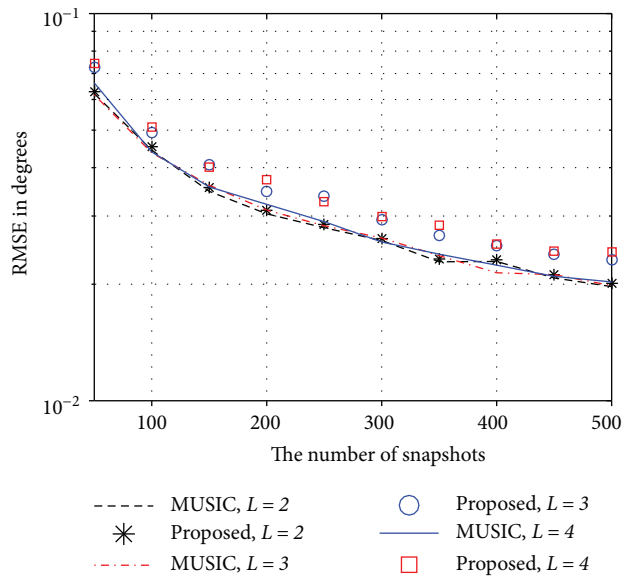


FIGURE 6: RMSE versus the number of snapshots respect to different numbers of signals, ULA, SNR = 10 dB and $M = 14$.

environment, where a common fine search grid $\Delta\theta = 0.0053^\circ$ is used the three methods. It can be concluded from Figure 7 that although the proposed method is slightly efficient than the RV-MUSIC algorithm, it is the most efficient one among the four techniques, and it costs a simulation time being about 4 times lower than that of MUSIC.

5. Conclusions

We have proposed an efficient DOA estimation algorithm, in which both tasks of eigenvalue decomposition and spectral search are implemented with low-complexity real-valued computations. In addition, the proposed method can be used

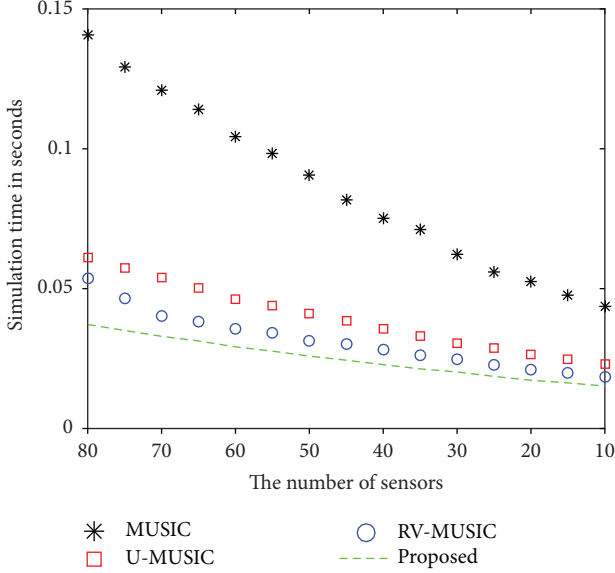


FIGURE 7: Simulation time versus the number of sensors, ULA, SNR = 10 dB, $N = 200$, $\theta_1 = 10^\circ$, and $\theta_2 = 20^\circ$.

with arbitrary array configurations, which shows implementation advantage over most existing unitary methods. Complexity analysis and simulation demonstrate that with about 75% reduced complexity, the new method is able to provide a good DOA estimation accuracy which is very close to the standard MUSIC.

Appendix

Proof of Equation (21)

We Begin the Proof by Using (6) to Rewrite R as

$$\begin{aligned} \mathbb{R} &= \frac{1}{2}(\mathbf{R} + \mathbf{R}^*) = \frac{1}{2}[\mathbf{A}(\Theta)\mathbb{R}_s\mathbf{A}^H(\Theta) + \mathbf{A}^*(\Theta)\mathbb{R}_s\mathbf{A}^T(\Theta)] \\ &+ \sigma_n^2\mathbb{I}_M = \frac{1}{2}[\mathbf{A}(\Theta)\mathbf{A}^*(\Theta)] \begin{bmatrix} \mathbb{R}_s & \mathbf{0} \\ \mathbf{0} & \mathbb{R}_s \end{bmatrix} \begin{bmatrix} \mathbf{A}^H(\Theta) \\ \mathbf{A}^H(\Theta) \end{bmatrix} \\ &+ \sigma_n^2\mathbb{I}_M = \mathbb{H}(\Theta)\widetilde{\mathbb{R}}_s\mathbb{H}^H(\Theta) + \sigma_n^2\mathbb{I}_M = \mathbb{D}(\Theta) + \sigma_n^2\mathbb{I}_M. \end{aligned} \quad (\text{A.1})$$

Since there are K pairs of symmetrical sources in Θ , we can divide Θ into two subsets as follows:

$$\Theta = \{\Theta_1, \Theta_2\} \quad (\text{A.2})$$

where Θ_1 contains all the symmetrical sources and we can write

$$\begin{aligned} \Theta_1 &= \{-\theta_1, \theta_1, -\theta_2, \theta_2, \dots, -\theta_K, \theta_K\}, \\ \Theta_2 &= \{\theta_{K+1}, \theta_{K+2}, \dots, \theta_L\}. \end{aligned} \quad (\text{A.3})$$

Note for any two DOAs $\theta_1, \theta_2 \in \Theta_2$, we have $\theta_1 \neq -\theta_2$. Because $\mathbf{A}(\Theta)$ has the Vandermonde structure and $\mathbf{A}^*(\Theta_1) = \mathbf{A}(-\Theta_1) = \mathbf{A}(\Theta_1)$, we must have

$$\text{rank}[\mathbb{H}(\Theta)] = \text{rank}[\mathbf{A}(\Theta)] + \text{rank}[\mathbf{A}^*(\Theta)] - K = 2L - K. \quad (\text{A.4})$$

Since $\widetilde{\mathbb{R}}_s$ is a diagonal matrix with full rank (note that $\mathbf{n}(t)$ is assumed to be uncorrelated), we can write $\widetilde{\mathbb{R}}_s = \mathbb{V}\mathbb{V}^T$, where \mathbb{V} is also a diagonal matrix with full rank. Thus, we further obtain [28]

$$\begin{aligned} \text{rank}[\mathbb{D}(\Theta)] &= \text{rank}[\mathbb{H}(\Theta)\widetilde{\mathbb{R}}_s\mathbb{H}^T(\Theta)] \\ &= \text{rank}[\mathbb{H}(\Theta)\mathbb{V}\mathbb{V}^T\mathbb{H}^T(\Theta)] \\ &= \text{rank}[\mathbb{H}(\Theta)\mathbb{V}] = 2L - K. \end{aligned} \quad (\text{A.5})$$

As $\beta_1, \beta_2, \dots, \beta_{2L-K}$ are the $2L - K$ eigenvalues of matrix $\mathbb{D}(\Theta)$, we have

$$\mathbb{U}^T\mathbb{D}(\Theta)\mathbb{U} = \text{diag}\{\beta_1, \beta_2, \dots, \beta_{2L-K}, 0, \dots, 0\}. \quad (\text{A.6})$$

Using (A.6), we have

$$\begin{aligned} \mathbb{U}^T\mathbb{R}\mathbb{U} &= \mathbb{U}^T\mathbb{D}(\Theta)\mathbb{U} + \sigma_n^2\mathbb{U}^T\mathbb{U} \\ &= \text{diag}\{\beta_1, \beta_2, \dots, \beta_{2L-K}, 0, \dots, 0\} + \sigma_n^2\mathbb{I}, \end{aligned} \quad (\text{A.7})$$

which implies that the eigenvalues of \mathbb{R} are given by

$$\xi_i = \begin{cases} \beta_i + \sigma_n^2, & i = 1, 2, \dots, 2L - K, \\ \sigma_n^2, & i = 2L - K + 1, 2, \dots, M, \end{cases} \quad (\text{A.8})$$

and the proof is completed.

Conflicts of Interest

The authors declare that there is no conflict of interest regarding the publication of this paper.

Acknowledgments

This work is supported by the National Natural Science Foundation of China (61501142), China Postdoctoral Science Foundation (2015M571414), Science and Technology Program of Weihai, and Discipline Construction Guiding Foundation in Harbin Institute of Technology (Weihai) (WH20160107).

References

- [1] H. Krim and M. Viberg, "Two decades of array signal processing research: the parametric approach," *IEEE Signal Processing Magazine*, vol. 13, no. 4, pp. 67–94, 1996.
- [2] D. H. Tuan and P. Russer, "Signal processing for wideband smart antenna array applications," *IEEE Microwave Magazine*, vol. 5, no. 1, pp. 57–67, 2004.
- [3] R. O. Schmidt, "Multiple emitter location and signal parameter estimation," *IEEE Transactions on Antennas and Propagation*, vol. 34, no. 3, pp. 276–280, 1986.
- [4] P. Stoica and K. C. Sharman, "Maximum likelihood methods for direction-of-arrival estimation," *IEEE Transactions on Acoustics, Speech, and Signal Processing*, vol. 38, no. 7, pp. 1132–1143, 1990.

- [5] A. Swindlehurst and M. Viberg, "Subspace fitting with diversely polarized antenna arrays," *IEEE Transactions on Antennas and Propagation*, vol. 41, no. 12, pp. 1687–1694, 1993.
- [6] R. Kumaresan and D. W. Tufts, "Estimating the angles of arrival of multiple plane waves," *IEEE Transactions on Aerospace and Electronic Systems*, vol. AES-19, no. 1, pp. 134–139, 1983.
- [7] W. Zheng, X. Zhang, and J. Shi, "Sparse extension Array geometry for DOA estimation with nested MIMO radar," *IEEE Access*, vol. 5, pp. 9580–9586, 2017.
- [8] F. G. Yan, M. Jin, and X. L. Qiao, "Low-complexity DOA estimation based on compressed MUSIC and Its performance analysis," *IEEE Transactions on Signal Processing*, vol. 61, no. 8, pp. 1915–1930, 2013.
- [9] R. Roy and T. Kailath, "ESPRIT-estimation of signal parameters via rotational invariance techniques," *IEEE Transactions on Acoustics, Speech, and Signal Processing*, vol. 37, no. 7, pp. 984–995, 1989.
- [10] A. Barabell, "Improving the resolution performance of eigenstructure-based direction-finding algorithms," in *ICASSP '83. IEEE International Conference on Acoustics, Speech, and Signal Processing*, vol. 8, pp. 336–339, Boston, MA, USA, April 1983.
- [11] G. Jiang, X. Mao, and Y. Liu, "Direction-of-arrival estimation for uniform circular arrays under small sample size," *Journal of Systems Engineering and Electronics*, vol. 27, no. 6, pp. 1142–1150, 2016.
- [12] D. Zhang, Y. Zhang, G. Zheng, C. Feng, and J. Tang, "Improved DOA estimation algorithm for co-prime linear arrays using root-MUSIC algorithm," *Electronics Letters*, vol. 53, no. 18, article 1279, 2017.
- [13] T. E. Tuncer, T. K. Yasar, and B. Friedlander, "Direction of arrival estimation for nonuniform linear arrays by using array interpolation," *Radio Science*, vol. 42, no. 4, 2007.
- [14] Y. Cao, Z. Zhang, F. Dai, and R. Xie, "Direction of arrival estimation for monostatic multiple-input multiple-output radar with arbitrary array structures," *IET Radar, Sonar & Navigation*, vol. 6, no. 7, p. 679, 2012.
- [15] M. Rbsamen and A. B. Gershman, "Direction-of-arrival estimation for nonuniform sensor arrays: from manifold separation to Fourier domain MUSIC methods," *IEEE Transactions on Signal Processing*, vol. 57, no. 2, pp. 588–599, 2009.
- [16] F. G. Yan, M. Jin, and X. L. Qiao, "Source localization based on symmetrical MUSIC and Its statistical performance analysis," *Science China Information Sciences*, vol. 56, no. 6, pp. 1–13, 2013.
- [17] K. C. Huarng and C. C. Yeh, "A unitary transformation method for angle-of-arrival estimation," *IEEE Transactions on Signal Processing*, vol. 39, no. 4, pp. 975–977, 1991.
- [18] D. A. Linebarger, R. D. DeGroat, and E. M. Dowling, "Efficient direction-finding methods employing forward/backward averaging," *IEEE Transactions on Signal Processing*, vol. 42, no. 8, pp. 2136–2145, 1994.
- [19] S. Akkar and A. Gharsallah, "Reactance domains unitary MUSIC algorithms based on real-valued orthogonal decomposition for electronically steerable parasitic array radiator antennas," *IET Microwaves, Antennas & Propagation*, vol. 6, no. 2, p. 223, 2012.
- [20] C. Qian, L. Huang, and H. C. So, "Improved unitary root-MUSIC for DOA estimation based on pseudo-noise resampling," *IEEE Signal Processing Letters*, vol. 21, no. 2, pp. 140–144, 2014.
- [21] G. Zheng, B. Chen, and M. Yang, "Unitary ESPRIT algorithm for bistatic MIMO radar," *Electronics Letters*, vol. 48, no. 3, p. 179, 2012.
- [22] A. B. Gershman and P. Stoica, "On unitary and forward-backward MODE," *Digital Signal Processing*, vol. 9, no. 2, pp. 67–75, 1999.
- [23] N. Yilmazer, J. Koh, and T. K. Sarkar, "Utilization of a unitary transform for efficient computation in the matrix pencil method to find the direction of arrival," *IEEE Transactions on Signal Processing*, vol. 54, no. 1, pp. 175–181, 2006.
- [24] F. G. Yan, T. Jin, M. Jin, and Y. Shen, "Subspace-based direction-of-arrival estimation using centro-symmetrical arrays," *Electronics Letters*, vol. 52, no. 22, pp. 1895–1896, 2016.
- [25] F. G. Yan, B. Cao, S. Liu, M. Jin, and Y. Shen, "Reduced-complexity direction of arrival estimation with centro-symmetrical arrays and Its performance analysis," *Signal Processing*, vol. 142, pp. 388–397, 2018.
- [26] F. G. Yan, Y. Shen, and M. Jin, "Fast DOA estimation based on a split subspace decomposition on the array covariance matrix," *Signal Processing*, vol. 115, pp. 1–8, 2015.
- [27] F. G. Yan, X. W. Yan, J. Shi et al., "MUSIClike direction of arrival estimation based on virtual array transformation," *Signal Processing*, vol. 139, pp. 156–164, 2017.
- [28] P. Pal and P. P. Vaidyanathan, "Nested arrays: a novel approach to array processing with enhanced degrees of freedom," *IEEE Transactions on Signal Processing*, vol. 58, no. 8, pp. 4167–4181, 2010.
- [29] Y. Tian and H. Xu, "Extended-aperture DOA estimation with unknown number of sources," *Electronics Letters*, vol. 51, no. 7, pp. 583–584, 2015.
- [30] F. G. Yan, Z. K. Chen, M. J. Sun, Y. Shen, and M. Jin, "Two-Dimensional Direction-of-Arrivals Estimation Based on One-Dimensional Search Using Rank Deficiency Principle," *International Journal of Antennas and Propagation*, vol. 2015, Article ID 127621, 8 pages, 2015.
- [31] J. D. Lin, W. H. Fang, Y. Y. Wang, and J. T. Chen, "FSF MUSIC for joint DOA and frequency estimation and Its performance analysis," *IEEE Transactions on Signal Processing*, vol. 54, no. 12, pp. 4529–4542, 2006.
- [32] F. Li, H. Liu, and R. J. Vaccaro, "Performance analysis for DOA estimation algorithms: unification, simplification, and observations," *IEEE Transactions on Aerospace and Electronic Systems*, vol. 29, no. 4, pp. 1170–1184, 1993.
- [33] F. Li, R. J. Vaccaro, and D. W. Tufts, "Performance analysis of the statespace realization (TAM) and ESPRIT algorithms for DOA estimation," *IEEE Transactions on Antennas and Propagation*, vol. 39, no. 3, pp. 418–423, 1991.
- [34] F. Liu, J. Wang, C. Sun, and R. Du, "Spatial differencing method for DOA estimation under the coexistence of both uncorrelated and coherent signals," *IEEE Transactions on Antennas and Propagation*, vol. 60, no. 4, pp. 2052–2062, 2012.
- [35] Z. Ye, Y. Zhang, and X. Xu, "Two-dimensional direction of arrival estimation in the presence of uncorrelated and coherent signals," *IET Signal Processing*, vol. 3, no. 5, pp. 416–429, 2009.
- [36] G. H. Golub and C. H. Van Loan, *Matrix computations*, The Johns Hopkins Univ. Press., Baltimore, MD, USA, 1996.
- [37] J. C. Chen, K. Yao, and R. E. Hudson, "Source localization and beamforming," *IEEE Signal Processing Magazine*, vol. 19, no. 2, pp. 30–39, 2002.

- [38] G. Xu and T. Kailath, "Fast subspace decomposition," *IEEE Transactions on Signal Processing*, vol. 42, no. 3, pp. 539–551, 1994.
- [39] F. G. Yan, M. Jin, S. Liu, and X. L. Qiao, "Real-valued MUSIC for efficient direction estimation with arbitrary array geometries," *IEEE Transactions on Signal Processing*, vol. 62, no. 6, pp. 1548–1560, 2014.
- [40] P. Stoica and A. Nehorai, "Performance study of conditional and unconditional direction-of-arrival estimation," *IEEE Transactions on Acoustics, Speech, and Signal Processing*, vol. 38, no. 10, pp. 1783–1795, 1990.
- [41] C. Chambers, T. C. Tozer, K. C. Sharman, and S. D. Tariq, "Temporal and spatial sampling influence on the estimates of superimposed narrowband signals: when less can mean more," *IEEE Transactions on Signal Processing*, vol. 44, no. 12, pp. 3085–3098, 2004.

Research Article

Joint DOA and DOD Estimation Based on Tensor Subspace with Partially Calibrated Bistatic MIMO Radar

Junxiang Wang ^{1,2} Ping Huang,¹ and Dingjie Xu²

¹College of Automation, Harbin Engineering University, Harbin, Heilongjiang 150001, China

²College of Electrical Engineering and Automation, Harbin Institute of Technology University, Harbin 150001, China

Correspondence should be addressed to Junxiang Wang; wangjunxiang@hrbeu.edu.cn

Received 2 August 2017; Accepted 18 December 2017; Published 22 April 2018

Academic Editor: Piotr Samczynski

Copyright © 2018 Junxiang Wang et al. This is an open access article distributed under the Creative Commons Attribution License, which permits unrestricted use, distribution, and reproduction in any medium, provided the original work is properly cited.

A joint direction-of-departure (DOD) and direction-of-arrival (DOA) estimation algorithm based on tensor subspace approach for partially calibrated bistatic multiple-input multiple-output (MIMO) radar is proposed. By exploiting the multidimensional structure of the received data, a third-order measurement tensor is constructed. Consequently, the tensor-based signal subspace is achieved using the higher-order singular value decomposition (HOSVD). To achieve accurate DOA estimation with partially calibrated array, a closed-form solution is provided to estimate the gain-phase uncertainties of the transmit and receive arrays by modeling the imperfections of the arrays. Simulation results demonstrate the effectiveness of the proposed calibration algorithm.

1. Introduction

Array signal processing, which includes parameter estimation [1, 2] and beamforming [3, 4] has been widely investigated in past decades [5] which has found various applications in radar, sonar, and satellite navigation system. In recent years, multiple-input multiple-output (MIMO) radar [6, 7] has drawn increasing attention due to its significant advantages, such as higher angular resolution and more degrees-of-freedom (DOFs). MIMO radar using multiple antennas to simultaneously emit orthogonal waveforms and multiple antennas to receive the reflected signals has recently drawn increasing attention owing to its superior performance over to the conventional phased array. Direction-of-departure (DOD) and direction-of-arrival (DOA) estimation is an important objective of bistatic MIMO radar system. Various algorithms for DOD and DOA estimation have been proposed in literatures [8–12]. In [8], the rotational invariance property of the MIMO radar is exploited which enables the DOD and DOA estimation with bistatic MIMO radar. However, this method determines the DODs and DOAs using two independent estimation of signal parameters via

rotational invariance technique (ESPRIT) and requires an extra procedure to achieve the paired DOD and DOA estimation. To avoid the pair matching procedure, the relationship between the two independent ESPRIT is exploited in [9] to estimate the DODs and DOAs. In [10], a reduced-dimension MULTiple Signal Classification (MUSIC) algorithm is proposed which only requires one-dimensional peak search. This method achieves a similar performance compared with the two-dimensional MUSIC algorithm and has a lower computational complexity. Based on the double polynomial root-finding procedure, a polynomial root-finding technique for joint DOD and DOA estimation is proposed in [11]. This algorithm allows an efficient estimation with automatic pairing. In [12], the property of the Kronecker product is utilized to formulate a cost function in the quadratic form. Then the DODs can be estimated from the constraint function. The DOAs can be achieved from the eigenvector which is related to the corresponding DODs.

However, the algorithms mentioned above are based on the assumption that arrays are well calibrated which is not true in practice. Therefore, the above algorithms will suffer from performance degradation or even fail to achieve

accurate DOD and DOA estimation in many scenarios. A number of algorithms have been proposed to deal with the array calibration problem [13–17]. An iterative algorithm based on the MUSIC technique is proposed in [13], which can simultaneously achieve the angle and gain-phase uncertainties estimation. Due to the iterative procedure, this algorithm has a high computational complexity. In addition, this method is based on the assumption that the gain-phase uncertainties are small, otherwise it will suffer from suboptimal convergence. The algorithms proposed in [15, 16] do not require iteration and exploit the ESPRIT-like technique to achieve accurate angle estimations. To achieve higher DOFs, the method proposed in [17] utilizes the property of the quasistationary signals to solve the underdetermined DOA estimation problem with partly calibrated arrays. Moreover, a kind of calibration methods based on the sparse reconstruction is discussed in [18, 19].

However, the multiple-dimensional property of the received signal is not exploited in the abovementioned algorithms. The inherently multiple-dimensional structure of the received signal can be utilized by expressing the received signal as a third-order tensor [20]. Thus, the higher-order singular value decomposition (HOSVD) can be used to achieve a tensor-based signal subspace which improves the estimation performance especially with low signal to noise ratio (SNR).

In this paper, we exploit a calibration algorithm based on tensor approach for partially calibrated bistatic MIMO radar. We first exploit the multidimensional structure of the received data, and then, the tensor-based signal subspace is calculated using HOSVD. By formulating the gain-phase imperfections in the generalized manifold matrix, a closed-form solution is achieved to estimate the gain-phase uncertainties of the transmit and receive arrays. With the estimated gain-phase uncertainties, the arrays can be calibrated and the DODs and DOAs of the sources can be estimated accurately. Simulation results demonstrate the effectiveness of the proposed joint DOD and DOA estimation algorithm for partially calibrated bistatic MIMO radar.

The rest of this paper is organized as follows. In Section 2, we briefly introduce the tensor algebra basics and the tensor-based signal model of the bistatic MIMO radar. In Section 3, we first describe the partially calibrated MIMO radar model. Then, the proposed method is introduced. Numerical simulation results are presented in Section 4. The conclusions are made in Section 5.

Notations used in this paper are as follows: lowercase (uppercase) bold characters are used to denote vectors (matrices). $[\mathcal{A}]_{i,j,k}$ stands for the (i, j, k) th entry of \mathcal{A} . \mathbf{I}_N denotes the $N \times N$ identity matrix. $(\cdot)^T$ and $(\cdot)^H$ denote the transpose and Hermitian operations of a matrix or vector, respectively. $\text{vec}(\cdot)$ stands for the vectorization operator. $\text{diag}(\mathbf{x})$ denotes a diagonal matrix with the elements of \mathbf{x} constituting the diagonal entries. \otimes denotes the Kronecker product, \circ denotes the Hadamard product, and \odot denotes the Khatri-Rao product. In addition, $\|\cdot\|_2$ denotes the ℓ_2 -norm, whereas $\mathbb{C}^{M \times N}$ and \mathbb{C}^M express an $M \times N$ complex matrix or $M \times 1$ vector set.

2. Tensor Algebra Basic and Signal Model

In this section, we first introduce tensor operations used in this paper and provide the bistatic MIMO radar signal model.

2.1. Tensor Algebra Basic. In this subsection, the tensor algebra basic is introduced for readers' convenience [20, 21].

Definition 1 (n -mode unfolding). Denote a N -order tensor as $\mathcal{A} \in I_1 \times I_2 \times \cdots \times I_n$, the corresponding n -mode unfolding is to convert \mathcal{A} into a matrix which is expressed as $[\mathcal{A}]_{(n)} \in \mathbb{C}^{I_n \times I_1 I_2 \cdots I_{n-1} I_{n+1} \cdots I_N}$. The (i_1, i_2, \dots, i_N) th entry of the tensor \mathcal{A} maps to the (i_n, j) entry of $[\mathcal{A}]_{(n)}$, where

$$j = 1 + \sum_{k=1, k \neq n}^N (i_k - 1) J_k, \quad \text{with } J_k = \prod_{m=1, m \neq n} I_m. \quad (1)$$

Definition 2 (n -mode tensor product). The n -mode matrix product of the tensor $\mathcal{A} \in I_1 \times I_2 \times \cdots \times I_n$ with a matrix $\mathbf{U}_n \in \mathbb{C}^{J \times I_n}$ is denoted by $\mathcal{Y} = \mathcal{A} \times_n \mathbf{U}_n$ with size $I_1 \times I_2 \times \cdots \times I_{n-1} \times J \times I_{n+1} \times \cdots \times I_N$ and

$$[\mathcal{Y}]_{i_1, \dots, i_{n-1}, j, i_{n+1}, \dots, i_N} = \sum_{i_n=1}^{I_n} \mathcal{X}_{i_1, i_2, \dots, i_n} \mathbf{U}_{j, i_n}, \quad (2)$$

$$\mathcal{Y} = \mathcal{X} \times_n \mathbf{U} \Leftrightarrow [\mathcal{Y}]_{(n)} = \mathbf{U} [\mathcal{X}]_{(n)}.$$

Moreover, the properties of the mode tensor product are provided below:

$$\mathcal{X} \times_m \mathbf{U}_m \times_n \mathbf{U}_n = \mathcal{X} \times_n \mathbf{U}_n \times_m \mathbf{U}_m, \quad m \neq n, \quad (3)$$

$$\mathcal{X} \times_m \mathbf{U} \times_m \mathbf{V} = \mathcal{X} \times_n (\mathbf{U}\mathbf{V}).$$

Definition 3 (HOSVD). The HOSVD of the tensor $\mathbf{A} \in I_1 \times I_2 \times \cdots \times I_N$ can be written as

$$\mathbf{A} = \mathbf{S} \times_1 \mathbf{U}_1 \times_2 \mathbf{U}_2 \times_3 \cdots \times_N \mathbf{U}_N, \quad (4)$$

where $\mathbf{S} \in \mathbb{C}^{I_1 \times I_2 \times \cdots \times I_n}$ is the core tensor of \mathbf{A} which can be calculated by

$$\mathbf{S} = \mathbf{A} \times_1 \mathbf{U}_1^H \times_2 \mathbf{U}_2^H \times_3 \cdots \times_N \mathbf{U}_N^H. \quad (5)$$

In addition, \mathbf{U}_n , $n = 1, \dots, N$, is a unitary $I_n \times I_n$, which is the left singular matrix of \mathbf{U}_n .

2.2. Bistatic MIMO Radar Signal Model. Consider a bistatic MIMO radar system where the transmit and receive arrays are both uniform linear arrays (ULAs) with M and N collocated antennas, respectively. In addition, both the transmit and receive antennas are arranged with half-wavelength interelement space. The transmit antennas simultaneously emit orthogonal waveforms $\mathbf{S} = [\mathbf{s}_1^T, \dots, \mathbf{s}_M^T]^T \in \mathbb{C}^{M \times L}$ where L is the number of samples during pulse period. Assume that there are K uncorrelated narrowband far-field source signals in the range bin of interest. The baseband received signal at the q th pulse can be expressed as:

$$\mathbf{X}_q = \mathbf{A}_r \boldsymbol{\Sigma}_q \mathbf{A}_t^T \mathbf{S} + \mathbf{Z}_q, \quad q = 1, \dots, Q, \quad (6)$$

where $\mathbf{A}_r = [\mathbf{a}_r(\theta_1), \dots, \mathbf{a}_r(\theta_K)]$ and $\mathbf{A}_t = [\mathbf{a}_t(\phi_1), \dots, \mathbf{a}_t(\phi_K)]$ are the receive and transmit manifold matrix, respectively. $\mathbf{a}_r(\theta_k) = [1, e^{-j\pi \sin \theta_k}, \dots, e^{-j\pi(M_r-1)\sin \theta_k}]^T$ and $\mathbf{a}_t(\phi_k) = [1, e^{-j\pi \sin \phi_k}, \dots, e^{-j\pi(M_t-1)\sin \phi_k}]^T$ are the steering vectors of the k th source, respectively. $\{\theta_k, \phi_k\}_{k=1}^K$ is the pair of the DOA and DOD of the k th source. $\Sigma_q = \text{diag}(\mathbf{c}_q)$ with $\mathbf{c}_q = [\gamma_{1q}, \dots, \gamma_{Kq}]^T$ accounts for the Doppler effect and the radar reflection coefficient fading which follows the Swerling I model [22]. Finally, $Z_q \in \mathbb{C}^{M_r \times L}$ is zero mean Gaussian noise term. Under the fact that the transmitted waveforms are orthogonal to each other, that is,

$$\left(\frac{1}{L}\right) \mathbf{s}_i \mathbf{s}_j^H = \begin{cases} 1, & i = j, \\ 0, & i \neq j, \end{cases} \quad i, j = 1, \dots, M_t. \quad (7)$$

Then, the received signal can be processed by matched filtering using \mathbf{S}^H . Thus, the output of the matched filter can be written as

$$\mathbf{Y}_q = \left(\frac{1}{L}\right) \mathbf{X}_q \mathbf{S}^H = \mathbf{A}_r \Sigma_q \mathbf{A}_t^T + \mathbf{N}_q, \quad q = 1, \dots, Q, \quad (8)$$

where $\mathbf{N}_q = (1/L)\mathbf{Z}_q \mathbf{S}^H$ is additive zero mean Gaussian noise term with unknown variance σ_n^2 after matched filtering.

Usually, the received signal matrix can be achieved by vectorizing and stacking the Q pulses received signal, that is,

$$\mathbf{Y} = [\text{vec}(\mathbf{Y}_1), \dots, \text{vec}(\mathbf{Y}_Q)] = (\mathbf{A}_t \circ \mathbf{A}_r) \mathbf{C} + \mathbf{N}, \quad (9)$$

where $\mathbf{C} = [\mathbf{c}_1, \dots, \mathbf{c}_Q]$ and $\mathbf{N} = [\text{vec}(\mathbf{N}_1), \dots, \text{vec}(\mathbf{N}_Q)]$. However, this expression ignores the multidimensional structure inherent of the received signals. In order to exploit the multidimensional structure of the received signal, we collect Q pulses and gather $\mathbf{Y}_q, q = 1, \dots, Q$, as a third-order tensor given by

$$\mathcal{Y} = \mathcal{I}_K \times_1 \mathbf{A}_r \times_2 \mathbf{A}_t \times_3 \mathbf{C}^T + \mathcal{N}, \quad (10)$$

where \mathbf{I}_K is the $K \times K \times K$ identity tensor. $\mathbf{N} \in \mathbb{C}^{M_r \times M_t \times Q}$ is the noise tensor. According to Definition 1, the relationship between (8) and (10) can be expressed as $[\mathcal{Y}]_{(3)}^T = \mathbf{Y}$.

3. Proposed Method

In this section, the partially calibrated MIMO radar signal model is first provided. Then, a robust DOA estimation algorithm based on tensor algebra is presented.

3.1. Partially Calibrated MIMO Radar Model. Consider the case where only a part of the transmit and receive antennas is well-calibrated. Without loss of generality, we assume that the first M_{tc} and M_{rc} antennas of the transmit and receive arrays are calibrated, respectively, whereas the rest of the sensors are uncalibrated with unknown gain-phase uncertainties. Moreover, we assume that the uncertainties are direction-independent. Thus, the transmit manifold matrix and the receive manifold matrix can be, respectively, expressed as

$$\begin{aligned} \tilde{\mathbf{A}}_t &= \Gamma(\gamma_t) \mathbf{A}_t, \\ \tilde{\mathbf{A}}_r &= \Gamma(\gamma_r) \mathbf{A}_r, \end{aligned} \quad (11)$$

where $\Gamma(\gamma_t) = \text{diag}(\gamma_t)$ and $\Gamma(\gamma_r) = \text{diag}(\gamma_r)$ with gain-phase uncertainties $\gamma_t = [1_{M_{tc}}^T, \rho_1 e^{j\varphi_1}, \dots, \rho_{M_t-M_{tc}} e^{j\varphi_{M_t-M_{tc}}}]^T$ and $\gamma_r = [1_{M_{rc}}^T, \alpha_1 e^{j\beta_1}, \dots, \alpha_{M_r-M_{rc}} e^{j\beta_{M_r-M_{rc}}}]^T$, respectively. Thus, the received signal matrix can be expressed as

$$\tilde{\mathcal{Y}} = \mathbf{I}_K \times_1 \tilde{\mathbf{A}}_r \times_2 \tilde{\mathbf{A}}_t \times_3 \mathbf{C} + \mathcal{N}. \quad (12)$$

For the case of partially calibrated array, the conventional DOD and DOA estimation algorithm will suffer from severe performance degradation. In order to achieve satisfactory angle estimation result, the partially calibrated problem should be concerned.

3.2. ESPRIT-Like Calibration Method. The HOSVD of the received signal (12) can be written as

$$\tilde{\mathcal{Y}} = \mathcal{S} \times_1 \mathbf{U}_1 \times_2 \mathbf{U}_2 \times_3 \mathbf{U}_3, \quad (13)$$

where $\mathcal{S} \in \mathbb{C}^{M_r \times M_t \times Q}$, $\mathbf{U}_1 \in \mathbb{C}^{M_r \times M_r}$, $\mathbf{U}_2 \in \mathbb{C}^{M_t \times M_t}$, and $\mathbf{U}_3 \in \mathbb{C}^{Q \times Q}$. Denote the signal subspace of \mathcal{Y} as

$$\mathcal{U}_s = \mathcal{S} \times_1 \mathbf{U}_{1s} \times_2 \mathbf{U}_{2s}, \quad (14)$$

where $\mathcal{S}_s = \tilde{\mathcal{Y}} \times_1 \mathbf{U}_{1s}^H \times_2 \mathbf{U}_{2s}^H \times_3 \mathbf{U}_{3s}^H$, \mathbf{U}_{ns} contains the first K dominant singular vectors of \mathbf{U}_n with $n=1,2,3$. Thus, according to Definition 3, we have

$$\mathcal{U}_s = \tilde{\mathcal{Y}} \times_1 (\mathbf{U}_{1s} \mathbf{U}_{1s}^H) \times_2 (\mathbf{U}_{2s} \mathbf{U}_{2s}^H) \times_3 \mathbf{U}_{3s}^H. \quad (15)$$

Then, the signal subspace in matrix form can be calculated from the 3-mode unfolding of \mathcal{U}_s , that is, $[\mathcal{U}_s]_{(3)}^T = \mathbf{E}_s$. Note that the signal subspace expands the same space with the manifold matrix, that is,

$$\mathbf{E}_s = \left(\tilde{\mathbf{A}}_t \circ \tilde{\mathbf{A}}_r \right) \mathbf{T}, \quad (16)$$

where \mathbf{T} is a full rank matrix.

The generalized manifold matrix can be rewritten as

$$\tilde{\mathbf{A}}_t \circ \tilde{\mathbf{A}}_r = \Gamma(\gamma_t \otimes \gamma_r) (\mathbf{A}_t \circ \mathbf{A}_r) = \Gamma(\tilde{\gamma}) (\mathbf{A}_t \circ \mathbf{A}_r), \quad (17)$$

where $\tilde{\gamma} = \gamma_t \otimes \gamma_r$. Thus, by selecting the first $(M_t - 1)M_r$ rows of \mathbf{E}_s , we have

$$\begin{aligned} \mathbf{E}_{t1} &= \left(\tilde{\mathbf{A}}_{t1} \circ \tilde{\mathbf{A}}_r \right) \mathbf{T} = \Gamma(\tilde{\gamma}_{t1}) (\mathbf{A}_{t1} \circ \mathbf{A}_r) \mathbf{T}, \\ \mathbf{E}_{t2} &= \left(\tilde{\mathbf{A}}_{t2} \circ \tilde{\mathbf{A}}_r \right) \mathbf{T} = \Gamma(\tilde{\gamma}_{t2}) (\mathbf{A}_{t2} \circ \mathbf{A}_r) \mathbf{T}, \end{aligned} \quad (18)$$

where $\tilde{\mathbf{A}}_{t1}$ and $\tilde{\mathbf{A}}_{t2}$ are the first and last $(M_t - 1)M_r$ rows of $\tilde{\mathbf{A}}_t$, respectively. $\tilde{\gamma}_{t1}$ and $\tilde{\gamma}_{t2}$ denote the first and last $(M_t - 1)M_r$ entries of $\tilde{\gamma}$, respectively. Obviously, \mathbf{A}_{t1} and \mathbf{A}_{t2} has the rotational invariance property, that is, $\mathbf{A}_{t2} = \mathbf{A}_{t1} \Phi_t$ with $\Phi_t = \text{diag}([e^{-j\pi \sin \phi_1}, \dots, e^{-j\pi \sin \phi_K}])$. Thus, we have the following expression

$$\Gamma(\tau_t)\mathbf{E}_{t2} = \mathbf{E}_{t1}\Psi_t, \quad (19)$$

where $\Psi_t = \mathbf{T}^{-1}\Phi_t\mathbf{T}$ and

$$\begin{aligned} \tau_t &= \tilde{\mathbf{y}}_{t1} \circ \tilde{\mathbf{y}}_{t2}^{-1} = (\mathbf{y}_{t1} \circ \mathbf{y}_{t2}^{-1}) \otimes \mathbf{1}_{M_r} \\ &= \left[\mathbf{1}_{M_{tc}-1}^T, (\rho_1 e^{j\phi_1})^{-1}, \rho_1 e^{j\phi_1} (\rho_2 e^{j\phi_2})^{-1}, \dots, \right. \\ &\quad \left. \rho_{M_t-M_{tc}-1} e^{j\phi_{M_t-M_{tc}-1}} (\rho_{M_t-M_{tc}} e^{j\phi_{M_t-M_{tc}}})^{-1} \right]^T \otimes \mathbf{1}_{M_r} \end{aligned} \quad (20)$$

with \mathbf{y}_{t1} and \mathbf{y}_{t2} denoting the first and last M_{t-1} entries of \mathbf{y}_t , respectively. Once the matrix Ψ_t is calculated, the DODs of the sources can be estimated. Thus, we construct the following optimization problem

$$\begin{aligned} \min_{\Psi_t, \tau_t} \quad & \|\Gamma(\tau_t)\mathbf{E}_{t2} - \mathbf{E}_{t1}\Psi_t\|_2^2 \\ \text{s.t.} \quad & \mathbf{W}_t \tau_t = \mathbf{1}_{(M_{tc}-1)M_r}, \end{aligned} \quad (21)$$

where $\mathbf{W}_t = [\mathbf{I}_{(M_{tc}-1)M_r}, \mathbf{0}_{(M_{tc}-1)M_r \times ((M_t-1)M_r - (M_{tc}-1)M_r)}]$ is used to ensure that the first M_{tc} sensors of the transmit array are well calibrated.

From (19), we can achieve the least square solution of Ψ_t as

$$\Psi_t = (\mathbf{E}_{t1}^H \mathbf{E}_{t1})^{-1} \mathbf{E}_{t1}^H \Gamma(\tau_t) \mathbf{E}_{t2}. \quad (22)$$

By substituting (22) into (21), we have

$$\begin{aligned} \min_{\Psi_t, \tau_t} \quad & \|\mathbf{P}_t \Gamma(\tau_t) \mathbf{E}_{t2}\|_2^2 \\ \text{s.t.} \quad & \mathbf{W}_t \tau_t = \mathbf{1}_{(M_{tc}-1)M_r}, \end{aligned} \quad (23)$$

where $\mathbf{P}_t = \mathbf{I}_{(M_t-1)M_r} - \mathbf{E}_{t1}(\mathbf{E}_{t1}^H \mathbf{E}_{t1})^{-1} \mathbf{E}_{t1}^H$.

Utilizing the fact that $\|\mathbf{A}\|_F^2 = \text{trace}\{\mathbf{A}^H \mathbf{A}\}$, $\text{trace}(\mathbf{A}\mathbf{B}) = \text{trace}(\mathbf{B}\mathbf{A})$, and $\text{trace}\{\mathbf{A}\Gamma(\mathbf{d})\mathbf{B}\Gamma(\mathbf{d})\} = \mathbf{d}^H (\mathbf{A}^T \circ \mathbf{B}) \mathbf{d}$ for matrices \mathbf{A} , \mathbf{B} , and vectors \mathbf{d} with proper dimensions, the objective function in (23) is further simplified as

$$\|\mathbf{P}_t \Gamma(\tau_t) \mathbf{E}_{t2}\|_2^2 = \tau_t^H \left((\mathbf{E}_{t2} \mathbf{E}_{t2}^H)^T \circ \mathbf{P}_t \right) \tau_t. \quad (24)$$

Thus, the optimization in (23) is expressed as

$$\begin{aligned} \min_{\tau_t} \quad & \tau_t^H \left((\mathbf{E}_{t2} \mathbf{E}_{t2}^H)^T \circ \mathbf{P}_t \right) \tau_t \\ \text{s.t.} \quad & \mathbf{W}_t \tau_t = \mathbf{1}_{(M_{tc}-1)M_r}. \end{aligned} \quad (25)$$

This problem can be solved through the Lagrange multiplier method and the optimal solution is expressed as:

$$\hat{\tau}_t = \mathbf{Q}_t^{-1} \mathbf{W}_t^T (\mathbf{W}_t \mathbf{Q}_t^{-1} \mathbf{W}_t^T)^{-1} \mathbf{1}_{(M_{tc}-1)M_r}, \quad (26)$$

where $\mathbf{Q} = (\mathbf{E}_{t2} \mathbf{E}_{t2}^H)^T \circ \mathbf{P}_t$. Thus, Ψ_t can be estimated through (22). Note that $\Psi_t = \mathbf{T}^{-1}\Phi_t\mathbf{T}$, we can use eigenvalue decomposition to achieve the estimation of Φ_t and the DOD estimation of the k th source can be calculated as

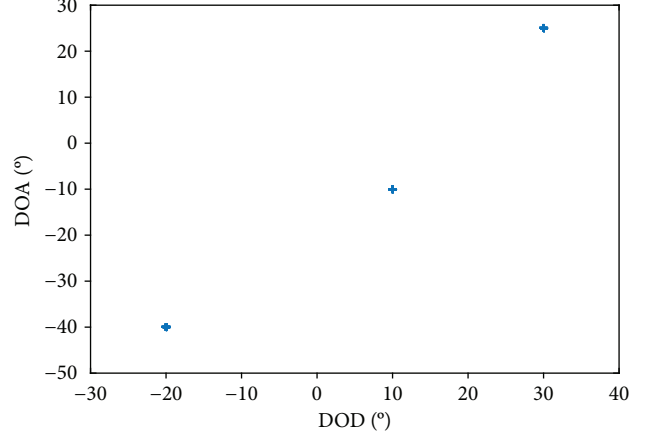


FIGURE 1: 100 realizations of the proposed method. SNR = 5 dB.

$$\hat{\phi}_k = \arcsin\left(-\frac{\text{angle}(v_{t,k})}{\pi}\right), \quad k = 1, \dots, K, \quad (27)$$

where $v_{t,k}$ is the k th eigenvalue of Φ_t .

In addition, the m th element of \mathbf{y}_t also can be estimated as

$$\hat{y}_{t,m} = \left(\prod_{i=1}^m \varepsilon(i) \right)^{-1}, \quad m = N_{tc} + 1, \dots, M_t, \quad (28)$$

where $\varepsilon(i) = 1/M_t \sum_{l=(i-1)M_r+1}^{iM_r} \hat{\tau}_{t,l}$, $\hat{\tau}_{t,l}$ is the l th elements of $\hat{\tau}_t$.

We select a transformation matrix \mathbf{J} which makes $\mathbf{E}'_s = \mathbf{J}\mathbf{E}_s = (\tilde{\mathbf{A}}_r \circ \tilde{\mathbf{A}}_t)\mathbf{T}$, then the DOAs of the sources can be estimated by using a similar manner with the estimation of DODs. Thus, the detailed procedure is omitted in this paper. Furthermore, the DODs and DOAs can be paired using the method proposed in [9].

4. Simulation Results

In this section, several experimental simulations are carried out to demonstrate the performance of the proposed method.

A bistatic MIMO radar with $M_t = 6$ transmit antennas and $M_r = 8$ receive antennas is used in the following simulations. In addition, both the transmit and receiver arrays are assumed to be partially calibrated. The corresponding gain-phase uncertainties are $\mathbf{y}_t = [1, 1, 1, 0.8e^{j0.6283}, 1.25e^{-j1.0472}, 0.75e^{j0.7854}]^T$ and $\mathbf{y}_r = [1, 1, 1.3712e^{-j0.2675}, 1.1199e^{j0.0676}, 1, 0.9730e^{-j0.2509}, 1, 0.96e^{j0.0381}]^T$. Thus, we have $M_{tc} = 3$ and $M_{rc} = 2$. The number of samples during one pulse period is $L = 256$, and the number of pulses is set as $Q = 200$ unless otherwise specified.

In the first simulation, 100 realizations of the proposed method are provided in Figure 1. In this simulation, the SNR is set as 5 dB. From Figure 1, it is clear that the proposed method achieves accurate DOD and DOA estimation which are paired correctly. The estimation of gain-phase uncertainties are provided in Table 1. The mean and standard deviation (STD) of the estimations are calculated from 100 independent Monte Carlo trials.

TABLE 1: Performance of gain and phase estimation.

| (a) Gain estimation results of γ_t | | | |
|---|------------|--------|--------|
| Index | True value | Mean | STD |
| $\hat{\rho}_1$ | 0.8000 | 0.7999 | 0.0020 |
| $\hat{\rho}_2$ | 1.2500 | 1.2502 | 0.0045 |
| $\hat{\rho}_3$ | 0.7500 | 0.7503 | 0.0037 |

| (b) Phase estimation results of γ_t (radian) | | | |
|---|------------|---------|--------|
| Index | True value | Mean | STD |
| $\hat{\phi}_1$ | 0.6283 | 0.6285 | 0.0030 |
| $\hat{\phi}_2$ | -1.0472 | -1.0468 | 0.0042 |
| $\hat{\phi}_3$ | 0.7854 | -0.7859 | 0.0057 |

| (c) Gain estimation results of γ_r | | | |
|---|------------|--------|--------|
| Index | True value | Mean | STD |
| $\hat{\alpha}_1$ | 1.3712 | 1.3722 | 0.0053 |
| $\hat{\alpha}_2$ | 1.1199 | 1.1212 | 0.0068 |
| $\hat{\alpha}_3$ | 1.0000 | 1.0016 | 0.0081 |
| $\hat{\alpha}_4$ | 0.9730 | 0.9744 | 0.0086 |
| $\hat{\alpha}_5$ | 1.0000 | 1.0018 | 0.0119 |
| $\hat{\alpha}_6$ | 0.9600 | 0.9622 | 0.0132 |

| (d) Phase estimation results of γ_r (radian) | | | |
|---|------------|---------|--------|
| Index | True value | Mean | STD |
| $\hat{\beta}_1$ | -0.2675 | -0.2677 | 0.0037 |
| $\hat{\beta}_2$ | 0.0676 | 0.0682 | 0.0064 |
| $\hat{\beta}_3$ | 0 | 0.0000 | 0.0084 |
| $\hat{\beta}_4$ | -0.2509 | -0.2500 | 0.0094 |
| $\hat{\beta}_5$ | 0 | -0.0011 | 0.0123 |
| $\hat{\beta}_6$ | 0.0381 | 0.0392 | 0.0147 |

To evaluate the performance of the proposed method, we utilize the root mean square error (RMSE) result in the following simulations. In this paper, the RMSE is calculated from the following formula

$$\text{RMSE} = \sqrt{\frac{1}{KP} \sum_{p=1}^L \sum_{k=1}^K \left[\left(\hat{\theta}_{k,p} - \theta_k \right)^2 + \left(\hat{\phi}_{k,p} - \phi_k \right)^2 \right]}, \quad (29)$$

where P is the number of Monte Carlo trials and $\hat{\theta}_{k,p}$ and $\hat{\phi}_{k,p}$ are the estimations of θ_k and ϕ_k of the p th trial, respectively. In the following experiments, we use $P = 200$ independent trails to calculate the RMSE of the angle estimation results.

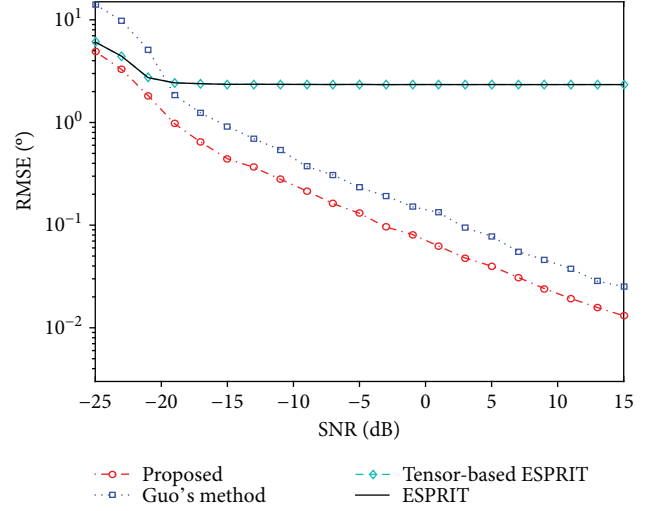


FIGURE 2: RMSE versus SNR.

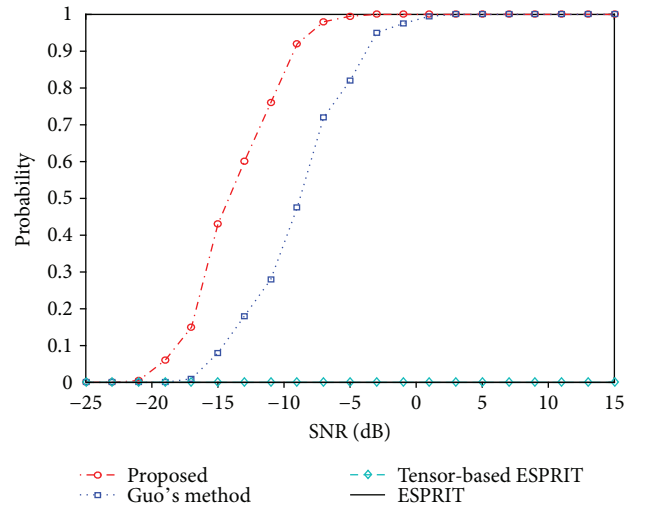


FIGURE 3: Probability of successful detection.

In Figure 2, the RMSEs of the conventional ESPRIT algorithm, tensor-based ESPRIT algorithm, method in [16] (denoted as Guo's method), and the proposed algorithm are compared with different SNRs. Due to the partially calibrated arrays, the conventional ESPRIT algorithm and the tensor-based ESPRIT algorithm fail to achieve accurate angle estimations. The Guo's method [16] is robust under the partially calibrated array case, however, it has a worse RMSE performance. On the other hand, the proposed method achieves the best estimation among the existing algorithms especially for the case of low SNR.

The probability of successful detection is provided in Figure 3. The successful detection means that the absolute error of all the DOA and DOD estimations is within 0.5° . As mentioned above, both the conventional ESPRIT and the tensor-based ESPRIT algorithms exhibit a 100% failed detection due to the partially calibrated arrays used in this simulation. However, the proposed method achieves a higher probability of successful detection especially for

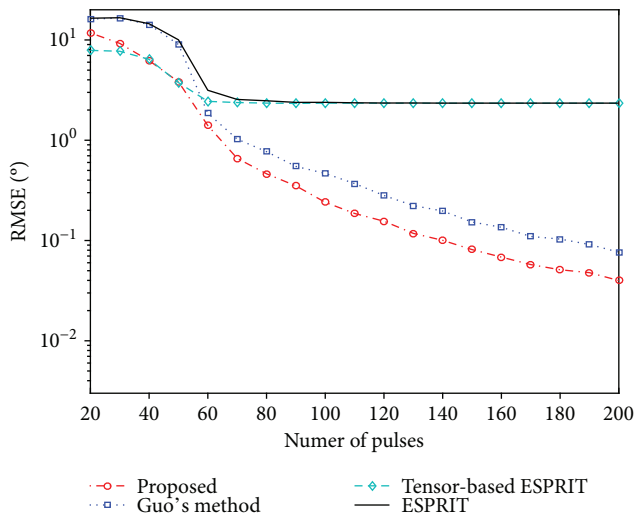


FIGURE 4: RMSE versus pulses.

SNR greater than -20 dB. This simulation result verifies the improved performance of the proposed algorithm over existing algorithms.

In Figure 4, we evaluate the performance of the algorithms under consideration for the case of varying number of the pulses. It is observed that the existing algorithms experience a heavily degraded estimation performance when the number of pulses is smaller than 60. In addition, both the proposed algorithm and Guo's method show improvement with the increased number of pulses. However, the proposed algorithm converges fast under low SNR and it always outperforms the other algorithms under consideration.

5. Conclusion

In this paper, we proposed a novel joint DOD-DOA estimation algorithm based on tensor subspace approach for the case of partially calibrated bistatic MIMO radar. We first develop a third-order measurement tensor of the received signal. The HOSVD is then exploited to evaluate the signal subspace of the tensor-based received signal matrix. A close-form expression for estimating the gain-phase uncertainties of the transmit and receive arrays is derived, which enables us to estimate the joint DOA-DOA effectively. Compared with the existing algorithms, the proposed algorithm achieves a significant improvement in estimation performance. Finally, the simulation results demonstrate the effectiveness of the proposed algorithm.

Conflicts of Interest

The authors declare that they have no conflicts of interest.

Acknowledgments

The work of Ping Huang is supported by the National Natural Science Foundation of China (61403091), the Heilongjiang Province Natural Science Foundation (QC2015049), and the

launch of the postdoctoral research in Heilongjiang Province (LBH-Q16065).

References

- [1] R. Schmidt, "Multiple emitter location and signal parameter estimation," *IEEE Transactions on Antennas and Propagation*, vol. 34, no. 3, pp. 276–280, 1986.
- [2] Z. Shi, C. Zhou, Y. Gu, N. A. Goodman, and F. Qu, "Source estimation using coprime array: a sparse reconstruction perspective," *IEEE Sensors Journal*, vol. 17, no. 3, pp. 755–765, 2017.
- [3] Y. Gu, N. A. Goodman, S. Hong, and Y. Li, "Robust adaptive beamforming based on interference covariance matrix sparse reconstruction," *Signal Process*, vol. 96, pp. 375–381, 2014.
- [4] Y. Gu and A. Leshem, "Robust adaptive beamforming based on interference covariance matrix reconstruction and steering vector estimation," *IEEE Transactions on Signal Processing*, vol. 60, no. 7, pp. 3881–3885, 2012.
- [5] H. Krim and M. Viberg, "Two decades of array signal processing research: the parametric approach," *IEEE Signal Processing Magazine*, vol. 13, no. 4, pp. 67–94, 1996.
- [6] E. Fishler, A. Haimovich, R. S. Blum, L. J. Cimini, D. Chizhik, and R. A. Valenzuela, "MIMO radar: an idea whose time has come," in *Proceedings of the 2004 IEEE Radar Conference (IEEE Cat. No.04CH37509)*, pp. 71–78, Philadelphia, PA, USA, 2004.
- [7] J. Li and P. Stoica, "MIMO radar with colocated antennas," *IEEE Signal Processing Magazine*, vol. 24, no. 5, pp. 106–114, 2007.
- [8] C. Duofang, C. Baixiao, and Q. Guodong, "Angle estimation using ESPRIT in MIMO radar," *Electronics Letters*, vol. 44, no. 12, p. 770, 2008.
- [9] C. Jinli, G. Hong, and S. Weimin, "Angle estimation using ESPRIT without pairing in MIMO radar," *Electronics Letters*, vol. 44, no. 24, p. 1422, 2008.
- [10] X. Zhang, L. Xu, L. Xu, and D. Xu, "Direction of departure (DOD) and direction of arrival (DOA) estimation in MIMO radar with reduced-dimension MUSIC," *IEEE Communications Letters*, vol. 14, no. 12, pp. 1161–1163, 2010.
- [11] M. L. Bencheikh, Y. Wang, and H. He, "Polynomial root finding technique for joint DOA DOD estimation in bistatic MIMO radar," *Signal Processing*, vol. 90, no. 9, pp. 2723–2730, 2010.
- [12] R. Xie, Z. Liu, and J. Wu, "Direction finding with automatic pairing for bistatic MIMO radar," *Signal Processing*, vol. 92, no. 1, pp. 198–203, 2012.
- [13] B. Friedlander and A. Weiss, "Eigenstructure methods for direction finding with sensor gain and phase uncertainties," in *ICASSP-88., International Conference on Acoustics, Speech, and Signal Processing*, pp. 2681–2684, New York, NY, USA, April 1988.
- [14] A. Liu, G. Liao, C. Zeng, Z. Yang, and Q. Xu, "An eigenstructure method for estimating DOA and sensor gain-phase errors," *IEEE Transactions on Signal Processing*, vol. 59, no. 12, pp. 5944–5956, 2011.
- [15] B. Liao and S. C. Chan, "Direction finding with partly calibrated uniform linear arrays," *IEEE Transactions on Antennas and Propagation*, vol. 60, no. 2, pp. 922–929, 2012.

- [16] Y. D. Guo, Y. S. Zhang, and N. N. Tong, "ESPRIT-like angle estimation for bistatic MIMO radar with gain and phase uncertainties," *Electronics Letters*, vol. 47, no. 17, p. 996, 2011.
- [17] B. Wang, W. Wang, Y. Gu, and S. Lei, "Underdetermined DOA estimation of quasi-stationary signals using a partly-calibrated array," *Sensors*, vol. 17, no. 4, p. 702, 2017.
- [18] B. Wang, Y. D. Zhang, and W. Wang, "Robust DOA estimation in the presence of miscalibrated sensors," *IEEE Signal Processing Letters*, vol. 24, no. 7, pp. 1073–1077, 2017.
- [19] B. Wang, S. Qin, Y. D. Zhang, and M. G. Amin, "Robust DOA estimation in the presence of mis-calibrated sensors," in *2017 IEEE International Conference on Acoustics, Speech and Signal Processing (ICASSP)*, pp. 3076–3080, New Orleans, LA, USA, March 2017.
- [20] D. Nion and N. D. Sidiropoulos, "Tensor algebra and multi-dimensional harmonic retrieval in signal processing for MIMO radar," *IEEE Transactions on Signal Processing*, vol. 58, no. 11, pp. 5693–5705, 2010.
- [21] T. G. Kolda and B. W. Bader, "Tensor decompositions and applications," *SIAM Review*, vol. 51, no. 3, pp. 455–500, 2009.
- [22] M. Skolnik, *Introduction to Radar Systems*, McGraw-Hill, New York, NY, USA, 3rd edition, 2002.

Research Article

Enhanced 2D-DOA Estimation for Large Spacing Three-Parallel Uniform Linear Arrays

Dong Zhang , Yongshun Zhang, and Cunqian Feng

Air and Missile Defense College, Air Force Engineering University, Xi'an, Shaanxi 710051, China

Correspondence should be addressed to Dong Zhang; zhangdongtougao@163.com

Received 15 September 2017; Revised 9 January 2018; Accepted 30 January 2018; Published 4 March 2018

Academic Editor: Elisa Giusti

Copyright © 2018 Dong Zhang et al. This is an open access article distributed under the Creative Commons Attribution License, which permits unrestricted use, distribution, and reproduction in any medium, provided the original work is properly cited.

An enhanced two-dimensional direction of arrival (2D-DOA) estimation algorithm for large spacing three-parallel uniform linear arrays (ULAs) is proposed in this paper. Firstly, we use the propagator method (PM) to get the highly accurate but ambiguous estimation of directional cosine. Then, we use the relationship between the directional cosine to eliminate the ambiguity. This algorithm not only can make use of the elements of the three-parallel ULAs but also can utilize the connection between directional cosine to improve the estimation accuracy. Besides, it has satisfied estimation performance when the elevation angle is between 70° and 90° and it can automatically pair the estimated azimuth and elevation angles. Furthermore, it has low complexity without using any eigen value decomposition (EVD) or singular value decomposition (SVD) to the covariance matrix. Simulation results demonstrate the effectiveness of our proposed algorithm.

1. Introduction

Two-dimensional DOA estimation has attracted extensive attention due to its wide range of applications [1–4], and there are many algorithms been proposed for DOA estimation. Among these algorithms, the subspace-based algorithms, such as MUSIC and ESPRIT, have received a lot of attention for its accurate estimation performance [5, 6]. However, the complexity of subspace-based algorithms is often too large because of the EVD or SVD. In [7], Marcos et al. put forward the well-known propagator method (PM) algorithm for 1D-DOA estimation. It uses linear partitioning instead of any EVD or SVD to reduce complexity. Then, Chen et al. [8] extend it to the DOA estimation of noncircular signal. References [9–11] extend the PM algorithm to 2D direction estimation. But these algorithms have some drawbacks. Reference [9] requires angle search operations. Reference [10] may fail in practical situation when elevation angle is between 70° and 90° . Reference [11] has worse estimation accuracy, because some element information is missing when calculating the propagation matrix (PMA). Based on this, Chen et al. [12] put forward an improved 2D angle estimation algorithm for three-parallel ULAs. It can solve all the problems mentioned in the

above literature. But, it still has some shortcomings, that is, the array aperture is reduced because of the adoption of three parallel arrays with half wavelength spacing. And the estimation accuracy is reduced. References [13, 14] establish the “array of subarrays” idea and “cyclic ambiguity” idea to improve the estimation accuracy of 2D-DOA. According to this, we expanded the spacing between the ULA and proposed an enhanced 2D-DOA estimation algorithm. What needs to be stressed here is that our method is different from the method in [13, 14], although our algorithm and the method in [13, 14] both use the large array spacing to obtain high accuracy but ambiguous estimation. However, the principle of resolving ambiguity is different. References [13, 14] use coarse estimation without ambiguity or based on eigen space to resolve ambiguity. However, our algorithm uses the triangular relation between the three directional cosine to resolve the ambiguity. By doing this, we do not have to limit ourselves to using subarrays or eigen spaces to solve ambiguity problems. That is the main difference between our method and the method in [13, 14]. And it is also the main innovation of this paper. The flow of our algorithm is as follows: Firstly, we use the method in [12] to obtain the estimation of three directional cosines. Because of the large spacing between array elements, the estimated directional

cosine is high precision and ambiguous. Then, we use the triangle relationship between the three directional cosines to eliminate the ambiguity. Then, we can get the true 2D-DOA of targets. Simulation results show that it cannot only avoid the problem in [8–11] simultaneously but also has better estimation accuracy than algorithm of [12] because of adopting large aperture. And the complexity of the algorithm is comparable to that algorithm of [12].

Notations. Superscripts $(\cdot)^*$, $(\cdot)^T$, $(\cdot)^\dagger$, $(\cdot)^{-1}$, and $(\cdot)^H$ denote complex conjugation, transpose, pseudo-inverse, inverse, and conjugate transpose, respectively. \mathbf{I}_K is $K \times K$ identity matrix. $\text{diag}[\cdot]$ denotes the diagonalization of the entity inside. $|\cdot|$ denotes take the absolute value of the element. $\lceil \cdot \rceil$ denotes round the element to the nearest integers less than or equal to the element. $\lfloor \cdot \rfloor$ denotes round the element to the nearest integers greater than or equal to the element. $E[\cdot]$ denotes the expectation operation. $\arg(\cdot)$ and $\text{Re}(\cdot)$ denote the phase and the real part of a complex number separately.

2. Problem Formulation

As shown in Figure 1, assume that there are three-parallel ULAs, namely, X, Y , and Z . Array X contains $N + 1$ sensors. Array Y and array Z have N sensors, respectively. The spacing between adjacent elements is d_x . The distance between array X and array Y is d_y , and the distance between array X and array Z is d_z . λ is the wavelength. It is assumed that P far-field narrowband uncorrelated signals are incident onto the array. The elevation angle and azimuth angle of i th target are θ_i and φ_i , respectively. Here, we assume that the range of 2D angle is the same with that of [12]. That is to say that the range value of θ_i is $[0, 1/2\pi]$ and the range value of φ_i is $[-1/2\pi, 1/2\pi]$. Then, the output of the three ULAs can be expressed as follows:

$$\begin{aligned} \mathbf{X}(t) &= \mathbf{A}_x \mathbf{S}(t) + \mathbf{W}_x(t), \\ \mathbf{Y}(t) &= \mathbf{A}_y \mathbf{\Omega}_y \mathbf{S}(t) + \mathbf{W}_y(t), \\ \mathbf{Z}(t) &= \mathbf{A}_y \mathbf{\Omega}_z \mathbf{S}(t) + \mathbf{W}_z(t), \end{aligned} \quad (1)$$

where $\mathbf{A}_x = [\mathbf{a}_x(\theta_1, \varphi_1), \mathbf{a}_x(\theta_2, \varphi_2), \dots, \mathbf{a}_x(\theta_P, \varphi_P)]$ and $\mathbf{a}_x(\theta_i, \varphi_i) = [1, e^{-j2\pi d_x \sin \theta_i \sin \varphi_i / \lambda}, \dots, e^{-j2\pi N d_x \sin \theta_i \sin \varphi_i / \lambda}]$. \mathbf{A}_y contains the first N row of \mathbf{A}_x . $\mathbf{\Omega}_y = \text{diag}([e^{-j2\pi d_y \cos \theta_1 / \lambda}, e^{-j2\pi d_y \cos \theta_2 / \lambda}, \dots, e^{-j2\pi d_y \cos \theta_P / \lambda}])$ and $\mathbf{\Omega}_z = \text{diag}([e^{-j2\pi d_z \sin \theta_1 \cos \varphi_1 / \lambda}, e^{-j2\pi d_z \sin \theta_2 \cos \varphi_2 / \lambda}, \dots, e^{-j2\pi d_z \sin \theta_P \cos \varphi_P / \lambda}])$. $\mathbf{W}_x(t), \mathbf{W}_y(t)$, and $\mathbf{W}_z(t)$ are assumed to be Gaussian white noise vectors whose mean value is zero and variance is σ^2 . Then a new vector $\mathbf{W}(t) = [\mathbf{X}(t)^T \mathbf{Y}(t)^T \mathbf{Z}(t)^T]^T$, with L snapshots, and $\mathbf{W} = [\mathbf{W}(1), \mathbf{W}(2), \dots, \mathbf{W}(L)]$ can be represented as

$$\mathbf{W} = \begin{bmatrix} \mathbf{X} \\ \mathbf{Y} \\ \mathbf{Z} \end{bmatrix} = \begin{bmatrix} \mathbf{A}_x \\ \mathbf{A}_y \mathbf{\Omega}_y \\ \mathbf{A}_y \mathbf{\Omega}_z \end{bmatrix} \mathbf{S} + \begin{bmatrix} \mathbf{W}_x \\ \mathbf{W}_y \\ \mathbf{W}_z \end{bmatrix} = \mathbf{A} \mathbf{S} + \mathbf{N}, \quad (2)$$

where $\mathbf{A} = [(\mathbf{A}_x)^T (\mathbf{A}_y \mathbf{\Omega}_y)^T (\mathbf{A}_y \mathbf{\Omega}_z)^T]^T$, $\mathbf{S} = [S(1), S(2), \dots, S(L)] \in \mathbb{C}^{P \times L}$, and $\mathbf{N} = [(\mathbf{W}_x)^T (\mathbf{W}_y)^T (\mathbf{W}_z)^T]^T \in \mathbb{C}^{(3N+1) \times L}$.

3. Enhanced 2D-DOA Estimation

3.1. Highly Accurate but Ambiguous Estimation of Directional Cosine. Assuming that $d_x = d_y = d = \lambda/2, d_z = Kd$, where K is a positive integer and $K > 1$. The difference between our model and the model in [12] is that the spacing between the ULA is larger than half wavelength. The large spacing will lead to ambiguity of the directional cosine, but it would not affect the estimation method for them. So the first several steps of our algorithm is same with the algorithm of [12]. We abbreviate the first several procedures as follows:

Step 1. Compute the covariance matrix of $\mathbf{W}(t)$ by $\mathbf{R}_W = E[\mathbf{W}\mathbf{W}^H]$.

Step 2. Divide \mathbf{R}_W into two parts, that is, $\mathbf{R}_W = [\mathbf{R}_{W1} \mathbf{R}_{W2}]$, where $\mathbf{R}_{W1} \in \mathbb{C}^{(3N+1) \times P}$ and $\mathbf{R}_{W2} \in \mathbb{C}^{(3N+1) \times (3N+1-P)}$. Compute the propagator matrix (PMA) \mathbf{P} by $\hat{\mathbf{P}} = (\mathbf{R}_{W1}^H \mathbf{R}_{W1})^{-1} \mathbf{R}_{W1}^H \mathbf{R}_{W2}$ and get the extended PMA by $\mathbf{P}_e = [\mathbf{I}_P^H \hat{\mathbf{P}}] =$

$$\begin{bmatrix} \underbrace{\mathbf{P}_x^T}_{P \times (N+1)} & \underbrace{\mathbf{P}_y^T}_{P \times N} & \underbrace{\mathbf{P}_z^T}_{P \times N} \end{bmatrix}^T.$$

Step 3. Implement EVD on $\mathbf{\Psi}_z = \mathbf{P}_{x1}^+ \mathbf{P}_z = \mathbf{A}_1 \mathbf{\Omega}_z \mathbf{A}_1^{-1}$ to get eigenvalues $\hat{\beta}_i$ and eigenvectors \mathbf{A}_1' . They correspond to the diagonal elements of $\mathbf{\Omega}_z$ and the estimation of \mathbf{A}_1 , separately. And \mathbf{P}_{x1}^+ is the first N rows of \mathbf{P}_x .

Step 4. Let $\mathbf{B}_1 = \mathbf{P}_{x1} \mathbf{A}_1'$, $\mathbf{B}_2 = \mathbf{P}_y \mathbf{A}_1'$. Attain $\hat{\alpha}_i$ by extracting the i th diagonal elements of $\mathbf{B}_1^+ \mathbf{B}_2$. Similarly, let $\mathbf{C}_1 = [\mathbf{P}_{x1}^T \mathbf{P}_{y1}^T \mathbf{P}_{z1}^T]^T \mathbf{A}_1'$ and $\mathbf{C}_2 = [\mathbf{P}_{x2}^T \mathbf{P}_{y2}^T \mathbf{P}_{z2}^T]^T \mathbf{A}_1'$. Attain $\hat{\gamma}_i$ by extracting the i th diagonal elements of $\mathbf{C}_1^+ \mathbf{C}_2$. And \mathbf{P}_{y1} and \mathbf{P}_{z1} are the first $N - 1$ rows of \mathbf{P}_y and \mathbf{P}_z . \mathbf{P}_{y2} and \mathbf{P}_{z2} are the last $N - 1$ rows of \mathbf{P}_y and \mathbf{P}_z . \mathbf{P}_{x2} represents the last N rows of \mathbf{P}_x .

Until now, we get the paired estimation of $\hat{\alpha}_i, \hat{\beta}_i$, and $\hat{\gamma}_i$ which represent $\cos \theta_i, \sin \theta_i \cos \varphi_i$, and $\sin \theta_i \sin \varphi_i$, respectively. Because d_z is larger than half wavelength, so the $\hat{\beta}_i$ is high accuracy but ambiguous. And all the ambiguous values are listed as follows:

$$\hat{\beta}_i^{(k)} = \hat{\beta}_i + k \frac{\lambda}{d_z}, \quad \left[(-1 - \hat{\beta}_i) \frac{d_z}{\lambda} \right] \leq k \leq \left[(1 - \hat{\beta}_i) \frac{d_z}{\lambda} \right], \quad (3)$$

where $i = 1, \dots, P$.

3.2. Highly Accurate Estimation of 2D-DOA. Before estimating the 2D-DOA, we need to eliminate the ambiguity first. Note that there exists a triangle relationship between these directional cosines:

$$(\cos \theta_i)^2 + (\sin \theta_i \cos \varphi_i)^2 + (\sin \theta_i \sin \varphi_i)^2 = 1. \quad (4)$$

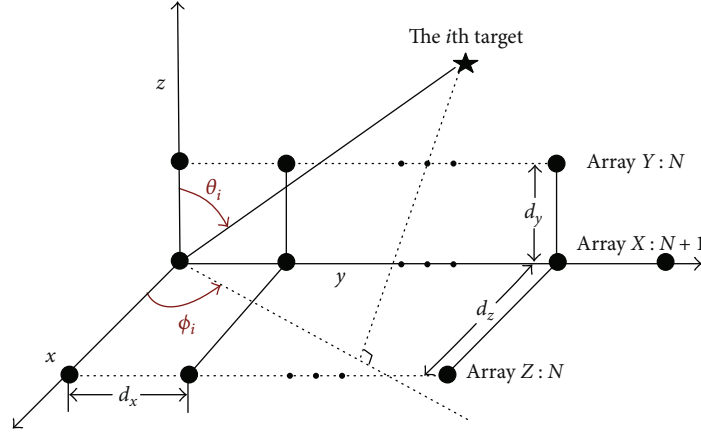


FIGURE 1: Sketch map of array structure.

And the true directional cosine of targets satisfies this equation. So, we can use this equation to select the true directional cosine from the ambiguous directional cosine.

But because there are square terms in the constraint, the mirror image of the true value also satisfies this equation. If the mirror image is exactly equal to an ambiguous value of the true value, we may make mistakes and treat the mirror image as the true value. Here, we set the range value of θ and φ as $[0, 1/2\pi]$ and $[-1/2\pi, 1/2\pi]$, separately. So the true value of $\sin \theta_i \cos \varphi_i$ is limited in the range of $[0, 1]$. And the mirror image can be avoided.

And the procedure of eliminating ambiguity can be got as follows:

Step 1. Get all the ambiguous value of $\sin \theta_i \cos \varphi_i$ by

$$\hat{\beta}_i^{(k)} = \hat{\beta}_i + k \frac{\lambda}{d_z}, \quad \left[\left(0 - \hat{\beta}_i\right) \frac{d_z}{\lambda} \right] \leq k \leq \left[\left(1 - \hat{\beta}_i\right) \frac{d_z}{\lambda} \right]. \quad (5)$$

Step 2. Find the true value by

$$\hat{\beta}_i^{(\hat{k})} = \hat{\beta}_i + \hat{k} \frac{\lambda}{d_z}, \quad \hat{k} = \arg \min_k \left| \alpha_i^2 + \left[\hat{\beta}_i^{(k)} \right]^2 + \gamma_i^2 - 1 \right|. \quad (6)$$

Lastly, we can get the 2D-DOA estimation for each source by

$$\begin{aligned} \hat{\varphi}_i &= \tan^{-1} \left[\frac{\arg(\hat{\gamma}_i)}{\arg(\hat{\beta}_i^{(\hat{k})})} \right], \\ \hat{\theta}_i &= \tan^{-1} \left[\frac{\arg(\hat{\beta}_i^{(\hat{k})})}{\arg(\hat{\alpha}_i) \cos \hat{\varphi}_i} \right]. \end{aligned} \quad (7)$$

3.3. Algorithm Analysis. Here, the analysis of the complexity, estimation performance, and some notices of our algorithm are as follows:

- (1) Our algorithm has an additional ambiguity elimination operation compared with the algorithm of [12]. And the complexity of ambiguity elimination is far less than the complexity of constructing the covariance. Thus, we can say that the algorithm has comparable computational complexity with the algorithm of [12].
- (2) Because our array aperture is larger than that in [12], so our proposed algorithm can obtain a better estimation accuracy.
- (3) Note that here we expand the spacing between the X-axis and Z-axis. Similarly, we can also expand the spacing between the X-axis and Y-axis or simultaneously expand the spacing in the X-axis, Y-axis, and Z-axis. Then, we can get high accuracy but ambiguous estimation of $\sin \theta_i \sin \varphi_i$ and $\cos \theta_i$, respectively. And we can still use (4) to eliminate the ambiguity. But considering the mirror image problem, the range of angle needs to be adjusted accordingly.
- (4) Because the first several steps of our algorithm are the same with those of [12], so our algorithm inherits the merits of algorithm of [12]. For example, (1) it can take full advantage of the elements of the three-parallel ULAs to estimate the PMA; (2) it has satisfied estimation accuracy in actual mobile elevation angles; (3) it can automatically pair the estimated 2D-DOA; (4) it has low complexity without using any EVD or SVD.

4. Computer Simulations

Here, we will conduct several simulation experiments to test the performance of our proposed method. The 2D-DOA of two uncorrelated targets are $(\theta_1, \varphi_1) = (35^\circ, 40^\circ)$ and $(\theta_2, \varphi_2) = (80^\circ, 75^\circ)$, separately. N is set to 6. So the total number of array elements is 19. The spacing between X-axis and Z-axis is set to $d_z = 3d$. The other spacing is set to $d_x = d_y = d$.

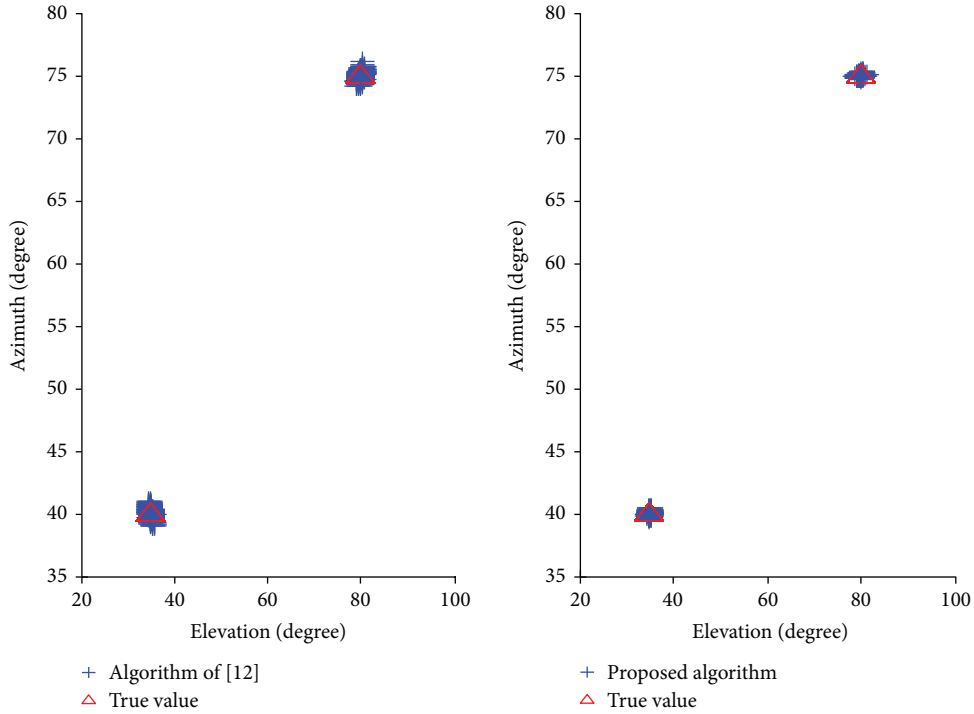


FIGURE 2: 2D-DOA scattergram at SNR = 10 dB.

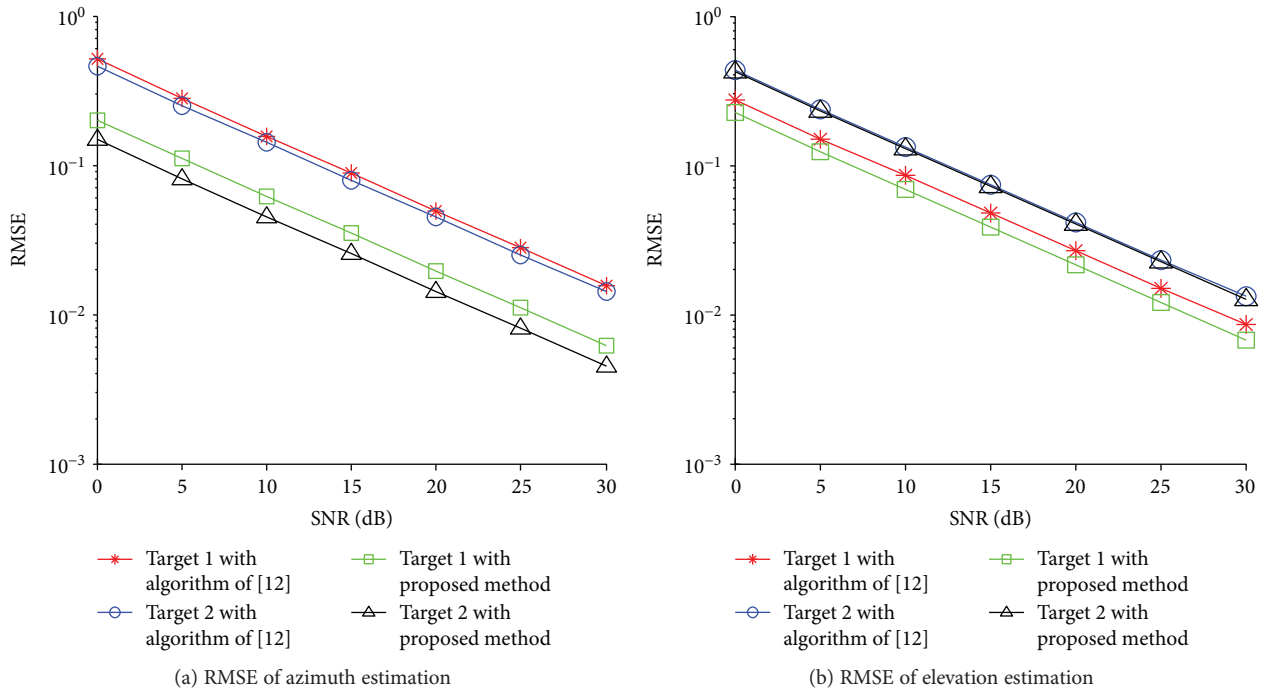


FIGURE 3: RMSE contrast of two algorithms with different SNR.

In the first simulation, Figure 2 shows the scattergram of 300 times 2D-DOA estimate results by our algorithm and the algorithm of [12]. The snapshot is set to 50. The SNR = 10 dB. As we can see, both the two algorithms can clearly observe the two targets. But our algorithm has better statistical properties. That is because we make better use of the information between ULAs.

In the second simulation, we compare the estimation performance of the two algorithms under different SNR which vary from 0 dB to 30 dB. The snapshot is set to 300. 200 times Monte Carlo simulations are conducted under each SNR. As illustrated in Figure 3, the RMSE curve of azimuth estimated by our algorithm is better than that estimated by the algorithm of [12]. The elevation estimation performance of our

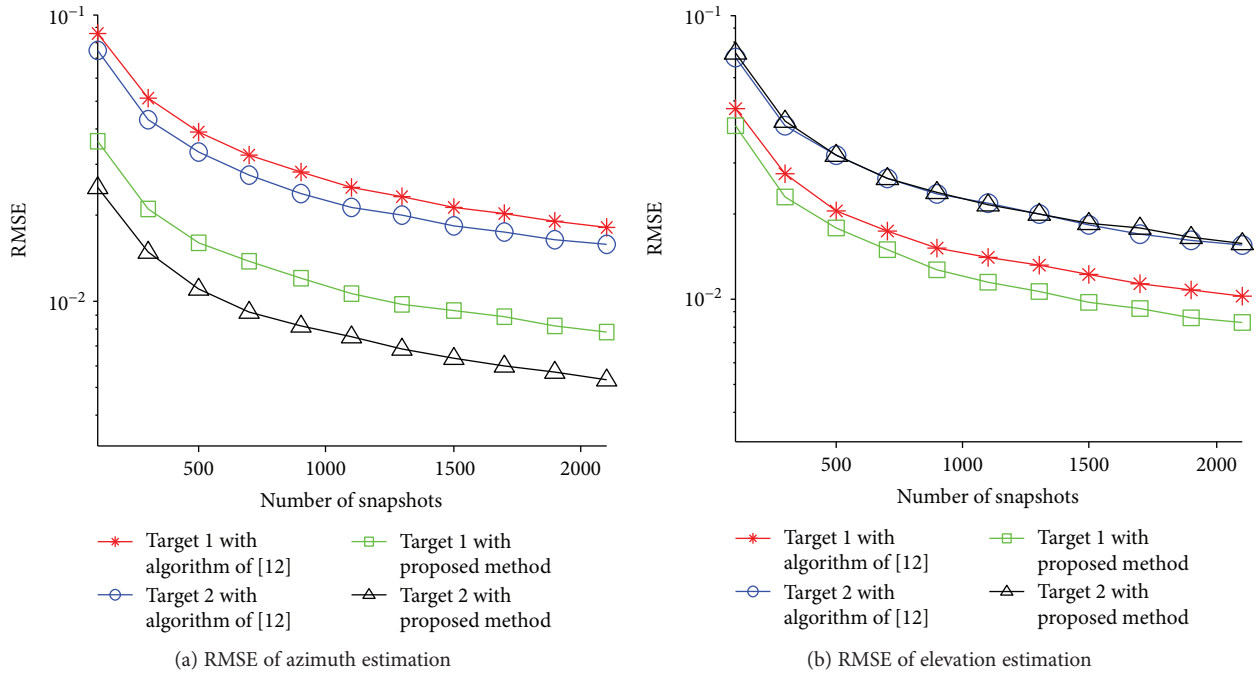


FIGURE 4: RMSE contrast of two algorithms with different snapshots.

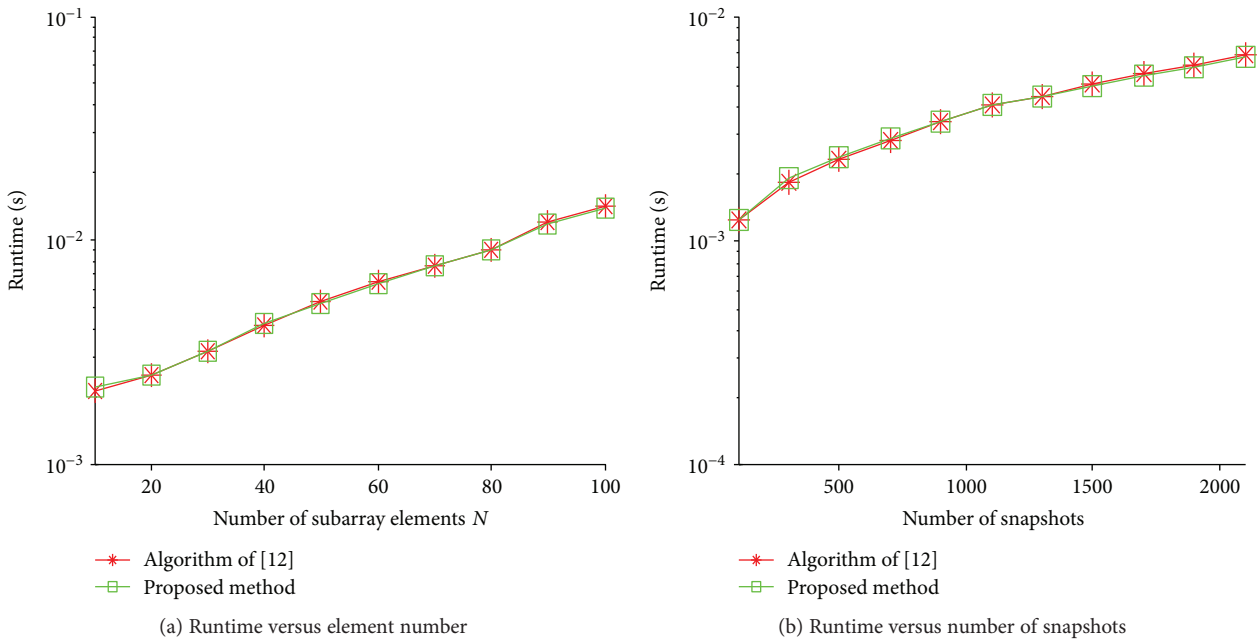


FIGURE 5: Runtime comparison of two algorithms.

algorithm is comparable with that estimated by the algorithm of [12]. The reason is that when estimating azimuth angle, the equivalent array aperture of our algorithm is larger than that of [12]. While when estimating elevation angle, the equivalent array aperture of our algorithm is equal with that of [12]. Note that if we want to improve the estimation accuracy of elevation angle, we can expand d_y instead of expanding d_z .

In the third simulation, we compare the estimation performance of the two algorithms under different snapshots which

vary from 100 to 2100. The SNR is set to 20 dB. 1000 times Monte Carlo simulations are conducted under each snapshot. As illustrated in Figure 4, the RMSE curve of azimuth estimated by our algorithm is better than that estimated by the algorithm of [12]. The elevation estimation performance of the two algorithms is similar. The reason is the same with the previous one. From the second and third simulations, we can also see that our algorithm has satisfied estimation performance when elevation is between 70° and 90° .

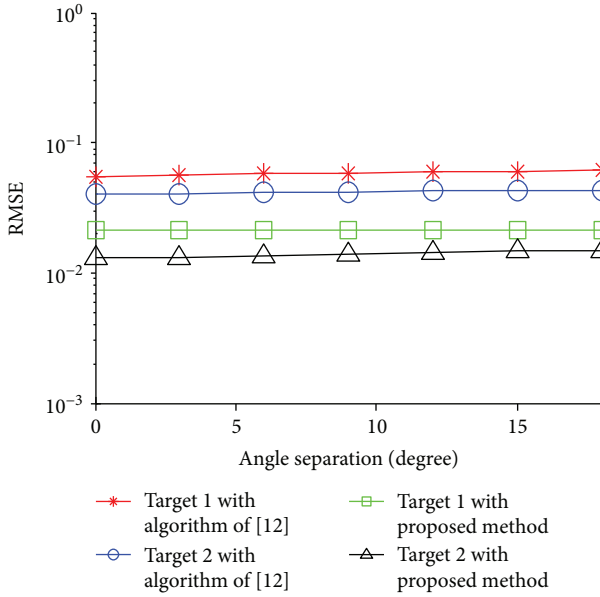


FIGURE 6: RMSE of azimuth estimation versus angular separation.

In the fourth simulation, we compare the complexity of our algorithm and that of [12]. We choose the runtime as the evaluation criteria. Two kinds of comparison were conducted. In the first comparison, the number of elements in subarray, that is, N , is set to vary from 10 to 100 and the snapshot is set to 300. The result is shown in Figure 5(a). In the second comparison, the snapshot is set to vary from 100 to 2100. The number of elements in subarray is set to 20. And the result is shown in Figure 5(b). From the two figures, we can see that the runtime of our algorithm is similar with that of [12] which has shown the efficiency of our proposed algorithm.

In the fifth simulation, we compare the azimuth estimation performance of the two algorithms with different separation of angle. The 2D-DOA of two targets are $(\theta_1, \varphi_1) = (30^\circ, 60^\circ + \Delta\varphi_1)$ and $(\theta_2, \varphi_2) = (50^\circ, 70^\circ + \Delta\varphi_2)$, respectively. Both $\Delta\varphi_1$ and $\Delta\varphi_2$ vary from 0° to 18° . The SNR is equal to 20 dB. The snapshot is set to 500. 200 times Monte Carlo simulations are conducted under each separation of angle. Here, the “angle separation” denotes $\Delta\varphi_1$ and $\Delta\varphi_2$ which vary from 0° to 18° . It is different from the common definition of “angle separation.” In fact, the separation angle of the two targets is fixed, what changes is the azimuth angle of the two targets. The purpose of doing this is to make the azimuth angle traverse all angles between 70° and 88° to prove the effectiveness of the algorithm in practical application. The result is shown in Figure 6. We can see that the performance of our proposed algorithm is better than that of the algorithm of [12].

In the sixth simulation, we compare the elevation estimation performance of the two algorithms with different separation of angle. Here, we set $d_x = d_z = d$ and $d_y = 3d$. The 2D-DOA of the two targets are $(\theta_1, \varphi_1) = (60^\circ + \Delta\theta_1, 30^\circ)$ and $(\theta_2, \varphi_2) = (70^\circ + \Delta\theta_2, 50^\circ)$, respectively. Both $\Delta\theta_1$ and $\Delta\theta_2$ vary from 0° to 18° . The other parameters are the same with the fifth simulation. The result is

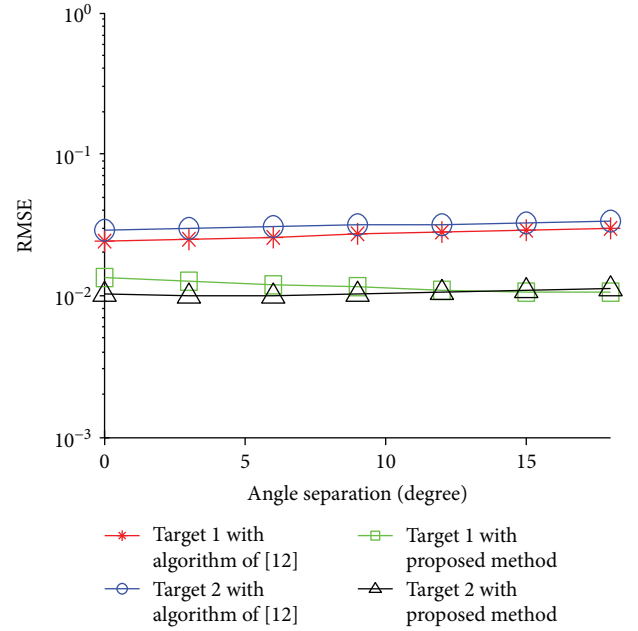


FIGURE 7: RMSE of elevation estimation versus angular separation.

shown in Figure 7. We can see that the performance of our proposed algorithm is better than that of the algorithm of [12].

5. Conclusions

An enhanced 2D-DOA estimation algorithm with three-parallel large spacing ULAs is proposed in this paper. It cannot only make use of the elements of the three-parallel ULAs to estimate the PMA but it can also utilize the information between three-parallel ULAs to improve the estimation accuracy. Besides, it has satisfied estimation performance when the elevation angle is between 70° and 90° and it can automatically pair the estimated 2D-DOA. Furthermore, it has low complexity without using any EVD or SVD to the covariance matrix. Simulations proved the effectiveness of the proposed algorithm.

Conflicts of Interest

The authors declare that they have no conflicts of interest.

References

- [1] J. Li and R. T. Compton, “Two-dimensional angle and polarization estimation using the ESPRIT algorithm,” *IEEE Transactions on Antennas and Propagation*, vol. 40, no. 5, pp. 550–555, 1992.
- [2] T.-H. Liu and J. M. Mendel, “Azimuth and elevation direction finding using arbitrary array geometries,” *IEEE Transactions on Signal Processing*, vol. 46, no. 7, pp. 2061–2065, 1998.
- [3] Z. Ye and C. Liu, “2-D DOA estimation in the presence of mutual coupling,” *IEEE Transactions on Antennas and Propagation*, vol. 56, no. 10, pp. 3150–3158, 2008.
- [4] M. D. Zoltowski and K. T. Wong, “ESPRIT-based 2-D direction finding with a sparse uniform array of electromagnetic

- vector sensors," *IEEE Transactions on Signal Processing*, vol. 48, no. 8, pp. 2195–2204, 2000.
- [5] R. Roy and T. Kailath, "ESPRIT-estimation of signal parameters via rotational invariance techniques," *IEEE Transactions on Acoustics, Speech, and Signal Processing*, vol. 37, no. 7, pp. 984–995, 1989.
- [6] R. O. Schmidt, "Multiple emitter location and signal parameter estimation," in *Proceedings RADC Spectrum Estimation Workshop*, pp. 243–258, Griffiss AFB, Rome, NY, USA, 1979.
- [7] S. Marcos, A. Marsal, and M. Benidir, "The propagator method for source bearing estimation," *Signal Processing*, vol. 42, no. 2, pp. 121–138, 1995.
- [8] X. Chen, C. Wang, and X. Zhang, "DOA and noncircular phase estimation of noncircular signal via an improved noncircular rotational invariance propagator method," *Mathematical Problems in Engineering*, vol. 2015, Article ID 235173, 12 pages, 2015.
- [9] M. Zhou, X. Zhang, X. Qiu, and C. Wang, "Two-dimensional DOA estimation for uniform rectangular array using reduced-dimension propagator method," *International Journal of Antennas and Propagation*, vol. 2015, Article ID 485351, 10 pages, 2015.
- [10] J. Li, X. Zhang, and H. Chen, "Improved two-dimensional DOA estimation algorithm for two-parallel uniform linear arrays using propagator method," *Signal Processing*, vol. 92, no. 12, pp. 3032–3038, 2012.
- [11] N. Tayem and H. M. Kwon, "Azimuth and elevation angle estimation with no failure and no eigen decomposition," *Signal Processing*, vol. 86, no. 1, pp. 8–16, 2006.
- [12] H. Chen, C. Hou, Q. Wang, L. Huang, W. Yan, and L. Pu, "Improved azimuth/elevation angle estimation algorithm for three-parallel uniform linear arrays," *IEEE Antennas and Wireless Propagation Letters*, vol. 14, pp. 329–332, 2015.
- [13] K. T. Wong and M. D. Zoltowski, "Direction-finding with sparse rectangular dual-size spatial invariance array," *IEEE Transactions on Aerospace and Electronic Systems*, vol. 34, no. 4, pp. 1320–1336, 1998.
- [14] M. D. Zoltowski and K. T. Wong, "Closed-form eigenstructure-based direction finding using arbitrary but identical subarrays on a sparse uniform Cartesian array grid," *IEEE Transactions on Signal Processing*, vol. 48, no. 8, pp. 2205–2210, 2000.

Research Article

Radio and Clutter Suppression Algorithm Based on Spatial Multiple Beams for Small-Aperture HFSWR

Di Yao ^{1,2}, Xin Zhang^{1,2}, Qiang Yang ^{1,2} and Weibo Deng^{1,2}

¹School of Electronic Engineering, Harbin Institute of Technology, Harbin 150001, China

²Collaborative Innovation Center of Information Sensing and Understanding at Harbin Institute of Technology, Harbin, China

Correspondence should be addressed to Qiang Yang; yq@hit.edu.cn

Received 29 September 2017; Revised 12 December 2017; Accepted 2 January 2018; Published 28 February 2018

Academic Editor: Piotr Samczynski

Copyright © 2018 Di Yao et al. This is an open access article distributed under the Creative Commons Attribution License, which permits unrestricted use, distribution, and reproduction in any medium, provided the original work is properly cited.

Radio and clutter that cover a certain number of range-Doppler-angle cells have a major impact on the detection performance of a high-frequency surface wave radar (HFSWR) system. Especially for a small-aperture array, the angle spectrums of radio and clutter suffer from severe broadening, so the targets that are more easily submerged in the broadened radio and clutter can be hardly detected. To tackle this issue, this paper proposes an algorithm for radio decontamination and clutter suppression to enable detection of the submerged targets. First, the spatial correlation of the array is derived, and the characteristics of radio and clutter are analyzed based on angle-Doppler joint eigenvector. Then owing to the analysis, the information of radio and clutter in the main beam can be accurately estimated from that in the auxiliary beams and eliminated by subtracting it. The results of simulations and measured data indicate that the proposed method offers a significant performance improvement and has a strong robustness against the array amplitude-phase errors.

1. Introduction

HFSWR has gained much attention in recent years due to its remarkable capabilities in target monitoring and remote sensing over the horizon [1–3]. However, the HF band is a heavily congested part of radio and clutter spectrum, which makes the desired signals easily submerged and difficult to detect. What is worse, among the HFSWR operated worldwide, large portion small-aperture array systems are utilized, such as WERA [4] (four-element configuration), OSMAR [5] (eight-element configuration), and CODAR [6]. Radio and clutter have much more serious effects on these radars than on those with large-aperture arrays. Because the broadened space beams owing to a small-aperture array will make the echo energy of radio and clutter from any observation direction overall exist in the main beam, few array degrees of freedom (DOF) can be used to cancel radio and clutter. Hence, how to overcome these problems in a practical radar system has been a key topic.

Radio, which works on HF band, can be received by an HFSWR receiver. It is a kind of strong direction interference

and occupies a large number of range cells [7, 8]. The clutter is composed of sea clutter and ionospheric clutter: Sea clutter is the collection of several spectrum lines in a narrow Doppler band, which is a part of the common area that we are concerned with for detecting moving vessels [9, 10]; ionospheric clutter comes from the nonideality of the antenna in the zenith direction and possibility contaminates all the range cells, Doppler cells, and angle cells above 100 km [11, 12].

In [13], an adaptive interference cancellation algorithm adding four auxiliary horizontal dipoles configured as two separate crosses to the HFSWR system is proposed. The interference component received by the vertically polarized antennas (main antennas) can be estimated from the auxiliary horizontal antennas. By subtracting this estimate, the interference is suppressed while this method is completely ineffective for a small-aperture array. Xianrong et al. proposed a scheme just using vertical antennas based on subarray technology to suppress the ionospheric clutter, instead of implementing any auxiliary facilities [14]. But its blocking module is only designed to protect two Bragg lines rather than the desired targets with unknown distribution characteristics,

which will cause the target self-cancellation. Another adaptive array processing with a 2D-array configuration has been proposed to restrain ionospheric clutter in [15] and reported to work well. However, this method increases the system complexity and degrades practicability when the antenna field is limited. Based on a single-notch filter, a main-lobe canceller of space spread clutter [16] is developed. Though the excellent suppression performance for sea clutter and ionospheric clutter can be achieved by an effective clutter estimation method, it needs a large-aperture array to ensure nulling depth of the filter and sufficient clutter sample statistics. To overcome the array aperture limit, many temporal and time-frequency approaches [17, 18] are also investigated to remove radio interference from HFSWR systems, but these methods are merely based on chirp signals.

In the small-aperture HFSWR system, considering the weak targets submerged by radio and clutter more easily and possessing a strong correlation between the beams, this paper proposes a novel radio and clutter suppression algorithm. Instead of exploiting the auxiliary array, subarray, and specific signal form, our presented method focuses on the space characteristics of the small-aperture array. Firstly, the conclusion that there is a strong correlation between the beams is deduced. Then, during the process of the proposed canceller, the radio and clutter in the main beam can be estimated and suppressed through the data set collected from the auxiliary beams. Finally, an important factor, namely, the robustness versus array amplitude-phase errors, is detailedly analyzed.

This paper is organized as follows. Section 2 introduces the system structure and spatial distribution characteristics of the small-aperture array. The proposed radio and clutter suppression algorithm is presented in Section 3. The radio and clutter with four typical distributions are simulated to demonstrate the effectiveness in theory in Section 4. The experiments, comparison, and analysis are provided in Section 5. Section 6 concludes this paper.

2. Space Distribution of Array, Radio, and Clutter in Small-Aperture HFSWR

In contrast to the large-aperture array, the spatial distribution of radio and clutter in the small-aperture array will change significantly since a smaller array aperture can cause the beams to widen severely. In addition, the study of radio and clutter suppression method is mostly conducted based on the comprehension of their properties; thus we need to do an accurate analysis of the correlation characteristics of radio and clutter in this section.

2.1. Small-Aperture HFSWR System. The small-aperture HFSWR system presented in this paper was developed by Harbin Institute of Technology in Weihai, whose receiving array composed of 8 vertically polarized elements is shown in Figure 1. The facility can transmit the phase-modulated signals or the frequency-modulated interrupting continuous wave at an operating frequency range from 4 to 10 MHz. System bandwidth and range resolution are 60 kHz and 2.5 km, respectively. In order to have abilities to detect



FIGURE 1: Small-aperture HFSWR system structure.

fast-moving and slow-moving targets, the coherent integration time will be set to 10~30 s (Doppler resolution is 0.1~0.033 Hz) and 120~393 s (Doppler resolution is 0.0083~0.0025 Hz) typically.

2.2. Space Characteristics of Array. The array steering vector is determined by the operating wavelength, the array geometry, and the array aperture. That is, the spatial distribution characteristics produced by the array itself can be acquired through solving the correlation coefficient between the array steering vectors with two different directions. Here, considering a uniform linear array, two array steering vectors with arbitrary directions are shown below:

$$a_1 = \left[1, e^{j2\pi d \sin(\theta_1)/\lambda}, \dots, e^{j2\pi(N-1)d \sin(\theta_1)/\lambda} \right], \quad (1)$$

$$a_2 = \left[1, e^{j2\pi d \sin(\theta_2)/\lambda}, \dots, e^{j2\pi(N-1)d \sin(\theta_2)/\lambda} \right], \quad (2)$$

where d is the element spacing, λ indicates operating wavelength, and N is the total element number. The correlation coefficient of both the above vectors can be calculated by the following equation:

$$\begin{aligned} \rho_{a_1, a_2} &= \text{abs} \left(\frac{(1/N) \sum_n a_1(n) a_2^*(n)}{\sqrt{(1/N) \sum_n |a_1(n)|^2 (1/N) \sum_n |a_2^*(n)|^2}} \right) \\ &= \text{abs} \left(\frac{1}{N} \left(1 + e^{j2\pi d (\sin(\theta_1) - \sin(\theta_2))/\lambda} + \dots + e^{j2\pi(N-1)d (\sin(\theta_1) - \sin(\theta_2))/\lambda} \right) \right), \end{aligned} \quad (3)$$

where $(\cdot)^*$ is the complex conjugation. Let $\Omega = 2\pi d (\sin(\theta_1) - \sin(\theta_2))/\lambda$; it is a variable that has no relation with array aperture as element spacing and wavelength are fixed. The expression of the correlation coefficient can be rewritten as

$$\begin{aligned} \rho_{a_1, a_2} &= \text{abs} \left(\frac{1}{N} \frac{1 - e^{jN\Omega}}{1 - e^{j\Omega}} \right) = \text{abs} \left(\frac{1}{N} \frac{e^{j(N/2)\Omega} (e^{-j(N/2)\Omega} - e^{j(N/2)\Omega})}{e^{j\Omega/2} (e^{-j\Omega/2} - e^{j\Omega/2})} \right) \\ &= \text{abs} \left(\frac{1}{N} \frac{\sin((N/2)\Omega)}{\sin(\Omega/2)} e^{j(N-2/2)\Omega} \right) = \frac{\sin((N/2)\Omega)}{(N/2)\Omega} \frac{\Omega/2}{\sin(\Omega/2)}. \end{aligned} \quad (4)$$

As shown above, it can be concluded that the array elements are fewer (i.e., the array aperture is smaller) and

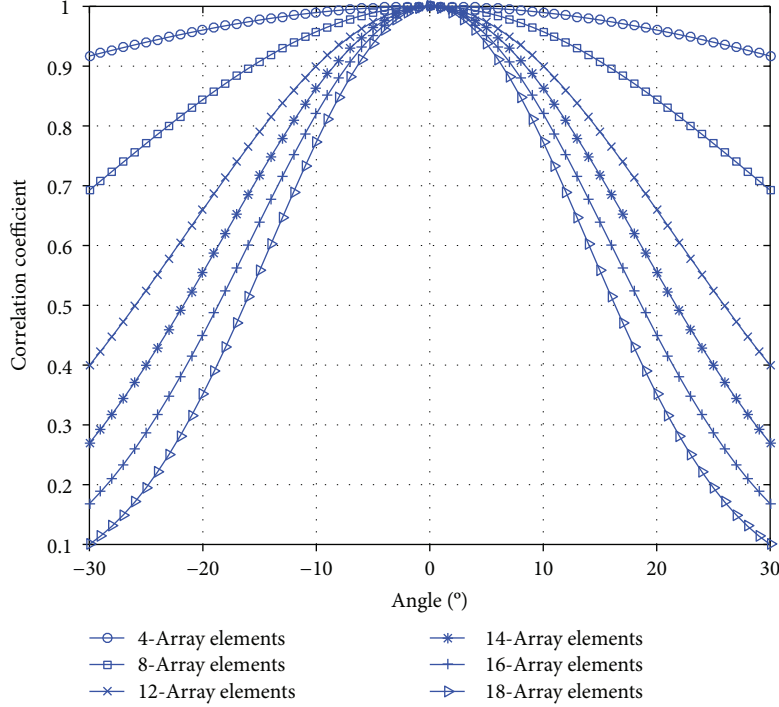


FIGURE 2: Array correlation coefficient.

the correlation between two steering vectors is stronger. The correlation results are shown in Figure 2. Suppose that 0° is a reference direction to calculate the correlation coefficients with all the other directions, element spacing is 10 m, and operating frequency is 5 MHz. Moreover, in the practical system, the window function usually is needed to limit side-lobe level when doing the digital beam forming (DBF). In this paper, the 25 dB Chebyshev coefficients are multiplied by the array steering vector to analyze the correlation.

According to the previous studies in [19], the correlation coefficient is larger than 0.7, which can be treated as homogeneity. And the homogeneity becomes stronger as the coefficient becomes larger. In order to avoid generating target self-cancellation in the proposed algorithm, the deviation angle between auxiliary beams and the desired direction of the main beam must be larger than 10° , at least based on experience. But as shown in Figure 2, the number of homogeneous beam bins is smaller than 13 when the number of array elements is larger than or equal to 16, which greatly reduces the number of clutter samples obtained by secondary beams. Hence, the proposed algorithm can be considered to be effective from 4 to 14 array elements concerning both beam width and sample number.

2.3. Investigation on Space Characteristics of Radio and Clutter. This section shows the spatial distribution characteristics of radio and clutter analyzed in the practical small-aperture HFSWR system. The measured data set comes from radar experiment conducted in Weihai, China, on May 12, 2016, using an eight-element configuration. It is processed in turn by pulse compression, Doppler, and DBF. The

range-Doppler maps of radio, sea clutter, and ionospheric clutter in 0° beam (the normal direction is 0°) are successively shown in Figure 3. The working frequencies are 4.47 MHz, 4.47 MHz, and 5.6 MHz, respectively.

A correlation analysis method whose correctness has been proved in [19] based on angle-Doppler joint eigenvector is used to effectively study the space property of radio and clutter with the real data. The detailed procedures are as follows:

- (1) Select a range-Doppler local region that consists of three adjacent range cells and Doppler cells contaminated by radio and clutter to construct a test matrix $\mathbf{X}_b = [\mathbf{x}_{b1}, \mathbf{x}_{b2}, \mathbf{x}_{b3}]^T \in \mathbb{C}^{3 \times 3}$.
- (2) Stack the columns of the test matrix \mathbf{X}_b under each other to form a new column vector $\mathbf{x}_b = [\mathbf{x}_{b1} \ \mathbf{x}_{b2} \ \mathbf{x}_{b3}] \in \mathbb{C}^{9 \times 1}$.
- (3) Calculate the self-correlation matrix $\mathbf{R}_b \in \mathbb{C}^{9 \times 9}$ by $\mathbf{R}_b = \mathbf{x}_b \mathbf{x}_b^H$; then eigen-decompose \mathbf{R}_b to acquire 9 eigenvalues $\lambda_1, \lambda_2, \dots, \lambda_9$ and corresponding 9 eigenvectors $\xi_1, \xi_2, \dots, \xi_9$; finally normalize the eigenvectors by $\bar{\xi}_i = \xi_i / |\xi_i|$, $i = 1, \dots, 9$.
- (4) Determine their contributions with $\lambda_i(\bar{\xi}_i, \mathbf{x}_b)$, $i = 1, \dots, 9$, and choose the eigenvector $\bar{\xi}_m$, which has the maximal contribution.
- (5) According to steps (1) to (4), the nB eigenvectors $\bar{\xi}_m^i$, $i = 1, 2, \dots, nB$, can be obtained by making the same processing, where nB is the number of total angle cells.

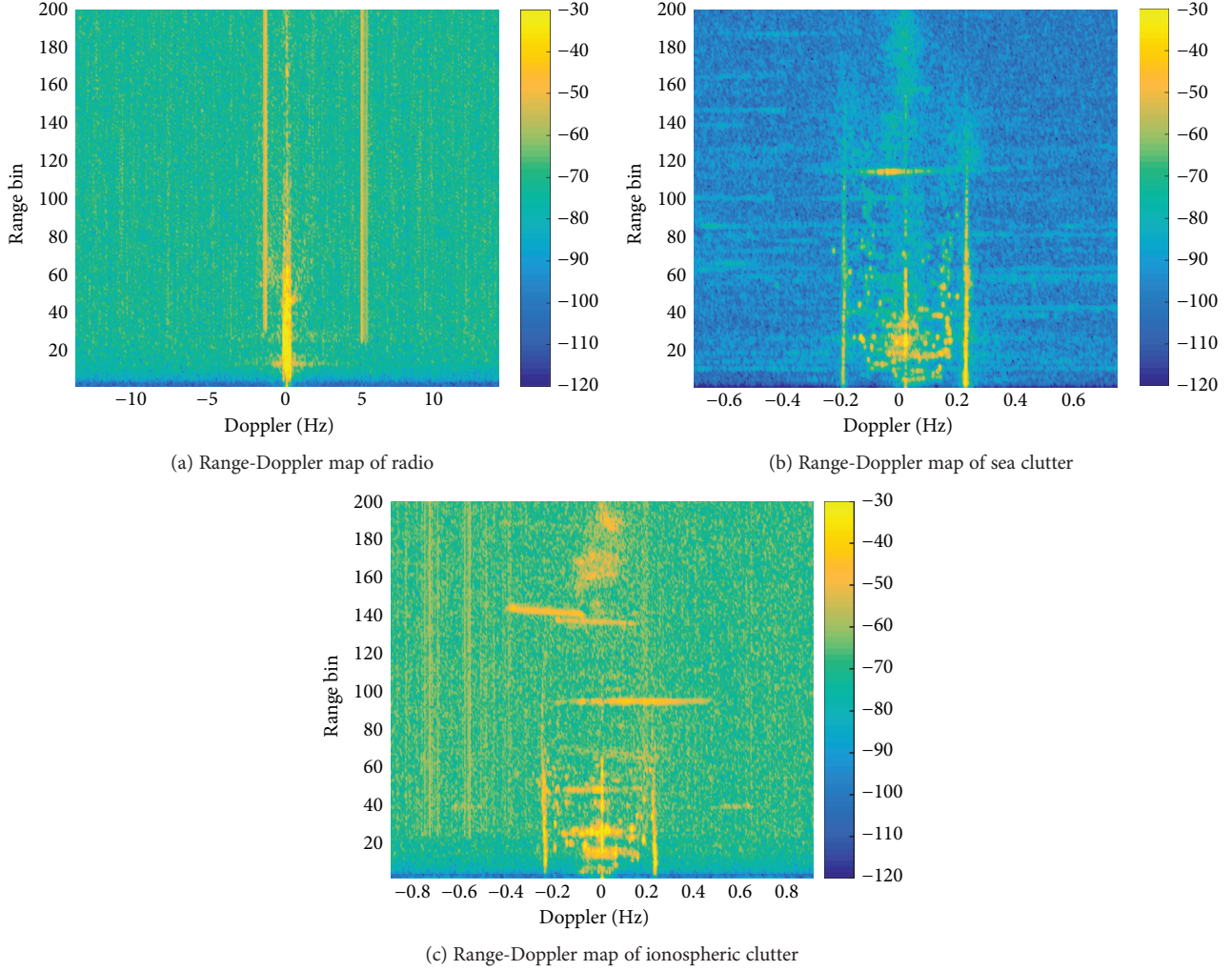


FIGURE 3: Range-Doppler map with measured data.

- (6) Calculate the correlation coefficients employing $\bar{\xi}_m^i$, $i = 1, 2, \dots, nB$, from step (5) by

$$\rho_{ij} = \bar{\xi}_m^i H \bar{\xi}_m^j, \quad i, j = 1, 2, \dots, nB. \quad (5)$$

The spatial scanning area is from -30° to 30° , angle interval of the digital beam forming is 1° , and the reference direction is 0° . We choose continuous radio and clutter region in the range-Doppler spectrum as the processing region to make the contained components as simple as possible. All the correlation coefficients are averaged over 50 independent trials with different processing regions for radio, sea clutter, and ionospheric clutter severally, and approximately equal to 1. As shown in Figure 4, radio and clutter both indicate the extreme strong space correlation in the practical small-aperture HFSWR system.

3. Radio and Clutter Decontamination Algorithm Utilizing Multiple Beam Method

3.1. Problem Formulation. Assume the considered small-aperture HFSWR consists of an array with N elements, and

it transmits a burst of K pulses (Doppler cell numbers) in a coherent processing interval; the sampling points in each transmitted signal pulse (range cell numbers) are L . The echo data of one range cell and Doppler cell can be expressed as

$$\mathbf{z} = \sum_{i=1}^{N_s} \sigma_{s_i} \mathbf{a}(\theta_i) + \sum_{j=1}^{N_c} \sigma_{c_j} \mathbf{a}(\theta_j) + \mathbf{n} \in \mathbb{C}^{N \times 1}, \quad (6)$$

where N_s and N_c , respectively, represent the number of the desired signal and radio and clutter; σ_{s_i} and σ_{c_j} are the complex envelopes of the i th desired signal and the j th radio and clutter; $\mathbf{a}(\theta_i)$ and $\mathbf{a}(\theta_j)$ indicate manifold vectors corresponding to the i th desired signal and the j th radio and clutter, which are the array response at the directions θ_i and θ_j ; \mathbf{n} denotes additive white Gaussian noise.

Signal-to-interference ratio (SIR) and signal-to-clutter ratio (SCR) are negative as the target energy is weak to interference and clutter; thus, the targets submerged in both cannot be detected. Minimum variance distortionless response (MVDR) is a classical space filter keeping the response to the expected direction distortionless and output power minimum. In the ideal condition, the signal to interference/

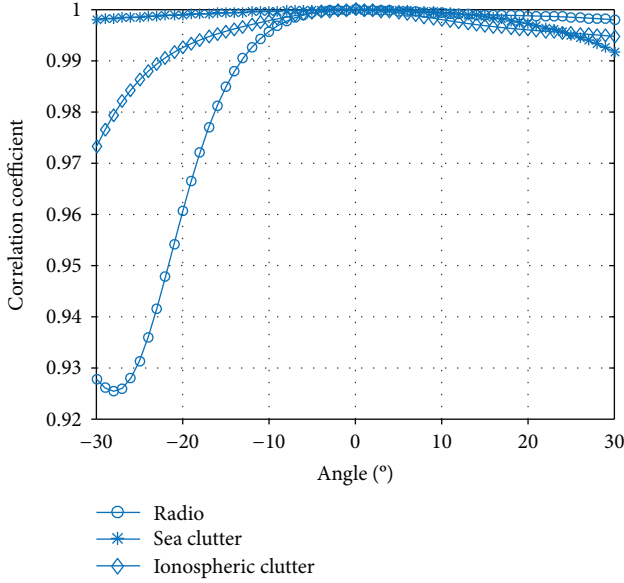


FIGURE 4: Correlation coefficient of the measured radio and clutter.

clutter and noise ratio (SINR/SCNR) can be maximum by MVDR. The correlated matrix of the echo can be indicated as

$$\mathbf{R}_z = E[\mathbf{z}\mathbf{z}^H] = \sum_{i=1}^{N_s} |\sigma_{s_i}|^2 \mathbf{a}(\theta_i) \mathbf{a}^H(\theta_i) + \mathbf{R}_{c+n}, \quad (7)$$

where \mathbf{R}_{c+n} is the covariance matrix of interference, clutter, and noise, which can be indicated as $\mathbf{R}_{c+n} = \sum_{j=1}^{N_c} |\sigma_{c_j}|^2 \mathbf{a}(\theta_j) \mathbf{a}^H(\theta_j) + \sigma_n^2 \mathbf{I}_n$; σ_n^2 is the power of noise; \mathbf{I}_n denotes the $N \times N$ dimensions identity matrix. Suppose θ_0 is the expected direction, and the optimal adaptive beamforming vector can be indicated as

$$\mathbf{w} = \frac{\mathbf{R}_{c+n}^{-1} \mathbf{s}(\theta_0)}{\mathbf{s}(\theta_0)^H \mathbf{R}_{c+n}^{-1} \mathbf{s}(\theta_0)}. \quad (8)$$

3.2. Proposed Algorithm. In the practical radar system, the signals' directions of arrival (DOA) and covariance matrix \mathbf{R}_{c+n} cannot be known in advance. The proposed algorithm is an effective way to solve these problems, and the framework is shown in Figure 5. This algorithm does not require prior access to the targets' DOA and covariance matrix \mathbf{R}_{c+n} . Firstly, the secondary samples that have similar distribution characteristics as the radio and clutter of the main beam can be obtained via auxiliary beams; then implement the information statistics in the range domain and Doppler domain to calculate matrix \mathbf{R}_{c+n} , which guarantees that the component of radio and clutter is greatly superior to that of the targets; finally, the optimal weight vector for suppressing radio and clutter and meanwhile protecting target nature can be achieved. This algorithm is applied in a uniform linear array but is not restricted to this array.

The echo in which the signals are blocked by a block matrix \mathbf{B} is used to deduce the adaptive weights

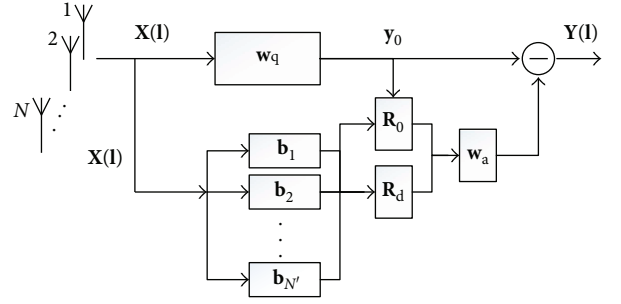


FIGURE 5: The framework of the proposed algorithm, where $\mathbf{X}(\mathbf{l}) = [\mathbf{x}_1(\mathbf{l}), \mathbf{x}_2(\mathbf{l}), \dots, \mathbf{x}_N(\mathbf{l})]^T \in \mathbb{C}^{N \times K}$ is the channel-Doppler dimension data in the l th range cell and $\mathbf{x}_n(\mathbf{l}) \in \mathbb{C}^{1 \times K}$ denotes K Doppler sampling points in the l th range cell and n th element. \mathbf{w}_q is the static weight to keep the main beam direction and the level of side lobe.

\mathbf{w}_a for the canceller. The output of the method can be expressed as

$$\mathbf{Y}(\mathbf{l}) = (\mathbf{w}_q - \mathbf{B}\mathbf{w}_a)^H \mathbf{X}(\mathbf{l}). \quad (9)$$

The output power is defined by

$$p = E[|\mathbf{Y}(\mathbf{l})|^2]. \quad (10)$$

The output power p is minimized to make radio and clutter suppression performance be optimal [14]. At this point, calculating the adaptive weight vector is equivalent to solving the following optimization problem:

$$\min_{\mathbf{w}_a} p = \min_{\mathbf{w}_a} (\mathbf{w}_q - \mathbf{B}\mathbf{w}_a)^H \mathbf{R}_x (\mathbf{w}_q - \mathbf{B}\mathbf{w}_a). \quad (11)$$

From this minimization, we obtain a steady-state optimal weight vector \mathbf{w}_a in the form of the Wiener solution

$$\mathbf{w}_a = (\mathbf{B}^H \mathbf{R}_x \mathbf{B})^{-1} \mathbf{B}^H \mathbf{R}_x \mathbf{w}_q = \mathbf{R}_{c+n}^{-1} \mathbf{R}_0, \quad (12)$$

where \mathbf{B} is a coefficient matrix of auxiliary beams, and let $\theta_1 \theta_2 \dots \theta_{N'}$ be the auxiliary beams' directions. The starting direction of this area is equal to the corresponding angle of -3 dB attenuation of the main beam, and other directions of auxiliary beams can be successively obtained in the direction away from the main beam with 1° angle interval. The beam structure is shown in Figure 6.

The black solid line displays the spatial response of the main beam, which consists of radio, clutter, noise, and targets. The dotted line is the spatial response of N' auxiliary beams to estimate radio and clutter information. Matrix \mathbf{B} is written as

$$\mathbf{B} = [\mathbf{b}_1 \ \mathbf{b}_2 \ \dots \ \mathbf{b}_{N'}]$$

$$= \begin{bmatrix} 1 & 1 & 1 \\ e^{j2\pi d \sin(\theta_1)/\lambda} & e^{j2\pi d \sin(\theta_2)/\lambda} & e^{j2\pi d \sin(\theta_{N'})/\lambda} \\ \vdots & \vdots & \vdots \\ e^{j2\pi(N-1)d \sin(\theta_1)/\lambda} & e^{j2\pi(N-1)d \sin(\theta_2)/\lambda} & e^{j2\pi(N-1)d \sin(\theta_{N'})/\lambda} \end{bmatrix}. \quad (13)$$

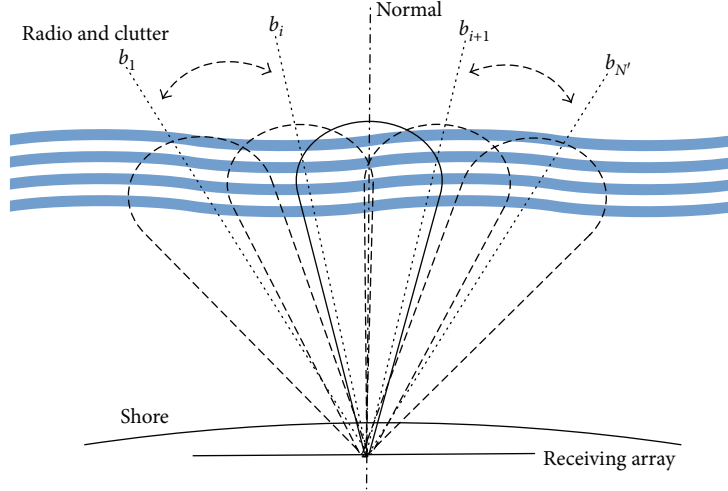


FIGURE 6: The spatial beam structure.

In (12), \mathbf{R}_{c+n} is a self-correlation matrix of radio and clutter counted via the auxiliary beams, and \mathbf{R}_0 is the cross-correlation matrix between the outputs of the auxiliary beams and those of the main beam, expressed as follows:

$$\begin{aligned} \mathbf{R}_{c+n} &= \mathbf{D}\mathbf{D}^H, \\ \mathbf{D} &= \mathbf{B}^H\mathbf{X}(\mathbf{1}), \end{aligned} \quad (14)$$

$$\mathbf{R}_0 = \mathbf{D}\mathbf{y}_0. \quad (15)$$

Suppose that the main beam direction is θ_0 (it can be an interesting arbitrary direction), so its output \mathbf{y}_0 is given by

$$\mathbf{y}_0 = \mathbf{w}_q^H \mathbf{X}(\mathbf{1}) = \begin{bmatrix} 1 \\ e^{j2\pi d \sin(\theta_0)/\lambda} \\ \vdots \\ e^{j2\pi(N-1)d \sin(\theta_0)/\lambda} \end{bmatrix}^H \mathbf{X}(\mathbf{1}). \quad (16)$$

3.3. Robustness Analysis for Amplitude-Phase Errors. In this section, we describe a metric called cancellation ratio (CR) [20, 21] to measure radio and clutter suppression performance. It is defined as the ratio of the output power of the main beam to the output power of the difference of output signals (residue). Mathematically, the CR is defined as

$$\text{CR} = \frac{E(|\mathbf{y}_0|^2)}{E(|\mathbf{y}_0 - \mathbf{w}_a^H \mathbf{y}_{\text{aux}}|^2)}, \quad (17)$$

$$\mathbf{y}_{\text{aux}} = \mathbf{B}^H \mathbf{X}(\mathbf{1}), \quad (18)$$

where \mathbf{y}_{aux} is the estimated radio and clutter information from auxiliary beams. In addition, (17) can be simplified as

$$\begin{aligned} \text{CR} &= \frac{E(|\mathbf{y}_0|^2)}{E\left((\mathbf{y}_0 - \mathbf{w}_a^H \mathbf{y}_{\text{aux}})(\mathbf{y}_0 - \mathbf{w}_a^H \mathbf{y}_{\text{aux}})^H\right)} \\ &= \frac{1}{1 - \left| E\left(\frac{(\mathbf{y}_0 \mathbf{y}_{\text{aux}}^H)}{\sqrt{E(|\mathbf{y}_0|^2)E(|\mathbf{y}_{\text{aux}}|^2)}}\right) \right|^2} = \frac{1}{1 - |\rho|^2}, \end{aligned} \quad (19)$$

where ρ is the correlation coefficient of radio and clutter between the main beam and auxiliary beams, which has a crucial effect on the output CR of the proposed algorithm. Note that by this definition, a good CR will be close to infinity (i.e., if expressed in decibels, it would have a large positive value). Combining the conclusion drawn in Section 2.2, this paper can receive the outstanding radio and clutter suppression performance by the derived space distribution and the presented new method to achieve training data set. Whereas amplitude-phase errors universally exist in the actual radar systems, the error robustness has been an important indicator to judge if the algorithm has practicability or not. Next, robustness analysis is provided, and then (1) and (2) can be rewritten, respectively, as

$$\begin{aligned} \mathbf{a}_1 &= \left[\delta_1 v_1 e^{j\delta_1 \varphi_1}, \delta_2 v_2 e^{j(2\pi d \sin(\theta_1)/\lambda + \delta_2 \varphi_2)}, \right. \\ &\quad \left. \dots, \delta_N v_N e^{j(2\pi(N-1)d \sin(\theta_1)/\lambda + \delta_N \varphi_N)} \right], \end{aligned} \quad (20)$$

$$\begin{aligned} \mathbf{a}_2 &= \left[\delta_1 v_1 e^{j\delta_1 \varphi_1}, \delta_2 v_2 e^{j(2\pi d \sin(\theta_2)/\lambda + \delta_2 \varphi_2)}, \right. \\ &\quad \left. \dots, \delta_N v_N e^{j(2\pi(N-1)d \sin(\theta_2)/\lambda + \delta_N \varphi_N)} \right], \end{aligned} \quad (21)$$

where $\delta_1 v_1, \delta_2 v_2, \dots, \delta_N v_N$ are amplitude errors and $\delta_1 \varphi_1, \delta_2 \varphi_2, \dots, \delta_N \varphi_N$ are phase errors; amplitude errors and phase errors are independent of each other. The error means indicate

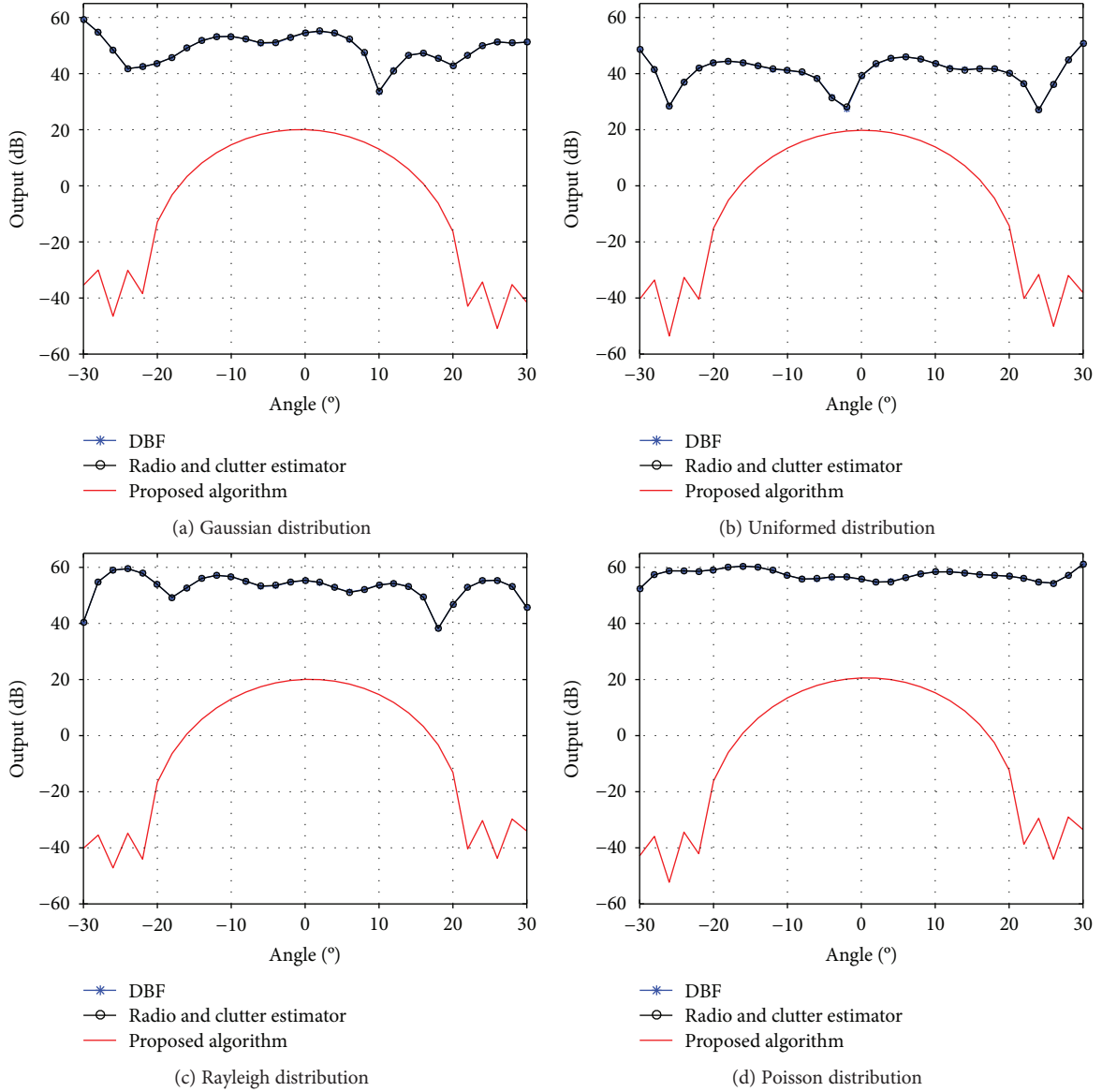


FIGURE 7: Simulations for radio and clutter submitted to four distributions.

$E(\delta_i v_i) = 0$ and $E(\delta_i \varphi_i) = 0$; variances denote $\text{Var}(\delta_i v_i) = \delta_v^2$ and $\text{Var}(\delta_i \varphi_i) = \delta_\varphi^2$. Right now, the correlation coefficient of the array steering vectors taking into account the above amplitude-phase errors is expressed as

$$\begin{aligned}
 \rho_{a_1, a_2} &= \text{abs} \left(E \left(\frac{1/N \sum_n a_1(n) a_2^*(n)}{\sqrt{1/N \sum_n |a_1(n)|^2 1/N \sum_n |a_2^*(n)|^2}} \right) \right) \\
 &= \text{abs} \left(\frac{\sum_{i=1}^N E(1 + 2\delta_i v_i + \delta_i^2 v_i^2) e^{j(i-1)\Omega}}{\sqrt{\sum_{i=1}^N E(1 + 2\delta_i v_i + \delta_i^2 v_i^2) \sum_{i=1}^N E(1 + 2\delta_i v_i + \delta_i^2 v_i^2)}} \right) \\
 &= \text{abs} \left(\frac{\sum_{i=1}^N (1 + \delta_v^2) e^{j(i-1)\Omega}}{N(1 + \delta_v^2)} \right) = \rho_{a_1, a_2}.
 \end{aligned} \tag{22}$$

TABLE 1: Injected target parameters.

| Range bin | Doppler frequency (Hz) | Beam bin | Input SIR before suppression (dB) | Output SIR after suppression (dB) |
|-----------|------------------------|----------|-----------------------------------|-----------------------------------|
| 147 | -1.43 | 7 | -6 | 17 |

The correlation coefficient is not affected by the amplitude-phase errors as the means equal to zero and variances are nonnegative. In other words, the radio and clutter correlation between the main beam and auxiliary beams is not degraded. As a result, this algorithm that has a strong robustness against the errors mainly benefits from sampling format of second training data of radio and clutter based on auxiliary beams.

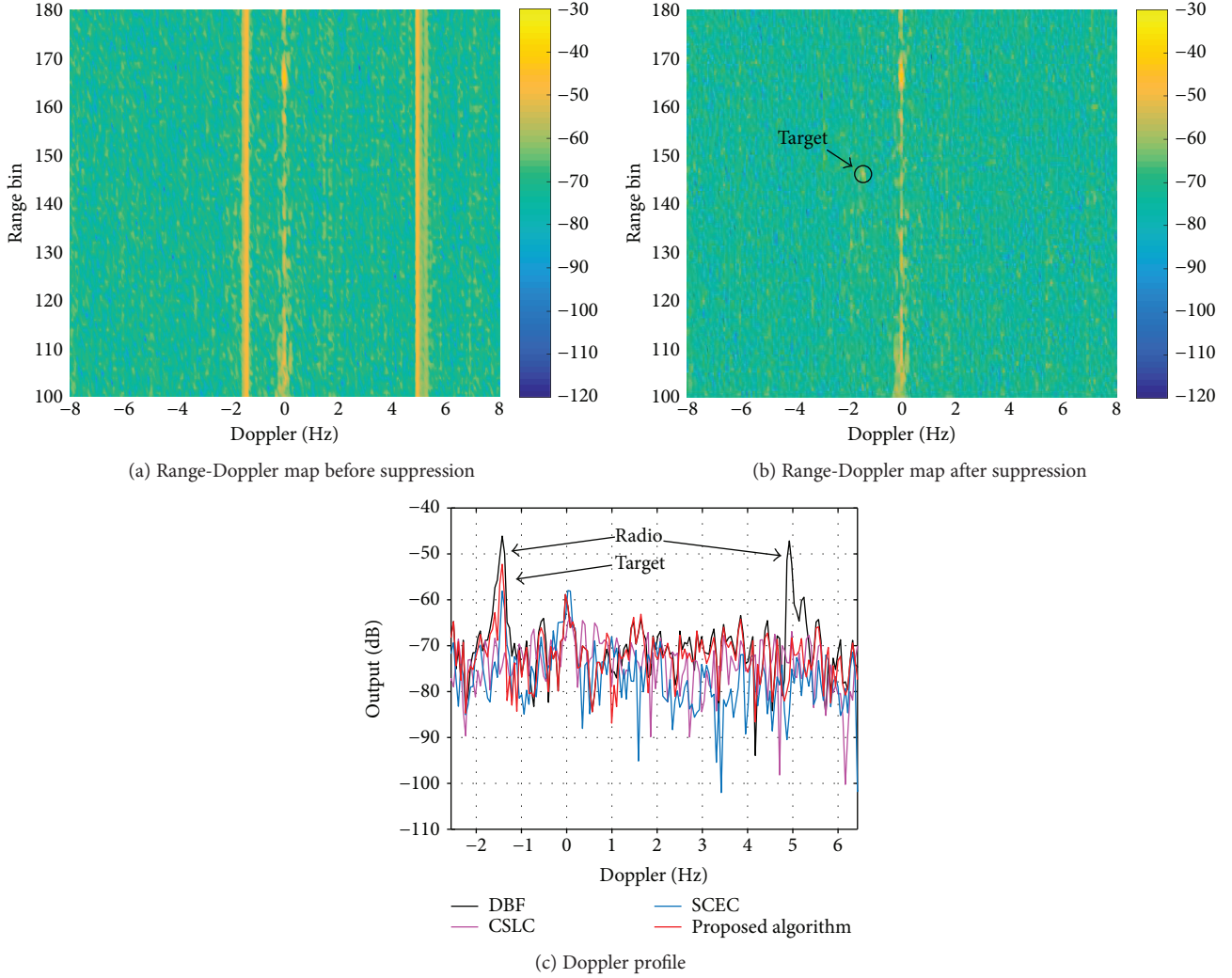


FIGURE 8: Comparison results for radio cancellation.

4. Simulation Trails

In the practical small-aperture radar system, the echo signals are usually polluted by the radio, sea clutter, and ionospheric clutter. The energy distributions of radio and clutter will be very different. In theory, the algorithm will have remarkable effects on any distribution characters based on a framework of statistical estimation. For the distribution characteristics of angle dimension, Gaussian distribution, uniformed distribution, Poisson distribution, and Rayleigh distribution are the four most typical distributions.

In this section, to verify radio and clutter suppression performance, a weaker signal than the radio and clutter has been injected in the 0° , with 8 array elements, 20 auxiliary beams, and 25 dB Chebyshev coefficient. Simulation results averaged over 500 Monte Carlo trials are shown in Figure 7, which obviously demonstrates that the radio and clutter can be accurately estimated by the auxiliary beams and that the injected signal is visible for all the distribution characters.

TABLE 2: Injected target parameters.

| Range bin | Doppler frequency (Hz) | Beam bin | Input SCR before suppression (dB) | Output SCR after suppression (dB) |
|-----------|------------------------|----------|-----------------------------------|-----------------------------------|
| 101 | 0.22 | 4 | -11 | 20 |

5. Measured Data Verification

In this part, the measured data are applied to illustrate the advancement and validity of the proposed algorithm, compared to DBF, coherent side-lobe cancellation (CSLC), and spread clutter estimated canceller (SCEC). The measured data of small-aperture HFSWR as introduced in Section 2 are used. The main beam and auxiliary beams, respectively, are formed for target detection and radio and clutter estimation using 25 dB Chebyshev weighting. The whole detection space (from -30° to 30°) is divided into 7 beam areas whose desired directions are as follows: -30° , -20° , -10° , 0° , 10° ,

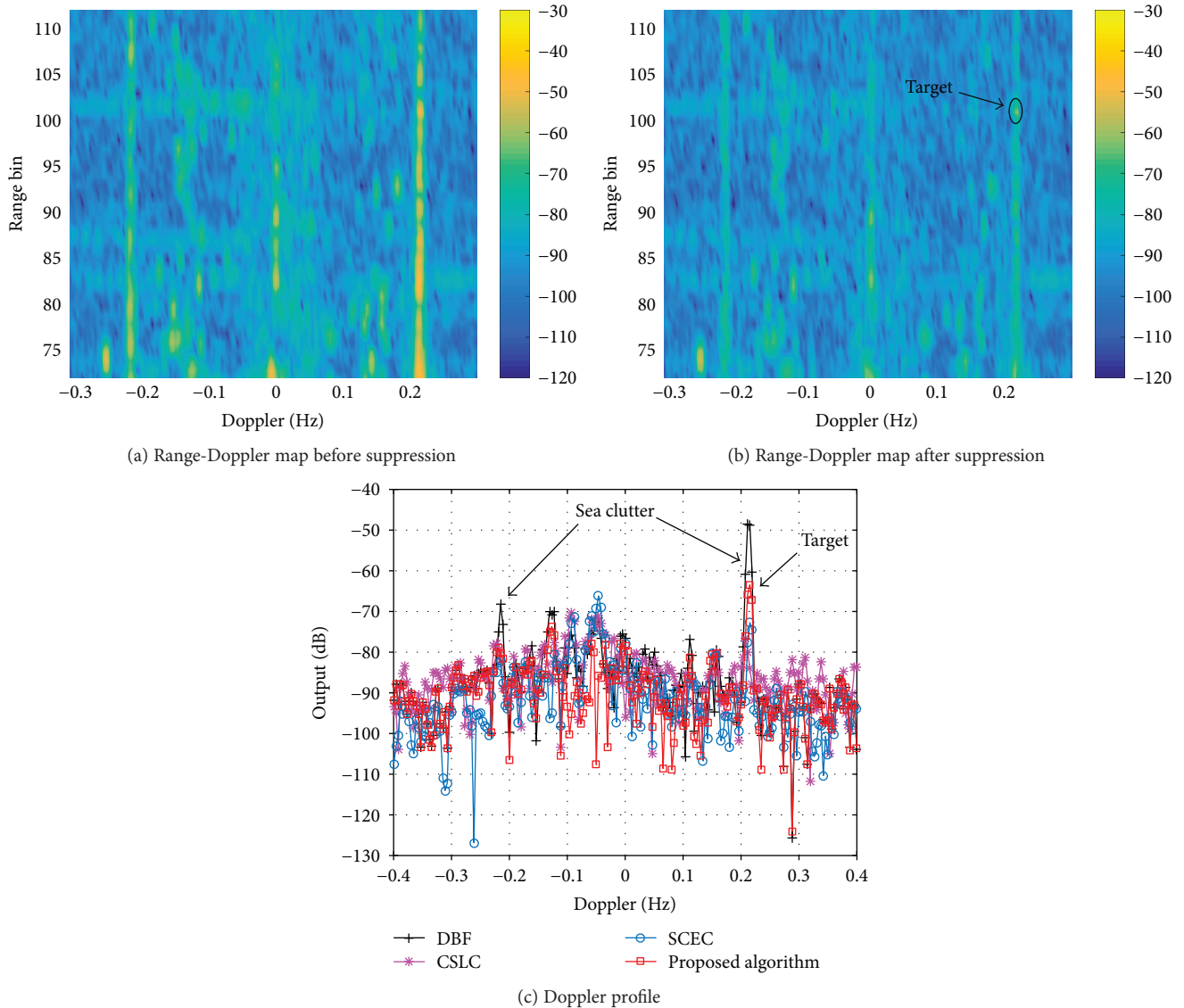


FIGURE 9: Comparison results for sea clutter cancellation.

20°, and 30°. The starting direction of auxiliary beams equals the corresponding angle of -3 dB attenuation of the main beam, and 20 auxiliary beams can be successively selected in the direction away from the starting direction with 1° angle interval.

5.1. Radio Result with Ideal Target. As depicted in Figure 3(a), there are two strong energy radios covering all the range units above the 30th range unit in the range-Doppler spectrum. A simulation target with the same azimuth as radio is injected into the real radio data; the detailed target information is shown in Table 1. In order to facilitate observation, an enlarged spectrum of the target's position is shown in Figure 8(a); the result after mitigating radio in the corresponding area is provided in Figure 8(b); to underline the advantage gained, Figure 8(c) shows a Doppler frequency profile at the range of the 147th range bin when the beam bin is set to the 7th. From Figure 8, it is obvious that the

TABLE 3: Injected target parameters.

| Range bin | Doppler frequency (Hz) | Beam bin | Input SCR before suppression (dB) | Output SCR after suppression (dB) |
|-----------|------------------------|----------|-----------------------------------|-----------------------------------|
| 141 | -0.19 | 2 | 3 | 25 |

performance of the proposed algorithm is superior to that of the others and that it obtains the optimal output SIR.

5.2. Sea Clutter Result with Ideal Target. The range-Doppler spectrum of the actual sea clutter is shown in Figure 3(b), and its theoretical first-order Bragg frequencies generated from working frequency are ± 0.215 Hz. Owing to current, the real Bragg frequencies are shifted to -0.215 Hz and 0.219 Hz. The echo of sea clutter will be received in all front directions because of the geographical environment that the receiving array faced. Therefore, the azimuth of the added

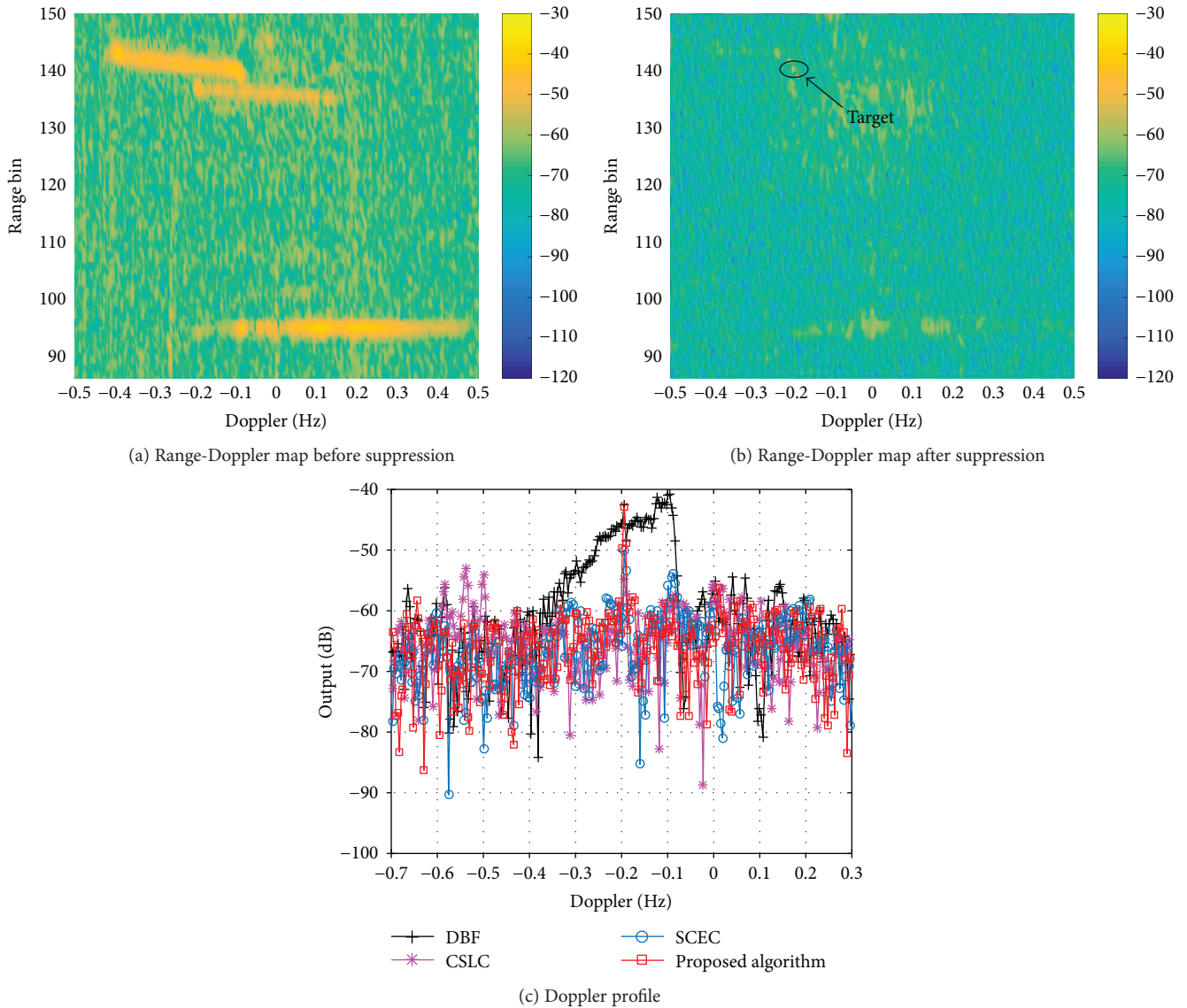


FIGURE 10: Comparison results for ionospheric clutter cancellation.

target is in the normal direction, and the detailed information is in Table 2. Figures 9(a) and 9(b) depict the target range-Doppler maps before and after the proposed method processing after injecting a simulation target. Figure 9(c) illustrates that the proposed algorithm can effectively suppress the sea clutter and detect the target submerged by sea clutter.

5.3. Ionospheric Clutter Result with Ideal Target. Three pieces of strong ionospheric clutter exist in Figure 3(c), which makes the target in this area difficult to be detected if the target echo is weaker than the echo of ionospheric clutter. The distribution characteristics of the target are introduced in Table 3. Figure 10(a) presents an original range-Doppler map that is contaminated by ionospheric clutter from Doppler frequency -0.4 Hz to 0.5 Hz, whereas Figure 10(b) illustrates the map after suppressing the clutter by the proposed method. To show the benefits more clearly, Figure 10(c) shows the Doppler profile with the 2nd beam bin and the

141st range bin, which have the same direction and range with the injected target. It is noticed that the clutter energy has been suppressed by the proposed method, even as the target energy has persevered. The output SCR has improved over 28 dB by the proposed algorithm, which is 5 dB higher than that of SCEC and 12 dB higher than that of CSLC.

5.4. Robustness Result. For the realistic situation as in the discussion in Section 3.3, the amplitude-phase errors generally exist between array elements of the small-aperture HFSWR system. In this section, to evaluate the robustness of the proposed algorithm, a set of the real array errors is first extracted by using 500 measured data files and then calculating statistical mean and variance based on the above files. At last, the statistical result is applied to the injected target, and the mitigating performance comparison of radio and clutter between errors and ideal cases is given in Figure 11. The amplitude-phase error parameters are shown in Table 4. As

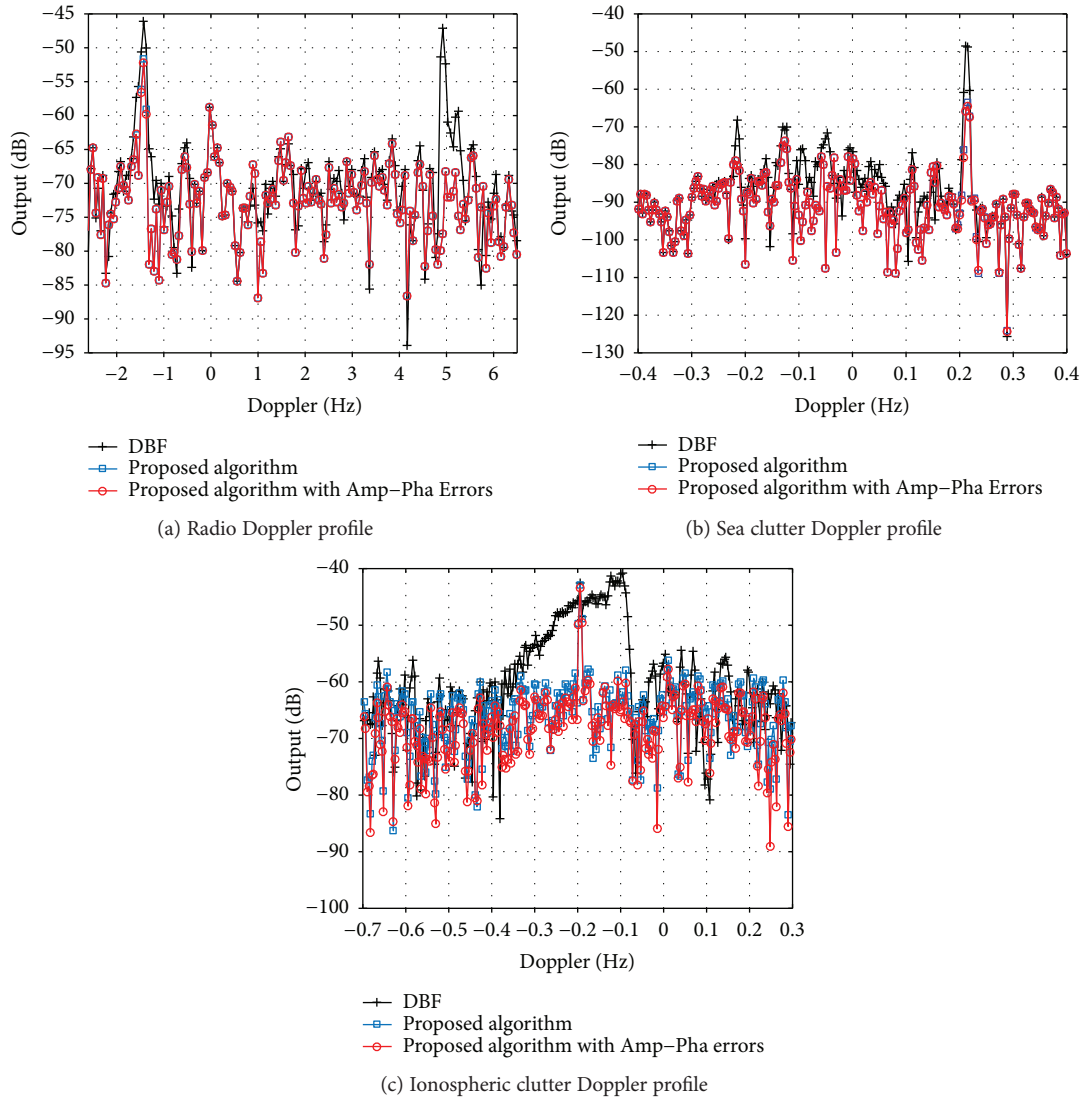


FIGURE 11: Robustness analysis of amplitude-phase errors with the measured data.

TABLE 4: Injected amplitude-phase error parameters.

| Amplitude error mean | Amplitude error variance | Phase error mean | Phase error variance | SIR/SCR loss of the injected target comparing to ideal cases |
|----------------------|--------------------------|------------------|----------------------|--|
| 0.203 dB | 5.47 dB | 0.12° | 9.875° | 0.55 dB/0.67 dB/0.43 dB |

TABLE 5: Injected target 1 parameters.

| Radio and clutter | Center range bin | Center Doppler frequency | Beam bin | Output SNR | Attenuation |
|---------------------|------------------|--------------------------|----------|------------|-------------|
| Radio | 147 | -5.13 Hz | 7 | 17.51 dB | 0.92 dB |
| Sea clutter | 101 | 0.246 Hz | 4 | 24.4 dB | 0.47 dB |
| Ionospheric clutter | 141 | -0.503 Hz | 2 | 24.75 dB | 0.87 dB |

TABLE 6: Injected target 2 parameters.

| Radio and clutter | Center range bin | Center Doppler frequency | Beam bin | Output SIR/SCR | Attenuation |
|---------------------|------------------|--------------------------|----------|----------------|-------------|
| Radio | 147 | -1.43 Hz | 7 | 17 dB | 1.43 dB |
| Sea clutter | 101 | 0.22 Hz | 4 | 20 dB | 4.86 dB |
| Ionospheric clutter | 141 | -0.19 Hz | 2 | 25 dB | 0.62 dB |

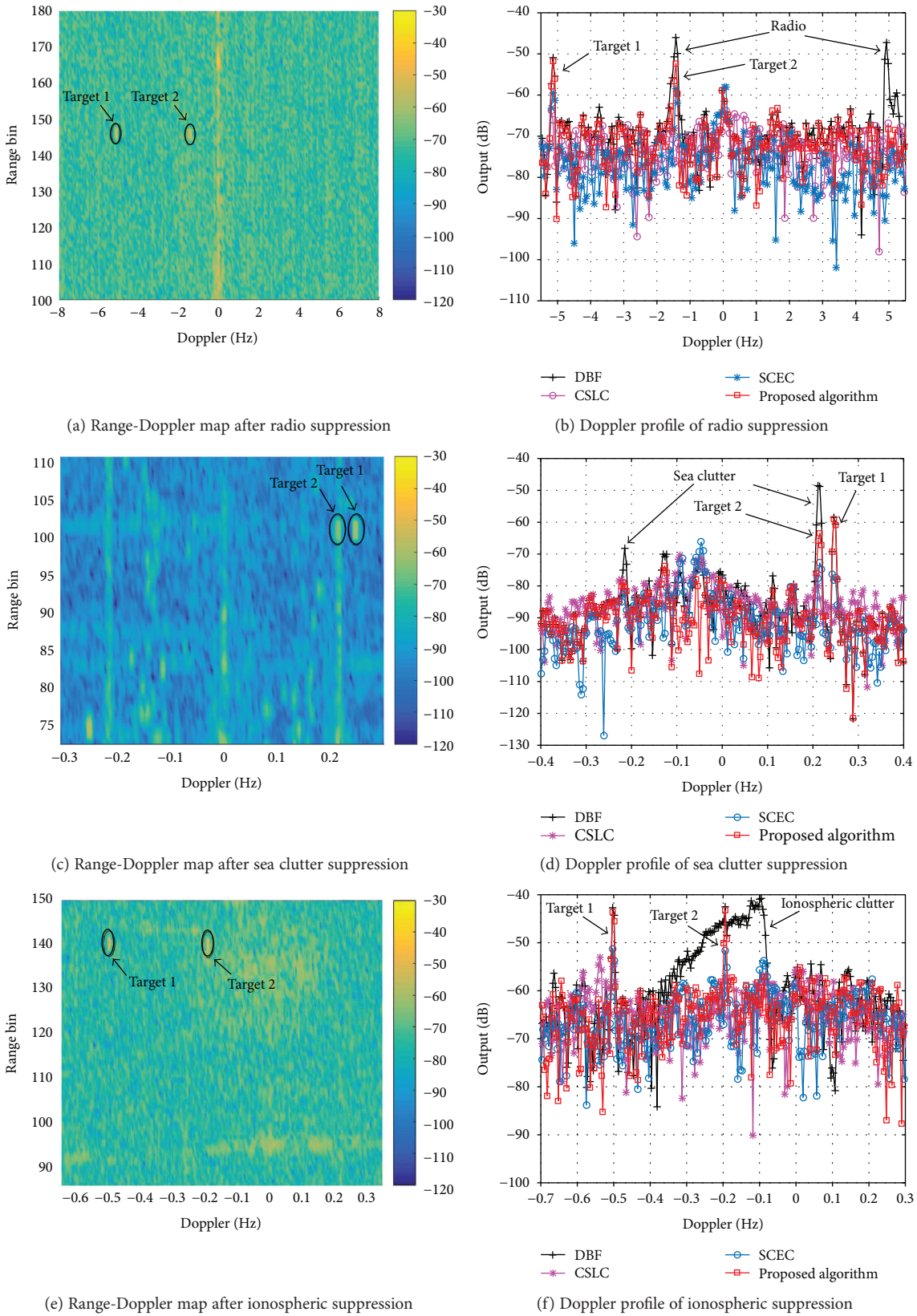


FIGURE 12: Comparison results for radio and clutter cancellation with the simulated real targets.

TABLE 7: Injected target parameters.

| Targets (radio/sea clutter/ionospheric clutter) | Beam directions | Target directions | Attenuation (dB) |
|---|------------------------------|-------------------------------|------------------|
| Target 1 | $30^\circ/0^\circ/-20^\circ$ | $25^\circ/4^\circ/-19^\circ$ | 0.62/0.58/0.35 |
| Target 2 | $30^\circ/0^\circ/-20^\circ$ | $23^\circ/-3^\circ/-22^\circ$ | 0.33/0.91/0.78 |

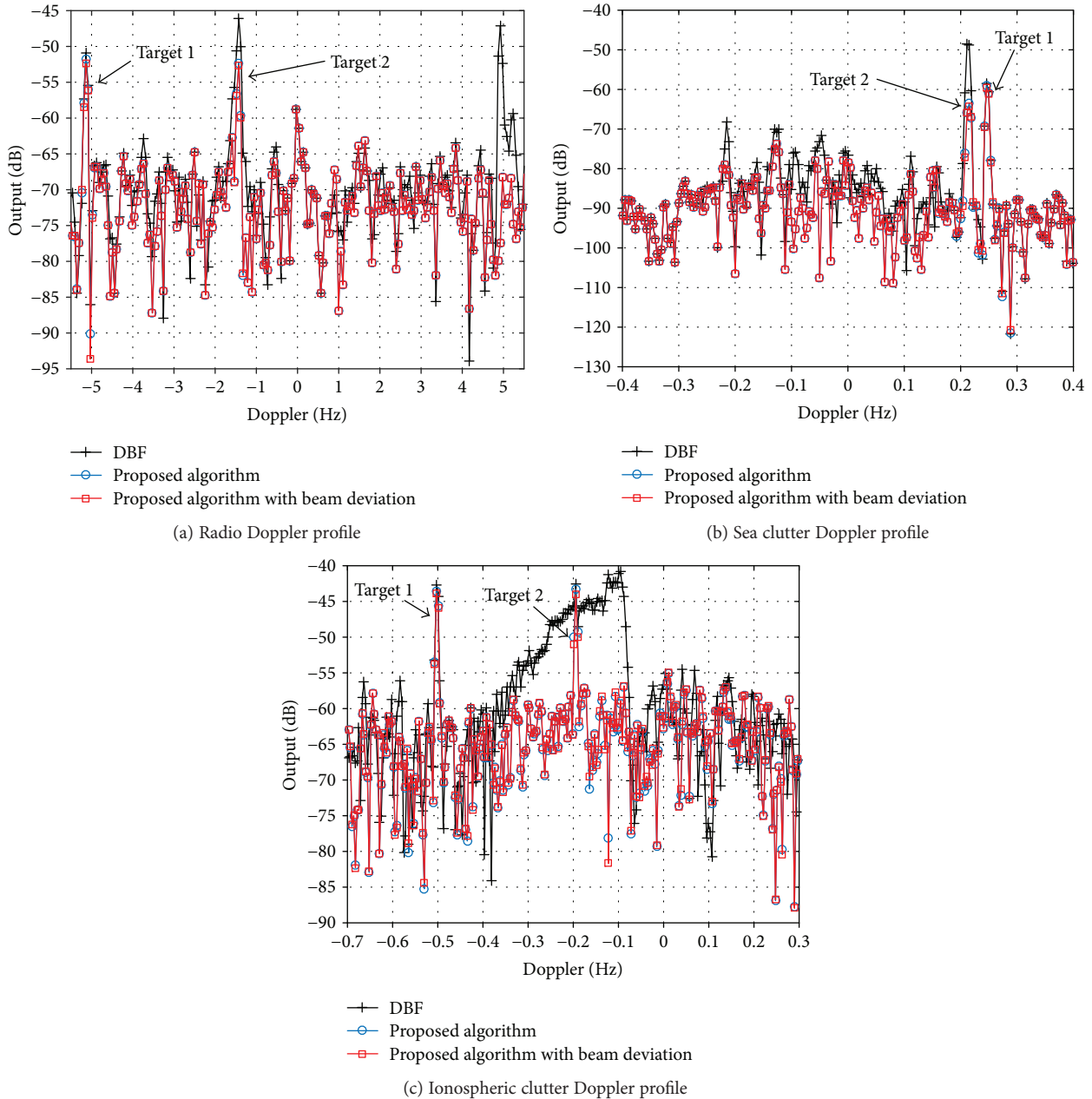


FIGURE 13: Robustness analysis of beam deviation with the simulated real data.

can be seen from Figure 11 and Table 4, the proposed algorithm has the same radio and clutter suppression ability and approximately optimal output SIR/SCR. The thinned performance loss is mainly derived from the nonzero mean of the errors in the practical system.

5.5. *Suppression Results with Simulated Real Targets.* Here, the capability of the proposed algorithm for suppressing radio and clutter in the case of the real target is studied. The real targets can be simulated by broadening Doppler bin and range bin of the ideal targets; that is, the number of

covering bin changes from one to three. Compared to the above trials, a marked target that has the same signal power as the submerged target is added in the noise area to contrast the attenuation of the signal before and after processing. The two target parameters used in this experiment are listed in Tables 5 and 6. Figures 12(a), 12(c), and 12(e) reveal that the radio and clutter are significantly suppressed while two injected targets are well preserved and clearly visible. Figures 12(b), 12(d), and 12(f) indicate that the marked targets almost do not suffer any attenuation of output SNR and that the submerged targets can also acquire 20–25 dB performance improvement of output SIR and SCR.

5.6. The Analysis of Beam Deviation. Two simulated real targets that have the same parameters as in Section 5.5 except azimuth are injected into the radio and clutter to quantize the performance degradation while the target directions are different from the desired directions of the main beam. The angular deviation between targets and the associated main beam varies from -5° to 5° considering that the angle interval of the main beam is 10° , and the detailed information is illustrated in Table 7. As shown in Figure 13 and Table 7, the proposed algorithm only suffers a small performance loss, not more than 1 dB, regardless of the kind of experimental situation.

5.7. Performance Analysis. The worst scenarios are considered in the above trials, that is, the target absolutely submerged by radio, sea clutter, and ionospheric clutter in range-Doppler-angle domains. From the comparison results in range-Doppler spectrum and Doppler profile, the proposed algorithm can absolutely restrain radio and clutter while introducing no false target outside the injected target position. Besides, our algorithm can obtain 26 dB output SIR/SCR improvement averaged from situation a to situation c, but only 0.55 dB and 0.6 dB performance loss for the real amplitude-phase errors and beam deviation severally. Hence, it is concluded that compared to the other methods, in the cases of ideal and real target characteristics, the proposed algorithm can have better radio and clutter restraint performance, higher output SIR/SCR, and stronger amplitude-phase error robustness.

6. Conclusion

In this paper, the spatial distribution characteristics of radio and clutter in the small-aperture HFSWR system are first derived. It is a theoretical basis of our proposed algorithm, which presents a cascaded method for radio decontamination and clutter suppression to enable detection of the submerged targets. Simulations and measured data have demonstrated that the radio and clutter in the main beam can be estimated by auxiliary beams and effectively cancelled by this algorithm while preserving almost all the target echo energy. Another contribution of the method is the robustness against amplitude-phase errors, which makes great sense for improving algorithm stability and reliability of a radar system. Compared with DBF, CSLC, and SCEC methods, the proposed algorithm has been shown to have better radio

and clutter suppression results and higher output SIR/SCR. The theory about how to choose auxiliary beams to achieve the optimal output performance will be studied in a future paper.

Conflicts of Interest

The authors declare that there are no conflicts of interest regarding the publication of this paper.

Acknowledgments

The authors would like to thank the associate editor and the anonymous reviewers for their helpful comments and suggestions. This work is supported by the National Science Fund Committer (NSFC) of China (61701140, 61032011, and 61171182).

References

- [1] D. Barrick, "History, present status, and future directions of HF surface-wave radars in the U.S.," in *2003 Proceedings of the International Conference on Radar (IEEE Cat. No.03EX695)*, pp. 652–655, Adelaide, Australia, 2003.
- [2] T. Ponsford and J. Wang, "A review of high frequency surface wave radar for detection and tracking of ships," *Turkish Journal of Electrical Engineering & Computer Sciences*, vol. 18, no. 3, pp. 409–428, 2010.
- [3] Y.-L. Shi and P.-L. Shui, "Target detection in high-resolution sea clutter via block-adaptive clutter suppression," *IET Radar, Sonar & Navigation*, vol. 5, no. 1, p. 48, 2011.
- [4] E. Kamli, C. Chavanne, and D. Dumont, "Experimental assessment of the performance of high-frequency CODAR and WERA radars to measure ocean currents in partially ice-covered waters," *Journal of Atmospheric and Oceanic Technology*, vol. 33, no. 3, pp. 539–550, 2016.
- [5] W. Xianrong, K. Hengyu, and W. Biyang, "Adaptive cochannel interference suppression based on subarrays for HFSWR," *IEEE Signal Processing Letters*, vol. 12, no. 2, pp. 162–165, 2005.
- [6] C. Y. Wang, C. L. Su, and K. H. Wu, "Cross spectral analysis of CODAR-SeaSonde echoes from sea surface and ionosphere at Taiwan," *International Journal of Antennas and Propagation*, vol. 2017, Article ID 1756761, 14 pages, 2017.
- [7] H. Zhou and B. Wen, "Radio frequency interference suppression in small-aperture high-frequency radars," *IEEE Geoscience and Remote Sensing Letters*, vol. 9, no. 4, pp. 788–792, 2012.
- [8] W. Wang and L. R. Wyatt, "Radio frequency interference cancellation for sea-state remote sensing by high-frequency radar," *IET Radar, Sonar & Navigation*, vol. 5, no. 4, p. 405, 2011.
- [9] K. Hasselmann, "Determination of ocean wave spectra from Doppler radio return from the sea surface," *Nature Physical Science*, vol. 229, no. 1, pp. 16–17, 1971.
- [10] D. Barrick, "First-order theory and analysis of MF/HF/VHF scatter from the sea," *IEEE Transactions on Antennas and Propagation*, vol. 20, no. 1, pp. 2–10, 1972.
- [11] S. Chen, E. W. Gill, and W. Huang, "A high-frequency surface wave radar ionospheric clutter model for mixed-path propagation with the second-order sea scattering," *IEEE Transactions*

- on Antennas and Propagation*, vol. 64, no. 12, pp. 5373–5381, 2016.
- [12] J. Wei, D. Weibo, and S. Jialin, “Characteristic study of ionospheric clutter in high-frequency over the horizon surface wave radar,” in *2009 IEEE Youth Conference on Information, Computing and Telecommunication*, pp. 154–157, Beijing, China, 2009.
- [13] H. Leong, “Adaptive nulling of skywave interference using horizontal dipole antennas in a coastal surveillance HF surface wave radar system,” in *Radar Systems (RADAR 97)*, pp. 26–30, Edinburgh, UK, 1997.
- [14] W. Xianrong, K. Hengyu, and W. Biyang, “Adaptive ionospheric clutter suppression based on subarrays in monostatic HF surface wave radar,” *IEE Proceedings - Radar, Sonar and Navigation*, vol. 152, no. 2, p. 89, 2005.
- [15] M. Wu, B. Y. Wen, and H. Zhou, “Ionospheric clutter suppression in HF surface wave radar,” *Journal of Electromagnetic Waves and Applications*, vol. 23, no. 10, pp. 1265–1272, 2009.
- [16] X. Zhang, Q. Yang, D. Yao, and W. Deng, “Main-lobe cancellation of the space spread clutter for target detection in HFSWR,” *IEEE Journal of Selected Topics in Signal Processing*, vol. 9, no. 8, pp. 1632–1638, 2015.
- [17] Y. Ji, J. Zhang, Y. Wang, and X. Chu, “Vessel target detection based on fusion range-Doppler image for dual-frequency high-frequency surface wave radar,” *IET Radar, Sonar & Navigation*, vol. 10, no. 2, pp. 333–340, 2016.
- [18] Y. Ji, J. Zhan, X. Chu, Y. Wang, and M. Li, “Vessel target detection using zero-Doppler spectra of radar echo for high-frequency surface wave radar,” *IET Radar, Sonar & Navigation*, vol. 10, no. 7, pp. 1243–1248, 2016.
- [19] X. Zhang, Q. Yang, and W. Deng, “Weak target detection within the nonhomogeneous ionospheric clutter background of HFSWR based on STAP,” *International Journal of Antennas and Propagation*, vol. 2013, Article ID 382516, 11 pages, 2013.
- [20] A. Farina and F. A. Studer, “Evaluation of sidelobe-canceller performance,” *IEE Proceedings F Communications, Radar and Signal Processing*, vol. 129, no. 1, p. 52, 1982.
- [21] I. J. Gupta and J. Ward, “Effects of desired signal on the performance of a sidelobe canceller,” *IEEE Transactions on Antennas and Propagation*, vol. 37, no. 9, pp. 1109–1115, 1989.

Research Article

Joint-2D-SL0 Algorithm for Joint Sparse Matrix Reconstruction

Dong Zhang, Yongshun Zhang, and Cunqian Feng

Air and Missile Defense College, Air Force Engineering University, Xi'an, Shaanxi 710051, China

Correspondence should be addressed to Dong Zhang; zhangdongtougao@163.com

Received 19 July 2017; Revised 4 November 2017; Accepted 26 November 2017; Published 20 December 2017

Academic Editor: Elisa Giusti

Copyright © 2017 Dong Zhang et al. This is an open access article distributed under the Creative Commons Attribution License, which permits unrestricted use, distribution, and reproduction in any medium, provided the original work is properly cited.

Sparse matrix reconstruction has a wide application such as DOA estimation and STAP. However, its performance is usually restricted by the grid mismatch problem. In this paper, we revise the sparse matrix reconstruction model and propose the joint sparse matrix reconstruction model based on one-order Taylor expansion. And it can overcome the grid mismatch problem. Then, we put forward the Joint-2D-SL0 algorithm which can solve the joint sparse matrix reconstruction problem efficiently. Compared with the Kronecker compressive sensing method, our proposed method has a higher computational efficiency and acceptable reconstruction accuracy. Finally, simulation results validate the superiority of the proposed method.

1. Introduction

Compressive sensing is becoming more and more popular for its superiority in parameter super-resolution estimation using short observation [1–3]. And as extensions to compressed sensing, sparse matrix reconstruction has received a lot of attention [4–6]. Many problems in signal processing can be seemed as sparse matrix reconstruction problem, such as the DOA estimation [7] and STAP [8]. In this paper, we consider the estimation of DOA and DOD in MIMO radar. It can be solved by the traditional subspace method, such as MUSIC and ESPRIT algorithm. But they usually need large snapshots to estimate the covariance matrix. Considering the advantages of sparse matrix reconstruction, here, we research the estimation of DOA and DOD in MIMO radar based on sparse matrix reconstruction method. And many algorithms have been proposed to solve the sparse matrix reconstruction efficiently. For instance, [9] puts forward the 2D-SL0 algorithm, and [10] puts forward the 2D-IAA algorithm. Both of them can reconstruct the sparse matrix efficiently. However, the sparse matrix model has some inherent shortcomings. Its performance is affected by the grid mismatch problem [11]. That is because no matter how thin we divide the mesh, we still cannot guarantee that all the parameters fall on the grid completely [12, 13]. So the estimation accuracy will be

affected by the grid number and how much do we divide the mesh.

In this paper, we revise the sparse matrix model by the one-order Taylor expansion and propose the joint sparse matrix model. This model eliminates the grid mismatch effect by introducing some joint sparse items. Then, in order to solve the joint sparse matrix reconstruction problem efficiently, we revise the 2D-SL0 algorithm and put forward the Joint-2D-SL0 algorithm. It can get a high estimation accuracy with satisfied speed.

Note that our method is different with the methods in [9, 10]. The methods in [9, 10] cannot deal with the off-grid problem. Our method can solve it by introducing some joint sparse items. And these sparse items have the same sparse structure. So the “Joint” means that our Joint-2D-SL0 algorithm can get their estimation simultaneously. However, the “Joint” in [14] means that it is jointly used to reconstruct the images at all available channels simultaneously. That is the difference between our method and the method in [14]. Both our method and the method in [14] are applied to the signal matrix without stacking the signal into 1D vector.

2. Problem Formulation

Assuming there is a bistatic MIMO radar which obtains K transmitters and L receivers, both the transmitting array

and the receiving array are collocated in uniform linear array. d_1 and d_2 are the element spacing of transmitters and receivers, respectively. $f^{(T)} = d_1 \cos(\varphi)/\lambda$ and $f^{(R)} = d_2 \cos(\theta)/\lambda$ are the normalized DOD and normalized DOA of targets. For convenience, we denote them as the DOD and DOA in our paper. Assuming the transmitting waveforms are normalized orthogonal signals, that is, $SS^H = I_K$, where $S = [s_1, s_2, \dots, s_K]^T$. After matched filtering, we get the received signal as follows:

$$\begin{aligned} \mathbf{Y} &= \left[\sum_{m=1}^M a_m \mathbf{a}_R(f_m^{(R)}) \mathbf{a}_T(f_m^{(T)})^T S + \mathbf{W} \right] S^H \\ &= \sum_{m=1}^M a_m \mathbf{a}_R(f_m^{(R)}) \mathbf{a}_T(f_m^{(T)})^T + \mathbf{Z}, \end{aligned} \quad (1)$$

where a_m is the scattering coefficient of m th target. \mathbf{W} represents the noise matrix. $\mathbf{Z} = \mathbf{W}S^H$. $\mathbf{a}_R(f_m^{(R)}) = [1, \dots, \exp(j(L-1)2\pi f_m^{(R)})]$ and $\mathbf{a}_T(f_m^{(T)}) = [1, \dots, \exp(j(K-1)2\pi f_m^{(T)})]$ are the receiving steering vectors and transmitting steering vectors corresponding to the DOA and DOD of the m th target, respectively.

Considering the sparsity of targets, the sparse reconstruction method can be used to estimate target's 2D parameters. Then, discretizing the range of DOD and DOA to $K_d > K$ and $L_a > L$ resolution grids, respectively, we can convert (1) into the following form:

$$\mathbf{Y} = \Phi_R(\theta) \Xi \Phi_T^T(\varphi) + \mathbf{Z}, \quad (2)$$

where Ξ is a sparse matrix and we can estimate the DOD and DOA of targets according to the position of nonzero elements. $\theta = [\theta_1, \theta_2, \dots, \theta_{K_d}]$ and $\varphi = [\varphi_1, \varphi_2, \dots, \varphi_{L_a}]$ are the predefined grids. $\Phi_R(\theta) = [\mathbf{a}_R(f_1^{(R)}), \mathbf{a}_R(f_2^{(R)}), \dots, \mathbf{a}_R(f_{K_d}^{(R)})]$ and $\Phi_T(\varphi) = [\mathbf{a}_T(f_1^{(T)}), \mathbf{a}_T(f_2^{(T)}), \dots, \mathbf{a}_T(f_{L_a}^{(T)})]$.

This sparse matrix reconstruction model requires that the targets must fall on the predefined grids. Practically, no matter how small we divide the mesh, the targets cannot be guaranteed to completely fall on the grids. So the performance of this method will depend on the way how we divide the mesh. Reference [11] puts forward an off-grid model to solve the grid mismatch problem in 1D-DOA estimation; this idea could be extended to the 2D parameter estimation situation.

3. Joint Sparse Matrix Reconstruction

The targets' true and unknown DOA and DOD are $\alpha = [\alpha_1, \alpha_2, \dots, \alpha_D]$ and $\beta = [\beta_1, \beta_2, \dots, \beta_D]$, respectively. Approximating the $\Phi_R(\alpha)$ and $\Phi_T(\beta)$ by the first-order Taylor expansion around the predefined grids θ and φ , respectively,

$$\begin{aligned} \Phi_R(\alpha) &= \Phi_R(\theta) + \Phi_R(\theta)' \Delta_1, \\ \Phi_T(\beta) &= \Phi_T(\varphi) + \Phi_T(\varphi)' \Delta_2, \end{aligned} \quad (3)$$

where $\Phi_R(\theta)' = [(\partial \mathbf{a}_R(\theta_1)/\partial \theta_1), \dots, (\partial \mathbf{a}_R(\theta_{L_a})/\partial \theta_{L_a})]$, $\Phi_T(\varphi)' = [(\partial \mathbf{a}_T(\varphi_1)/\partial \varphi_1), \dots, (\partial \mathbf{a}_T(\varphi_{K_d})/\partial \varphi_{K_d})]$, $\Delta_1 = \text{diag}(\alpha - \theta)$, and $\Delta_2 = \text{diag}(\beta - \varphi)$. We can get the following joint sparse matrix model:

$$\begin{aligned} \mathbf{Y} &= \left[\Phi_R(\theta) + \Phi_R(\theta)' \Delta_1 \right] \Xi \left[\Phi_T(\varphi) + \Phi_T(\varphi)' \Delta_2 \right]^T + \mathbf{Z} \\ &= \begin{bmatrix} \Phi_R(\theta) & \Phi_R(\theta)' \end{bmatrix} \begin{bmatrix} I \\ \Delta_1 \end{bmatrix} \Xi \begin{bmatrix} I & \Delta_2^T \end{bmatrix} \begin{bmatrix} \Phi_T(\varphi) & \Phi_T(\varphi)' \end{bmatrix}^T + \mathbf{Z} \\ &= \begin{bmatrix} \Phi_R(\theta) & \Phi_R(\theta)' \end{bmatrix} \begin{bmatrix} \Xi & \Xi \Delta_2^T \\ \Delta_1 \Xi & \Delta_1 \Xi \Delta_2^T \end{bmatrix} \begin{bmatrix} \Phi_T(\varphi) & \Phi_T(\varphi)' \end{bmatrix}^T + \mathbf{Z} \\ &= \begin{bmatrix} \Phi_R(\theta) & \Phi_R(\theta)' \end{bmatrix} \begin{bmatrix} \Xi & \mathbf{P}_2 \\ \mathbf{P}_1 & \mathbf{P}_3 \end{bmatrix} \begin{bmatrix} \Phi_T(\varphi) & \Phi_T(\varphi)' \end{bmatrix}^T + \mathbf{Z}, \end{aligned} \quad (4)$$

where $\mathbf{P}_1 = \Delta_1 \Xi$, $\mathbf{P}_2 = \Xi \Delta_2^T$, $\mathbf{P}_3 = \Delta_1 \Xi \Delta_2^T$, and Ξ are joint sparse matrix, that is, they have the same sparse structure. That is because whether left multiplied or right multiplied, a diagonal matrix will not change the sparsity of a sparse matrix. So we can use (4) to estimate the targets' DOD and DOA, and it will not be affected by the grid mismatch problem.

Using Φ_R and Φ_T to represent $\Phi_R(\theta)$ and $\Phi_T(\varphi)$, respectively, (4) can be rewritten as follows:

$$\mathbf{Y} = \begin{bmatrix} \Phi_R & \Phi_R' \end{bmatrix} \begin{bmatrix} \Xi & \mathbf{P}_2 \\ \mathbf{P}_1 & \mathbf{P}_3 \end{bmatrix} \begin{bmatrix} \Phi_T & \Phi_T' \end{bmatrix}^T + \mathbf{Z}. \quad (5)$$

But how to efficiently solve the joint sparse reconstruction problem? If we use the Kronecker compressive sensing method (solve (5) by converting it into 1D problem), it will bring much more computation burden because of the huge computation complexity of Kronecker product. Can we directly solve the joint sparse matrix reconstruction problem in (5)? Reference [9] proposes the 2D smoothed L0 (2D-SL0) algorithm, and it solves the 2D sparse problem more easily than the 1D-SL0 algorithm. Based on this, we revise the 2D-SL0 algorithm and propose the Joint-2D-SL0 algorithm to solve the joint sparse matrix reconstruction problem. They can be applied to situations where the number of targets is unknown.

The Gaussian function adopted in the 2D-SL0 is $G_\sigma(\mathbf{X}) = \sum_{i,j} \exp(-(x_{ij}^2)/\sigma^2)$ [9]. Here, the Gaussian function we adopt in the Joint-2D-SL0 algorithm is

$$G_\sigma \left(\begin{bmatrix} \Xi & \mathbf{P}_2 \\ \mathbf{P}_1 & \mathbf{P}_3 \end{bmatrix} \right) = \sum_{i,j} \exp \left(-\frac{\Xi_{ij}^2 + \mathbf{P}_{1ij}^2 + \mathbf{P}_{2ij}^2 + \mathbf{P}_{3ij}^2}{\sigma^2} \right). \quad (6)$$

It will lead to a joint sparse of $\Xi, \mathbf{P}_1, \mathbf{P}_2$, and \mathbf{P}_3 , that is, the special case of block sparse of $\begin{bmatrix} \Xi & \mathbf{P}_2 \\ \mathbf{P}_1 & \mathbf{P}_3 \end{bmatrix}$. The joint 2D gradient projection method is put forward to solve the Joint-2D-SL0 function. The gradient of the Joint-2D-SL0 function is

$$\delta \triangleq \nabla G_\sigma \left(\begin{bmatrix} \Xi & \mathbf{P}_2 \\ \mathbf{P}_1 & \mathbf{P}_3 \end{bmatrix} \right) = \begin{bmatrix} -\Xi_{i,j} \exp \left(-\frac{\Xi_{i,j}^2 + \mathbf{P}_{1i,j}^2 + \mathbf{P}_{2i,j}^2 + \mathbf{P}_{3i,j}^2}{\sigma^2} \right) & \cdots & -\mathbf{P}_{2i,j} \exp \left(-\frac{\Xi_{i,j}^2 + \mathbf{P}_{1i,j}^2 + \mathbf{P}_{2i,j}^2 + \mathbf{P}_{3i,j}^2}{\sigma^2} \right) \\ \vdots & \ddots & \vdots \\ -\mathbf{P}_{1i,j} \exp \left(-\frac{\Xi_{i,j}^2 + \mathbf{P}_{1i,j}^2 + \mathbf{P}_{2i,j}^2 + \mathbf{P}_{3i,j}^2}{\sigma^2} \right) & \cdots & -\mathbf{P}_{3i,j} \exp \left(-\frac{\Xi_{i,j}^2 + \mathbf{P}_{1i,j}^2 + \mathbf{P}_{2i,j}^2 + \mathbf{P}_{3i,j}^2}{\sigma^2} \right) \end{bmatrix}, \quad (7)$$

where σ_1 is chosen as $\sigma_1 > 8 \max_{i,j} |W_{i,j}|$ and $\mathbf{W} =$

$$\begin{bmatrix} \Xi^0 & \mathbf{P}_2^0 \\ \mathbf{P}_1^0 & \mathbf{P}_3^0 \end{bmatrix}.$$

The initialization of the joint sparse matrix is

$$\begin{bmatrix} \Xi^0 & \mathbf{P}_2^0 \\ \mathbf{P}_1^0 & \mathbf{P}_3^0 \end{bmatrix} = \begin{bmatrix} \Phi_R & \Phi_R' \end{bmatrix}^\dagger \mathbf{Y} \begin{bmatrix} \Phi_T^T \\ \Phi_T'^T \end{bmatrix}. \quad (8)$$

The proof is as follows:

Proof

$$\begin{aligned} \text{vec} \left(\begin{bmatrix} \Xi^0 & \mathbf{P}_2^0 \\ \mathbf{P}_1^0 & \mathbf{P}_3^0 \end{bmatrix} \right) &= \left(\begin{bmatrix} \Phi_T & \Phi_T' \end{bmatrix} \otimes \begin{bmatrix} \Phi_R & \Phi_R' \end{bmatrix} \right)^\dagger \text{vec}(\mathbf{Y}) \\ &= \left(\begin{bmatrix} \Phi_T & \Phi_T' \end{bmatrix}^\dagger \otimes \begin{bmatrix} \Phi_R & \Phi_R' \end{bmatrix}^\dagger \right) \text{vec}(\mathbf{Y}) \\ &= \text{vec} \left(\begin{bmatrix} \Phi_R & \Phi_R' \end{bmatrix}^\dagger \mathbf{Y} \begin{bmatrix} \Phi_T^T \\ \Phi_T'^T \end{bmatrix} \right)^\dagger. \end{aligned} \quad (9)$$

The projection onto the feasible set can be obtained by

$$\begin{aligned} \begin{bmatrix} \Xi & \mathbf{P}_2 \\ \mathbf{P}_1 & \mathbf{P}_3 \end{bmatrix} &= \begin{bmatrix} \Xi^l & \mathbf{P}_2^l \\ \mathbf{P}_1^l & \mathbf{P}_3^l \end{bmatrix} + \begin{bmatrix} \Phi_R & \Phi_R' \end{bmatrix}^\dagger \\ &\cdot \left\{ \mathbf{Y} - \begin{bmatrix} \Phi_R & \Phi_R' \end{bmatrix} \begin{bmatrix} \Xi^l & \mathbf{P}_2^l \\ \mathbf{P}_1^l & \mathbf{P}_3^l \end{bmatrix} \begin{bmatrix} \Phi_T^T \\ \Phi_T'^T \end{bmatrix} \right\} \\ &\cdot \begin{bmatrix} \Phi_T^T \\ \Phi_T'^T \end{bmatrix}^\dagger. \end{aligned} \quad (10)$$

The proof is as follows:

Proof. When reconstructing a sparse matrix using the model

$$\mathbf{Y} = \begin{bmatrix} \Phi_R & \Phi_R' \end{bmatrix} \begin{bmatrix} \Xi^l & \mathbf{P}_2^l \\ \mathbf{P}_1^l & \mathbf{P}_3^l \end{bmatrix} \begin{bmatrix} \Phi_T^T \\ \Phi_T'^T \end{bmatrix} + \mathbf{Z}, \text{ we have}$$

$$\begin{aligned} \mathbf{Y} &- \begin{bmatrix} \Phi_R & \Phi_R' \end{bmatrix} \begin{bmatrix} \Xi^l & \mathbf{P}_2^l \\ \mathbf{P}_1^l & \mathbf{P}_3^l \end{bmatrix} \begin{bmatrix} \Phi_T^T \\ \Phi_T'^T \end{bmatrix} \\ &= \begin{bmatrix} \Phi_R & \Phi_R' \end{bmatrix} \begin{bmatrix} \Xi & \mathbf{P}_2 \\ \mathbf{P}_1 & \mathbf{P}_3 \end{bmatrix} \begin{bmatrix} \Phi_T^T \\ \Phi_T'^T \end{bmatrix} \\ &- \begin{bmatrix} \Phi_R & \Phi_R' \end{bmatrix} \begin{bmatrix} \Xi^l & \mathbf{P}_2^l \\ \mathbf{P}_1^l & \mathbf{P}_3^l \end{bmatrix} \begin{bmatrix} \Phi_T^T \\ \Phi_T'^T \end{bmatrix} \\ &= \begin{bmatrix} \Phi_R & \Phi_R' \end{bmatrix} \left\{ \begin{bmatrix} \Xi & \mathbf{P}_2 \\ \mathbf{P}_1 & \mathbf{P}_3 \end{bmatrix} - \begin{bmatrix} \Xi^l & \mathbf{P}_2^l \\ \mathbf{P}_1^l & \mathbf{P}_3^l \end{bmatrix} \right\} \begin{bmatrix} \Phi_T^T \\ \Phi_T'^T \end{bmatrix}. \end{aligned} \quad (11)$$

So the minimum L_2 estimate of $\left\{ \begin{bmatrix} \Xi & \mathbf{P}_2 \\ \mathbf{P}_1 & \mathbf{P}_3 \end{bmatrix} - \right.$

$$\left. \begin{bmatrix} \Xi^l & \mathbf{P}_2^l \\ \mathbf{P}_1^l & \mathbf{P}_3^l \end{bmatrix} \right\}$$
 is

$$\begin{aligned} &\begin{bmatrix} \Phi_R & \Phi_R' \end{bmatrix}^\dagger \left\{ \mathbf{Y} - \begin{bmatrix} \Phi_R & \Phi_R' \end{bmatrix} \begin{bmatrix} \Xi^l & \mathbf{P}_2^l \\ \mathbf{P}_1^l & \mathbf{P}_3^l \end{bmatrix} \begin{bmatrix} \Phi_T^T \\ \Phi_T'^T \end{bmatrix} \right\} \\ &\cdot \left\{ \begin{bmatrix} \Phi_T^T \\ \Phi_T'^T \end{bmatrix} \right\}^\dagger. \end{aligned} \quad (12)$$

So the projection onto the feasible set can be obtained by

$$\begin{aligned} \begin{bmatrix} \Xi & \mathbf{P}_2 \\ \mathbf{P}_1 & \mathbf{P}_3 \end{bmatrix} &= \begin{bmatrix} \Xi^l & \mathbf{P}_2^l \\ \mathbf{P}_1^l & \mathbf{P}_3^l \end{bmatrix} + \begin{bmatrix} \Phi_R & \Phi_R' \end{bmatrix}^\dagger \\ &\cdot \left\{ \mathbf{Y} - \begin{bmatrix} \Phi_R & \Phi_R' \end{bmatrix} \begin{bmatrix} \Xi^l & \mathbf{P}_2^l \\ \mathbf{P}_1^l & \mathbf{P}_3^l \end{bmatrix} \begin{bmatrix} \Phi_T^T \\ \Phi_T'^T \end{bmatrix} \right\} \\ &\cdot \begin{bmatrix} \Phi_T^T \\ \Phi_T'^T \end{bmatrix}^\dagger. \end{aligned} \quad (13)$$

Now we get the Joint-2D-SL0 algorithm which is shown in Algorithm 1.

Remark 1. The internal loop is repeated a fixed and small number of times (L). That is to say, for increasing the speed, we do not wait for the steepest ascent algorithm to converge. This can be justified by the gradual decrease in the value of σ . And for each σ , we do not need the exact maximizer of G_σ . We just need to enter the region near the (global) maximizer of G_σ to escape from its local maximizers.

Initialize:

$$(1) \text{ Let } \begin{bmatrix} \mathbf{\Xi}^0 & \mathbf{P}_2^0 \\ \mathbf{P}_1^0 & \mathbf{P}_3^0 \end{bmatrix} = \left[\Phi_R \quad \Phi_R' \right]^\dagger \mathbf{Y} \begin{bmatrix} \Phi_T^T \\ \Phi_T'^T \end{bmatrix}^\dagger.$$

(2) Choose a suitable decreasing sequence for σ , $[\sigma_1, \sigma_2, \dots, \sigma_J]$.

For $j = 1, 2, \dots, J$:

(1) Let $\sigma = \sigma_j$

$$(2) \text{ Minimise the function } G_\sigma \left(\begin{bmatrix} \mathbf{\Xi} & \mathbf{P}_2 \\ \mathbf{P}_1 & \mathbf{P}_3 \end{bmatrix} \right) = \sum_{i,j} \exp \left(-\frac{\mathbf{\Xi}_{ij}^2 + \mathbf{P}_{1ij}^2 + \mathbf{P}_{2ij}^2 + \mathbf{P}_{3ij}^2}{\sigma^2} \right),$$

$$\text{on the feasible set } \begin{bmatrix} \mathbf{\Xi} & \mathbf{P}_2 \\ \mathbf{P}_1 & \mathbf{P}_3 \end{bmatrix} = \left\{ \begin{bmatrix} \mathbf{\Xi} & \mathbf{P}_2 \\ \mathbf{P}_1 & \mathbf{P}_3 \end{bmatrix} : \left| \left[\Phi_R \quad \Phi_R' \right] \begin{bmatrix} \mathbf{\Xi} & \mathbf{P}_2 \\ \mathbf{P}_1 & \mathbf{P}_3 \end{bmatrix} \begin{bmatrix} \Phi_T^T \\ \Phi_T'^T \end{bmatrix} - \mathbf{Y} \right|_2 < \varepsilon \right\},$$

using L iterations of the steepest descent algorithm (then project $\begin{bmatrix} \mathbf{\Xi} & \mathbf{P}_2 \\ \mathbf{P}_1 & \mathbf{P}_3 \end{bmatrix}$ onto the feasible set):

$$\text{Initialize: } \begin{bmatrix} \mathbf{\Xi} & \mathbf{P}_2 \\ \mathbf{P}_1 & \mathbf{P}_3 \end{bmatrix} = \begin{bmatrix} \mathbf{\Xi}^{j-1} & \mathbf{P}_2^{j-1} \\ \mathbf{P}_1^{j-1} & \mathbf{P}_3^{j-1} \end{bmatrix}$$

For $l = 1, 2, \dots, L$

(a) Let

$$\delta \triangleq \sigma^2 \nabla G_\sigma \left(\begin{bmatrix} \mathbf{\Xi} & \mathbf{P}_2 \\ \mathbf{P}_1 & \mathbf{P}_3 \end{bmatrix} \right) = \begin{bmatrix} -\mathbf{\Xi}_{ij} \exp \left(-\frac{\mathbf{\Xi}_{ij}^2 + \mathbf{P}_{1ij}^2 + \mathbf{P}_{2ij}^2 + \mathbf{P}_{3ij}^2}{\sigma^2} \right) & \dots & -\mathbf{P}_{2ij} \exp \left(-\frac{\mathbf{\Xi}_{ij}^2 + \mathbf{P}_{1ij}^2 + \mathbf{P}_{2ij}^2 + \mathbf{P}_{3ij}^2}{\sigma^2} \right) \\ \vdots & \ddots & \vdots \\ -\mathbf{P}_{1ij} \exp \left(-\frac{\mathbf{\Xi}_{ij}^2 + \mathbf{P}_{1ij}^2 + \mathbf{P}_{2ij}^2 + \mathbf{P}_{3ij}^2}{\sigma^2} \right) & \dots & -\mathbf{P}_{3ij} \exp \left(-\frac{\mathbf{\Xi}_{ij}^2 + \mathbf{P}_{1ij}^2 + \mathbf{P}_{2ij}^2 + \mathbf{P}_{3ij}^2}{\sigma^2} \right) \end{bmatrix}.$$

$$(b) \text{ Let } \begin{bmatrix} \mathbf{\Xi} & \mathbf{P}_2 \\ \mathbf{P}_1 & \mathbf{P}_3 \end{bmatrix} \leftarrow \begin{bmatrix} \mathbf{\Xi} & \mathbf{P}_2 \\ \mathbf{P}_1 & \mathbf{P}_3 \end{bmatrix} + \mu \delta \quad (\mu \text{ is a small positive constant})$$

(c) Project $\begin{bmatrix} \mathbf{\Xi} & \mathbf{P}_2 \\ \mathbf{P}_1 & \mathbf{P}_3 \end{bmatrix}$ back onto the feasible set:

$$\begin{bmatrix} \mathbf{\Xi} & \mathbf{P}_2 \\ \mathbf{P}_1 & \mathbf{P}_3 \end{bmatrix} \leftarrow \begin{bmatrix} \mathbf{\Xi} & \mathbf{P}_2 \\ \mathbf{P}_1 & \mathbf{P}_3 \end{bmatrix} + \left[\Phi_R \quad \Phi_R' \right]^\dagger \left\{ \mathbf{Y} - \left[\Phi_R \quad \Phi_R' \right] \begin{bmatrix} \mathbf{\Xi} & \mathbf{P}_2 \\ \mathbf{P}_1 & \mathbf{P}_3 \end{bmatrix} \begin{bmatrix} \Phi_T^T \\ \Phi_T'^T \end{bmatrix} \right\} \begin{bmatrix} \Phi_T^T \\ \Phi_T'^T \end{bmatrix}^\dagger.$$

$$(3) \text{ Set } \begin{bmatrix} \mathbf{\Xi}^j & \mathbf{P}_2^j \\ \mathbf{P}_1^j & \mathbf{P}_3^j \end{bmatrix} = \begin{bmatrix} \mathbf{\Xi} & \mathbf{P}_2 \\ \mathbf{P}_1 & \mathbf{P}_3 \end{bmatrix}.$$

$$\text{Final answer is: } \begin{bmatrix} \mathbf{\Xi} & \mathbf{P}_2 \\ \mathbf{P}_1 & \mathbf{P}_3 \end{bmatrix} = \begin{bmatrix} \mathbf{\Xi}^j & \mathbf{P}_2^j \\ \mathbf{P}_1^j & \mathbf{P}_3^j \end{bmatrix}.$$

ALGORITHM 1: The Joint-2D-SL0 algorithm.

Remark 2. Steepest ascent consists of iterations of the form $\begin{bmatrix} \mathbf{\Xi} & \mathbf{P}_2 \\ \mathbf{P}_1 & \mathbf{P}_3 \end{bmatrix} \leftarrow \begin{bmatrix} \mathbf{\Xi} & \mathbf{P}_2 \\ \mathbf{P}_1 & \mathbf{P}_3 \end{bmatrix} + \mu_j \nabla G_\sigma$. Here, the step-size parameters μ_j should be decreasing, that is, for smaller values of σ , smaller values of μ_j should be applied. Note that instead

of μ_j only a constant μ appeared. The reason is that by letting

$$\mu_j = \mu \sigma^2 \text{ for some constant } \mu, \text{ we have } \begin{bmatrix} \mathbf{\Xi} & \mathbf{P}_2 \\ \mathbf{P}_1 & \mathbf{P}_3 \end{bmatrix} \leftarrow$$

$$\begin{bmatrix} \mathbf{\Xi} & \mathbf{P}_2 \\ \mathbf{P}_1 & \mathbf{P}_3 \end{bmatrix} + \mu \sigma^2 \nabla G_\sigma = \begin{bmatrix} \mathbf{\Xi} & \mathbf{P}_2 \\ \mathbf{P}_1 & \mathbf{P}_3 \end{bmatrix} + \mu \delta.$$

$$\delta = \sigma^2 \nabla G_\sigma = \begin{bmatrix} -\mathbf{\Xi}_{ij} \exp \left(-\frac{\mathbf{\Xi}_{ij}^2 + \mathbf{P}_{1ij}^2 + \mathbf{P}_{2ij}^2 + \mathbf{P}_{3ij}^2}{\sigma^2} \right) & \dots & -\mathbf{P}_{2ij} \exp \left(-\frac{\mathbf{\Xi}_{ij}^2 + \mathbf{P}_{1ij}^2 + \mathbf{P}_{2ij}^2 + \mathbf{P}_{3ij}^2}{\sigma^2} \right) \\ \vdots & \ddots & \vdots \\ -\mathbf{P}_{1ij} \exp \left(-\frac{\mathbf{\Xi}_{ij}^2 + \mathbf{P}_{1ij}^2 + \mathbf{P}_{2ij}^2 + \mathbf{P}_{3ij}^2}{\sigma^2} \right) & \dots & -\mathbf{P}_{3ij} \exp \left(-\frac{\mathbf{\Xi}_{ij}^2 + \mathbf{P}_{1ij}^2 + \mathbf{P}_{2ij}^2 + \mathbf{P}_{3ij}^2}{\sigma^2} \right) \end{bmatrix}. \quad (14)$$

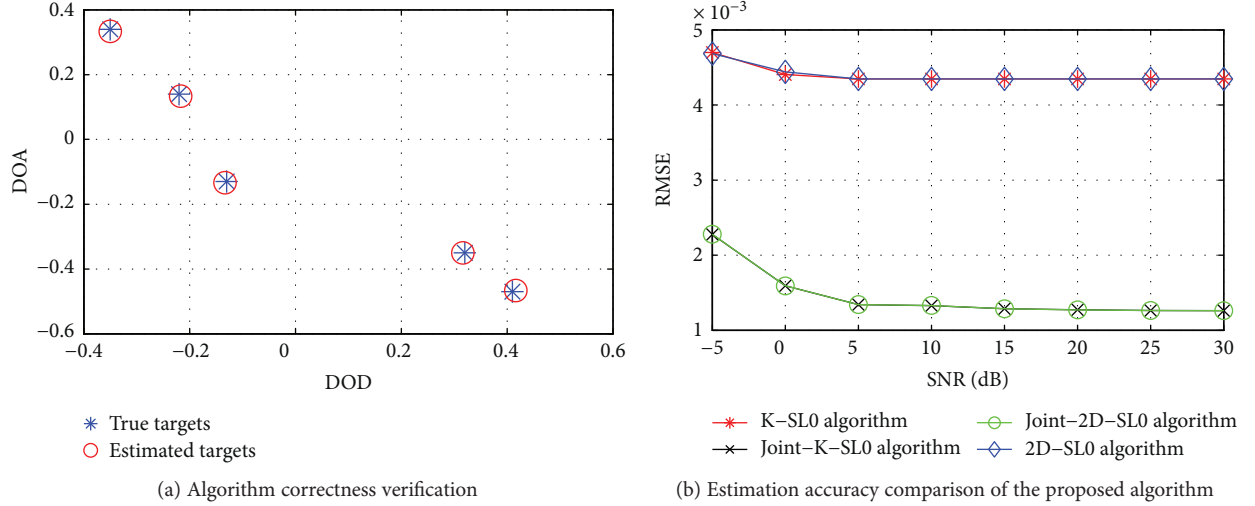


FIGURE 1: The estimation performance of the proposed algorithms.

Remark 3. The initial value our algorithm is the minimum L_2 norm solution of $\mathbf{Y} = \begin{bmatrix} \Phi_{\mathbf{R}} & \Phi_{\mathbf{R}}' \end{bmatrix} \begin{bmatrix} \Xi^l & \mathbf{P}_2^l \\ \mathbf{P}_1^l & \mathbf{P}_3^l \end{bmatrix} \begin{bmatrix} \Phi_{\mathbf{T}} & \Phi_{\mathbf{T}}' \end{bmatrix}^T + \mathbf{Z}$, which corresponds to $\sigma \rightarrow \infty$. And the specific proof can refer to [15].

Remark 4. Having initiated the algorithm with the minimum L_2 norm solution (which corresponds to $\sigma \rightarrow \infty$), the next value for σ (i.e., σ_1) may be about 6 to 12 times of the maximum absolute value of the obtained sources. Here, we select $\sigma_1 > 8 \max_{i,j} |\mathbf{W}_{i,j}|$. To see the reason, if we take, for example, $\sigma_1 > 8 \max_{i,j} |\mathbf{W}_{i,j}|$, then $\exp((\Xi_{1i,j}^2 + \mathbf{P}_{1i,j}^2 + \mathbf{P}_{2i,j}^2 + \mathbf{P}_{3i,j}^2) / \sigma^2) > 0.93 \approx 1$ for all i and j . And it shows that this value of σ acts virtually like infinity for all the values of $(\Xi_{1i,j}^2 + \mathbf{P}_{1i,j}^2 + \mathbf{P}_{2i,j}^2 + \mathbf{P}_{3i,j}^2)^{0.5}$.

Remark 5. The smallest value of σ should be about three to six times of (a rough estimation of) the standard deviation of this noise. This is because, while σ is in this range, the cost function treats small (noisy) samples as zeros (i.e., for which $\exp((\Xi_{1i,j}^2 + \mathbf{P}_{1i,j}^2 + \mathbf{P}_{2i,j}^2 + \mathbf{P}_{3i,j}^2) / \sigma^2) \approx 1$). However, below this range, the algorithm tries to “learn” these noisy values and moves away from the true answer.

Remark 6. The sequence of σ is always chosen as a decreasing geometrical sequence $\sigma_j = c\sigma_{j-1}$, $j \geq 2$, which is determined by the first and last elements, σ_1 and σ_J , and the scale factor c . In our simulation, for increasing the speed, we set $J = 100$. So $c = (\sigma_J / \sigma_1)^{1/J}$.

4. Simulation Results

In this section, we conduct several simulation experiments to verify the performance of the proposed model and algorithm.

In the first simulation, we show the correctness of the proposed Joint-2D-SL0 algorithm. Assume there are 5

targets, their normalized DOA and DOD are $[0.34, 0.14, -0.13, -0.35, \text{ and } -0.47]$ and $[-0.35, -0.22, -0.13, 0.32, \text{ and } 0.41]$, respectively. There are 20 transmitters and 20 receivers. The grid number of DOD and DOA is 60 and 60, respectively. The noise is white Gaussian noise. And the SNR is 20 dB. The input parameters are $\sigma_{\min} = 0.1$, $J = 100$, $\mu = 2$, and $L = 3$. The result is shown in Figure 1(a). We can see that the proposed Joint-2D-SL0 algorithm can accurately estimate the parameters of the target which verifies the correctness of the proposed algorithm.

Then, we compare the estimation accuracy of the proposed Joint-2D-SL0 algorithm with the estimation accuracy of Joint-K-SL0 algorithm (solving (5) using Kronecker compressive sensing method) and K-SL0 algorithm (solving (2) using Kronecker compressive sensing method) and 2D-SL0 algorithm (solving (2) using the method in [9]). The SNR varies from -5 dB to 30 dB. And the other parameters remain the same. 200 times simulation is conducted in each SNR. The simulation result is in Figure 1(b). We can see that the estimation error of the proposed model decreases significantly with the increase of SNR while the estimated error of the traditional model does not decrease when the SNR is bigger than 0 dB. That is because when $\text{SNR} > 0$ dB, the estimation error of traditional model is mainly affected by the grid mismatch problem. And the increase of SNR will not bring accuracy improvement. So the proposed off-grid model has a better performance than the model without considering grid mismatch problem which proves the validity of the proposed model. From Figure 1(b), we can see that the estimation accuracy of standard 2D-SL0 is similar with the estimation accuracy of K-SL0 algorithm. And their estimation accuracy is much lower than the estimation accuracy of Joint-2D-SL0. We also can see that the proposed Joint-2D-SL0 algorithm has a similar performance with Joint-K-SL0 algorithm which verifies the effectiveness of the proposed algorithm.

In the third simulation, we compare the running time of these algorithms. For the convenience of comparison, we conduct two kinds of contrast experiment. In the first

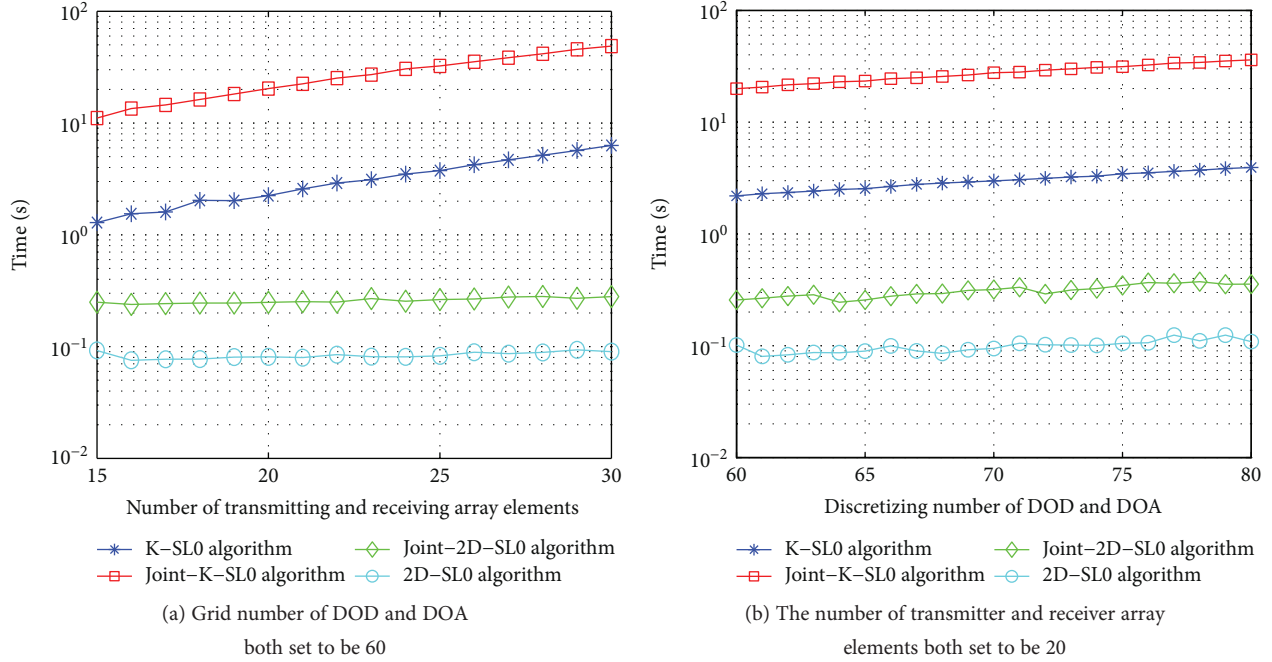
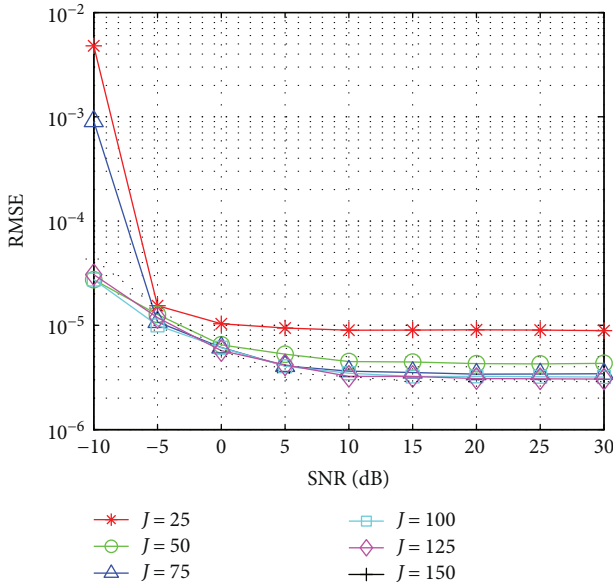


FIGURE 2: Runtime comparison of algorithm.

FIGURE 3: Comparison of different J .

comparative experiment, we set the grid number of DOD and DOA both to be 60, the number of transmitter and receiver elements is set to the same value which varies from 15 to 30. And the result is shown in Figure 2(a). In the second comparative experiment, the number of transmitter and receiver elements is both set to be 20 while the grid number of DOD and DOA is set to the same value which varies from 60 to 80. And the result is shown in Figure 2(b). The other simulation parameters are the same with the first simulation. We can see that the runtime of the proposed 2D algorithm is the fastest algorithm compared with the K-

SL0 and Joint-K-SL0 algorithms in the two contrast simulation. And the runtime increasing tendency of the proposed 2D method is the lowest compared with the runtime increasing tendency of the other two algorithms which proves the efficiency of the proposed Joint-2D-SL0 algorithm. From Figure 2, we can see that the runtime of standard 2D-SL0 is shorter than that of Joint-2D-SL0. But the estimation accuracy of standard 2D-SL0 is much lower than that of Joint-2D-SL0, so we can say that the proposed Joint-2D-SL0 algorithm can get high estimation accuracy with acceptable computation complexity.

In the fourth experiment, to show the affection of the number of iterations, we set $J=25, 50, 75, 100, 125,$ and $150,$ respectively. The other parameters are same with the second experiment. And the result is shown in Figure 3. From this figure, we can see that the estimation accuracy improved with the increase of J . However, when J reaches to a certain number, the estimation accuracy remains constant and does not increase anymore. So, the optimal choice of J depends on the application. When SNR is the essential criterion, J should be chosen large, but this will result in a higher computational cost. Therefore, the choice of J is a trade-off between SNR and computational cost.

5. Conclusion

In this paper, we propose the joint sparse matrix reconstruction model based on the one-order Taylor expansion and it can overcome the grid mismatch problem efficiently. Then, we put forward the Joint-2D-SL0 algorithm to solve the joint sparse matrix reconstruction problem. Our algorithm can get high estimation accuracy with acceptable computational complexity. Simulation experiences verify the effectiveness of the proposed model and algorithm.

Conflicts of Interest

The authors declare that they have no conflicts of interest.

Acknowledgments

This work was supported by the National Natural Science Foundation of China under Grants 61571459, 61372166, and 61701526.

References

- [1] D. L. Donoho, "Compressed sensing," *IEEE Transactions on Information Theory*, vol. 52, no. 4, pp. 1289–1306, 2006.
- [2] E. J. Candes, J. Romberg, and T. Tao, "Robust uncertainty principles: exact signal reconstruction from highly incomplete frequency information," *IEEE Transactions on Information Theory*, vol. 52, no. 2, pp. 489–509, 2006.
- [3] E. J. Candes and J. Romberg, "Quantitative robust uncertainty principles and optimally sparse decompositions," *Foundations of Computational Mathematics*, vol. 6, no. 2, pp. 227–254, 2006.
- [4] Z. Dornooosh and A. K. Ashraf, "Low rank and sparse matrix reconstruction with partial support knowledge for surveillance video processing," in *2013 IEEE International Conference on Image Processing*, pp. 335–339, Melbourne, VIC, Australia, 2013.
- [5] K. Anastasios and C. Volkan, "MATRIX ALPS: accelerated low rank and sparse matrix reconstruction," in *2012 IEEE Statistical Signal Processing Workshop (SSP)*, pp. 185–188, Ann Arbor, MI, USA, 2012.
- [6] X. Y. Cui, J. Z. Huang, S. T. Zhang, and D. N. Metaxas, "Background subtraction using low rank and group sparsity constraints," in *European Conference on Computer Vision*, pp. 612–625, Springer, Berlin, Heidelberg, 2012.
- [7] Y. Liu, M. Y. Wu, and S. J. Wu, "Fast OMP algorithm for 2D angle estimation in MIMO radar," *Electronics Letters*, vol. 46, no. 6, p. 444, 2010.
- [8] W. Feng, X. Y. He, Y. S. Zhang, and Y. D. Guo, "2D OMP algorithm for space-time parameters estimation of moving targets," *Electronics Letters*, vol. 51, no. 22, pp. 1809–1811, 2015.
- [9] A. Ghaffari, M. Babaie-Zadeh, and C. Jutten, "Sparse decomposition of two dimensional signal," in *2009 IEEE International Conference on Acoustics, Speech and Signal Processing*, pp. 3157–3160, Taipei, Taiwan, April 2009.
- [10] M. J. Jahromi and M. H. Kahaei, "Two-dimensional iterative adaptive approach for sparse matrix solution," *Electronics Letters*, vol. 50, no. 1, pp. 45–47, 2014.
- [11] Z. Tan and A. Nehorai, "Sparse direction of arrival estimation using co-prime arrays with off-grid targets," *IEEE Signal Processing Letters*, vol. 21, no. 1, pp. 26–29, 2014.
- [12] Y. Chi, L. L. Scharf, A. Pezeshki, and A. R. Calderbank, "Sensitivity to basis mismatch in compressed sensing," *IEEE Transactions on Signal Processing*, vol. 59, no. 5, pp. 2182–2195, 2011.
- [13] Z. Tan, P. Yang, and A. Nehorai, "Joint sparse recovery method for compressed sensing with structured dictionary mismatches," *IEEE Transactions on Signal Processing*, vol. 62, no. 19, pp. 4997–5008, 2014.
- [14] A. Bacci, D. Staglianò, E. Giusti, S. Tomei, F. Berizzi, and M. Martorella, "Compressive sensing for interferometric inverse synthetic aperture radar applications," *IET Radar, Sonar & Navigation*, vol. 10, no. 8, pp. 1446–1457, 2016.
- [15] H. Mohimani, M. Babaie-Zadeh, and C. Jutten, "A fast approach for overcomplete sparse decomposition based on smoothed ℓ^0 norm," *IEEE Transactions on Signal Processing*, vol. 57, no. 1, pp. 289–301, 2009.

Research Article

Ocean Surface Current Observation with a Dual Monopole-Cross-Loop Antenna Array

Yeping Lai, Hao Zhou, Yuming Zeng, and Biyang Wen

School of Electronic Information, Wuhan University, Wuhan 430072, China

Correspondence should be addressed to Hao Zhou; zhou.h@whu.edu.cn

Received 21 July 2017; Revised 7 November 2017; Accepted 22 November 2017; Published 18 December 2017

Academic Editor: Amerigo Capria

Copyright © 2017 Yeping Lai et al. This is an open access article distributed under the Creative Commons Attribution License, which permits unrestricted use, distribution, and reproduction in any medium, provided the original work is properly cited.

The high-frequency radars (HFRs) receiving the sea echoes backscattered from the fluctuating ocean surface to remotely sense ocean surface currents are a popular and powerful tool in oceanic observation. Dominant error source in current measurement for HFR systems has been recognized to be the direction of arrival (DOA) determination of the sea echoes. To eliminate this error and therefore improve the performance of direction-finding HFR system in current measurement, we have investigated a dual monopole-cross-loop (MCL) antenna array in current observation. Simulations indicated that the dual MCL antenna array has a better performance than the conventional single MCL antenna system in current mapping, especially for the complex current profile. And comparisons of radar field data and buoy measurements suggested that the *RMSE* value was larger than 15 cm/s for the conventional MCL antenna. But it decreased to 12.64 cm/s for the dual MCL antenna array. Moreover, the temporal coverage rate also showed the benefit of using this antenna system in current mapping. The results demonstrated that it is advisable to adopt the dual MCL antenna array in operational applications.

1. Introduction

The HFRs operating at a frequency range of 3 MHz to 30 MHz have been extensively used to provide ocean surface current in real time [1]. These radars may sense current velocity up to a range of 300 km from the shore relying on the parameters of the radar configuration. And the data products derived from these radars can be used in many fields, including oceanographic and meteorological researches, monitoring the dispersal of pollution and other floating objects, as well as coastal and harbor management.

The current observation HFRs can be roughly divided into two types based on the method employed to determine the bearing of the radial currents: beam forming (e.g., WERA [2]) and direction finding (e.g., CODAR [3] and OSMAR-S [4, 5]). Beam forming radars electronically steer a linear phased array of receiving antennas toward a patch of the ocean surface. This type of radar can provide an excellent angular resolution to separate the sea echoes scattered from different patch efficiently but with a cost of occupying a large space in practice, while the direction-finding method is usually adopted by transportable radar systems, which are

equipped with a MCL antenna comprising one monopole and two loops [6]. These radars exploit the directional properties of the conventional MCL antenna to determine bearing using the multiple signal classification (MUSIC) [7] algorithm. Because of the small size, this type of HFR has been widely used across the world.

Many studies of HFR surface current measurements have validated the capacity of the direction-finding HFR to remote sensing the ocean surface currents through comparisons with in situ current measurements, such as [8–12]. These studies demonstrated that there is a 7–20 cm/s differences between the current measurements derived from the direction-finding HFRs and those from the in situ instrument. And the DOA determination error is the dominant contributor to these differences.

To alleviate the DOA determination error and improve the performance of direction-finding HFR system in current measuring, a dual MCL antenna array, composed of two MCL elements, was investigated in this study. Because of the special structure of this antenna system, only the MUSIC direction-finding algorithm can be used to determine the DOA of the sea echoes. Thus, the relationship between the

DOA estimation performance and the relative position of the two MCL elements was investigated, and we found that the spacing between the two antenna elements is not limited to the conventional half-wavelength condition due to the amplitude directional properties of the MCL element. And the simulation results suggested that the dual MCL antenna array has a better performance than the conventional single MCL antenna in current measuring, especially for the complex current pattern. Moreover, this performance improvement of the dual MCL antenna array relative to the conventional MCL antenna is also confirmed by the field experiment.

2. Dual Monopole-Cross-Loop Antenna Array

A MCL antenna array is composed of multiple MCL antenna elements. And a MCL antenna element consists of a monopole and two orthogonal loops. The antenna pattern of the MCL antenna element can be expressed as

$$\begin{aligned} a_1(\theta) &= 1, \\ a_2(\theta) &= \cos \theta, \\ a_3(\theta) &= \sin \theta, \end{aligned} \quad (1)$$

where a_1 , a_2 , and a_3 represent the monopole and the two loops. Thus, the steering vector for signal coming from the direction of θ is $\mathbf{A}(\theta) = [a_1(\theta), a_2(\theta), a_3(\theta)]^T$. On the other hand, the steering vector for uniform linear array consisting of identical omnidirectional element with a spacing of d can be given as

$$\mathbf{A}_u(\theta) = [1, e^{j\beta(\theta)}, e^{j2\beta(\theta)}, \dots, e^{j(m-1)\beta(\theta)}]^T, \quad (2)$$

where m is the number of antenna elements; $\beta(\theta) = -2\pi d \sin \theta / \lambda$ is the phase shift for adjacent elements; and λ is the wavelength. Actually, the MCL antenna array is a synthesis of the MCL antenna and the linear antenna array. Thus, the steering vector of this hybrid array can be written as

$$\mathbf{A}_v(\theta) = [\mathbf{A}^T(\theta), e^{j\beta(\theta)} \mathbf{A}^T(\theta), e^{j2\beta(\theta)} \mathbf{A}^T(\theta), \dots, e^{j(m-1)\beta(\theta)} \mathbf{A}^T(\theta)]^T. \quad (3)$$

For a dual MCL array, the steering vector can be reduced to

$$\begin{aligned} \mathbf{A}_D(\theta) &= [\mathbf{A}^T(\theta), e^{j\beta(\theta)} \mathbf{A}^T(\theta)]^T \\ &= [1, \cos \theta, \sin \theta, e^{j\beta(\theta)}, e^{j\beta(\theta)} \cos \theta, e^{j\beta(\theta)} \sin \theta]^T. \end{aligned} \quad (4)$$

The amplitude directional properties denoted by $\mathbf{A}_u^T(\theta)$ in (3) and (4) result in the difference between MCL array and the conventional uniform linear array. In conventional uniform linear array, the spacing, d , must be no more than half wavelength. If the spacing goes against this criterion, there will be ambiguity in DOA determination, because the condition leading to ambiguity is $\mathbf{A}_u(\theta) = \mathbf{A}_u(\theta')$ with

$\theta \in [-90^\circ, 90^\circ]$, $\theta' \in [-90^\circ, 90^\circ]$, and $\theta \neq \theta'$, that is, $e^{jn\beta(\theta)} = e^{jn\beta(\theta')}$, with n being an integer. Thus, the ambiguity condition is equivalent to

$$\beta(\theta) - \beta(\theta') = \frac{2\pi d \sin \theta}{\lambda} - \frac{2\pi d \sin \theta'}{\lambda} = 2k\pi, \quad (5)$$

where k is an integer. And it is straightforward to rewrite (5) as

$$\frac{d}{\lambda} = \frac{k}{\sin \theta - \sin \theta'}. \quad (6)$$

If the absolute value of the right side in (6) is larger than 0.5, d/λ being smaller than 0.5 will result in no solutions for θ and θ' in (6), that is, no ambiguity in DOA determination. On the contrary, if d/λ is more than 0.5, the ambiguity will appear. Therefore, the spacing of adjacent element in conventional uniform linear array has to be no more than half wavelength for avoiding ambiguity in DOA estimation. But this is not the case for the MCL array. The ambiguity condition for MCL array is $\mathbf{A}_v(\theta) = \mathbf{A}_v(\theta')$, which is equivalent to simultaneously satisfy the following:

$$\begin{aligned} e^{jn\beta(\theta)} &= e^{jn\beta(\theta')}, \\ \mathbf{A}(\theta) &= \mathbf{A}(\theta'), \\ \theta &\in [0^\circ, 360^\circ], \\ \theta' &\in [0^\circ, 360^\circ], \\ \theta &\neq \theta'. \end{aligned} \quad (7)$$

Clearly, there is no θ and θ' satisfying (7) due to the presence of $\mathbf{A}(\theta) = \mathbf{A}(\theta')$, so there is no ambiguity in DOA estimation even for arbitrary spacing of the adjacent elements and for 360-degree look angle space.

But the performance of direction-finding algorithm is always related to the configuration of the antenna array, so that investigation of the effects of the number of elements and the spacing of the MCL array on DOA estimation in terms of MUSIC direction-finding algorithm is significant. In fact, Stoica and Nehorai [13] have proven that the estimated DOA, $\hat{\theta}$, in MUSIC for arbitrary antenna system is a Gaussian distribution with a mean value being equal to the actual DOA, θ , and the variance given by

$$\text{var}(\hat{\theta}) = \frac{1}{2N \cdot \text{SNR} \cdot h(\theta)} \left[1 + \frac{\mathbf{b}^H(\theta) \mathbf{b}(\theta)}{\text{SNR}} \right], \quad (8)$$

where θ is the actual DOA of the incident signal; $\mathbf{b}(\theta)$ is the steering vector; N is the number of samples; SNR is signal-to-noise ratio; and $h(\theta) = \mathbf{d}^H(\theta) \{ I - \mathbf{b}(\theta) [\mathbf{b}^H(\theta) \mathbf{b}(\theta)]^{-1} \mathbf{b}^H(\theta) \} \mathbf{d}(\theta)$ with $\mathbf{d}(\theta) = d\mathbf{b}(\theta)/d\theta$. Thus, in the case of a MCL array composed of m identical MCL elements with a uniform spacing of d , we have $\mathbf{b}(\theta) = \mathbf{A}_v(\theta)$ and $\mathbf{d}(\theta) = d\mathbf{A}_v(\theta)/d(\theta)$, which gives

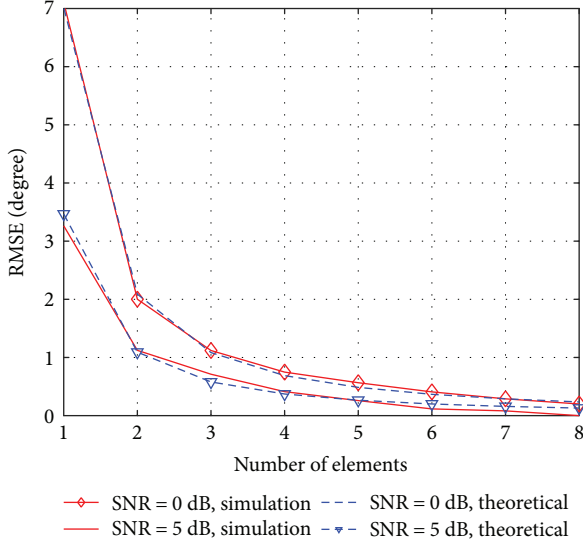


FIGURE 1: The root-mean-square error (RMSE) of the DOA estimation versus the number of antenna element with the signal coming from 30° and the spacing between adjacent elements being equal to half wavelength.

$$\text{var}^v[\hat{\theta}] = \frac{1}{2N \cdot \text{SNR}} \times \left(1 + \frac{1}{2m \cdot \text{SNR}}\right) \times \left[\frac{6}{6m + m(m^2 - 1)} [\beta'(\theta)]^2 \right], \quad (9)$$

where $\beta'(\theta) = d\beta(\theta)/d\theta = 2\pi d \cos \theta / \lambda$. Figure 1 shows the DOA estimation error varying with the number of the MCL elements. The simulation results shown in this figure are achieved by a Monte-Carlo simulation of 300 independent runs with 50 snapshots for each trial, while the theoretical results are directly calculated by (9) with the same parameters used in the simulation. To make the unit of the results obtained from (9) being the same as the unit of the DOA, the square root of the the variance (standard deviation), which is equal to the root-mean-square error due to the mean value of the DOA estimation error being zero, is used in Figure 1. These results displayed in Figure 1 indicate that the DOA estimation error decreases with the antenna element increases expectedly. Besides, the rate of the decrease gradually slows down and, eventually, the DOA estimation accuracy levels off at almost the same level for different signal-to-noise ratio (SNR). Taking the occupation of space of an antenna system into consideration, we suggest that an MCL antenna array composed of two or three MCL elements is an optimal scheme in practice. But in this study, we only focus on dual MCL antenna array composed of only two MCL elements.

In the case of the dual MCL antenna array, (9) can be reduced to

$$\text{var}^D[\hat{\theta}] = \frac{1}{2N \cdot \text{SNR}} \times \left(1 + \frac{1}{4 \cdot \text{SNR}}\right) \times \left[\frac{1}{2 + (2\pi d \cos \theta / \lambda)^2} \right]. \quad (10)$$

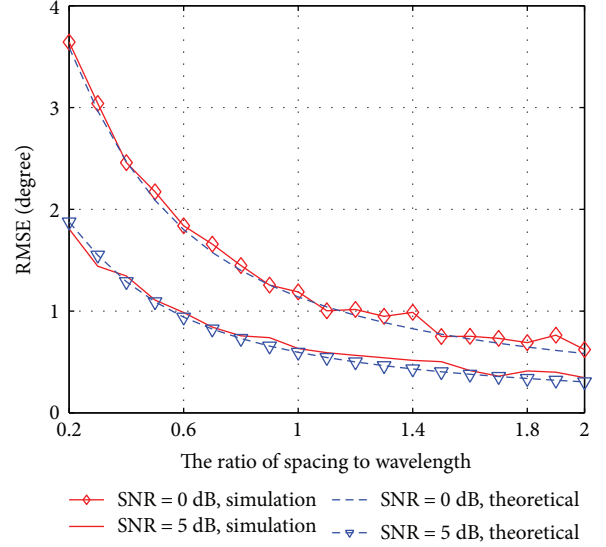


FIGURE 2: The RMSE value of the DOA estimation versus the spacing in dual MCL antenna array with signal coming from 30° .

In the foregoing analysis, we have concluded that the spacing for the MCL array can be arbitrary value. Thus, discussing the effect of the spacing on the DOA estimation performance for the dual MCL array is necessary. Figure 2 shows the RMSE value of the DOA estimation varying with the spacing. The simulation results are obtained from Monte-Carlo simulation with the same independent runs and snapshots as in Figure 1. The theoretical results are computed as (10). From this figure, we can clearly see that the RMSE values decrease with the spacing increase. But the decrease is very limited especially for a high SNR. These results guide us that the spacing can be relaxed, and the deployment of the dual MCL antenna array is relatively convenient for real applications. In this study, the parameter of this spacing was set to be equal to the wavelength. With this setting, Figure 3 shows the comparison of the DOA estimation performance between the dual MCL antenna array and the conventional single MCL antenna system. The performance of the conventional single MCL antenna system can be expressed as

$$\text{var}^C[\hat{\theta}] = \frac{1}{2N \cdot \text{SNR}} \times \left(1 + \frac{1}{2 \cdot \text{SNR}}\right). \quad (11)$$

Comparing (11) with (10), we can clearly know that $\text{var}^C[\hat{\theta}]$ is always more than $\text{var}^D[\hat{\theta}]$, which indicates that the performance of the dual MCL array is superior to the single MCL antenna. And Figure 3, showing the DOA estimation error for dual and single MCL antenna system, also clearly indicates this result. Thus, using two MCL antenna elements to jointly observe sea surface current is an advisable scheme.

3. Ocean Surface Current Extraction

3.1. *Extraction Current Mappings with MUSIC Algorithm.* To obtain the current velocity mappings, radar signal processing

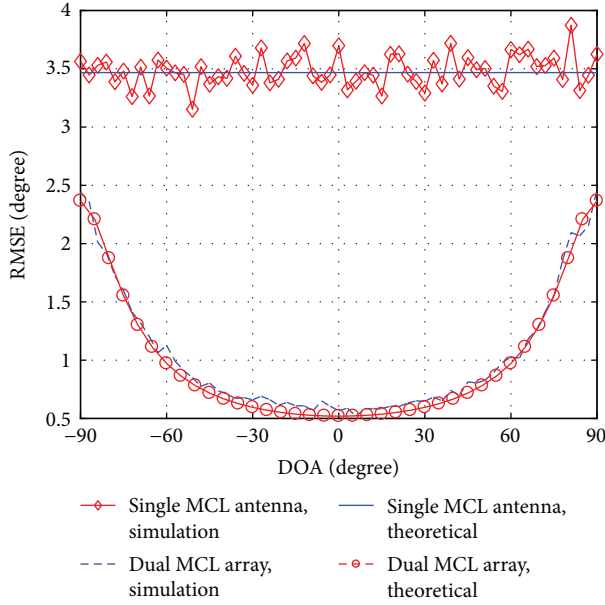


FIGURE 3: DOA estimation errors for the conventional single MCL antenna and the dual MCL antenna array vary with the DOA with a signal to noise ratio of 5 dB.

involves the resolving of the range, Doppler, and direction of arrival (DOA) of the backscattered signals. The time delay of this backscattered signal is used to measure the distance of the patch to the radar, while the frequency difference between observed Doppler shift and expected position of the Bragg peaks is used to deduce the current velocity. The DOA is determined either by the MUSIC or the beam forming. But only the MUSIC is able to address the DOA of the sea echo received by a conventional or dual MCL antenna system due to the special geometry of the antenna system.

The DOA estimation using MUSIC was introduced by Schmidt [7]. This method determines a noise space via diagonalizing the covariance matrix formed from the multichannel signals, and it determines the signal bearing by finding the smallest projection of the steering vectors on that noise space. For the conventional MCL antenna, the covariance matrix is formed from the signals received by the monopole and the two loops, while the covariance matrix is derived from the two MCL antenna array for the dual MCL antenna system. After diagonalizing the covariance matrix, we have to determine the number of sources involved in current samples. Barrick and Lipa [14, 15] have proposed a hypothesis-testing method to determine the number of sources for the conventional MCL antenna system. In this study, we also use this hypothesis-testing method to determine the number of sources when we extract current mappings in conventional MCL antenna system with the three parameters: eigenvalue ratio, signal power ratio, and diagonal ratio, being 40, 20, and 3, respectively. Extraction current mappings involved in dual MCL array also use the way of hypothesis testing to determine the number of sources. We first test the number of sources of three with the same approach

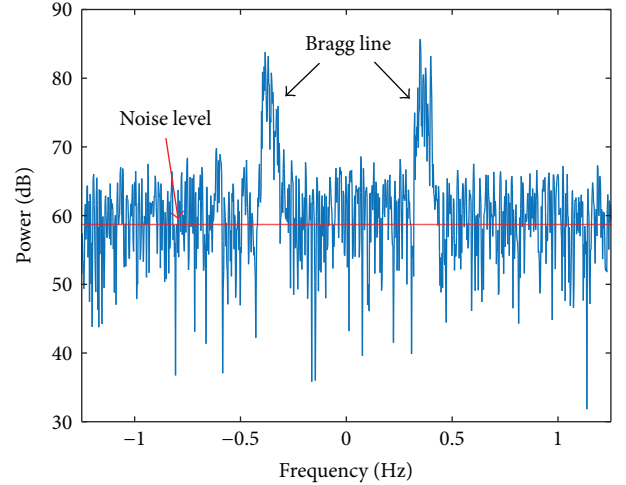


FIGURE 4: An example of the Doppler spectrum for monopole channel in the simulations.

used in the conventional MCL antenna system with the three parameters: eigenvalue ratio, signal power ratio, and diagonal ratio, being 50, 20, and 2, respectively. If this testing indicates that the number of sources is not three, we then do testing the number of sources of two with the same approach and parameters involved in the conventional MCL antenna system. If this testing of two sources also indicates that the number of sources is not two, we regard these samples as single source in DOA estimation process.

3.2. Simulation on Current Retrieval. To validate the performance improvement of this antenna array to the conventional MCL antenna, we carried out simulations on retrieving current velocities and compared the performance of these two antenna systems. These simulations generated the complex time series for each antenna channel received from a range cell (which is a circular annulus defined by the range from the radar) based on the method adopted by Wang and Gill [16]. Practically, these time series are induced by backscatter from the sea due to the first-order Bragg scattering. In this study, we investigated three radial current scenarios in this range cell: a uniform current flowing parallel to shore (which is a representation of single DOA for any current velocity), a parabola-shaped current (which involves dual DOAs for some current velocity), and a current jet superimposed with a uniform parallel-to-shore current (which implies three DOAs for some current velocity). In addition, we assumed a uniform parallel-to-shore wind and its speed, duration, and fetch were assumed to be sufficient for fully developed Bragg scattering waves having a broad cardioid directional distribution of spectral energy [17]. The additive Gaussian noise was added to these time series with an SNR of 20 dB (defined as the ratios of the Bragg lines power to the noise level, say Figure 4). Then, a Doppler spectrum is obtained by performing FFT on each time series. An example of the Doppler spectrum in our simulation is shown in Figure 4.

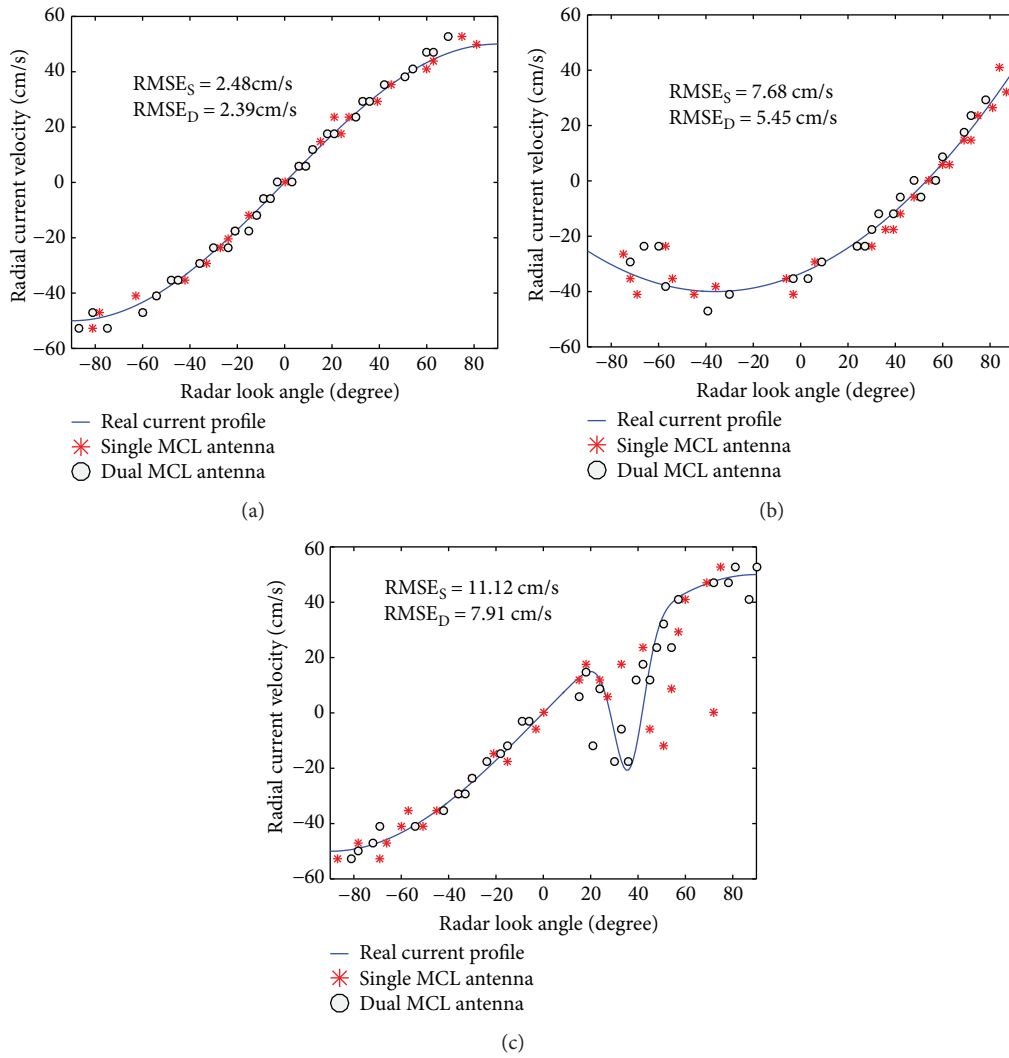


FIGURE 5: Examples of the radial current profiles (solid line) with measurements from conventional single MCL antenna (star) and those from dual MCL antenna array (circle). The $RMSE_S$ and $RMSE_D$ are the RMSE values of current comparison results for conventional single MCL antenna and the dual MCL antenna array, respectively.

For each radial current profile scenarios, we performed 100 independent runs for both single MCL antenna and dual MCL antenna systems. The indicator of the root-mean-square error (RMSE) was adopted to assess the accuracy of the retrieved radial current velocities. Examples for the mentioned three current profiles and the estimated radial currents, as well as the RMSE values for all the 100 runs, are shown in Figure 5. From this figure, we can conclude that the dual MCL antenna configuration has a better performance than the conventional single MCL antenna system in current mapping, especially for the complex current profile. Surely, the current pattern displayed in Figure 5(c) is unfair for the conventional MCL antenna system because the current velocities ranging -20 cm/s to 10 cm/s have three DOAs, which is beyond the angular solving capacity of single MCL element. Fortunately, this scenario is rare encounter in practice, so that the conventional single MCL antenna system can often retrieve acceptable current mappings. But this scenario, sometimes, may indeed be present in reality.

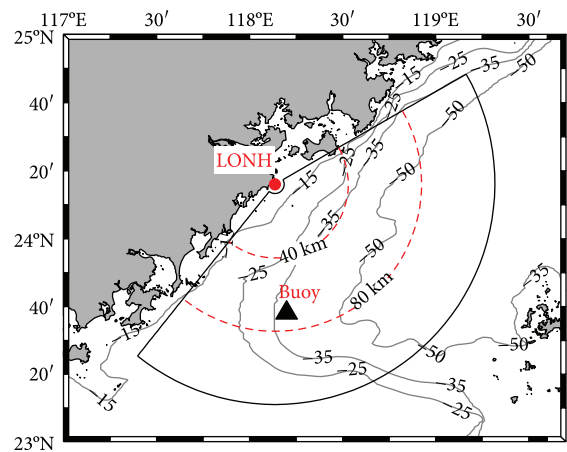


FIGURE 6: Map of the deployment of the radar (red dot) and the buoy (black triangle). The buoy is at a distance about 75 km from the radar site. The gray thin lines are the isobaths. The fanwise area denotes the radar detection region.

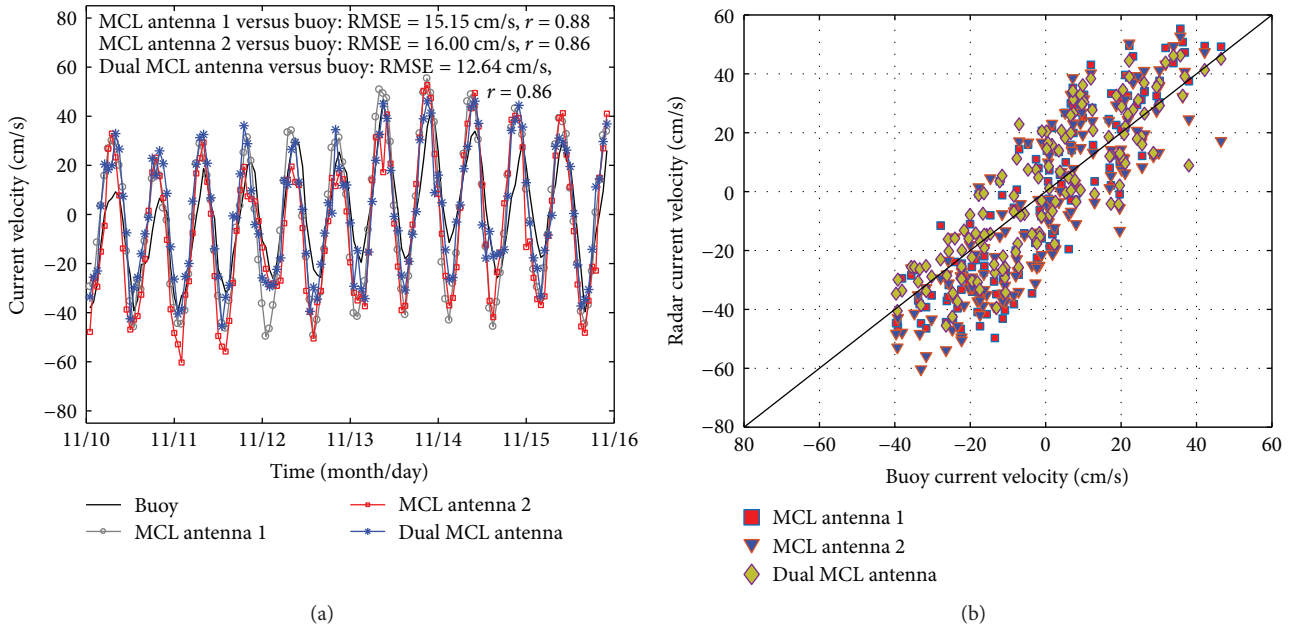


FIGURE 7: Radial current velocity comparisons. (a) Time series of the buoy-derived radial current velocity and that derived by LONH radar site with the MCL antenna 1, MCL antenna 2, and the dual MCL antenna system. Statistics, correlation coefficient (r), and root-mean-square error ($RMSE$) of each radar-ADCP current comparison pairs are shown on the top of (a). (b) Scatter plot of the radial current velocities.

4. Field Data Evaluation

To assess the performance improvement of the dual MCL antenna system for practical radial current velocity retrieval, a field experiment was conducted in November 2015. In the experiment, an Ocean State Measuring and Analyzing Radar type S (OSMAR-S) radar system was deployed on the coast of Fujian province, China, as illustrated in Figure 6. The radar emitted a frequency-modulated interrupting continuous waveform (FMICW) signal toward the ocean surface with a center frequency of 13 MHz. The bandwidth of the radar was 60 kHz which theoretically produced a 2.5 km range resolution. Two MCL antennas with a spacing equaling to the wavelength of the radar-transmitted signal were set for receiving the echo scattered from the ocean surface. Thus, we could simultaneously sample the sea echoes in six channels. And both the first three channels (antenna 1) and the rest three channels (antenna 2) are a conventional MCL antenna, which is able to extract the ocean surface maps. The samples in these channels were collected at an interval of 0.54 s. And a 512-point FFT was performed on these samples to yield a coherent integration time of about 276.5 s or a current velocity resolution of 4.1 cm/s.

The in situ measurements used in this study were from a buoy-mounted acoustic Doppler current profile (ADCP). The location of the buoy is about 75 km away from the radar site (Figure 6). This single-point ADCP provided current velocity every 10 minutes with a velocity resolution of 0.1 cm/s. The depth of the ADCP measurements used in this study is 6 meters under the water.

The radar-derived radial currents in this experiment for the two antenna configurations (one MCL antenna and dual MCL antenna array combining the two MCL antenna

elements) were compared with the buoy measurements. In the current extraction process, the ideal antenna patterns were used and the two MCL antennas have been calibrated independently on the basis of the geometrical relationship for the three-channel collocated MCL antenna [3]. For the dual MCL antenna array, the channel errors between the two MCL antenna elements were also calibrated using known sources. The radial currents derived by single MCL antenna and dual MCL antenna are shown in Figure 7 where comparison statistics are also provided. Comparison of the radial currents derived from antenna 1 and antenna 2 with the ADCP measurements yields $RMSE$ values of 15.15 cm/s and 16.00 cm/s, respectively. While the $RMSE$ value for the radial current velocities derived from the dual MCL antenna configuration reduces to 12.64 cm/s. This really suggests the improvement of the dual MCL antenna system to the single MCL antenna. However, the correlation coefficient between the dual MCL antenna deduced radial currents and those observed by ADCP is nearly the same with that of either of the single MCL antennas.

Another indicator of the quality of the radial currents extracted from HF radar is the temporal coverage rate. The spatial distributions of the temporal coverage rates for radial currents derived from antenna 1, antenna 2, and dual MCL antenna are achieved and shown in Figure 8. These temporal coverage rate maps are calculated for each radial sector as the total number of the valid radial current estimators divided by the total number of the radial current maps. From Figure 8, we can see an obvious consistency that the temporal coverage rate has a decrease with distance from the radar site origin. But the radial current derived from dual antenna with a temporal coverage rate greater than 0.6 extends to a much larger area than either that from single conventional MCL

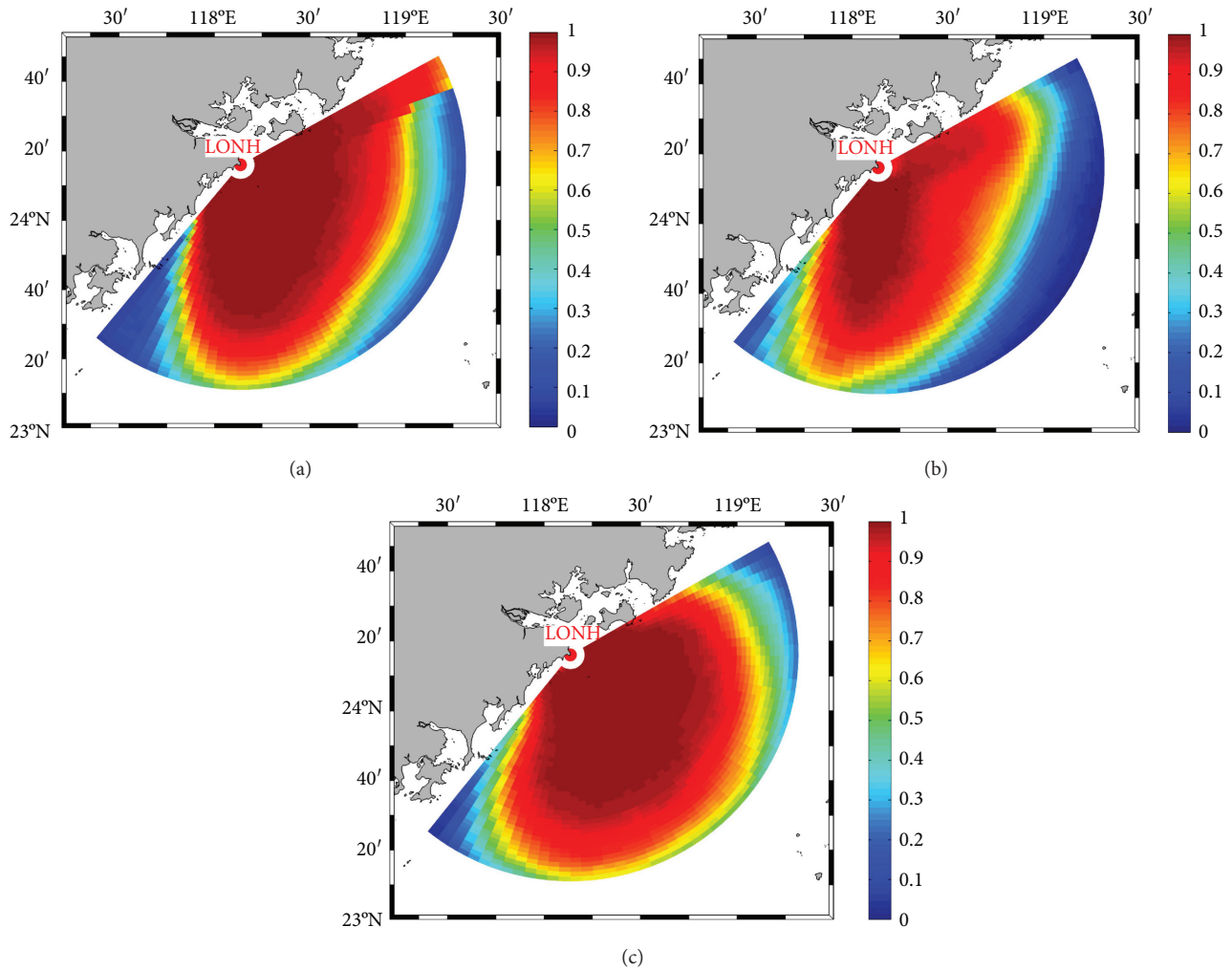


FIGURE 8: Temporal coverage rate of valid radial currents for LONH site with MCL antenna 1 (a), MCL antenna 2 (b), and dual MCL antenna system (c).

antennas. Thus, the quality of the ocean surface currents observed by a dual MCL antenna is really better than the conventional single MCL antenna system. Due to the fact that temporal coverage rate of the retrieved current maps is interested by the current-dataset user, using the dual MCL array to observe oceanic surface current field is an advisable approach.

5. Conclusions

In this study, we have investigated the performance improvement of the dual MCL antenna array to the conventional single MCL antenna. We analyzed the effects of the MCL antenna array parameters on DOA estimation. An analysis of pointing error related to the number of MCL elements shows that a MCL antenna array consisted of two or three MCL elements is an optimal scheme in practice. And the examination of the spacing between the MCL elements suggests that the spacing between the two antenna elements is permitted to exceed the conventional half wavelength limitation for the linear phased array. Simulation on current extraction for a dual MCL antenna array with wavelength

spacing indicates that this antenna system can improve the radar performance in current retrieval relative to the conventional single MCL antenna system, especially for the complex current profile. Moreover, this performance improvement has been validated by the field experiment. The results of the field experiment show that the RMSE value of the radial current retrieved by conventional single MCL antenna was larger than 15 cm/s with respect to the ADCP measurements, but it decreased to 12.64 cm/s when the dual MCL antenna array was adopted in current observation.

Conflicts of Interest

The authors declare that there is no conflict of interest regarding the publication of this paper.

Acknowledgments

This work was supported by the National Natural Science Foundation of China (NSFC) under Grant 61371198 and the National Special Program for Key Scientific Instrument and Equipment Development of China under Grant

2013YQ160793. The authors would like to thank the personnel of Wuhan Device Electronic Technology Co. Ltd. for carrying out the experiment.

References

- [1] J. D. Paduan and L. Washburn, "High-frequency radar observations of ocean surface currents," *Annual Review of Marine Science*, vol. 5, no. 1, pp. 115–136, 2013.
- [2] K. W. Gurgel, G. Antonischki, H. H. Essen, and T. Schlick, "Wellen radar (WERA): a new ground-wave HF radar for ocean remote sensing," *Coastal Engineering*, vol. 37, no. 3-4, pp. 219–234, 1999.
- [3] B. Lipa and D. Barrick, "Least-squares methods for the extraction of surface currents from codar crossed-loop data: application at ARSLOE," *IEEE Journal of Oceanic Engineering*, vol. 8, no. 4, pp. 226–253, 1983.
- [4] H. Zhou and B. Wen, *Portable High Frequency Surface Wave Radar OSMAR-S*, Springer International Publishing, Cham, 2015.
- [5] H. Zhou and B. Wen, "Wave height extraction from the first-order bragg peaks in high-frequency radars," *IEEE Geoscience and Remote Sensing Letters*, vol. 12, no. 11, pp. 2296–2300, 2015.
- [6] A. R. Carr, "Three-element antenna formed of orthogonal loops mounted on a monopole," US Patent 4,433,336, 1984.
- [7] R. Schmidt, "Multiple emitter location and signal parameter estimation," *IEEE Transactions on Antennas and Propagation*, vol. 34, no. 3, pp. 276–280, 1986.
- [8] S. Cosoli, A. Mazzoldi, and M. Gačić, "Validation of surface current measurements in the northern Adriatic sea from high-frequency radars," *Journal of Atmospheric and Oceanic Technology*, vol. 27, no. 5, pp. 908–919, 2010.
- [9] Y. Liu, R. H. Weisberg, and C. R. Merz, "Assessment of CODAR seasonde and WERA HF radars in mapping surface currents on the west Florida shelf," *Journal of Atmospheric and Oceanic Technology*, vol. 31, no. 6, pp. 1363–1382, 2014.
- [10] P. Lorente, S. Piedracoba, and E. A. Fanjul, "Validation of high-frequency radar ocean surface current observations in the NW of the Iberian peninsula," *Continental Shelf Research*, vol. 92, pp. 1–15, 2015.
- [11] A. Kalampokis, M. Uttieri, P. M. Poulain, and E. Zambianchi, "Validation of HF radar-derived currents in the Gulf of Naples with lagrangian data," *IEEE Geoscience and Remote Sensing Letters*, vol. 13, no. 10, pp. 1452–1456, 2016.
- [12] Y. Lai, H. Zhou, J. Yang, Y. Zeng, and B. Wen, "Submesoscale eddies in the Taiwan Strait observed by high-frequency radars: detection algorithms and eddy properties," *Journal of Atmospheric and Oceanic Technology*, vol. 34, no. 4, pp. 939–953, 2017.
- [13] P. Stoica and A. Nehorai, "MUSIC, maximum likelihood, and cramer-rao bound," *IEEE Transactions on Acoustics, Speech, and Signal Processing*, vol. 37, no. 5, pp. 720–741, 1989.
- [14] D. E. Barrick and B. J. Lipa, "Evolution of bearing determination in HF current mapping radars," *Oceanography*, vol. 10, pp. 72–75, 1997.
- [15] D. E. Barrick and B. J. Lipa, "Radar angle determination with MUSIC direction finding," US Patent 5,990,834, 1999.
- [16] W. Wang and E. W. Gill, "Evaluation of beamforming and direction finding for a phased array HF ocean current radar," *Journal of Atmospheric and Oceanic Technology*, vol. 33, no. 12, pp. 2599–2613, 2016.
- [17] M. S. Longuet-Higgins, "Observations of the directional spectrum of sea waves using the motions of a floating buoy," in *Ocean Wave Spectra: Proceedings of a Conference*, Prentice-Hall, pp. 111–136, 1961.

Research Article

Robust STAP for MIMO Radar Based on Direct Data Domain Approach

Cheng Chen,¹ Junjie He,² Zeshi Yuan,¹ Xiaohua Zhu,¹ and Hongtao Li¹

¹Nanjing University of Science and Technology, Nanjing, Jiangsu 210094, China

²The 28th Research Institute of China Electronics Technology Group Corporation, Nanjing 210094, China

Correspondence should be addressed to Xiaohua Zhu; njust_zxh@163.com

Received 3 August 2017; Accepted 18 October 2017; Published 23 November 2017

Academic Editor: Elisa Giusti

Copyright © 2017 Cheng Chen et al. This is an open access article distributed under the Creative Commons Attribution License, which permits unrestricted use, distribution, and reproduction in any medium, provided the original work is properly cited.

The detection performance of direct data domain (D^3) space-time adaptive processing (STAP) will be extremely degraded when there are mismatches between the actual and the presumed signal steering vectors. In this paper, a robust D^3 STAP method for multiple-input multiple-output (MIMO) radar is developed. The proposed method utilizes the worst-case performance optimization (WCPO) to prevent the target self-nulling effect. An upper bound for the norm of the signal steering vector error is given to ensure that the WCPO problem has an admissible solution. Meanwhile, to obtain better detection performance in the low signal-to-noise ratio (SNR) environment, the proposed method gives a modified objective function to minimize the array noise while mitigating the interferences. Simulation results demonstrate the validity of our proposed method.

1. Introduction

Space-time adaptive processing (STAP) is a key technology for airborne surveillance radar system to detect moving targets in a strong interference environment [1]. The working principles of STAP can be classified into two categories: statistical STAP and deterministic STAP (also known as direct data domain (D^3) STAP) [2–7]. In statistical STAP, the covariance matrices of the interference and the clutter environment are usually estimated from the target-free training data, which is collected from range cells adjacent to the range gate under test [2, 3]. To approach the adequate detection performance, the required amount of the training data is at least twice the STAP filter dimension [8]. However, in the scenarios where the ranges of the interferences change fast or the clutters are nonhomogeneous in the target-free training data, the statistical characteristics of the interference environment are difficult to be precisely estimated. To cope with the aforementioned problems, some methods based on the D^3 approach are given in [5–7]. The D^3 approach can minimize the interference power while preserving unit gain for the target in a coherent processing interval (CPI). In the

D^3 approach, the target signal is firstly removed from the received signal to remain the contributions of the interferences. However, in the practical application, there are mismatches between the actual and the presumed signal steering vectors due to the direction of arrival (DOA) and Doppler frequency errors, imperfect array calibration, and distorted antenna shape [9]. Hence, in such situations, the processed signal also retains the contribution of the target, which may cause the target self-nulling effect.

In this paper, we propose a robust D^3 STAP method for colocated multiple-input multiple-output (MIMO) radar, where superior capabilities arouse significant attentions among radar scholars [10–14]. In the presented robust method, the worst-case performance optimization (WCPO) [9] is used as the approach to avoid the target self-nulling effect. An upper bound for the norm of the target steering vector error is given to ensure the existence of a numerical solution for the WCPO problem. For the reason that the statistical characteristics of the array noise are changed in the D^3 approach, the D^3 approach based on the WCPO cannot minimize the array noise power effectively while mitigating the interferences. Hence, a modified D^3 approach is given to

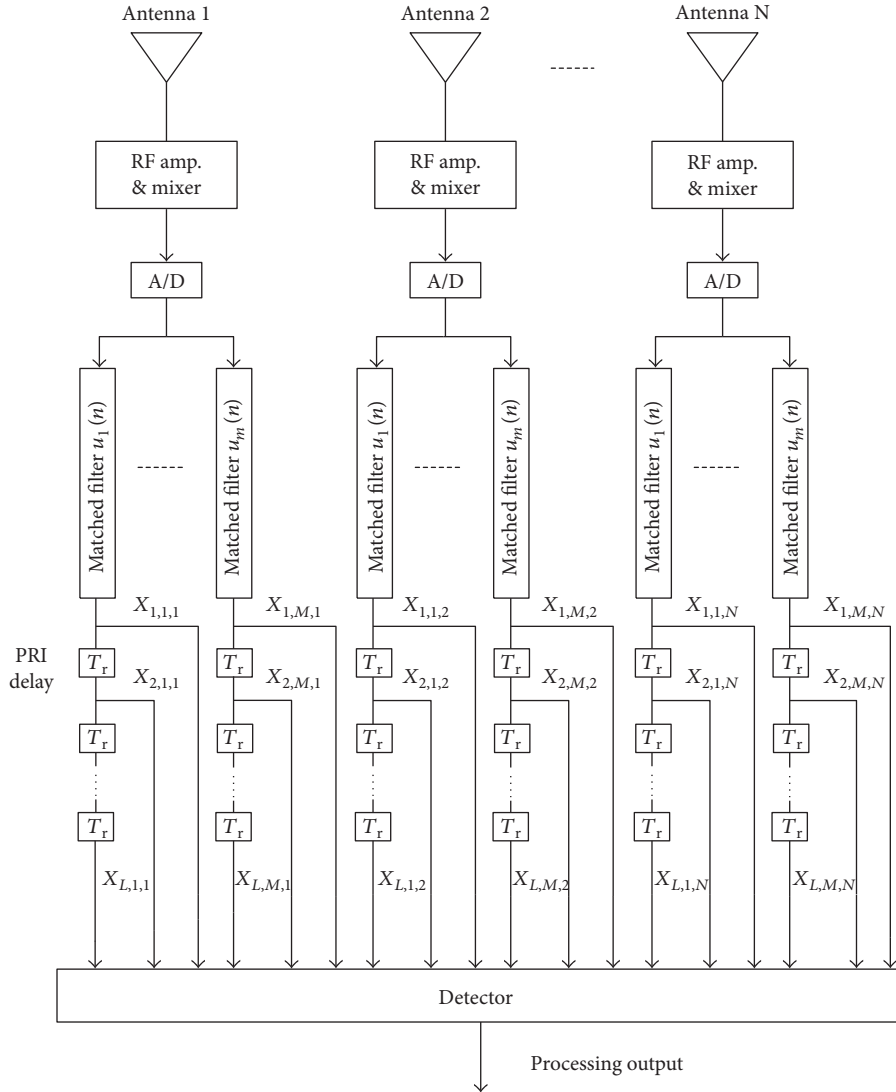


FIGURE 1: Structure of MIMO radar receiver in a CPI.

obtain a better detection performance in the low signal-to-noise ratio (SNR) environment. In the modified method, the objective function of the D^3 approach is replaced by a linear combination of the original objective function and the output of the array noise. Simulation results show that the proposed method can avoid the target self-nulling effect and outperforms the conventional robust D^3 approach in the low SNR environment.

2. Signal Model

Consider a MIMO radar system equipped with a transmit uniform linear array (ULA) of M elements and a receive ULA of N elements. Each transmit array element emits a burst of L pulses in a CPI with a pulse repetition frequency (PRF) f_r . The waveforms of M transmit array elements are mutually orthogonal and repeated pulse to pulse. Hence, the waveform of the i th transmit array element in a CPI can be written as [15]

$$\tilde{u}_i(t) = \sum_{l=1}^L u_i(t - lT_r), \quad i = 1, 2, \dots, M, \quad (1)$$

where $T_r = 1/f_r$ is the pulse repetition interval (PRI) and $u_i(t)$ is the i th orthogonal waveform which satisfies the following property:

$$\int_{T_r} u_i(t) u_j^*(t) dt = \begin{cases} 0, & i \neq j; \\ 1, & i = j, \end{cases} \quad (2)$$

where $(\cdot)^*$ denotes the conjugate operator.

Figure 1 depicts the structure of the MIMO radar receiver in a CPI. As is shown, received signals are collected over MN matched filters in L successive pulses. Assume that there are a point target located at angle θ_t with Doppler frequency f_t and K interferences located at θ_k ($k = 1, 2, \dots, K$) with Doppler frequency f_k ($k = 1, 2, \dots, K$) in the range cell under test. Then, the m th matched filter output from the n th receive array element at the l th pulse can be represented as [16]

$$\begin{aligned}
x_{l,m,n} = & \alpha_t \cdot \exp \left\{ j2\pi \left[\frac{(m-1)d_t}{\lambda} \sin(\theta_t) + \frac{(n-1)d_r}{\lambda} \sin(\theta_t) \right. \right. \\
& \left. \left. + \frac{(l-1)f_t}{f_r} \right] \right\} \\
& + \sum_{k=1}^K \alpha_k \cdot \exp \left\{ j2\pi \left[\frac{(m-1)d_t}{\lambda} \sin(\theta_k) \right. \right. \\
& \left. \left. + \frac{(n-1)d_r}{\lambda} \sin(\theta_k) + \frac{(l-1)f_k}{f_r} \right] \right\} + r_{l,m,n},
\end{aligned} \quad (3)$$

where d_t is the interspace distance of the adjacent transmit array elements, d_r is the interspace distance of the adjacent receive array elements, λ is the carrier wavelength, and $r_{l,m,n}$ is the noise with zero mean and variance σ_n^2 .

By rearranging $x_{l,m,n}$ ($l = 1, 2, \dots, L, m = 1, 2, \dots, M, n = 1, 2, \dots, N$), the match filter outputs can be written in a vectorial form as

$$\begin{aligned}
\mathbf{x} = & \alpha_t \mathbf{a}_d(f_t) \otimes \mathbf{a}_r(\theta_t) \otimes \mathbf{a}_t(\theta_t) \\
& + \sum_{k=1}^K \alpha_k \mathbf{a}_d(f_k) \otimes \mathbf{a}_r(\theta_k) \otimes \mathbf{a}_t(\theta_k) + \mathbf{r},
\end{aligned} \quad (4)$$

where \mathbf{r} is the noise vector, \otimes denotes the Kronecker product, $\mathbf{a}_d(f)$, $\mathbf{a}_r(\theta)$, and $\mathbf{a}_t(\theta)$ are Doppler steering vector, receive spatial steering vector, and transmit steering vector, respectively, which are given by

$$\mathbf{a}_d(f) = \left[1, \exp\left(j2\pi \frac{f}{f_r}\right), \dots, \exp\left(j2\pi(L-1) \frac{f}{f_r}\right) \right]^T, \quad (5)$$

$$\mathbf{a}_r(\theta) = \left[1, \exp\left(j2\pi \frac{d_r}{\lambda} \sin(\theta)\right), \dots, \exp\left(j2\pi \frac{(N-1)d_r}{\lambda} \sin(\theta)\right) \right]^T, \quad (6)$$

$$\mathbf{a}_t(\theta) = \left[1, \exp\left(j2\pi \frac{d_t}{\lambda} \sin(\theta)\right), \dots, \exp\left(j2\pi \frac{(N-1)d_t}{\lambda} \sin(\theta)\right) \right]^T. \quad (7)$$

3. Proposed Method

In a rapidly changing environment, the D³ STAP outperforms the statistical STAP for MIMO radar, due to the inaccurate interference covariance matrix estimation of the statistical STAP [7]. However, the detection performance of the D³ STAP will be extremely degraded, when there are steering vector errors [6]. Moreover, the statistical characteristics of the array noise are changed in the D³ approach, which will cause an adverse effect on the detection performance in the low signal-to-noise ratio (SNR) environment. To tackle the above problems, we introduce a modified robust D³ STAP for MIMO radar in the following subsections.

3.1. Conventional D³ STAP for MIMO Radar. In this subsection, we briefly introduce the D³ STAP for MIMO radar in absence of steering vector errors. The corresponding work

can also be found in [7]. Define three complex scalar quantities as follows:

$$\begin{aligned}
z_d &= \exp\left(j2\pi \frac{f_t}{f_r}\right), \\
z_r &= \exp\left(j2\pi \frac{d_r}{\lambda} \sin(\theta_t)\right), \\
z_t &= \exp\left(j2\pi \frac{d_t}{\lambda} \sin(\theta_t)\right),
\end{aligned} \quad (8)$$

which are determined by the DOA and the Doppler frequency of the target under test. Through removing the contributions of the target, we can obtain the following seven quantities which only contain the interference and the noise contributions:

$$\begin{aligned}
x_{l,m,n} - z_d^{-1} x_{l+1,m,n} & \quad l = 1, 2, \dots, L-1; m = 1, 2, \dots, M; \\
& \quad n = 1, 2, \dots, N; \\
x_{l,m,n} - z_t^{-1} x_{l,m+1,n} & \quad l = 1, 2, \dots, L; m = 1, 2, \dots, M-1; \\
& \quad n = 1, 2, \dots, N; \\
x_{l,m,n} - z_r^{-1} x_{l,m,n+1} & \quad l = 1, 2, \dots, L; m = 1, 2, \dots, M; \\
& \quad n = 1, 2, \dots, N-1; \\
x_{l,m,n} - z_d^{-1} z_t^{-1} x_{l+1,m+1,n} & \quad l = 1, 2, \dots, L-1; \\
& \quad m = 1, 2, \dots, M-1; n = 1, 2, \dots, N; \\
x_{l,m,n} - z_d^{-1} z_r^{-1} x_{l+1,m,n+1} & \quad l = 1, 2, \dots, L-1; m = 1, 2, \dots, M; \\
& \quad n = 1, 2, \dots, N-1; \\
x_{l,m,n} - z_t^{-1} z_r^{-1} x_{l,m+1,n+1} & \quad l = 1, 2, \dots, L; m = 1, 2, \dots, M-1; \\
& \quad n = 1, 2, \dots, N-1; \\
x_{l,m,n} - z_d^{-1} z_t^{-1} z_r^{-1} x_{l+1,m+1,n+1} & \quad l = 1, 2, \dots, L-1; \\
& \quad m = 1, 2, \dots, M-1; \\
& \quad n = 1, 2, \dots, N-1.
\end{aligned} \quad (9)$$

By arranging the relationships in (9) as rows in a linear system matrix \mathbf{F} , a weight vector \mathbf{w} of dimension $K_l K_n K_m$ can be designed to minimize the interferences while preserving unit gain for the target [7]. The corresponding problem can be formulated as

$$\begin{aligned}
\min_{\mathbf{w}} & \quad \|\mathbf{F}^* \mathbf{w}\|, \\
\text{s.t.} & \quad \mathbf{w}^H \mathbf{a}^{(K_l K_n K_m)}(f_t, \theta_t) = 1,
\end{aligned} \quad (10)$$

where $(\cdot)^H$ is the conjugate transpose operator and $\|\cdot\|$ denotes the Euclidean norm. $\mathbf{a}^{(K_l K_n K_m)}(f_t, \theta_t) = \tilde{\mathbf{a}}_d(f_t) \otimes \tilde{\mathbf{a}}_r(\theta_t) \otimes \tilde{\mathbf{a}}_t(\theta_t)$ is a truncated version of the target steering vector, while $\tilde{\mathbf{a}}_d(f_t)$, $\tilde{\mathbf{a}}_r(\theta_t)$, and $\tilde{\mathbf{a}}_t(\theta_t)$ are the $K_l \times 1$, $K_n \times 1$, and $K_m \times 1$ truncated versions of the steering vectors $\mathbf{a}_d(f_t)$, $\mathbf{a}_r(\theta_t)$, and $\mathbf{a}_t(\theta_t)$, respectively. Note that $\|\mathbf{F}^* \mathbf{w}\|$ is only minimized (not nulled) when the

number of the rows in \mathbf{F} is greater or equal to $K_l K_n K_m$, and the degrees of freedom (DOFs) in the temporal and spatial domain are set to $K_l \leq (L+1)/2$, $K_n \leq (N+1)/2$, and $K_m \leq (M+1)/2$. It is easy to see that problem (10) is equivalent to the following MVDR problem [17]:

$$\begin{aligned} \min_{\mathbf{w}} \quad & \mathbf{w}^H \mathbf{F}^T \mathbf{F}^* \mathbf{w}, \\ \text{s.t.} \quad & \mathbf{w}^H \mathbf{a}^{(K_l K_n K_m)}(f_t, \theta_t) = 1. \end{aligned} \quad (11)$$

The solution is given by

$$\mathbf{w} = \frac{(\mathbf{F}^T \mathbf{F}^*)^{-1} \mathbf{a}^{(K_l K_n K_m)}(f_t, \theta_t)}{(\mathbf{a}^{(K_l K_n K_m)}(f_t, \theta_t))^H (\mathbf{F}^T \mathbf{F}^*)^{-1} \mathbf{a}^{(K_l K_n K_m)}(f_t, \theta_t)}. \quad (12)$$

3.2. D^3 STAP for MIMO Radar Based on the WCPO

3.2.1. Formulation of the Problem Based on the WCPO. When there are mismatches between the actual and the presumed target steering vectors, the linear system matrix \mathbf{F} also contains the contribution of the target. Hence, the solution of problem (10) will cause the target self-nulling effect. In this subsection, a robust D^3 STAP method based on the WCPO is presented to prevent the target self-nulling effect. Let \mathbf{e} be a norm-bounded target steering vector error with $\|\mathbf{e}\| \leq \varepsilon$. By employing the WCPO, problem (10) can be reformulated as

$$\begin{aligned} \min_{\mathbf{w}} \quad & \|\mathbf{F}^* \mathbf{w}\|, \\ \text{s.t.} \quad & \left| \mathbf{w}^H \left(\mathbf{a}^{(K_l K_n K_m)}(f_t, \theta_t) + \mathbf{e} \right) \right| \geq 1. \end{aligned} \quad (13)$$

According to the derivation in [9], problem (13) is equivalent to the following problem:

$$\begin{aligned} \min_{\mathbf{w}} \quad & \|\mathbf{F}^* \mathbf{w}\|, \\ \text{s.t.} \quad & \mathbf{w}^H \mathbf{a}^{(K_l K_n K_m)}(f_t, \theta_t) - \varepsilon \|\mathbf{w}\| \geq 1, \\ & \text{Im} \left\{ \mathbf{w}^H \mathbf{a}^{(K_l K_n K_m)}(f_t, \theta_t) \right\} = 0, \end{aligned} \quad (14)$$

where $\text{Im}\{\cdot\}$ denotes the imaginary part of the matrix in the bracket. The problem stated in (14) is convex, which can be easily solved by the convex optimization toolbox CVX [18]. In the next subsection, we will discuss the upper bound for the norm of the signal steering vector error.

3.2.2. Upper Bound for the Norm of the Signal Steering Vector Error. Let \mathbf{e}_t , \mathbf{e}_r , and \mathbf{e}_d be the error vectors of the transmit spatial steering vector, receive spatial steering vector, and the Doppler steering vector, respectively. Then, the actual signal steering vector can be written as

$$\begin{aligned} & (\tilde{\mathbf{a}}_d(f_t) + \mathbf{e}_d) \otimes (\tilde{\mathbf{a}}_r(\theta_t) + \mathbf{e}_r) \otimes (\tilde{\mathbf{a}}_t(\theta_t) + \mathbf{e}_t) \\ &= (\tilde{\mathbf{a}}_d(f_t) \otimes \tilde{\mathbf{a}}_r(\theta_t) + \tilde{\mathbf{a}}_d(f_t) \otimes \mathbf{e}_r + \mathbf{e}_d \otimes \tilde{\mathbf{a}}_r(\theta_t) \\ & \quad + \mathbf{e}_d \otimes \mathbf{e}_r) \otimes (\tilde{\mathbf{a}}_t(\theta_t) + \mathbf{e}_t) \\ &= \tilde{\mathbf{a}}_d(f_t) \otimes \tilde{\mathbf{a}}_r(\theta_t) \otimes \tilde{\mathbf{a}}_t(\theta_t) + \tilde{\mathbf{a}}_d(f_t) \otimes \tilde{\mathbf{a}}_r(\theta_t) \otimes \mathbf{e}_t \\ & \quad + \tilde{\mathbf{a}}_d(f_t) \otimes \mathbf{e}_r \otimes \tilde{\mathbf{a}}_t(\theta_t) + \tilde{\mathbf{a}}_d(f_t) \otimes \mathbf{e}_r \otimes \mathbf{e}_t \\ & \quad + \mathbf{e}_d \otimes \tilde{\mathbf{a}}_r(\theta_t) \otimes \tilde{\mathbf{a}}_t(\theta_t) + \mathbf{e}_d \otimes \tilde{\mathbf{a}}_r(\theta_t) \otimes \mathbf{e}_t + \mathbf{e}_d \otimes \mathbf{e}_r \otimes \tilde{\mathbf{a}}_t(\theta_t) \\ & \quad + \mathbf{e}_d \otimes \mathbf{e}_r \otimes \mathbf{e}_t. \end{aligned} \quad (15)$$

Inspecting on (15), the signal steering vector error is

$$\begin{aligned} \mathbf{e} &= \tilde{\mathbf{a}}_d(f_t) \otimes \tilde{\mathbf{a}}_r(\theta_t) \otimes \mathbf{e}_t + \tilde{\mathbf{a}}_d(f_t) \otimes \mathbf{e}_r \otimes \tilde{\mathbf{a}}_t(\theta_t) + \tilde{\mathbf{a}}_d(f_t) \otimes \mathbf{e}_r \otimes \mathbf{e}_t \\ & \quad + \mathbf{e}_d \otimes \tilde{\mathbf{a}}_r(\theta_t) \otimes \tilde{\mathbf{a}}_t(\theta_t) + \mathbf{e}_d \otimes \tilde{\mathbf{a}}_r(\theta_t) \otimes \mathbf{e}_t + \mathbf{e}_d \otimes \mathbf{e}_r \otimes \tilde{\mathbf{a}}_t(\theta_t) \\ & \quad + \mathbf{e}_d \otimes \mathbf{e}_r \otimes \mathbf{e}_t. \end{aligned} \quad (16)$$

Assume that the transmit spatial steering vector error \mathbf{e}_t , the receive spatial steering vector error \mathbf{e}_r , and the Doppler steering vector error \mathbf{e}_d are norm-bounded with $\|\mathbf{e}_t\| \leq \varepsilon_t$, $\|\mathbf{e}_r\| \leq \varepsilon_r$, and $\|\mathbf{e}_d\| \leq \varepsilon_d$. Then, the upper bound for the norm of \mathbf{e} is given by

$$\begin{aligned} \|\mathbf{e}\| &\leq \|\tilde{\mathbf{a}}_d(f_t) \otimes \tilde{\mathbf{a}}_r(\theta_t) \otimes \mathbf{e}_t\| + \|\tilde{\mathbf{a}}_d(f_t) \otimes \mathbf{e}_r \otimes \tilde{\mathbf{a}}_t(\theta_t)\| \\ & \quad + \|\tilde{\mathbf{a}}_d(f_t) \otimes \mathbf{e}_r \otimes \mathbf{e}_t\| + \|\mathbf{e}_d \otimes \tilde{\mathbf{a}}_r(\theta_t) \otimes \tilde{\mathbf{a}}_t(\theta_t)\| \\ & \quad + \|\mathbf{e}_d \otimes \tilde{\mathbf{a}}_r(\theta_t) \otimes \mathbf{e}_t\| + \|\mathbf{e}_d \otimes \mathbf{e}_r \otimes \tilde{\mathbf{a}}_t(\theta_t)\| \\ & \quad + \|\mathbf{e}_d \otimes \mathbf{e}_r \otimes \mathbf{e}_t\| \\ &\leq \sqrt{K_l K_n} \varepsilon_t + \sqrt{K_l K_m} \varepsilon_r + \sqrt{K_l} \varepsilon_t \varepsilon_r + \sqrt{K_n K_m} \varepsilon_d \\ & \quad + \sqrt{K_n} \varepsilon_d \varepsilon_t + \sqrt{K_m} \varepsilon_d \varepsilon_r + \varepsilon_d \varepsilon_r \varepsilon_t \\ &= \varepsilon_e. \end{aligned} \quad (17)$$

Additionally, to ensure that problem (14) has an admissible solution, the norm of the signal steering vector error also has an upper bound as follows [6]:

$$\|\mathbf{e}\| \leq \frac{K_l K_n K_m - 1}{\sqrt{K_l K_n K_m}}. \quad (18)$$

Hence, the upper bound for the norm of the signal steering vector error \mathbf{e} can be found as

$$\varepsilon_{\max} = \min \left(\frac{K_l K_n K_m - 1}{\sqrt{K_l K_n K_m}}, \varepsilon_e \right) \quad (19)$$

3.3. Modified Robust D^3 STAP for MIMO Radar. The output signal-to-interference-plus-noise ratio (SINR) of the D^3 STAP for MIMO radar is defined by

$$\text{SINR} = 10 \log_{10} \frac{\alpha_t^2 |\mathbf{w}^H \mathbf{a}^{(K_l K_n K_m)}(f_t, \theta_t)|^2}{\mathbf{w}^H \mathbf{R}_{i+n} \mathbf{w}}, \quad (20)$$

where \mathbf{R}_{i+n} is the interference-plus-noise covariance matrix, which is given by

$$\mathbf{R}_{i+n} = \sum_{k=1}^K \alpha_k^2 \mathbf{a}^{(K_l K_n K_m)}(f_k, \theta_k) \left(\mathbf{a}^{(K_l K_n K_m)}(f_k, \theta_k) \right)^H + \sigma_n^2 \mathbf{I}_{K_l K_n K_m}. \quad (21)$$

We can clearly see from (20) and (21) that the average noise power of the system output is $\sigma_n^2 \|\mathbf{w}\|^2$. However, the weight vector \mathbf{w} is designed to minimize the interference and noise contributions in the linear system matrix \mathbf{F} . And the statistical characteristics of the noise contributions in the linear system matrix \mathbf{F} are determined by the relationships in (9). For example, one of the noise vectors in the linear system matrix \mathbf{F} can be represented as

$$\begin{aligned} \mathbf{n}_1 = & \left[r_{1,1,1} - z_d^{-1} r_{2,1,1}, \dots, r_{1,K_m,1} - z_d^{-1} r_{2,K_m,1}, \right. \\ & r_{1,1,2} - z_d^{-1} r_{2,1,2}, \dots, r_{1,K_m,K_n} - z_d^{-1} r_{2,K_m,K_n}, \\ & r_{2,1,1} - z_d^{-1} r_{3,1,1}, \dots, r_{2,K_m,1} - z_d^{-1} r_{3,K_m,1}, \\ & r_{2,1,2} - z_d^{-1} r_{3,1,2}, \dots, r_{2,K_m,K_n} - z_d^{-1} r_{3,K_m,K_n}, \dots, \\ & r_{K_l,1,1} - z_d^{-1} r_{K_l+1,1,1}, \dots, r_{K_l,K_m,1} - z_d^{-1} r_{K_l+1,K_m,1}, \\ & \left. r_{K_l,1,2} - z_d^{-1} r_{K_l+1,1,2}, \dots, r_{K_l,K_m,K_n} - z_d^{-1} r_{K_l+1,K_m,K_n} \right]. \end{aligned} \quad (22)$$

From (22), it is easy to see that the noise component $r_{1,1,1} - z_d^{-1} r_{2,1,1}$ is correlated with the other noise component $r_{2,1,1} - z_d^{-1} r_{3,1,1}$. Therefore, the noise vector of any row of the linear system matrix \mathbf{F} does not obey the distribution of zero mean and covariance matrix $\sigma_n^2 \mathbf{I}_{K_l K_n K_m}$. In this situation, minimizing the objective function of problem (14) cannot ensure the minimum array noise power. To minimize array noise power while mitigating the interferences, we reformulate the robust D^3 STAP problem as follows:

$$\begin{aligned} \min_{\mathbf{w}} \quad & \eta \|\mathbf{F}^* \mathbf{w}\| + (1 - \eta) \|\mathbf{w}\| \\ \text{s.t.} \quad & \mathbf{w}^H \mathbf{a}^{(K_l K_n K_m)}(f_t, \theta_t) - \varepsilon \|\mathbf{w}\| \geq 1, \\ & \text{Im} \left\{ \mathbf{w}^H \mathbf{a}^{(K_l K_n K_m)}(f_t, \theta_t) \right\} = 0. \end{aligned} \quad (23)$$

where $\eta \in [0, 1]$ is a parameter which balances the weight between the performance of mitigating interferences and that of mitigating noises.

Inspecting on (23), the first and the second parts of the objective function are used to minimize the power of the interferences and array noise, respectively. When η is equal to one, problem (23) is equivalent to problem (14). And when η is equal to zero, the output signal power spectrum can only preserve a gain for the target without mitigating the interferences. Hence, it is necessary to select an appropriate η to solve problem (23). Generally, the value of η is proportional to the interference-to-interference-plus-noise ratio. The solution of problem (23) can also be solved by the convex optimization toolbox CVX.

4. Simulations

In this section, several examples are given to investigate the performances of the proposed methods. Consider that the transmit and the receive ULAs are equipped with $M = 5$ elements and $N = 5$ elements. The interspace distance of the adjacent receive array elements is half the carrier wavelength $\lambda/2$, and the interspace distance of the adjacent transmit array elements is given as $d_t = 5d_r$. The PRF is $f_r = 1150$ Hz, and the number of pulses in a CPI is $L = 65$. The DOFs of the proposed methods are set to $K_l = 33$, $K_m = 3$, and $K_n = 3$. The upper bound for the norm of the signal steering vector error in (14) and (22) is $\varepsilon = 0.5 \sqrt{K_l K_m K_n}$. In the range cell under test, we suppose that the presumed target is located at $\theta_t = 30^\circ$ with Doppler frequency $f_t = 100$ Hz. There are also two interferences located at $\theta_1 = -10^\circ$ with Doppler frequency $f_t = -150$ Hz and $\theta_2 = 65^\circ$ with Doppler frequency $f_t = 200$ Hz. The interference-to-noise ratio (INR) is assumed to be 20 dB for both interferences. And in the following examples, $\eta = 0.001$ is chosen for the modified robust D^3 STAP.

Example 1. In the first example, the SNR is assumed to be 10 dB and there are no mismatches between the presumed and the actual signal steering vectors. Figures 2(a) and 2(b) depict the two-dimensional adaptive weight patterns for the conventional D^3 STAP and the modified robust D^3 STAP, respectively. As shown in Figure 2, both the adaptive weight patterns can form a gain in the target position and place nulls in the interference positions. In addition, we can see that the sidelobe of the adaptive weight pattern obtained by the modified robust D^3 STAP is lower than that of the other.

Example 2. In this example, the signal steering vector error is considered. The SNR is assumed to be 10 dB, and the actual target is located at $\tilde{\theta}_t = 29.5^\circ$ with Doppler frequency $\tilde{f}_t = 95$ Hz. From Figures 3(a) and 3(b), both the adaptive weight patterns place nulls in the interference positions. However, the adaptive weight pattern obtained by the conventional D^3 STAP places a null in the actual target position while the adaptive weight pattern obtained by the modified robust D^3 STAP preserves a gain in the actual target position.

Example 3. In this example, the output SINRs versus the input SNR are shown in Figures 4(a) and 4(b). The actual target position for Figure 4(b) is the same as that in Example 2. For a comparison, the loaded D^3 approach is also given in the simulations, which is a robust method to design the weight vector of (11) like the loaded SMI (LSMI) [19]. The fixed diagonal loading parameter $\gamma = 10$ is chosen for the loaded D^3 STAP. From Figures 4(a) and 4(b), we can see that the modified robust D^3 STAP shows better performance than other methods. This improvement is especially remarkable when the SNR is less than 0 dB.

5. Conclusion

In this paper, a robust D^3 STAP method for MIMO radar has been presented. The proposed method uses the WCPO

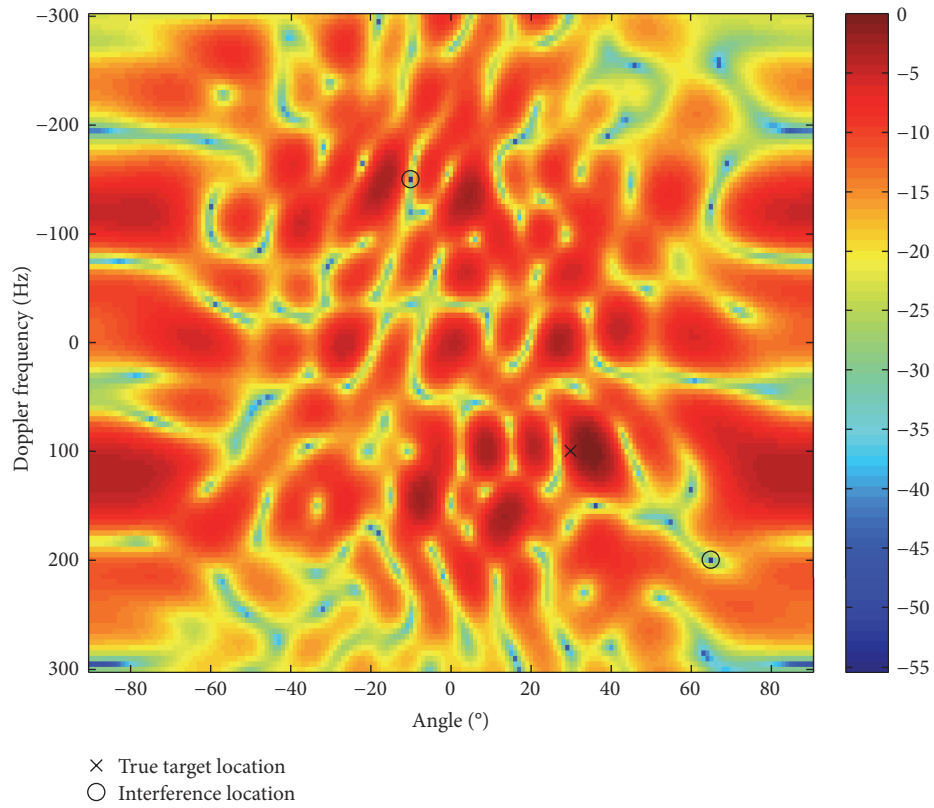
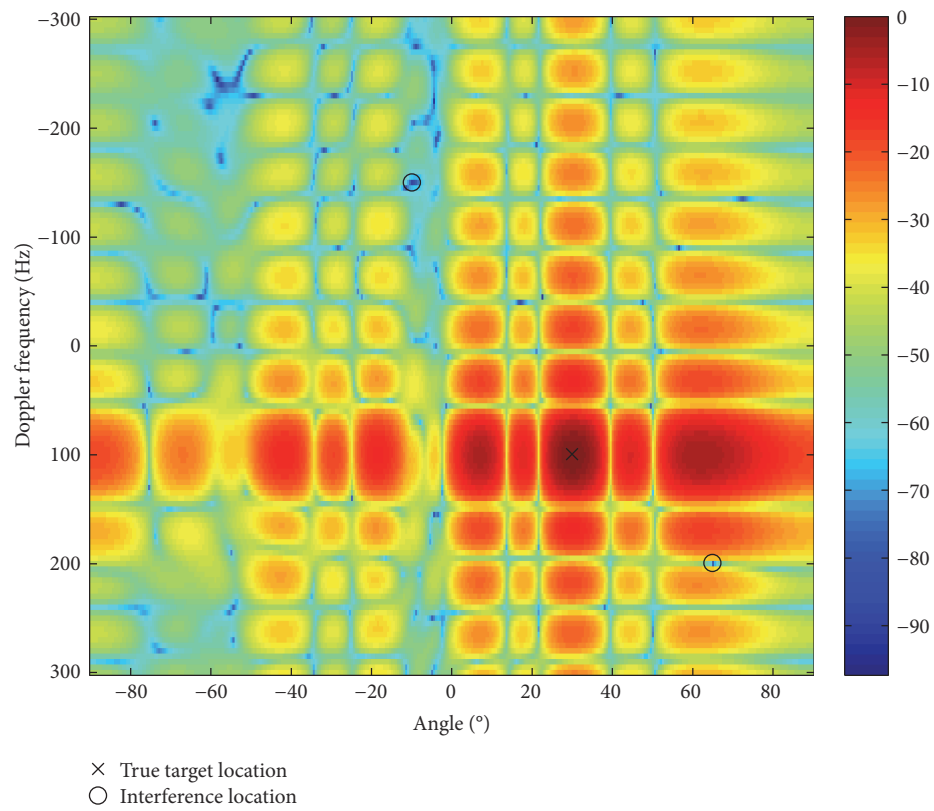
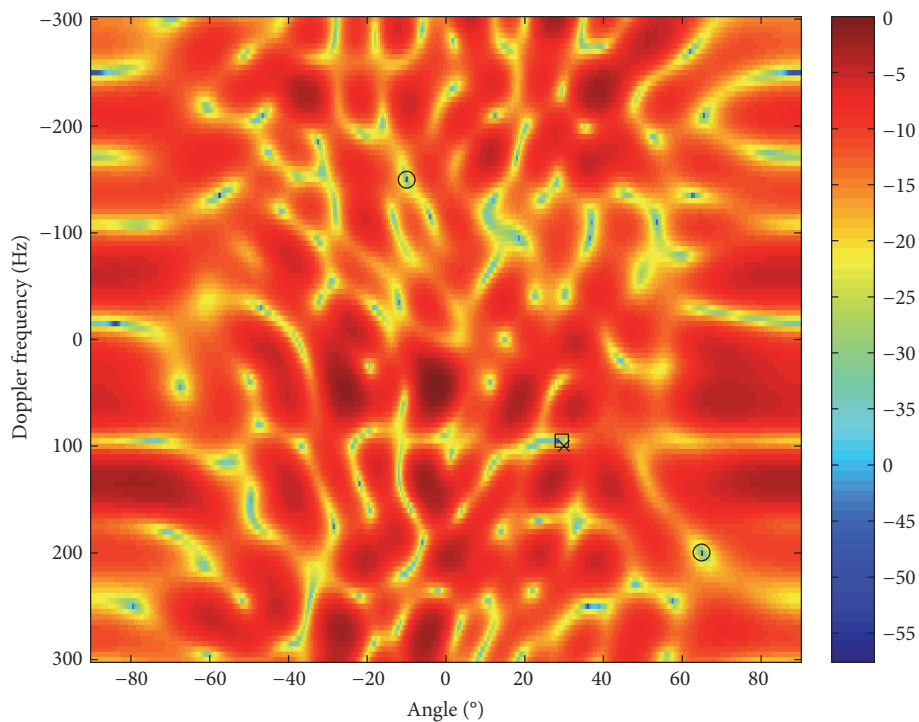
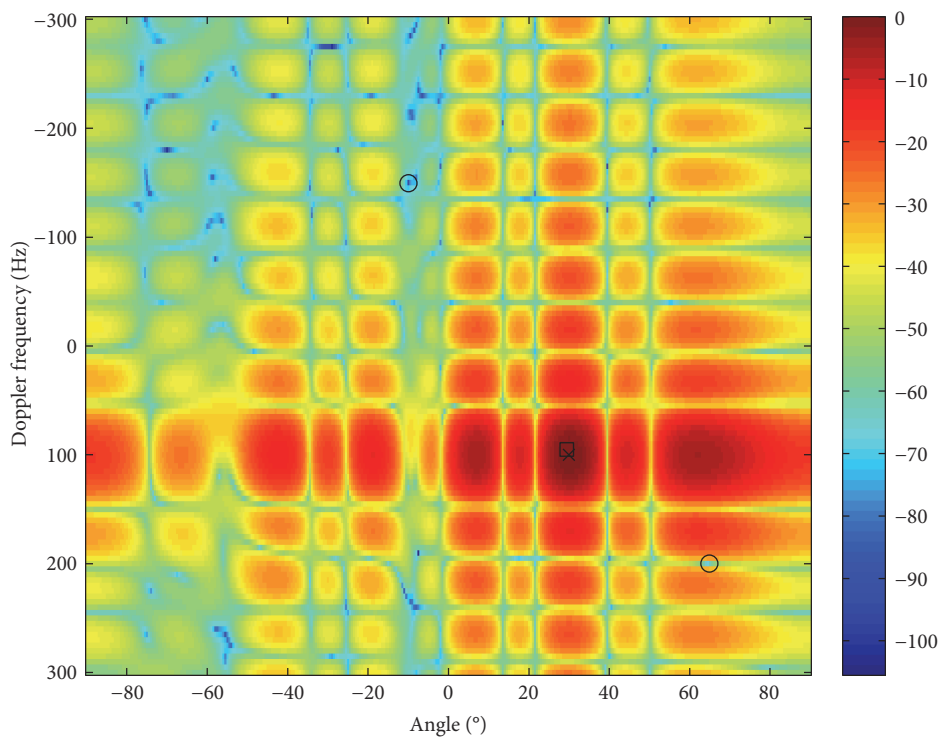
(a) The conventional D^3 STAP(b) The modified robust D^3 STAP

FIGURE 2: Adaptive weight patterns without signal steering vector error.



- × Presumed target location
- True target location
- Interference location

(a) The conventional D^3 STAP



- × Presumed target location
- True target location
- Interference location

(b) The modified robust D^3 STAP

FIGURE 3: Adaptive weight patterns with signal steering vector error.

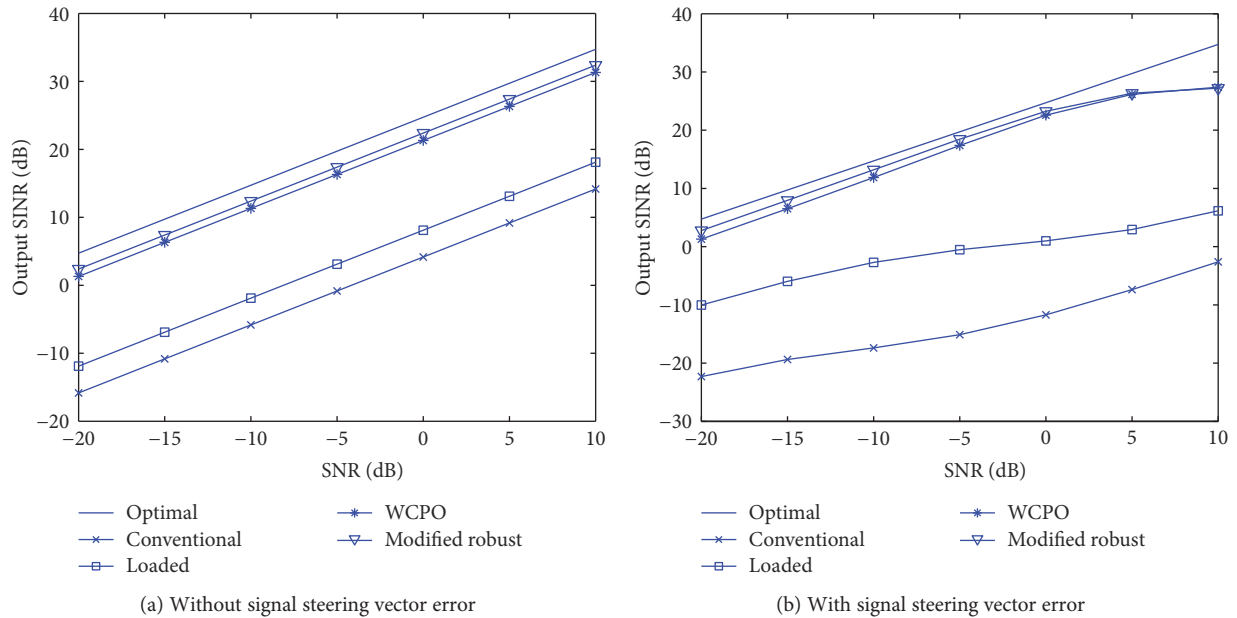


FIGURE 4: Output SINR versus input SNR.

to avoid the target self-nulling effect. Moreover, to improve the output SINR, a modified objective function is proposed to minimize the array noise output while mitigating the interferences. Simulation results show that the proposed method can prevent the target self-nulling effect and provide higher output SINR than other methods in the low SNR environment.

Conflicts of Interest

The authors declare that there is no conflict of interests regarding the publication of this paper.

Acknowledgments

This work was supported by the National Natural Science Foundation of China (Grant no. 61401204), Postdoctoral Science Foundation of Jiangsu Province (Grant no. 1501104C), and Technology Research and Development Program of Jiangsu Province (Grant no. BY2015004-03).

References

- [1] H. Wang and L. Cai, "On adaptive spatial-temporal processing for airborne surveillance radar systems," *IEEE Transactions on Aerospace and Electronic Systems*, vol. 30, no. 3, pp. 660–670, 1994.
- [2] H. Jie, F. Zheng, and M. Lun, "Reduced-dimension clutter suppression method for airborne multiple-input multiple-output radar based on three iterations," *IET Radar, Sonar & Navigation*, vol. 9, no. 3, pp. 249–254, 2015.
- [3] Y. Wu, T. Wang, J. Wu, and J. Duan, "Training sample selection for space-time adaptive processing in heterogeneous environments," *IEEE Geoscience and Remote Sensing Letters*, vol. 12, no. 4, pp. 691–695, 2015.
- [4] Z. Yang, R. Fa, Y. Qin, X. Li, and H. Wang, "Direct data domain sparsity-based STAP utilizing subaperture smoothing techniques," *International Journal of Antennas and Propagation*, vol. 2015, Article ID 171808, 10 pages, 2015.
- [5] T. K. Sarkar, H. Wang, S. Park et al., "A deterministic least-squares approach to space-time adaptive processing (STAP)," *IEEE Transactions on Antennas and Propagation*, vol. 49, no. 1, pp. 91–103, 2001.
- [6] D. Cristallini and W. Burger, "A robust direct data domain approach for STAP," *IEEE Transactions on Signal Processing*, vol. 60, no. 3, pp. 1283–1294, 2012.
- [7] M. Ahmadi, K. Mohamedpour, and F. Keshvari, "Direct data domain (D^3) approach for space-time adaptive processing in colocated MIMO radar," in *2013 21st Iranian Conference on Electrical Engineering (ICEE)*, pp. 1–4, Mashhad, Iran, September 2013.
- [8] I. S. Reed, J. D. Mallet, and L. E. Brennan, "Rapid convergence rate in adaptive arrays," *IEEE Transactions on Aerospace and Electronic Systems*, vol. AES-10, no. 6, pp. 853–863, 1974.
- [9] S. A. Vorobyov, A. B. Gershman, and Z. Luo, "Robust adaptive beamforming using worst-case performance optimization: a solution to the signal mismatch problem," *IEEE Transactions on Signal Processing*, vol. 51, no. 2, pp. 313–324, 2003.
- [10] J. Li and P. Stoica, "MIMO radar with colocated antennas," *IEEE Signal Processing Magazine*, vol. 24, no. 5, pp. 106–114, 2007.
- [11] X. W. N. Tong, Y. Zhang, G. Hu, and X. He, "Multiple-input multiple-output radar super-resolution three-dimensional imaging based on a dimension-reduction compressive sensing," *IET Radar, Sonar & Navigation*, vol. 10, no. 4, pp. 757–764, 2016.
- [12] N. Pandey and L. P. Roy, "Convex optimization based transmit beam pattern synthesis for MIMO radar," *Electronics Letters*, vol. 52, no. 9, pp. 761–763, 2016.
- [13] B. Jiu, H. Liu, X. Wang, L. Zhang, Y. Wang, and B. Chen, "Knowledge-based spatial-temporal hierarchical MIMO radar waveform design method for target detection in heterogeneous clutter zone," *IEEE Transactions on Signal Processing*, vol. 63, no. 3, pp. 543–554, 2015.

- [14] Y. Li, S. Gu, and N. Zheng, "MIMO radar transmit beam pattern design for DOA estimation with sidelobe suppression," *International Journal of Antennas and Propagation*, vol. 2016, Article ID 1512843, 10 pages, 2016.
- [15] B. Tang and J. Tang, "Joint design of transmit waveforms and receive filters for MIMO radar space-time adaptive processing," *IEEE Transactions on Signal Processing*, vol. 64, no. 18, pp. 4707–4722, 2016.
- [16] W. Wang, Z. Chen, X. Li, and B. Wang, "Space time adaptive processing algorithm for multiple-input-multiple-output radar based on Nyström method," *IET Radar, Sonar & Navigation*, vol. 10, no. 3, pp. 459–467, 2016.
- [17] J. Capon, "High-resolution frequency-wavenumber spectrum analysis," *Proceedings of the IEEE*, vol. 57, no. 8, pp. 1408–1418, 1969.
- [18] S. Boyd and L. Vandenberghe, *Convex Optimization*, Cambridge University Press, 2004.
- [19] O. Besson and F. Vincent, "Performance analysis of beamformers using generalized loading of the covariance matrix in the presence of random steering vector errors," *IEEE Transactions on Signal Processing*, vol. 53, no. 2, pp. 452–459, 2005.

Research Article

Circularly Polarized Dielectric Resonator Antenna Arrays with Fractal Cross-Slot-Coupled DRA Elements

Jia-Hong Lin, Wen-Hui Shen, Zhi-Dong Shi, and Shun-Shi Zhong

School of Communication and Information Engineering, Shanghai University, Shanghai 200072, China

Correspondence should be addressed to Jia-Hong Lin; reallylin@hotmail.com

Received 4 July 2017; Revised 28 September 2017; Accepted 12 October 2017; Published 14 November 2017

Academic Editor: Piotr Samczynski

Copyright © 2017 Jia-Hong Lin et al. This is an open access article distributed under the Creative Commons Attribution License, which permits unrestricted use, distribution, and reproduction in any medium, provided the original work is properly cited.

In the design of circularly polarized (CP) dielectric resonator antenna (DRA) arrays, the regular-shaped DRAs with simple feeding configurations are mostly used as array elements to make the design procedure more efficient. However, such array element DRA usually achieves only about 6% axial ratio (AR) bandwidth. In this paper, a CP DRA element coupled by a fractal cross-slot which can radiate efficiently and excite the rectangular DRA simultaneously is considered. By adjusting the dimensions of the fractal cross-slot properly, the resonances of the fractal cross-slot and the dielectric resonator can be merged to obtain a wider AR bandwidth. Based on the proposed fractal cross-slot-coupled CP DRA element, two different CP DRA arrays are designed: a wideband CP DRA array and a low-sidelobe-level (SLL) CP DRA array. The designed DRA arrays are fabricated and measured, and structures and performances of the arrays are presented and discussed.

1. Introduction

Over the last decades, DRAs have become more and more popular because of their high radiation efficiency due to the absence of conductor as well as surface wave loss. On the other hand, DRAs can be fed by various feeding techniques, such as the microstrip line feed, the coaxial probe feed, the coplanar waveguide feed, and the aperture coupling feed.

Initial studies of DRAs were concentrated on linearly polarized (LP) designs. In 1985, Haneishi and Takazawa [1] designed the first CP DRA by truncating two opposite corners of a rectangular DRA, and since then many designs of CP DRAs have been proposed. Nowadays, most designs of CP DRA arrays are based on the sequential feeding technique which was proposed by Huang to generate the CP array with LP elements [2]. Moreover, three different kinds of microstrip feeding network for sequential feeding technique are studied in [3], and the hybrid ring feeding network shows a better performance than the parallel feeding network and the series one.

Except for the performance of feeding network, the performance of CP DRA array will also be affected by the array element. Several techniques have been proposed to enhance the axial ratio (AR) bandwidth of the single DRA,

such as multiple-feed techniques [4–6], traveling wave excitation [7, 8], and novel DRA geometries [9–11]. However, such designs are not very suitable in the design of DRA array. The multiple-feed designs are complicated to implement because they need a complex feeding network. The lumped resistance in traveling wave excitation will cause a decrease in the radiation efficiency. And compared with the novel DRA geometries, regular-shaped DRAs can make the design procedure more efficient because their resonant frequencies can be predicted easily by the dielectric waveguide model (DWM) method [12].

For these reasons cited above, most designers prefer to use regular-shaped DRAs (e.g., rectangular, cylindrical, and elliptical DRAs) and simple feeding configurations (e.g., single microstrip feed and slot aperture feed) in the design of DRA array. Especially, to avoid the parasitic radiation from feeding network affecting the radiation pattern of the array, the slot aperture feed is mostly widely used. In [13], a cross-slot-coupled cylindrical DRA with 5.6% effective AR bandwidth ($S_{11} < -10$ dB and $AR < 3$ dB) is used as the array element in the CP DRA array. In [3], the slot-coupled elliptical DRA with 5% effective AR bandwidth is used as the array element. It can be seen that such regular-shaped DRAs with

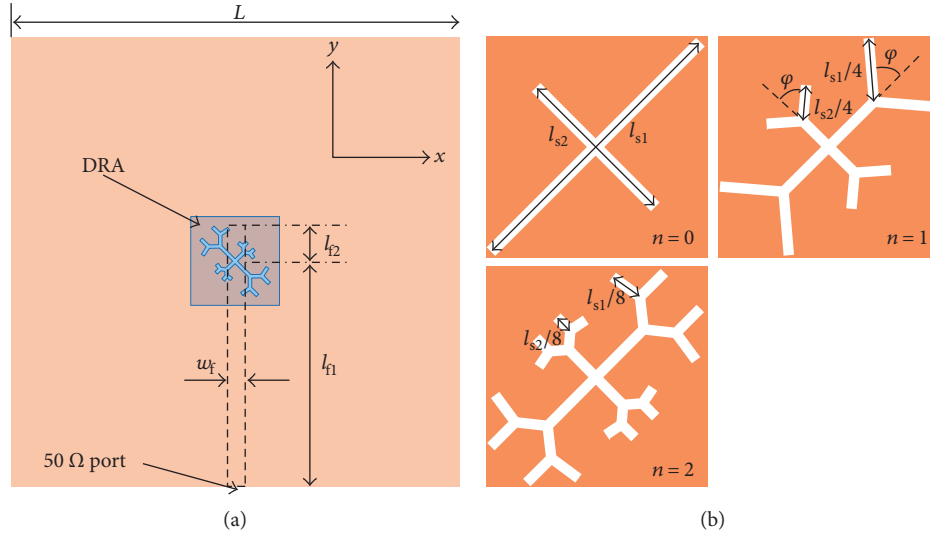


FIGURE 1: Antenna structure. (a) Top view and (b) structures of the fractal cross-slot with iterations $n = 0, 1,$ and $2.$

simple feeding configurations usually suffer from a narrow effective AR bandwidth. To enhance the effective AR bandwidth of the array element, a structure of two-layered substrates is used in the design of a cross-slot-coupled rectangular DRA, and corresponding effective AR bandwidth of the array element is enhanced to about 9% [14].

In this paper, a CP rectangular DRA element is designed using a relative permittivity $\epsilon_r = 8.9$, which has an effective AR bandwidth of about 12% by introducing a fractal cross-slot on the ground plane under the resonator. The proposed DRA element has a simple structure without dual feeds or two-layered substrates, and the mutual coupling between two elements of the proposed structure is found to be small although the distance between the elements is relatively small. Based on the fractal cross-slot-coupled CP DRA element, a wideband CP DRA array and a low-sidelobe-level CP DRA array are designed and studied. The arrays are fabricated and their measured results are verified with the simulated one.

2. Design of the Array Element

2.1. Antenna Structure. The structure of the array element is shown in Figure 1. A Rogers RT/duroid 5880 (tm) substrate with relative permittivity $\epsilon_r = 2.2$, dielectric loss tangent 0.0009, and thickness = 0.508 mm is used in the design, and the length and width of the substrate are both 50 mm. A ceramic cube with relative permittivity $\epsilon_r = 8.9$, length = 9.8 mm, width = 9.8 mm, and height = 9.1 mm is mounted on the center of the ground plane, and beneath the ceramic cubic is a fractal cross-slot etched on the ground plane. The 50 Ω microstrip line on the bottom side of the substrate has a length of $l_{f1} + l_{f2}$ and a width of w_f . As shown in Figure 1(a), l_{f1} is the distance between the 50 Ω port and the center of the ceramic cubic, and l_{f2} is the distance between the center of the ceramic cubic and the terminal of the 50 Ω microstrip line.

2.2. Effect of the Fractal Cross-Slot. Figure 1(b) shows the structures of the fractal cross-slot with iterations $n = 0, 1,$

and $2.$ The fractal structure is developed from the ordinary cross-slot ($n = 0$) which has lengths of l_{s1}, l_{s2} ($l_{s2} = k_s \times l_{s1}$) and a width of w_s . In the iterative procedure, the width of the slot is constant, and the iterative angle and iterative length coefficient are ϕ and 0.5, respectively.

To explain the effect of the fractal structure, simulated S_{11} and ARs of the array element with different values of n and l_{s1} are presented in Figure 2. According to the DWM method, the theoretical resonant frequencies of TE_{111}^x and TE_{111}^y modes in the proposed rectangular DRA are both 6.67 GHz. To obtain the CP radiation, these two modes should be excited simultaneously in the DRA. Of course, the practical resonant frequency in the DRA will also be affected by the feeding structure. Generally speaking, practical resonant frequencies of TE_{111}^x and TE_{111}^y modes will not be identical. As long as these two modes are excited at the adjacent frequency band, the effective CP radiation can be obtained. However, the AR bandwidth due to the resonances of the dielectric resonator is usually narrow. To enhance the AR bandwidth, dimensions of the cross-slot need to be adjusted suitably, so that the resonances of the cross-slot and the dielectric resonator can be merged to obtain a wider AR bandwidth, and then, the corresponding DRA will be a hybrid-radiation CP DRA.

However, when the ordinary cross-slot ($n = 0$) is used, such hybrid-radiation CP DRA is difficult to be obtained. As shown in Figure 2, when $n = 0$ and $l_{s1} = 7.9$ mm, two resonant frequencies can be found in the S_{11} curve. The lower resonant frequency (about 7.2 GHz) is due to the resonance of the DRA, and the higher one (about 8.6 GHz) is due to the resonance of the slot. In fact, the TE_{111}^x and TE_{111}^y modes in the DRA are not effectively excited here. According to the DWM method, the resonant frequency at 7.2 GHz is due to the TE_{111}^z mode in the DRA (the theoretical resonant frequency of TE_{111}^z mode is about 7.4 GHz). Besides the ineffective excitation of TE_{111}^x and TE_{111}^y modes, the resonant frequency of the slot is too far away from that of the DRA.

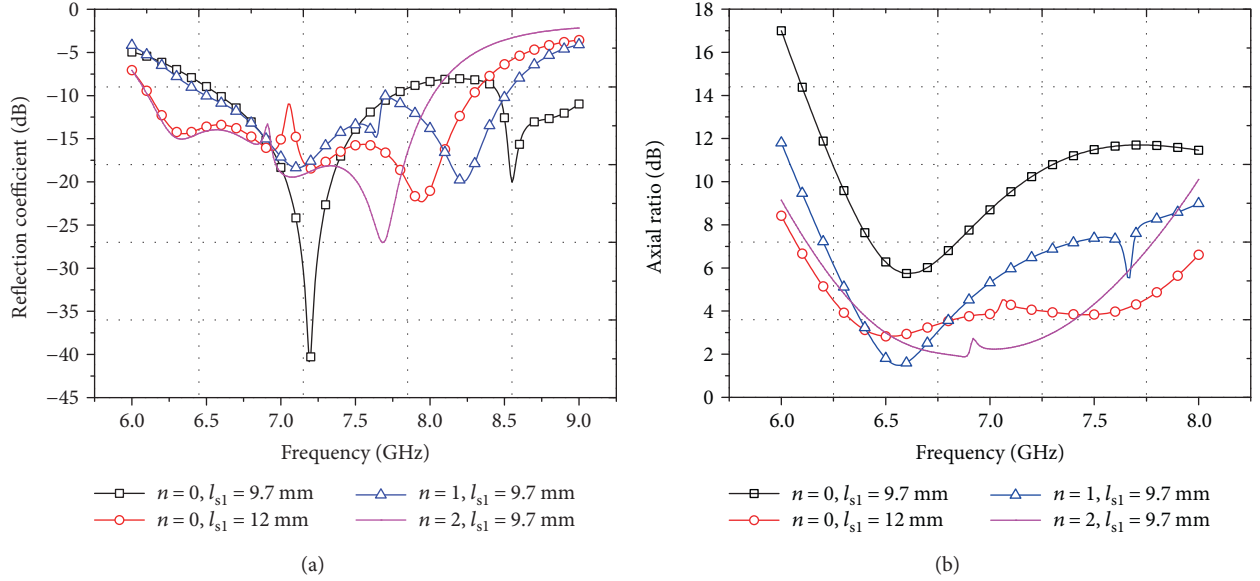


FIGURE 2: Simulated results of the DRA with different values of n and l_{s1} . (a) Reflection coefficient and (b) axial ratio ($w_f=1.52$ mm, $l_{f1}=25$ mm, $l_{f2}=4$ mm, $w_s=0.4$ mm, $k_s=0.57$, and $\varphi=500$).

To effectively excite the TE_{111}^x and TE_{111}^y modes and lower the resonant frequency of the slot, the simplest method is to increase the value of l_{s1} . By simulation, we found that the TE_{111}^x and TE_{111}^y modes can be most effectively excited when $l_{s1}=12$ mm. At this time, the resonant frequencies of the above two modes are about 6.4 GHz and 6.8 GHz, and resonant frequencies of two orthogonal modes in the slot can be lowered to 7.2 GHz and 7.9 GHz, as shown in Figure 2(a). In this situation, the corresponding CP bands of DRA and slot are found to be around 6.5 GHz and 7.5 GHz, respectively. However, according to Figure 2(b), we can find that these two CP bands are also too far away from each other to be merged.

Compared with the ordinary cross-slot, the fractal structure can lower the resonant frequency of the slot more efficiently. When the second iteration ($n=2$) is used, the resonant frequencies of TE_{111}^x and TE_{111}^y modes are also about 6.4 GHz and 6.8 GHz, but resonant frequencies of two orthogonal modes in the slot are further lowered to 7.0 GHz and 7.6 GHz. In this situation, CP bands of DRA and slot are found to be well merged, which can effectively enhance the AR bandwidth of the array element.

2.3. Simulated Results. In our design, the parameters of the array element are optimized by the FEM-based commercial software HFSS, and the final parameters of the array element are as follows: $w_f=1.52$ mm, $l_{f1}=25$ mm, $l_{f2}=4$ mm, $l_{s1}=9.7$ mm, $w_s=0.4$ mm, $k_s=0.57$, and $\varphi=50^\circ$.

Figure 3 is the simulated AR and S_{11} of the array element. The impedance bandwidth of the array element is 26.8% (from 6.12 to 8.01 GHz), and the 3 dB AR bandwidth is 11.9% (from 6.49 to 7.31 GHz). Compared with the results in [3, 13] and [14], the proposed array element coupled by the fractal cross-slot can achieve the widest effective AR bandwidth (11.9%, from 6.49 to 7.31 GHz).

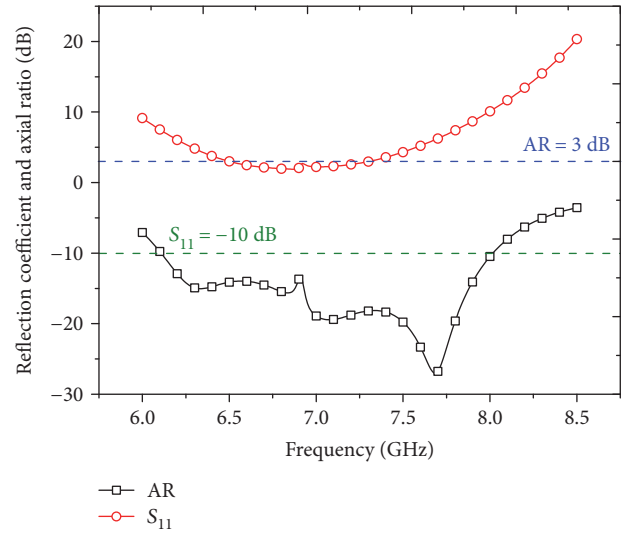


FIGURE 3: Simulated AR and S_{11} of the array element.

Figure 4 is the simulated radiation patterns across the effective AR bandwidth. It can be seen that the radiation patterns are stable across the effective AR bandwidth. Moreover, the radiation pattern has no sidelobe in the upper half space at every frequency, and the maximum radiation happens at $\theta=0^\circ$ and $\varphi=0^\circ$, which can ensure the design of a low-sidelobe-level array. The left-hand circular polarization (LHCP) gain at 6.5 GHz, 6.75 GHz, 7.0 GHz, and 7.25 GHz are 7.16 dBi, 7.02 dBi, 6.61 dBi, and 6.33 dBi, respectively.

Since we are proposing the proposed fractal cross-slot coupled DRA for array applications, the mutual coupling between two array elements is studied. The positions of two DRAs in Figures 5(a) and 5(b) are roughly equal to that in a sequential feeding network and a series feeding network which will be used in our design, respectively.

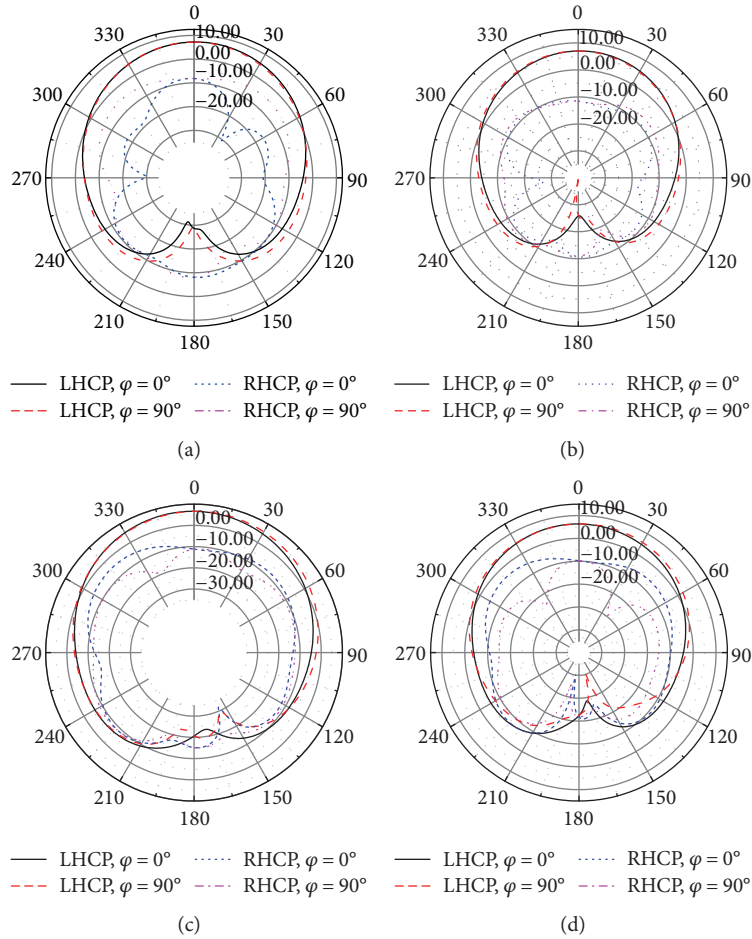


FIGURE 4: Simulated radiation patterns of the array element. (a) 6.5 GHz, (b) 6.75 GHz, (c) 7.0 GHz, and (d) 7.25 GHz.

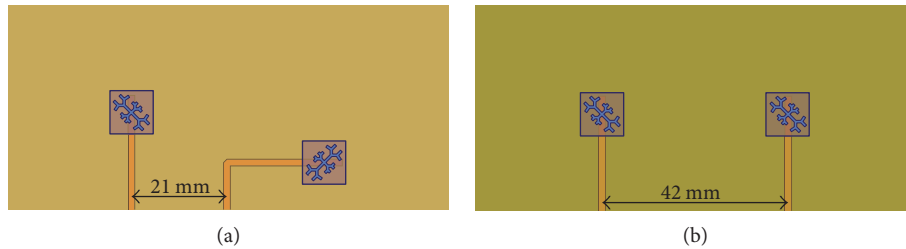


FIGURE 5: Drawings of two array elements. (a) In a sequential feeding network and (b) in a series feeding network.

The simulated port mutual coupling is shown in Figure 6. The maximum mutual coupling between two elements is lower than -20 dB, which shows a good isolation between array elements.

3. Design of the Wideband CP DRA Array

3.1. Antenna Structure. The structure of the proposed 2×2 wideband CP DRA array is shown in Figure 7. The length l and width w of the substrate are 100 mm and 84 mm, respectively. In our design, the hybrid ring feeding network for sequential feeding technique is used, and details of the feeding network designs and analyses can be found in [3].

To get the best performance of the DRA array, parameters of the array are optimized by HFSS. In the design of the array element, the distance between the center of the DRA and the 50Ω port is $l_{f1} = 25$ mm. In fact, the value of l_{f1} in the array element is decided by dimensions of the substrate. For the array element, a large enough substrate is needed to guarantee the performance of the DRA (mainly the radiation pattern and AR), which means that the value of l_{f1} cannot be too small. But in the design of the array, the substrate is much larger than that in the array element, which can ensure the performance of the DRA array. In this situation, a smaller value of l_{f1} can be selected to accelerate the simulation without degrading the performance of the array.

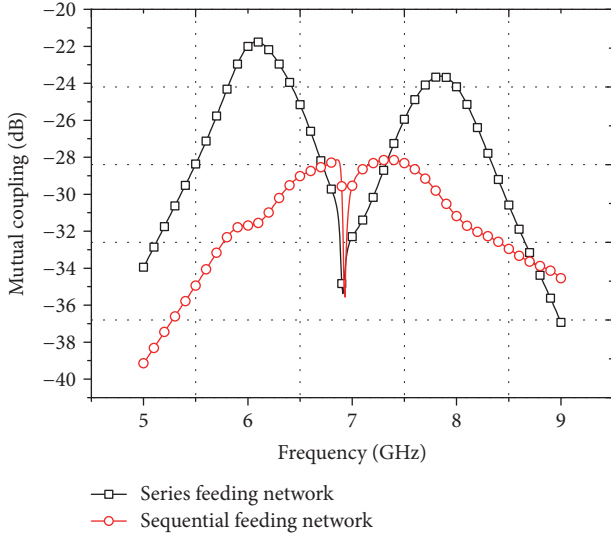


FIGURE 6: Simulated mutual coupling between two array elements.

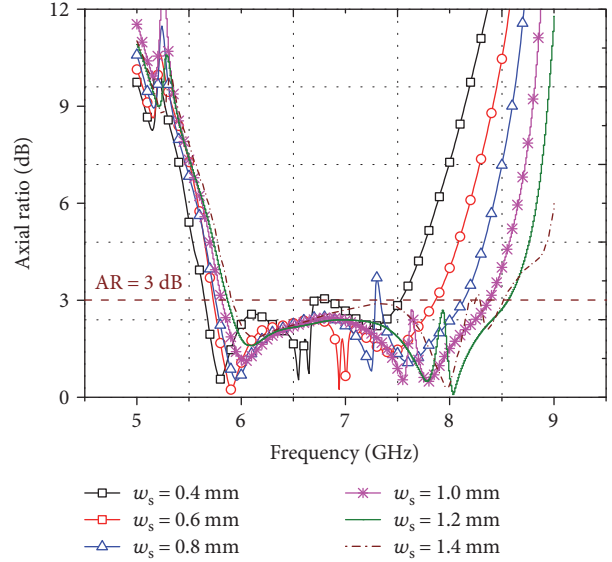


FIGURE 8: The effect of w_s on AR of the DRA array.

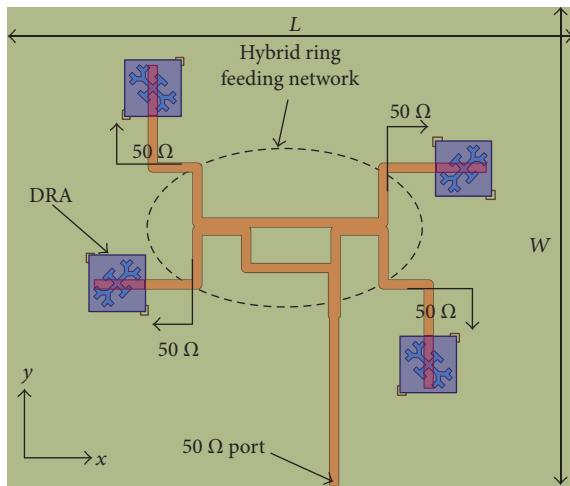


FIGURE 7: Structure of the proposed wideband CP DRA array.

Besides the value of l_{f1} , dimensions of the fractal cross-slot are also optimized in the design, and we find that value of w_s can affect the array more than other parameters.

3.2. Discussion of the Effect of w_s . Figure 8 shows the effect of w_s on AR of the DRA array. When w_s increases, the curve of AR is found to move to the higher frequency band, and the 3 dB AR bandwidth is enhanced due to a lower AR over the frequency band above 8 GHz. When $w_s = 1.2$ mm, the widest 3 dB AR bandwidth can be obtained. This is an interesting conclusion, which means that the value of w_s , which can lead the widest 3 dB AR bandwidth in the array, is very different from that in the array element.

To explain this problem more clearly, the effect of w_s on the AR of the array element is presented in Figure 9. It is true that the widest 3 dB AR bandwidth can be obtained when $w_s = 0.4$ mm. However, when $w_s = 0.4$ mm is used, AR of the array element will increase quickly with the increase of

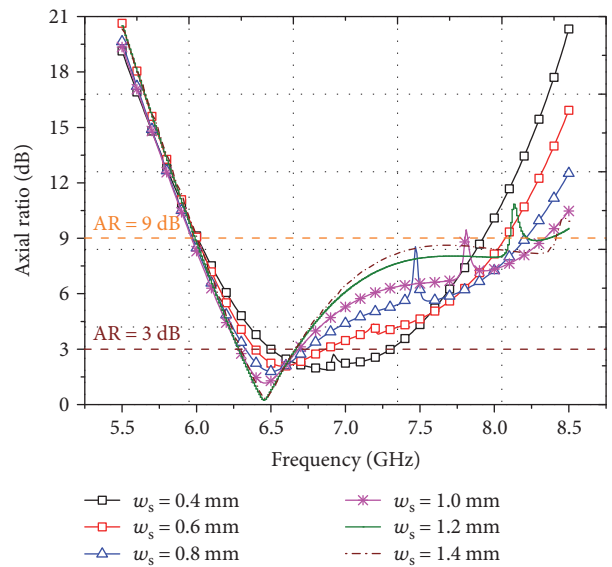


FIGURE 9: The effect of w_s on AR of the array element.

TABLE 1: Optimized parameters of the DRA array.

| Parameters | Values | Parameters | Values |
|------------|--------|------------|---------|
| l_{s1} | 9.6 mm | l_{f1} | 14 mm |
| w_s | 1.2 mm | l_{f2} | 4 mm |
| k_s | 0.6 | w_f | 1.52 mm |
| φ | 45 deg | | |

frequency. In this situation, the AR of the array element over the frequency band above 8 GHz is higher than 9 dB. When a larger value of w_s is used, the 3 dB AR bandwidth will deteriorate, but a lower AR can be found in the higher

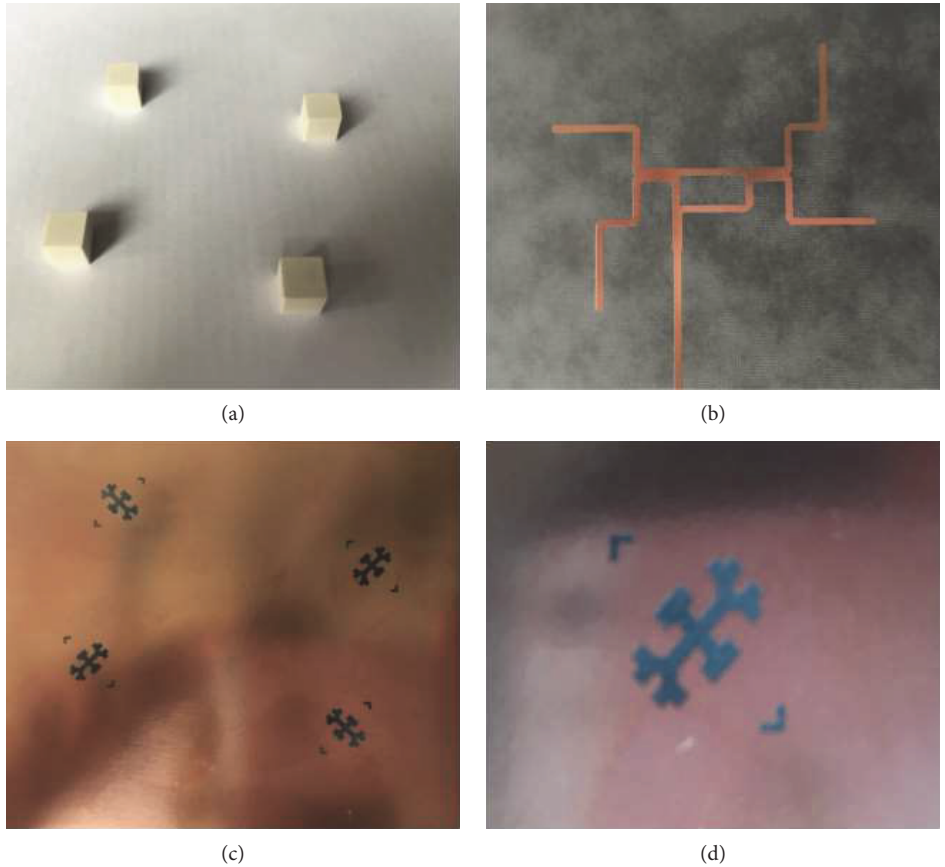


FIGURE 10: Photo of the fabricated DRA array. (a) Four DRAs, (b) sequential feeding network, (c) ground plane with slots, and (d) detailed structure of the fractal cross-slot and L-shaped slots.

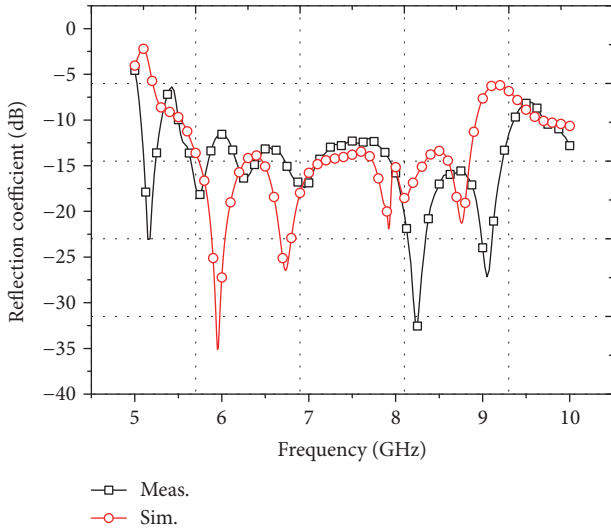


FIGURE 11: Simulated and measured S_{11} of the array.

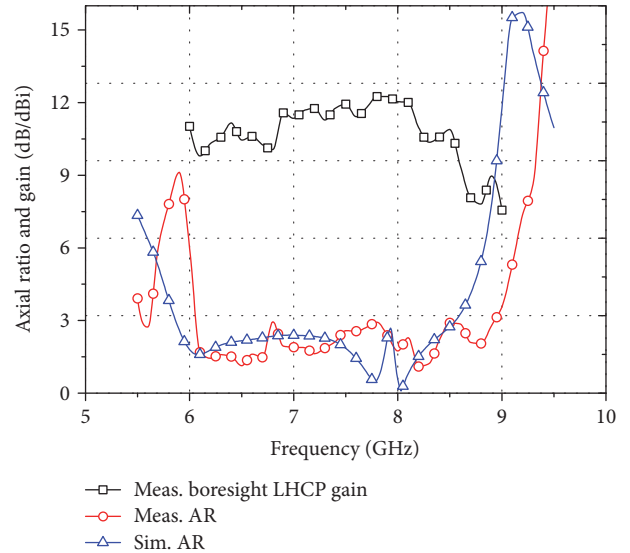


FIGURE 12: Simulated/measured AR and measured boresight LHCP gain of the array.

frequency band. When the value of w_s is larger than 1.0 mm, AR of the array element is basically lower than 9 dB from 6.0 to 8.5 GHz.

Through analyzing, we think that the above interesting phenomenon is due to the intrinsic characteristic of the sequential feeding network. As mentioned before, the

sequential feeding technique can be used to generate CP array with LP elements, which means that the sequential feeding network can be used to lower the AR of the array element. For example, assume that AR of an array element

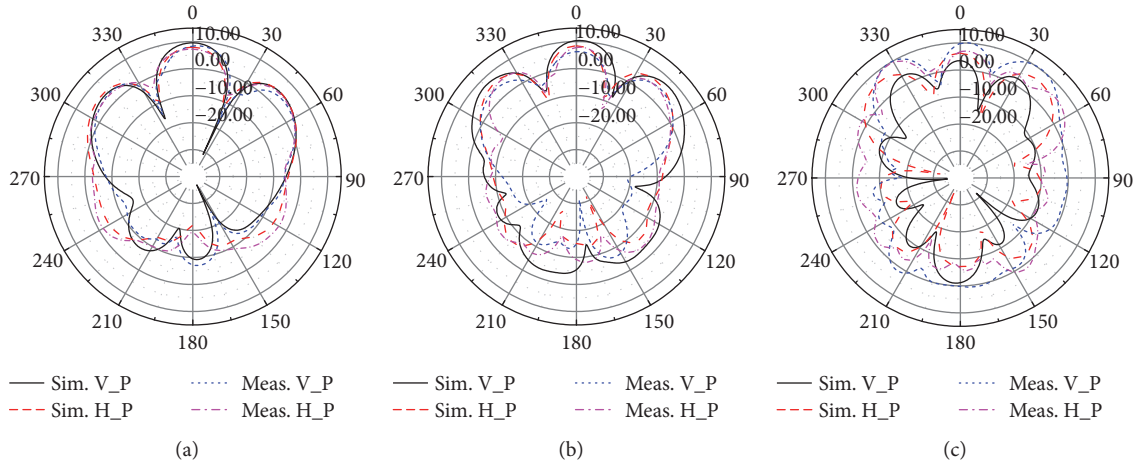


FIGURE 13: Simulated and measured radiation patterns with vertical and horizontal polarization in x - z plane. (a) 6.5 GHz, (b) 7.5 GHz, and (c) 8.5 GHz.

at frequency f_0 is AR_0 , if we use the sequential feeding technique to structure an array, the corresponding AR of the array at the same frequency f_0 should be lower than AR_0 . So, if we want to obtain the widest 3 dB AR bandwidth in the DRA array, we can use another value of AR (AR') as the design objective in the design of the array element, and AR' should be higher than 3 dB.

Comparing the results in Figures 8 and 9, we can find that, considering the frequency band from 6.0 to 8.5 GHz, once the AR of the array element at a particular frequency (f_0) is not higher than 9 dB, the corresponding AR of the DRA array at the same frequency f_0 can be lowered to below 3 dB by the sequential feeding network. So, even though $w_s = 0.4$ mm can lead the widest 3 dB AR bandwidth in the array element, the larger value of w_s can lead a wider 9 dB AR bandwidth in the array element, which can finally lead a wider 3 dB AR bandwidth in the DRA array. Finally, we select $w_s = 1.2$ mm in our design, because in this situation, the widest 3 dB AR bandwidth can be obtained in the DRA array.

Of course, it must be point out that the above conclusion “once the AR of the array element at a particular frequency (f_0) is not higher than 9 dB, the corresponding AR of the DRA array at the same frequency f_0 can be lowered to below 3 dB” is not obtained by theoretical analysis or computation, but by the comparison of results in Figures 8 and 9. However, even though it is not a quantitative conclusion, we think that it is a correct qualitative conclusion, which can have a guiding significance in the design of antenna arrays.

3.3. Simulated and Measured Results. In our design, parameters of the DRA array are optimized by HFSS, and all optimized parameters of the array are shown in Table 1.

The proposed wideband CP DRA array is fabricated and measured, and the photo of the fabricated array is shown in Figure 10. To mount the dielectric resonator properly, two extra L-shaped slots are etched around the fractal cross-slot which can show an accurate position of the rectangular dielectric resonator, and by simulation,

we ensure that such extra structure will not affect the performance of the array.

Figure 11 is the S_{11} of the proposed DRA array. The simulated impedance bandwidth is 46.5% (from 5.54 to 8.90 GHz), and the measured one is 51.5% (from 5.52 to 9.35 GHz). According to Figure 11, the measured result has a wider impedance bandwidth than the simulated one due to a better impedance matching over the frequency band above 9.0 GHz.

The standard linearly polarized horn antennas are employed for radiation measurements. The simulated and measured boresight ARs of the array are shown in Figure 12. The simulated 3 dB AR bandwidth is 37.7% (from 5.84 to 8.55 GHz), and the measured one is 38.3% (from 6.06 to 8.93 GHz). A good agreement is obtained between the simulated and measured ARs, except for about 300 MHz shift between the simulated and measured results. The measured boresight LHCP gain of the array is also shown in Figure 12. Across most of the 3 dB AR bandwidth, the measured boresight LHCP gain is higher than 10 dBi (from 6.06 to 8.51 GHz), and a highest 12.17 dBi gain is found at 7.9 GHz.

The simulated and measured radiation patterns with vertical and horizontal polarization at 6.5 GHz, 7.5 GHz, and 8.5 GHz in x - z plane are shown in Figure 13. Over the lower frequency band, the patterns are stable, and symmetric radiation can be found in the broadside directions. Moreover, good agreements are obtained between the simulated and measured results at 6.5 GHz and 7.5 GHz. When frequency increases to 8.5 GHz, about 5° beam tilt can be found in the measured pattern. Compared with the simulated result, a higher gain can also be found at 8.5 GHz, as well as a higher back-lobe level.

3.4. Comparisons. Table 2 gives the comparisons of the proposed DRA array to other reported wideband CP DRA arrays. It can be seen that the proposed DRA array in this paper can provide a wider effective AR bandwidth than others. It is necessary to point out that the sequential feeding

TABLE 2: Comparisons to other reported DRAAs.

| Reference | Yang et al. [3] | Pang et al. [13] | Akbari et al. [14] | Rana and Parui [19] | This work |
|----------------------------|---|------------------------------------|------------------------------------|--|--|
| Type of array element | Rectangular-slot coupled elliptical DRA | Cross-slot coupled-cylindrical DRA | Cross-slot-coupled rectangular DRA | Microstrip line-fed rectangular DRA (dual feeds) | Fractal cross-slot-coupled rectangular DRA |
| Type of feeding network | Sequential feeding network | Parallel feeding network | Sequential feeding network | Series feeding network | Sequential feeding network |
| Experiment verification | Yes | Yes | No | Yes | Yes |
| Element number | 2×2 | 2×2 | 2×2 | 1×4 | 2×2 |
| Impedance bandwidth | 43.9% | 19% | 48.31% | 17% | 51.5% |
| 3 dB axial ratio bandwidth | 26.1% | 16% | 21.67% | 10% | 38.3% |
| Effective AR bandwidth | 26.1% | 16% | 21.67% | 10% | 38.3% |
| Peak gain | About 12 dBi | About 12 dBi | 12.6 dBi | 13.6 dBi | 12.17 dBi |

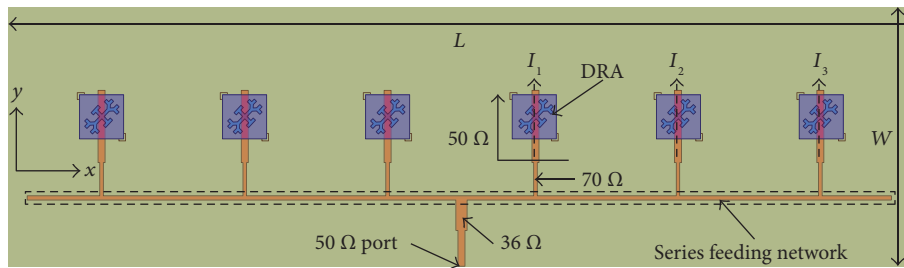


FIGURE 14: Structure of the proposed low-sidelobe-level CP DRA array.

technique and the corresponding hybrid ring feeding network are all used in [3, 14], and this design. So, we can ensure that it is the structure of fractal cross-slot and the careful parameter optimization that provide a wider effective AR bandwidth in our design.

4. Design of the Low-Sidelobe-Level CP DRA Array

In recent years, more and more attentions have been paid to the design of low-sidelobe-level DRA arrays. In [15], low-sidelobe-level DRA array fed by dielectric insular image guide (DIIG) is investigated. In [16], slot windows and reflector are used in the design of DRA array. In [17], DRA array with parasitic DRA elements is proposed. However, it seems that most of the designs mentioned in this paper are either on generating circular polarization or suppressing the SLL of DRA array, but not both.

In this paper, a low-sidelobe-level CP DRA array is also designed based on the proposed fractal cross-slot-coupled array element, which can be another verification of the proposed DRA element.

4.1. Antenna Structure. Figure 14 shows the structure of the designed 1×6 low-sidelobe-level CP DRA array. In this design, we rotate all slots to 90° to generate the right-handed circularly polarized (RHCP) radiation. Six ceramic cubes are mounted on a substrate with length $L = 206$ mm and width $W = 59$ mm. The proposed DRA array is designed to operate at 7.0 GHz with a -20 dB SLL. To achieve such

TABLE 3: Optimized parameters of the DRA array.

| Parameters | Values | Parameters | Values |
|------------|--------|------------|---------|
| l_{s1} | 9.7 mm | l_{f1} | 10 mm |
| w_s | 0.5 mm | l_{f2} | 5.8 mm |
| k_s | 0.59 | w_f | 1.52 mm |
| φ | 50 deg | | |

goal, a Chebyshev amplitude distribution and the corresponding series feeding network are used. To achieve a -20 dB SLL, the current ratios of the 6-element Chebyshev array is $I_1 : I_2 : I_3 = 1 : 0.777 : 0.551$. Details of series feeding network designs and analyses can be found in [18].

When the series feeding network is used, we need to adjust the input impedance of the array element to get 50Ω input impedance in the sum port of the DRA array. In our design, the required input impedance of the array element is 190Ω . To reduce the discontinuity of the width of the microstrip line in the feeding network, two $\lambda/4$ lines are used for impedance conversion in our design. Firstly, the 70Ω microstrip line is used between the array element and series feeding network, which can convert the input impedance of the array element to 98Ω . Thus, the input impedance in the sum port becomes 25.85Ω . So, another 36Ω microstrip line is used to get the 50Ω input impedance in the sum port.

The parameters of the DRA array are optimized by HFSS, and the final results are shown in Table 3. Different from the sequential feeding network, the series feeding network has no

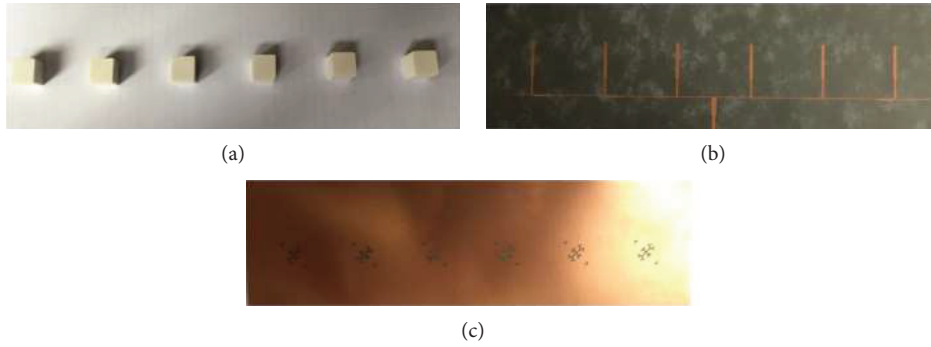


FIGURE 15: Photo of fabricated DRA array. (a) Six DRAs, (b) series feeding network, and (c) ground plane with slots.

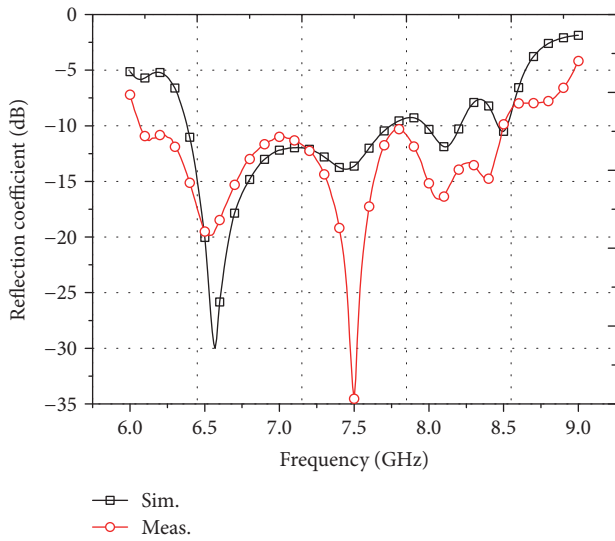


FIGURE 16: Simulated and measured S_{11} of the array.

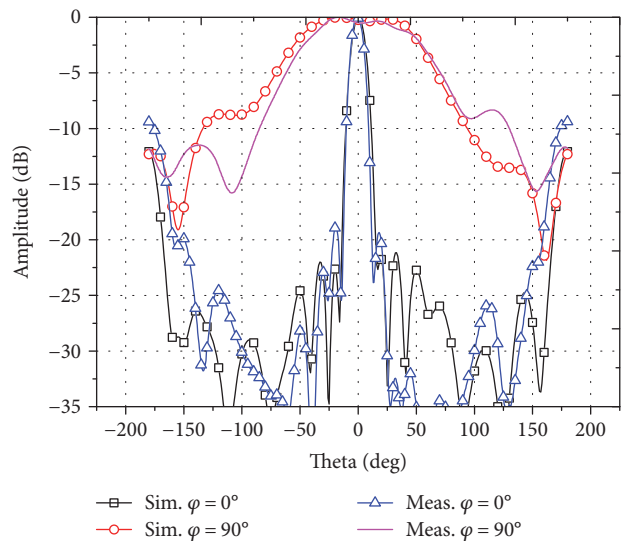


FIGURE 18: Simulated and measured normalized radiation pattern of the array at 7.0 GHz.

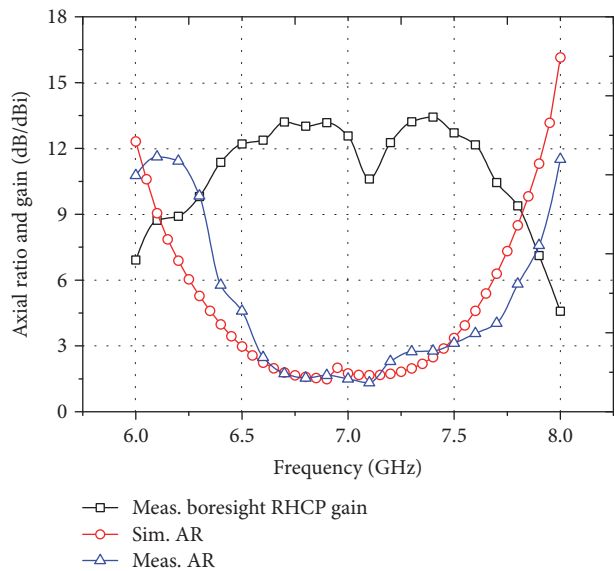


FIGURE 17: Simulated/measured AR and measured boresight RHCP gain of the array.

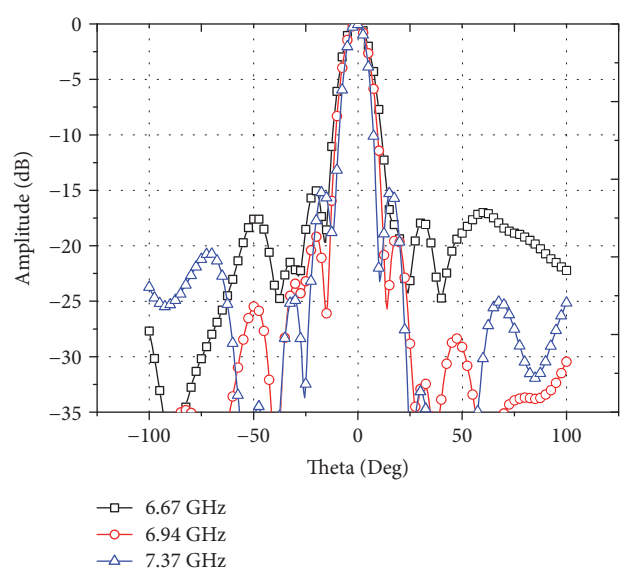


FIGURE 19: Measured normalized radiation patterns of the array at 6.67 GHz, 6.94 GHz, and 7.37 GHz.

TABLE 4: Comparisons to other reported low-sidelobe-level DRA arrays.

| Reference | Jin et al. [15] | Lin et al. [16] | Nikkhah et al. [17] | Gupta et al. [20] | This work |
|----------------------------|----------------------|-----------------------------------|-----------------------------------|---|-----------------------------------|
| Type | DRA array using DIIG | Series microstrip feeding network | Series microstrip feeding network | Parallel substrate integrated waveguide | Series microstrip feeding network |
| Experiment verification | Yes | Yes | No | No | Yes |
| Element number | 2×10 | 1×8 | 2×8 | 1×8 | 1×6 |
| Impedance bandwidth | >28.6% | 38.1% | 22.4% | 13.3% | 33.1% |
| Design objective of SLL | -20 dB | -25 dB | -24 dB | <i>Not given</i> | -20 dB |
| Obtained SLL | -17.5 dB | -23.01 dB | -22.6 dB | -21.4 dB | -19.23 dB |
| Peak gain | 15.8 dBi | 15.7 dBi | 17.4 dBi | 13.41 dBi | 13.43 dBi |
| 3 dB axial ratio bandwidth | | | | | 12.4% |

effect on AR, so it can be found that the optimized value of w_s in Table 3 is close to the optimized value in array element.

4.2. Simulated and Measured Results. The proposed DRA array is fabricated and measured, and a photo of the array is shown in Figure 15.

Figures 16 and 17 show the S_{11} , AR, and boresight RHCP gain of the array. The simulated and measured impedance bandwidths of the array are 18.1% (from 6.38 to 7.65 GHz) and 33.1% (from 6.07 to 8.48 GHz), respectively. The simulated 3 dB AR bandwidth is 13.9% (from 6.51 to 7.48 GHz), and the measured one is 12.4% (from 6.58 to 7.45 GHz). Due to a better impedance matching over the frequency band from 7.8 to 8.5 GHz, the measured impedance is much wider than the simulated one. However, it is obvious that the real performance of DRA array will be subject to the measured 3 dB AR bandwidth, which is 1.5% narrower than the simulated AR bandwidth. Across the measured 3 dB AR bandwidth, the boresight RHCP gain of the array is about 12.5 dBi, except a lowest measured RHCP gain around 7.1 GHz (about 10.0 dBi), and the highest measured RHCP gain is 13.43 dBi at 7.4 GHz.

Figures 18 and 19 are the normalized radiation patterns of the array. It is necessary to point out that all data in Figures 18 and 19 are based on the total gain of the DRA array. As mentioned above, two standard linearly polarized horn antennas are employed for radiation measurements, so the measured results of radiation pattern consist of two parts: the vertical polarized gain G_V and the horizontal polarized gain G_H , and the corresponding total gain can be computed by

$$G_{\text{total}} = 10 \lg(10^{G_H/10} + 10^{G_V/10}). \quad (1)$$

Figure 18 shows the normalized radiation patterns of the array at 7.0 GHz. The simulated SLL in x - z plane ($\varphi=0^\circ$) is about -21 dB, which is lower than our design target. Of course, we think that such result is derived from the errors in simulation. The measured SLL at 7.0 GHz is -18.72 dB, which is very close to the design target.

As shown in Figure 19, the frequency band over which $\text{SLL} < -15$ dB is found to be from 6.67 to 7.37 GHz, which is 9.97%. As mentioned above, over such frequency band ($\text{SLL} < -15$ dB), $S_{11} < -10$ dB and $\text{AR} < 3$ dB can also be

satisfied. The lowest measured SLL of -19.23 dB happens at 6.94 GHz.

4.3. Comparisons. Because no reported results of low-sidelobe-level CP DRA arrays are found, we present the comparisons of the proposed array to other reported low-sidelobe-level and wideband DRA arrays (LP arrays) in recent years in Table 4. The proposed low-sidelobe-level CP DRA array shows a wider impedance bandwidth than other designs (except [16], in which the slot windows and reflector are used), and the minor difference between the expected SLL and the obtained SLL can show a successful suppression of sidelobe. Of course, compared to our design, higher antenna gain can be found in others. We think the cause of that is the difference in element number. Through the abovementioned comparisons, we believe that our design can be considered as a good design of low-sidelobe-level and wideband DRA array. On this basis, an extra 3 dB AR bandwidth of 12.4% can be obtained in our design. Compared with the purely LP arrays, we think that the proposed low-sidelobe-level DRA array with CP characteristic is more attractive and valuable.

5. Conclusion

Based on the proposed fractal cross-slot-coupled CP DRA, designs of a wideband CP DRA array and a low-sidelobe-level DRA array are proposed in this paper. Effective AR bandwidth of the proposed wideband CP DRA array is 38.3% (from 6.06 to 8.93 GHz), and 12.17 dBi peak gain is obtained. The proposed low-sidelobe-level CP DRA array has an effective AR bandwidth of 12.4% (from 6.58 to 7.45 GHz), and a 9.97% (from 6.67 to 7.37 GHz) for -15 dB SLL bandwidth is obtained. The results of our work show that the proposed fractal cross-slot-coupled DRA element, which has a simple structure without dual feeds or two-layered substrates, is quite suitable for the design of DRA arrays.

Conflicts of Interest

The authors declare that there are no competing interests regarding the publication of this paper.

Acknowledgments

This work was supported by the Natural Science Foundation of China under Grant no. 61171031.

References

- [1] M. Haneishi and H. Takazawa, "Broadband circularly polarised planar array composed of a pair of dielectric resonator antennas," *Electronics Letters*, vol. 21, no. 10, pp. 437-438, 1985.
- [2] J. Huang, "A technique for an array to generate circular polarization with linearly polarized elements," *IEEE Transactions on Antennas and Propagation*, vol. 34, no. 9, pp. 1113-1124, 1986.
- [3] S.-l. S. Yang, R. Chair, A. A. Kishk, K.-F. Lee, and K.-M. Luk, "Study on sequential feeding networks for subarrays of circularly polarized elliptical dielectric resonator antenna," *IEEE Transactions on Antennas and Propagation*, vol. 55, no. 2, pp. 321-333, 2007.
- [4] R.-C. Han, S.-S. Zhong, and J. Liu, "Broadband circularly polarised dielectric resonator antenna fed by wideband switched line coupler," *Electronics Letters*, vol. 50, no. 10, pp. 725-726, 2014.
- [5] K.-W. Khoo, Y.-X. Guo, and L. C. Ong, "Wideband circularly polarized dielectric resonator antenna," *IEEE Transactions on Antennas and Propagation*, vol. 55, no. 7, pp. 1929-1932, 2007.
- [6] G. Massie, M. Caillet, M. Clenet, and Y. M. M. Antar, "A new wideband circularly polarized hybrid dielectric resonator antenna," *IEEE Antennas and Wireless Propagation Letters*, vol. 9, pp. 347-350, 2010.
- [7] M. I. Sulaiman and S. K. Khamas, "A singly fed rectangular dielectric resonator antenna with a wideband circular polarization," *IEEE Antennas and Wireless Propagation Letters*, vol. 9, pp. 615-618, 2010.
- [8] M. Zou, J. Pan, Z. Nie, and P. Li, "A wideband circularly polarized rectangular dielectric resonator antenna excited by a lumped resistively loaded monofilar-spiral-slot," *IEEE Antennas and Wireless Propagation Letters*, vol. 12, pp. 1646-1649, 2013.
- [9] R. Chair, S. L. S. Yang, A. A. Kishk, K. F. Lee, and K. M. Luk, "Aperture fed wideband circularly polarized rectangular stair shaped dielectric resonator antenna," *IEEE Transactions on Antennas and Propagation*, vol. 54, no. 4, pp. 1350-1352, 2006.
- [10] V. Hamsakutty, A. V. Praveen Kumar, J. Yohannan, and K. T. Mathew, "Coaxial fed hexagonal dielectric resonator antenna for circular polarization," *Microwave and Optical Technology Letters*, vol. 48, no. 3, pp. 581-582, 2006.
- [11] M. Simeoni, R. Cicchetti, A. Yarovoy, and D. Caratelli, "Plastic-based supershaped dielectric resonator antennas for wide-band applications," *IEEE Transactions on Antennas and Propagation*, vol. 59, no. 12, pp. 4820-4825, 2011.
- [12] R. K. Mongia, "Theoretical and experimental resonant frequencies of rectangular dielectric resonators," *IEE Proceedings-H*, vol. 139, no. 1, pp. 98-104, 1992.
- [13] K. K. Pang, H. Y. Lo, K. W. Leung, K. M. Luk, and E. K. N. Yung, "Circularly polarized dielectric resonator antenna sub-arrays," *Microwave and Optical Technology Letters*, vol. 27, no. 6, pp. 377-379, 2000.
- [14] M. Akbari, S. Gupta, R. Movahedinia, and A. R. Sebak, "Comparison of sequential subarrays of circularly polarized DR and patch antennas based on hybrid ring feeding in MMW," in *2016 Progress in Electromagnetics Research Symposium (PIERS)*, pp. 4009-4012, Shanghai, China, 2016.
- [15] L. Jin, R. Lee, and I. Robertson, "A dielectric resonator antenna array using dielectric insular image guide," *IEEE Transactions on Antennas and Propagation*, vol. 63, no. 2, pp. 859-862, 2015.
- [16] J. Lin, W. Shen, and K. Yang, "A low-sidelobe and wideband series-fed linear dielectric resonator antenna array," *IEEE Antennas and Wireless Propagation Letters*, vol. 16, pp. 513-516, 2017.
- [17] M. Ranibar Nikkhah, J. Rashed-Mohassel, and A. A. Kishi, "Wide-band and low sidelobe array of rectangular dielectric resonator antennas with parasitic elements," in *2014 International Conference on Multimedia Computing and Systems (ICMCS)*, pp. 1422-1425, Marrakech, Morocco, 2014.
- [18] R. Garg, P. Bhartia, I. Bahl, and A. Ittipiboon, *Microstrip Antenna Design Handbook*, Artech House, Norwood, MA, USA, 2001.
- [19] B. Rana and S. K. Parui, "Microstrip line fed wideband circularly-polarized dielectric resonator antenna array for microwave image sensing," *IEEE Sensors Letters*, vol. 1, no. 3, 2017.
- [20] S. Gupta, M. Akbari, R. Movahedinia, S. ZARBakhsh, and A. R. Sebak, "Low-side lobe level aperture coupled dielectric resonator antenna array fed by SIW," in *2016 10th European Conference on Antennas and Propagation (EuCAP)*, pp. 1-4, Davos, Switzerland, 2016.

Research Article

Estimating Direction of Arrival by Using Two-Dimensional State-Space Balance Method

Jun Wang, Hong Xiang, Shaoming Wei, and Zhongsheng Sun

School of Electronic and Information Engineering, Beihang University, Beijing 100191, China

Correspondence should be addressed to Shaoming Wei; weishaoming@126.com

Received 24 May 2017; Revised 20 September 2017; Accepted 4 October 2017; Published 2 November 2017

Academic Editor: Amerigo Capria

Copyright © 2017 Jun Wang et al. This is an open access article distributed under the Creative Commons Attribution License, which permits unrestricted use, distribution, and reproduction in any medium, provided the original work is properly cited.

A study of a two-dimensional state-space balance (2D SSB) method for estimating direction of arrival (DOA) for uniform rectangular array (URA) is presented in this letter. The comprehensive utilization of controllability and observability matrices and automatic pairing technique are considered in this method by using the single snapshot. Therefore, the DOAs of elevation angle and azimuth angle can pair automatically and acquire better estimation performance compared with 2D matrix pencil method or unitary matrix pencil method. In addition, the proposed method can handle correlated signals directly without preprocessing. Simulation is conducted to verify the effectiveness of the proposed method.

1. Introduction

In array signal processing, target direction of arrival (DOA) estimation has been widely applied in radar, sonar, wireless indoor positioning [1–3] and so on. Since the uniform rectangular array (URA) can provide the information of azimuth and elevation angles, a lot of 2D DOA methods have been developed, such as multiple signal classification (MUSIC) algorithm [4–6], root-MUSIC [7], estimation of signal parameters via rotational invariance technique (ESPRIT) algorithm [8, 9], and rank reduce (RARE) algorithm [10]. These conventional high resolution DOA parameter estimation techniques are mainly based on the statistical data by using the covariance matrix under the uncorrelated conditions. In the nonstationary environment, these DOA estimation methods performed poorly without preprocessing, but the matrix pencil (MP) method [11] got good performance by processing the received data directly based on the single snapshot. The unitary matrix pencil (UMP) method [12] can reduce the computation compared with the MP method by using a unitary matrix transformation, which can convert the complex operations to the real operations. The accuracy of both methods is nearly the same. The MP or UMP methods can also be regarded as a state-space method via observability or controllability processing. However, the method that using both observability and

controllability matrices was not considered to estimate the DOAs in the spatial domain which may be acquire a good performance. On the other hand, the additional search of the angle pairing is essential to the MP/UMP method by maximizing the cost function, which exploits the orthogonal property between signal subspace and noise subspace. However, the computational complexity of the MP/UMP method is high, and the angle pairing is always mismatched in the low SNR condition. Therefore, many automatic pairing techniques were presented to solve this problem, such as simultaneous diagonalization [13, 14], simultaneous Schur decomposition [15], and eigenvalue pairing [16].

This paper presents a two-dimensional state-space balance (2D SSB) method that is applied to the DOA estimation in order to get better DOA estimation than the 2D MP/UMP method. On one hand, the comprehensive utilization of controllability and observability matrices has been considered to improve direction abilities. On the other hand, this method can obtain the elevation angle and azimuth angle without pair matching process via automatic pairing technique.

2. Signal Model

The uniform rectangular array (URA) in Figure 1 consists of $M \times N$ identical and omnidirectional sensors with

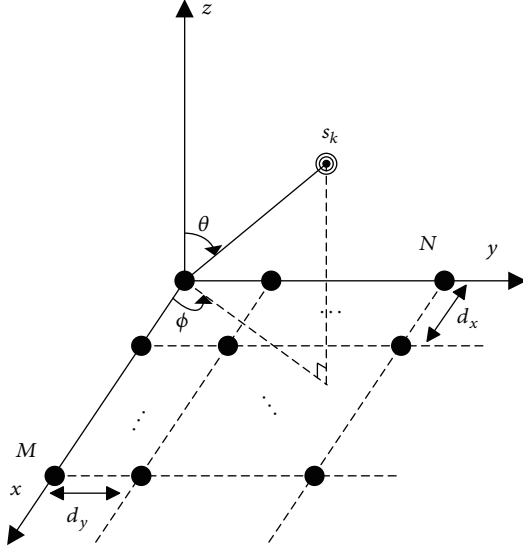


FIGURE 1: Array geometry of the URA.

interelement spacing of $d_x = d_y = \lambda/2$, where λ is the carrier wavelength.

Suppose K far-field narrowband signals impinge on the URA. s_k denotes the k th incident signal, θ_k is the k th elevation angle, and ϕ_k is the k th azimuth angle, respectively. The received data $z(m, n)$ at the (m, n) th feeding point of the omnidirectional antennas without noise can be expressed as [17]

$$z(m, n) = \sum_{k=1}^K g_k e^{j\pi u_k m} e^{j\pi v_k n}, \quad (1)$$

$$0 \leq m \leq M-1, \quad 0 \leq n \leq N-1,$$

where $u_k = \sin \theta_k \cos \phi_k$ and $v_k = \sin \theta_k \sin \phi_k$ are direction cosines mapping with azimuth and elevation angles and g_k is the gain of the k th incident signal.

3. 2D State-Space Balance Method

Equation (1) can be rewritten in a matrix form akin to that of a state-space impulse response as

$$z(m, n) = \mathbf{G} \Phi_x^m \Phi_y^n \mathbf{B}, \quad (2)$$

$$0 \leq m \leq M-1, \quad 0 \leq n \leq N-1,$$

where $\Phi_x = \text{diag}(e^{j\pi u_1}, e^{j\pi u_2}, \dots, e^{j\pi u_K})$ and $\Phi_y = \text{diag}(e^{j\pi v_1}, e^{j\pi v_2}, \dots, e^{j\pi v_K})$ are diagonal matrices so that they can commute under state-space system equivalence transformations [18]. $\text{diag}(\cdot)$ denotes the square matrix. $\mathbf{G} = [g_1, g_2, \dots, g_K]$ is the gain vector. Diagonal matrices Φ_x and Φ_y contain the DOA information about u_k and v_k . So we will isolate and solve Φ_x and Φ_y by using the 2D SSB method. Firstly, Hankel

matrix \mathbf{D}_m is formed by using the m th row of the received data array $z(m, n)$ as follows:

$$\mathbf{D}_m = \begin{bmatrix} z(m, 0) & z(m, 1) & \cdots & z(m, N-C) \\ z(m, 1) & z(m, 2) & \cdots & z(m, N-C+1) \\ \vdots & \vdots & \ddots & \vdots \\ z(m, C-1) & z(m, C) & \cdots & z(m, N-1) \end{bmatrix}, \quad (3)$$

where C is the window pencil parameter [17]. We define Hankel matrices \mathbf{D}_m^+ and \mathbf{D}_m^- as follows:

$$\mathbf{D}_m^+ = \mathbf{D}_m \mathbf{J}_1 \quad (4)$$

$$\mathbf{D}_m^- = \mathbf{D}_m \mathbf{J}_2,$$

where $\mathbf{J}_1 = [\mathbf{I}_{(N-C) \times (N-C)}; \mathbf{0}_{1 \times (N-C)}]$ and $\mathbf{J}_2 = [\mathbf{0}_{1 \times (N-C)}; \mathbf{I}_{(N-C) \times (N-C)}]$ are selection matrices. $\mathbf{I}_{(N-C) \times (N-C)}$ is identity matrix. Then, Hankel matrices \mathbf{D}_m^+ and \mathbf{D}_m^- are used to structure the Hankel block matrices \mathbf{H}_{00} , \mathbf{H}_{01} , and \mathbf{H}_{10} as follows:

$$\mathbf{H}_{00} = \begin{bmatrix} \mathbf{D}_0^+ & \mathbf{D}_1^+ & \cdots & \mathbf{D}_{M-B-1}^+ \\ \mathbf{D}_1^+ & \mathbf{D}_2^+ & \cdots & \mathbf{D}_{M-B}^+ \\ \vdots & \vdots & \ddots & \vdots \\ \mathbf{D}_{B-1}^+ & \mathbf{D}_{B-1}^+ & \cdots & \mathbf{D}_{M-2}^+ \end{bmatrix}$$

$$\mathbf{H}_{01} = \begin{bmatrix} \mathbf{D}_0^- & \mathbf{D}_1^- & \cdots & \mathbf{D}_{M-B-1}^- \\ \mathbf{D}_1^- & \mathbf{D}_2^- & \cdots & \mathbf{D}_{M-B}^- \\ \vdots & \vdots & \ddots & \vdots \\ \mathbf{D}_{B-1}^- & \mathbf{D}_{B-1}^- & \cdots & \mathbf{D}_{M-2}^- \end{bmatrix} \quad (5)$$

$$\mathbf{H}_{10} = \begin{bmatrix} \mathbf{D}_1^+ & \mathbf{D}_2^+ & \cdots & \mathbf{D}_{M-B}^+ \\ \mathbf{D}_2^+ & \mathbf{D}_3^+ & \cdots & \mathbf{D}_{M-B+1}^+ \\ \vdots & \vdots & \ddots & \vdots \\ \mathbf{D}_B^+ & \mathbf{D}_{B+1}^+ & \cdots & \mathbf{D}_{M-1}^+ \end{bmatrix},$$

where B is also the window pencil parameter. Substituting (2) and (4) into (5), Hankel matrices \mathbf{H}_{00} , \mathbf{H}_{01} , and \mathbf{H}_{10} can be rewritten as

$$\mathbf{H}_{00} = \mathbf{O} \mathbf{C} \quad (6)$$

$$\mathbf{H}_{01} = \mathbf{O} \Phi_x \mathbf{C} \quad (7)$$

$$\mathbf{H}_{10} = \mathbf{O} \Phi_y \mathbf{C}, \quad (8)$$

where $\mathbf{O} = [\mathbf{G} \Phi_x^0 \Phi_y^0, \mathbf{G} \Phi_x^1 \Phi_y^0, \dots \mid \mathbf{G} \Phi_x^0 \Phi_y^1, \mathbf{G} \Phi_x^1 \Phi_y^1, \dots \mid \dots]^T$ is the observability matrix, $\mathbf{C} = [\Phi_x^0 \Phi_y^0 \mathbf{B}, \Phi_x^1 \Phi_y^0 \mathbf{B}, \dots \mid \Phi_x^0 \Phi_y^1 \mathbf{B}, \Phi_x^1 \Phi_y^1 \mathbf{B}, \dots \mid \dots]$ is the controllability matrix, and $[\cdot]^T$ denotes the transpose.

Considering the singular value decomposition (SVD) of matrix \mathbf{H}_{00} , (6) can be expressed as

$$\mathbf{H}_{00} = \mathbf{U}\mathbf{\Sigma}\mathbf{V}^H = [\mathbf{U}_s \ \mathbf{U}_n] \begin{bmatrix} \mathbf{\Sigma}_s & 0 \\ 0 & \mathbf{\Sigma}_n \end{bmatrix} [\mathbf{V}_s^H \ \mathbf{V}_n^H]. \quad (9)$$

The noise effect should be cut off in order to obtain the high accuracy DOA estimation. Hence, observability matrix $\tilde{\mathbf{O}}$ and controllability matrix $\tilde{\mathbf{C}}$ can be acquired as

$$\begin{aligned} \tilde{\mathbf{O}} &= \mathbf{U}_{1:K} \sqrt{\mathbf{\Sigma}_{1:K,1:K}} \\ \tilde{\mathbf{C}} &= \sqrt{\mathbf{\Sigma}_{1:K,1:K}} \mathbf{V}_{1:K}^H, \end{aligned} \quad (10)$$

where K is the number of signals, which can be adopted by Akaike information criterion (AIC) [19] and minimum description length (MDL) [20]. Then, through the comprehensive utilization of controllability matrix $\tilde{\mathbf{O}}$ and observability matrix $\tilde{\mathbf{C}}$, $\tilde{\mathbf{\Phi}}_x$ and $\tilde{\mathbf{\Phi}}_y$ can be obtained as

$$\begin{aligned} \tilde{\mathbf{\Phi}}_x &= \text{pinv}(\tilde{\mathbf{O}}) \mathbf{H}_{01} \text{pinv}(\tilde{\mathbf{C}}) \\ \tilde{\mathbf{\Phi}}_y &= \text{pinv}(\tilde{\mathbf{O}}) \mathbf{H}_{10} \text{pinv}(\tilde{\mathbf{C}}), \end{aligned} \quad (11)$$

where $\text{pinv}(\cdot)$ is pseudoinverse. For the implementation simplicity, the eigenvalue pairing [16] technique is applied. Therefore, diagonal matrices $\mathbf{\Phi}_x$ and $\mathbf{\Phi}_y$ can be obtained through eigendecomposition of matrices $\tilde{\mathbf{\Phi}}_x$ and $\tilde{\mathbf{\Phi}}_y$,

$$\begin{aligned} \mathbf{\Phi}_x &= \mathbf{T}^{-1} \tilde{\mathbf{\Phi}}_x \mathbf{T} \\ \mathbf{\Phi}_y &= \mathbf{T}^{-1} \tilde{\mathbf{\Phi}}_y \mathbf{T}, \end{aligned} \quad (12)$$

where \mathbf{T} can diagonalize both $\tilde{\mathbf{\Phi}}_x$ and $\tilde{\mathbf{\Phi}}_y$ in a similarity transformation. Finally, (u_k, v_k) pairs can automatically be paired from diagonal matrices $\mathbf{\Phi}_x$ and $\mathbf{\Phi}_y$. Therefore, we can get the final results

$$\begin{aligned} \theta_k &= \arctan\left(\frac{v_k}{u_k}\right) \\ \phi_k &= \arcsin\sqrt{u_k^2 + v_k^2}. \end{aligned} \quad (13)$$

Then the solving steps can be written as follows

Step 1. Construct the Hankel matrices \mathbf{H}_{00} , \mathbf{H}_{01} , and \mathbf{H}_{10} from the received data $z(m, n)$.

Step 2. Use the singular value decomposition of Hankel matrix \mathbf{H}_{00} to acquire the left singular vector \mathbf{U} , right singular vector \mathbf{V} , and singular value $\mathbf{\Sigma}$.

Step 3. Construct the controllability matrix $\tilde{\mathbf{O}}$ and observability matrix $\tilde{\mathbf{C}}$.

Step 4. Use (11) to obtain matrices $\tilde{\mathbf{\Phi}}_x$ and $\tilde{\mathbf{\Phi}}_y$;

Step 5. Use eigenvalue pairing technique to get the diagonal matrices $\mathbf{\Phi}_x$ and $\mathbf{\Phi}_y$.

Step 6. Use (13) to estimate final results $\{(\theta_k, \phi_k)\}_{k=1}^K$.

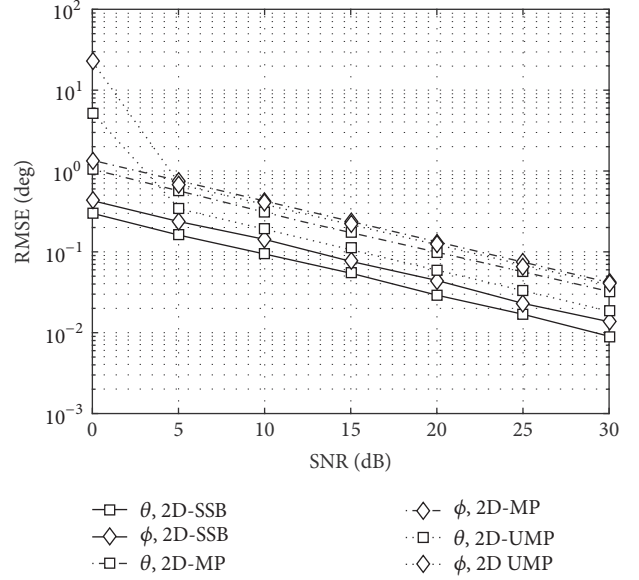


FIGURE 2: RMSEs of azimuth and elevation angles against with SNR for the dispersed sources, where $(\theta_1, \phi_1) = (25^\circ, 55^\circ)$ and $(\theta_2, \phi_2) = (45^\circ, 65^\circ)$.

4. Simulation

Firstly, two far-field narrowband signals impinge on the 20×20 URA with $(\theta_1, \phi_1) = (25^\circ, 55^\circ)$ and $(\theta_2, \phi_2) = (45^\circ, 65^\circ)$, where the source positions are relatively dispersed. The distance between any two elements of the URA is half a wavelength. The window pencil parameters are $B = 10$ and $C = 10$. The root mean square errors (RMSEs) of azimuth and elevation angles against with SNR for the URA are illustrated in Figure 2, where 500 Monte Carlo experiments are tested for each data. The RMSEs for the estimates of source DOAs θ and ϕ are defined as

$$\begin{aligned} \text{RMSE}_\theta &= \sqrt{\frac{1}{JK} \sum_{j=1}^J \sum_{k=1}^K (\hat{\theta}_{jk} - \theta_k)^2} \\ \text{RMSE}_\phi &= \sqrt{\frac{1}{JK} \sum_{j=1}^J \sum_{k=1}^K (\hat{\phi}_{jk} - \phi_k)^2}, \end{aligned} \quad (14)$$

where J is the number of Monte Carlo experiments. As can be seen from Figure 2, the RMSEs of DOAs θ and ϕ decrease as SNR increases, and the 2D SSB method has a better performance than 2D MP/UMP method [17] at the same SNR, which validates the proposed 2D SSB method.

Secondly, the challenging scenario of closely positioned sources impinging on the same URA is taken into consideration with $(\theta_1, \phi_1) = (10^\circ, 12^\circ)$ and $(\theta_2, \phi_2) = (12^\circ, 10^\circ)$. Figure 3 shows the results. The 2D SSB method still has a better performance than the 2D MP/UMP method while the performance of 2D MP method deteriorated sharply even the SNR is very high. In addition, the SNR threshold of 2D SSB is much lower than the 2D UMP method. However, in order to acquire a good DOA estimation, a higher SNR threshold is

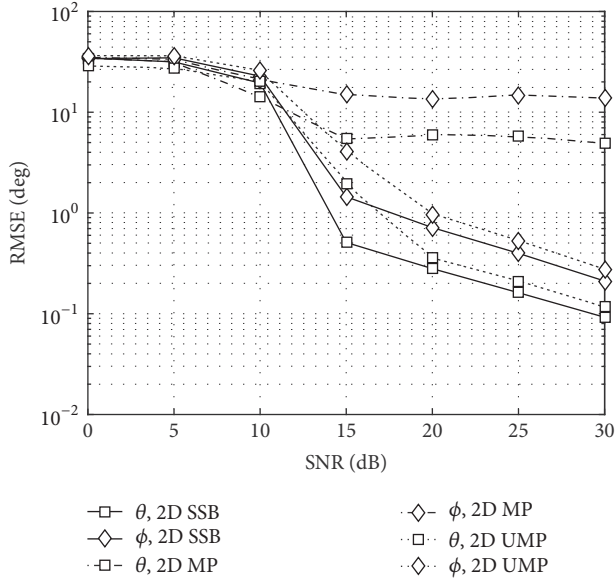


FIGURE 3: RMSEs of azimuth and elevation angles against with SNR for the closely positioned sources, where $(\theta_1, \phi_1) = (10^\circ, 12^\circ)$ and $(\theta_2, \phi_2) = (12^\circ, 10^\circ)$.

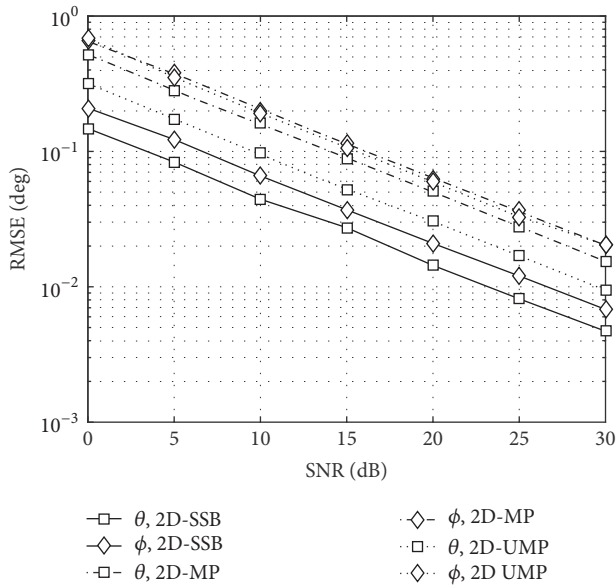


FIGURE 4: RMSEs of azimuth and elevation angles against with SNR for correlated sources, where $(\theta_1, \phi_1) = (25^\circ, 55^\circ)$ and $(\theta_2, \phi_2) = (45^\circ, 65^\circ)$.

necessary compared with the scenario in the first simulation. All in all, 2D SSB performs more robustness and effectiveness than 2D MP/UMP method.

Thirdly, same scenario with correlated signals and uncorrelated signals is also taken into consideration in Figures 4 and 5. In order to describe the correlated signals and uncorrelated signals, multiple snapshot case is considered. 2D SSB can easily deal with multiple snapshot case by using the method in [21]. The number of snapshots is set to be

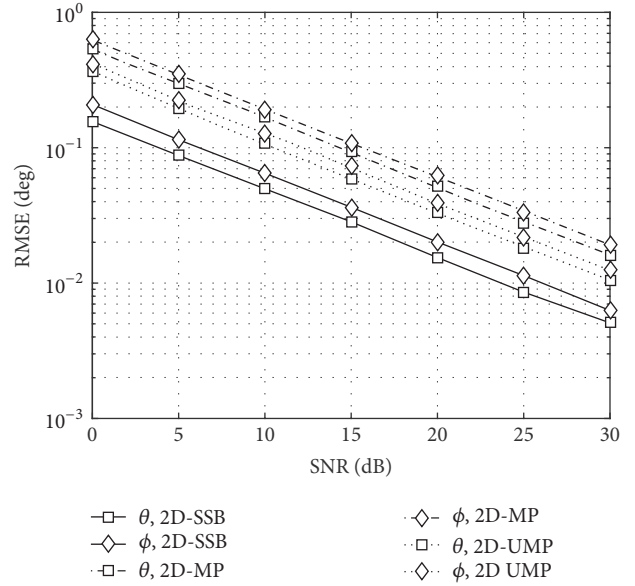


FIGURE 5: RMSEs of azimuth and elevation angles against with SNR for uncorrelated sources, where $(\theta_1, \phi_1) = (25^\circ, 55^\circ)$ and $(\theta_2, \phi_2) = (45^\circ, 65^\circ)$.

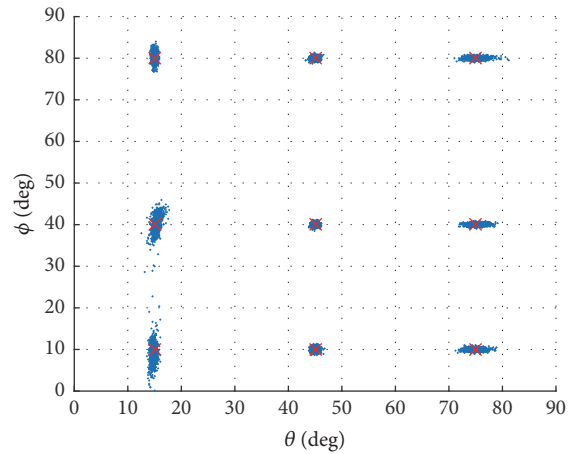


FIGURE 6: 2D DOA estimation results of 9 incident signals, SNR = -5 dB.

4. As illustrated in Figures 4 and 5, 2D SSB also performs better.

In the last simulation, 9 incident signals impinge on the same URA. The 2D DOA estimation results for 300 Monte Carlo simulations are shown in Figures 6 and 7 with SNR = -5 dB and SNR = 5 dB, and the estimate values are quite close to the real values indicated by the cross mark. Obviously, the results demonstrate that the angles of azimuth and elevation are paired correctly and effectively. In addition, the proposed method can compute the same azimuths when the elevations are different or the same elevations when the azimuths are different.

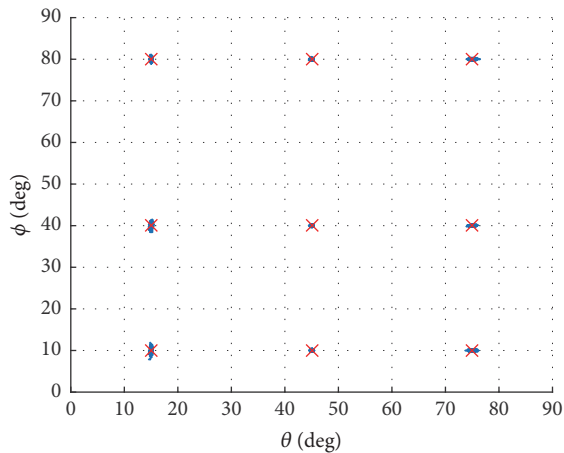


FIGURE 7: 2D DOA estimation results of 9 incident signals, SNR = 5 dB.

5. Conclusion

A 2D SSB method is proposed in this paper to estimate the angles of azimuth and elevation. This algorithm indicates high performance by using both observability and controllability matrices. Additionally, this method can provide automatically paired 2D direction cosine estimates without matching pair and deal with the correlated signals directly. Simulations demonstrate the effectiveness of our method.

Conflicts of Interest

The authors declare that there are no conflicts of interest regarding the publication of this paper.

Acknowledgments

This work was supported by the National Natural Science Foundation of China (Grants nos. 61671035 and 61501012).

References

- [1] A. Gaber and A. Omar, "A study of wireless indoor positioning based on joint TDOA and DOA estimation using 2-D matrix pencil algorithms and IEEE 802.11ac," *IEEE Transactions on Wireless Communications*, vol. 14, no. 5, pp. 2440–2454, 2015.
- [2] H. Krim and M. Viberg, "Two decades of array signal processing research," *IEEE Signal Processing Magazine*, vol. 13, no. 4, pp. 67–94, 1996.
- [3] M. Y. Cao, S. A. Vorobyov, and A. Hassanien, "Transmit array interpolation for DOA estimation via tensor decomposition in 2-D MIMO radar," *IEEE Transactions on Signal Processing*, vol. 65, no. 19, pp. 5225–5239, 2017.
- [4] R. O. Schmidt, "Multiple emitter location and signal parameter estimation," *IEEE Transactions on Antennas and Propagation*, vol. 34, no. 3, pp. 276–280, 1986.
- [5] F.-G. Yan, Z.-K. Chen, M.-J. Sun, Y. Shen, and M. Jin, "Two-dimensional direction-of-arrivals estimation based on one-dimensional search using rank deficiency principle," *International Journal of Antennas and Propagation*, vol. 2015, Article ID 127621, pp. 1–8, 2015.
- [6] Y. Dong, C. Dong, W. Liu, H. Chen, and G. Zhao, "2-D DOA Estimation for L-Shaped Array With Array Aperture and Snapshots Extension Techniques," *IEEE Signal Processing Letters*, vol. 24, no. 4, pp. 495–499, 2017.
- [7] A. Ghobadzadeh and R. Adve, "Low-complexity 2D root-MUSIC pairing for an L-shaped array," in *Proceedings of the IEEE Radar Conference (RadarConf '17)*, pp. 0957–0962, Seattle, Wash, USA, May 2017.
- [8] R. Roy and T. Kailath, "ESPRIT-estimation of signal parameters via rotational invariance techniques," *IEEE Transactions on Signal Processing*, vol. 37, no. 7, pp. 984–995, 1989.
- [9] Y. Fayad, C. Wang, and Q. Cao, "Improved ESPRIT method used for 2D-DOA estimation in tracking radars," in *Proceedings of the 13th European Radar Conference (EuRAD '16)*, pp. 113–116, London, UK, October 2016.
- [10] X. Lan, Y. Li, and E. Wang, "A RARE Algorithm for 2D DOA Estimation Based on Nested Array in Massive MIMO System," *IEEE Access*, vol. 4, pp. 3806–3814, 2016.
- [11] T. K. Sarkar and O. Pereira, "Using the matrix pencil method to estimate the parameters of a sum of complex exponentials," *IEEE Antennas and Propagation Magazine*, vol. 37, no. 1, pp. 48–55, 1995.
- [12] N. Yilmazer, J. Koh, and T. K. Sarkar, "Utilization of a unitary transform for efficient computation in the matrix pencil method to find the direction of arrival," *IEEE Transactions on Antennas and Propagation*, vol. 54, no. 1, pp. 175–181, 2006.
- [13] J.-F. Cardoso and A. Souloumiac, "Jacobi angles for simultaneous diagonalization," *SIAM Journal on Matrix Analysis and Applications*, vol. 17, no. 1, pp. 161–164, 1996.
- [14] Y.-Y. Dong, C.-X. Dong, Z.-B. Shen, and G.-Q. Zhao, "Conjugate augmented spatial temporal technique for 2-D DOA estimation with L-shaped array," *IEEE Antennas and Wireless Propagation Letters*, vol. 14, pp. 1622–1625, 2015.
- [15] M. Haardt and J. A. Nossek, "Simultaneous schur decomposition of several nonsymmetric matrices to achieve," *IEEE Transactions on Signal Processing*, vol. 46, no. 1, pp. 161–169, 1998.
- [16] M. L. Burrows, "Two-dimensional ESPRIT with tracking for radar imaging and feature extraction," *IEEE Transactions on Antennas and Propagation*, vol. 52, no. 2, pp. 524–532, 2004.
- [17] N. Yilmazer and T. K. Sarkar, "2-D unitary matrix pencil method for efficient direction of arrival estimation," *Digital Signal Processing*, vol. 16, no. 6, pp. 767–781, 2006.
- [18] J. H. David, *State-Space Approaches to Ultra-Wideband Doppler Processing*, Worcester Polytechnic Institute, Worcester, Mass, USA, 2007.
- [19] M. Wax and T. Kailath, "Detection of signals by information theoretic criteria," *IEEE Transactions on Acoustics, Speech and Signal Processing*, vol. 33, no. 2, pp. 387–392, 1985.
- [20] M. Wax and I. Ziskind, "Detection of the number of coherent signals by the MDL principle," *IEEE Transactions on Signal Processing*, vol. 37, no. 8, pp. 1190–1196, 1989.
- [21] N. Yilmazer, S. Ari, and T. K. Sarkar, "Multiple snapshot direct data domain approach and ESPRIT method for direction of arrival estimation," *Digital Signal Processing*, vol. 18, no. 4, pp. 561–567, 2008.

Research Article

DOA Estimation of Noncircular Signals Using Quaternions

Tianzhen Meng, Minjie Wu, and Naichang Yuan

Department of Electronic Science and Engineering, National University of Defense Technology, Deya Street 109, Changsha 410073, China

Correspondence should be addressed to Minjie Wu; wmj601@nuaa.edu.cn

Received 21 May 2017; Revised 8 August 2017; Accepted 5 September 2017; Published 8 October 2017

Academic Editor: Elisa Giusti

Copyright © 2017 Tianzhen Meng et al. This is an open access article distributed under the Creative Commons Attribution License, which permits unrestricted use, distribution, and reproduction in any medium, provided the original work is properly cited.

The two-dimensional (2D) direction-of-arrival (DOA) estimation problem for noncircular signals using quaternions is considered in this paper. In the framework of quaternions, we reconstruct the conjugate augmented output vector which reduces the dimension of covariance matrix. Compared with existing methods, the proposed one has two main advantages. Firstly, the estimation accuracy is higher since quaternions have stronger orthogonality. Secondly, the dimension of covariance matrix is reduced by half which decreases the computational complexity. Simulation results are presented verifying the efficacy of the algorithm.

1. Introduction

In the wake of developments in array signal processing, noncircular signals have been widely used in modern communication systems, such as amplitude modulation (AM) and binary phase shift keying (BPSK) signals. By exploiting the noncircular properties, both the second-order characteristics and the conjugate relation characteristics can be used. Thus, the resolution is improved [1].

In recent years, considerable alternatives have been proposed to take care of noncircular signals, for example, [2, 3]. In [4], the author proposed the extended 2q-MUSIC method for noncircular sources. Subsequently, Chen et al. presented a method to deal with the mixed noncircular and circular signals in [5]. However, most existing algorithms are based on the conjugate augmented output vector. Recently, a few methods for direction-of-arrival (DOA) estimation were presented based on the hypercomplex framework [6–8]. In [9, 10], Gou et al. used biquaternion-based algorithms to estimate the DOAs of noncircular signals. Instead of concatenating the data recorded by different sensors to a long vector, hypercomplex can link the data to different imaginary parts. And it has been proved that the hypercomplex vector orthogonality provides a more accurate estimation of the signal subspace than the long vector orthogonality constraint [6]. Nevertheless, compared with biquaternions, quaternion-based methods will be more attractive for decreasing the computational complexity.

In this paper, the problem of DOA estimation for noncircular signals within the quaternion framework is considered. We reconstruct the conjugate augmented output vector which can lead to the dimension reduction of covariance matrix. Thus, the computational load required by eigendecomposition is decreased. Additionally, since quaternions have stronger orthogonality compared with complex number, the proposed algorithm exhibits better performance in accuracy. It is also worthwhile to note that most existing algorithms using hypercomplex frames are based on vector sensor. Motivated by this fact, we want to break the platform limitations and extend it to a wider usage.

The rest of this paper is organized as follows. In Section 2, we briefly introduce some notations about quaternions, and on this basis, we use it to construct the data model for noncircular signals. Section 3 analyzes the computational complexity. Some numerical examples to illustrate the performances of the proposed algorithm are given in Section 4, followed by concluding remarks.

2. The Proposed Algorithm

2.1. Some Notations about Quaternions. A quaternion $q \in H$ is a four-dimensional (4D) hypercomplex number [11] and has a Cartesian form given by

$$q = a + ib + jc + kd, \quad (1)$$

where $a, b, c, d \in \mathbb{R}$ are called its components. In view of its widespread usage in subsequent sections, it is worthwhile to review some notations before proceeding to the physical problems of interest. The three imaginary units i, j, k are square roots of -1 and are related through the famous relations:

$$\begin{aligned} ij &= -ji = k \\ ki &= -ik = j \\ jk &= -kj = i \\ i^2 &= j^2 = k^2 = ijk = -1. \end{aligned} \quad (2)$$

In what follows, we will list some of the properties of quaternions that will be used throughout this correspondence.

- (a) The product of quaternions is associative: $(qp)r = q(pr)$.
- (b) The product of two quaternions is not commutative: $qp \neq pq$.
- (c) Just as with the complex numbers, the conjugate of a quaternion q is obtained by negating its imaginary part and is defined as $q = a - ib - jc - kd$.
- (d) The norm of a quaternion q is defined as $\|q\| = a^2 + b^2 + c^2 + d^2$; in addition, it also equals the product of a quaternion and its conjugate; that is, $\|q\| = q\bar{q}$.
- (e) A quaternion $q \in \mathbb{H}$ with $\|q\| = 1$ is said to be a unit quaternion.
- (f) Quaternion vector orthogonality provides a more accurate estimation of the signal subspace than the long vector orthogonality constraint.

As stated above, since the product of two quaternions is not commutative, there are two kinds of quaternion eigenvalues, that is, right eigenvalue and left eigenvalue. In this paper, quaternion eigenvalue and eigenvector refer to right eigenvalue and right eigenvector whenever there is no possibility of confusion.

2.2. Modeling Noncircular Signals Using Quaternions. Without loss of generality, we consider an array with N ($N = 8$) identical antenna elements as shown in Figure 1. The elements are uniformly distributed around a circle with radius R in the xOy plane. The circular array is not the conventional uniform circular array (UCA) for the dipoles point towards different directions. It is essentially the polarization sensitive array. Moreover, we assume that each dipole in the array is a short dipole whose output voltage is proportional to the electric field along the dipole.

The first element is taken as the reference with respect to other elements. The general expression for the element location is $\mathbf{r}_n = (R \cos(w_n), R \sin(w_n), 0)^T$, where $w_n = 2\pi(n-1)/N$ and $(\cdot)^T$ represent the angle from the x -axis and the transpose operator, respectively.

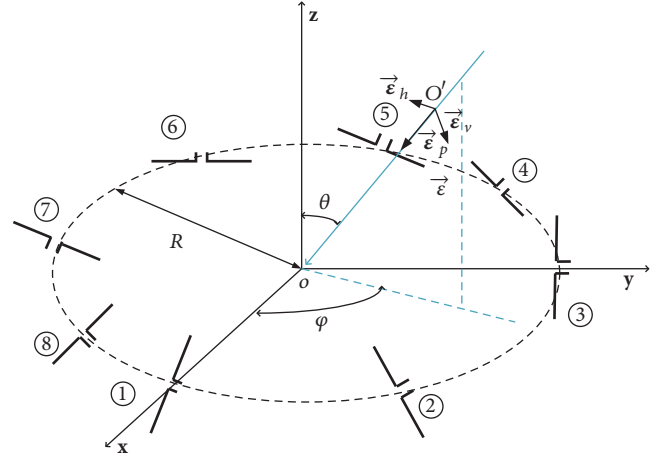


FIGURE 1: The geometry of the circular array.

Provided that \mathbf{a}_m is the signal steering vector and there are M incident narrowband signals impinging on the array from distinct directions, then the array output can be expressed as

$$\mathbf{x}(t) = \sum_{m=1}^M \mathbf{a}_m s_m(t) + \mathbf{n}(t), \quad (3)$$

where $s_m(t)$ is the signal and $\mathbf{n}(t)$ is assumed to be zero mean, complex Gaussian processes statistically independent of each other, with covariance σ_n^2 . The m th signal has an elevation angle θ_m and an azimuth angle φ_m . And the signals are assumed to be in the far-field with respect to the sensor location.

As a side note, for circular signals, the data model in (3) is qualified and the traditional MUSIC algorithm [12] can handle them. The processing procedure involves constructing the covariance matrix of $\mathbf{x}(t)$ and carrying out the eigenvalue decomposition to separate the signal subspace from the noise subspace. By using the orthogonality of these two subspaces, the DOA estimation can be performed. However, for noncircular sources, the above model is not satisfied. The conventional solution is to create the conjugate augmented output vector by exploiting noncircular properties; that is,

$$\begin{aligned} \mathbf{y}(t) &= \begin{bmatrix} \mathbf{x}(t) \\ \mathbf{x}^*(t) \end{bmatrix} = \sum_{m=1}^M \begin{bmatrix} \mathbf{a}_m s_m(t) \\ \mathbf{a}_m^* s_m^*(t) \end{bmatrix} + \begin{bmatrix} \mathbf{n}(t) \\ \mathbf{n}^*(t) \end{bmatrix} \\ &= \sum_{m=1}^M \begin{bmatrix} \mathbf{a}_m \\ \mathbf{a}_m^* \end{bmatrix} \begin{bmatrix} s_m(t) \\ s_m^*(t) \end{bmatrix} + \begin{bmatrix} \mathbf{n}(t) \\ \mathbf{n}^*(t) \end{bmatrix} \\ &= \sum_{m=1}^M \begin{bmatrix} \mathbf{a}_m \\ \mathbf{a}_m^* \end{bmatrix} \begin{bmatrix} 1 \\ e^{-j\omega_m} \end{bmatrix} \begin{bmatrix} s_m(t) \\ s_m(t) \end{bmatrix} + \begin{bmatrix} \mathbf{n}(t) \\ \mathbf{n}^*(t) \end{bmatrix} \\ &= \sum_{m=1}^M \underbrace{\begin{bmatrix} \mathbf{a}_m \\ \mathbf{a}_m^* e^{-j\omega_m} \end{bmatrix}}_{\mathbf{a}_{cm}} s_m(t) + \begin{bmatrix} \mathbf{n}(t) \\ \mathbf{n}^*(t) \end{bmatrix}, \end{aligned} \quad (4)$$

where $(\cdot)^*$ and $\bar{\omega}_m$ denote the conjugation and the noncircular phase, respectively. In [13], the author constructed the data

covariance matrix through (4) and, on this basis, estimated the DOAs of noncircular signals. However, the dimension of the covariance matrix was increased to $2N \times 2N$. In view of this, we can reconstruct the conjugate augmented vector and transform it to a quaternion vector:

$$\begin{aligned} \mathbf{y}_Q(t) &= \mathbf{x}(t) + i\mathbf{x}^*(t) \\ &= \sum_{m=1}^M (\mathbf{a}_m s_m(t) + i\mathbf{a}_m^* e^{-j\omega_m} s_m(t)) + \mathbf{n}(t) + i\mathbf{n}^*(t). \end{aligned} \quad (5)$$

This reconstructed model is reasonable since eigenstructure methods are based on the decomposition of the vector space spanned by the observation vector \mathbf{x} in orthogonal subspaces using energy criteria. Thus, the eigenvalue and its corresponding eigenvector derived from the quaternion covariance matrix are also satisfied the subspace condition.

Then, the covariance matrix can be represented as follows:

$$\mathbf{R}_{yy} = E \{ \mathbf{y}_Q(t) \overline{\mathbf{y}_Q(t)} \}, \quad (6)$$

where $\overline{(\cdot)}$ represents the conjugate-transpose operator in quaternion field. And the dimension of (6) is $N \times N$. However, under this circumstance, using spectral estimation to find the peak is expensive for the covariance matrix involving four parameters, that is, θ , φ , γ , and η . The parameters γ and η , the auxiliary polarization angle and the polarization phase difference [14], are used to depict the polarization state. The multidimensional search costs a lot and the efficiency is not high. In fact, the polarization parameters can be separated from the covariance matrix. Towards this purpose, it is necessary to obtain the analytical expression of the steering vector.

We first introduce the array element spatial phase matrix of the m th signal as follows:

$$\mathbf{Y}_m = \mathbf{Y}_{\theta_m, \varphi_m} = \begin{bmatrix} u_{m,1} & & \\ & \ddots & \\ & & u_{m,N} \end{bmatrix}. \quad (7)$$

\mathbf{Y}_m is the $N \times N$ diagonal matrix and it describes the spatial coherent structure of the output [15].

The k th diagonal element denotes the space phase factor

$$u_{m,k} = e^{-j2\pi(\boldsymbol{\varepsilon}_p^T(\theta_m, \varphi_m) \mathbf{r}_k) / \lambda_m}, \quad (8)$$

where

$$\boldsymbol{\varepsilon}_p(\theta_m, \varphi_m) = -[\sin \theta_m \cos \varphi_m, \sin \theta_m \sin \varphi_m, \cos \theta_m]^T \quad (9)$$

with λ_m representing the wavelength of the m th signal.

We assume that g represents the matched gain, and the generalized polarization sensitive matrix of the array can be expressed as follows:

$$\mathbf{\Gamma} = g \begin{bmatrix} \sin \beta_1 \cos \alpha_1 & \sin \beta_1 \sin \alpha_1 & \cos \beta_1 \\ \vdots & \vdots & \vdots \\ \sin \beta_n \cos \alpha_n & \sin \beta_n \sin \alpha_n & \cos \beta_n \\ \vdots & \vdots & \vdots \\ \sin \beta_N \cos \alpha_N & \sin \beta_N \sin \alpha_N & \cos \beta_N \end{bmatrix}. \quad (10)$$

The dimension of $\mathbf{\Gamma}$ is $N \times 3$. The pair of variables (α_n, β_n) represents the direction of the n th dipole in the array.

Then, the signal steering vector is obtained

$$\mathbf{a}_m = \mathbf{a}_{\theta_m, \varphi_m, \gamma_m, \eta_m} = \frac{\mathbf{Y}_m \mathbf{\Gamma} \Psi_m \mathbf{h}_m}{\Lambda_m}, \quad (11)$$

where

$$\begin{aligned} \mathbf{h}_m &= [\cos \gamma_m \quad \sin \gamma_m e^{j\eta_m}]^T \\ \Psi_m &= \begin{bmatrix} -\sin \varphi_m & \cos \theta_m \cos \varphi_m \\ \cos \varphi_m & \cos \theta_m \sin \varphi_m \\ 0 & \sin \theta_m \end{bmatrix}. \end{aligned} \quad (12)$$

Up to this point, we have found that the polarization information only exists in \mathbf{h}_m . In this case, we rewrite \mathbf{a}_{cm} in (4):

$$\begin{aligned} \mathbf{a}_{cm} &= \begin{bmatrix} \mathbf{a}_m \\ \mathbf{a}_m^* e^{-j\omega_m} \end{bmatrix} = \begin{bmatrix} \Lambda_m \mathbf{h}_m \\ \Lambda_m^* \mathbf{h}_m^* e^{-j\omega_m} \end{bmatrix} \\ &= \underbrace{\begin{bmatrix} \Lambda_m & \\ & \Lambda_m^* \end{bmatrix}}_{\Lambda_{cm}} \underbrace{\begin{bmatrix} \mathbf{h}_m \\ \mathbf{h}_m^* e^{-j\omega_m} \end{bmatrix}}_{\mathbf{h}_{cm}} \end{aligned} \quad (13)$$

Then, Λ_{cm} has nothing to do with polarization and is successfully separated from the array manifold. The dimension of Λ_{cm} is $2N \times 4$. So, we only need to traverse the angle parameters to determine the DOAs which largely reduces the amount of computations. Please note that Λ_{cm} derived from (13) corresponds to the conjugate augmented vector. To apply it to the quaternion case, we transform it as follows:

$$\Lambda_{qm} = \Lambda_m + i\Lambda_m^*. \quad (14)$$

From (14), it appears that Λ_{qm} is a complex number. In fact, Λ_m has the exponential part which makes Λ_{qm} a quaternion. Thus, the spatial spectra function can be expressed as

$$P(\theta, \varphi) = \frac{1}{\overline{\Lambda_{qm}} G_q \overline{G_q} \Lambda_{qm}}, \quad (15)$$

where G_q is $N \times (N - M)$ quaternion matrix composed of the $(N - M)$ eigenvectors corresponding to the $(N - M)$ minimum eigenvalues of \mathbf{R}_{yy} . Then, the DOAs can be obtained by varying (θ, φ) within a given domain with a chosen step.

3. Complexity Analysis

This section will evaluate the computational complexity of the proposed algorithm. To better demonstrate the superiority in computation, the conventional conjugate augmented vector (CAV) method is included for comparison. We focus on the estimation of the covariance matrix and evaluate it in terms of memory requirements and arithmetical operations (i.e., floating additions and multiplications).

As stated above, the dimension of the CAV method is $2N \times 2N$ in complex field. And it requires $4N^2$ complex memory units, corresponding to $8N^2$ floating memory units. However, the dimension of the proposed method is $N \times N$ in quaternion field. Thus, it takes up N^2 quaternion memory units, which equals $4N^2$ floating memory units. In this case, the proposed algorithm reduces by half the memory units.

As for the second aspect, that is, the arithmetical operations, we know that the multiplication between two quaternions contains 16 floating multiplications and 12 floating additions. And for the complex case, it involves 4 floating multiplications and 3 floating additions. Thus, constructing the covariance matrix costs $(16 + 12) \times N^2$ operations for the proposed method and $(4 + 3) \times 4N^2$ operations for the CAV method. Next, the computation in eigenvalue decomposition will be considered. As is known to all, the complexity for the decomposition operation is $O(N^3)$. So, the values for CAV method and the proposed one are $O(8N^3)$ in complex field and $O(N^3)$ in quaternion field, respectively. The above values will become $O(32N^3)$ and $O(16N^3)$, respectively, in terms of floating point number.

Thus, it is obvious that the computational burden is equivalent for these two methods in constructing the covariance matrix. However, the proposed method outperforms the CAV one in eigenvalue decomposition. To sum up, the use of quaternions in algorithms reduces both the computational complexity and memory requirements.

4. Simulation Results

In this section, Monte-Carlo simulation experiments are implemented to verify the effectiveness of the proposed algorithm. The array structure is shown in Figure 1. The root mean squared error (RMSE) is utilized as the performance measure. And 100 independent simulation experiments are carried out. The RMSE is defined as

$$\text{RMSE} = \sqrt{\frac{1}{100} \sum_{i=1}^{100} [(\hat{\theta}_i - \theta_i)^2 + (\hat{\phi}_i - \phi_i)^2]}, \quad (16)$$

where $\{\hat{\theta}_i, \hat{\phi}_i\}$ are the estimates of elevation angles and azimuth angles, respectively, at the i th run. In addition, the CAV method and Gou's method [10] are included for comparison.

We assume that there are three BPSK signals that can be received. The corresponding incident angles are $(15^\circ, 20^\circ)$, $(35^\circ, 40^\circ)$, and $(60^\circ, 65^\circ)$, respectively. The corresponding polarization auxiliary angle and the polarization phase difference are $(20^\circ, 25^\circ)$, $(55^\circ, 45^\circ)$, and $(65^\circ, 65^\circ)$. In addition, the

DOA estimation of noncircular signals using quaternions

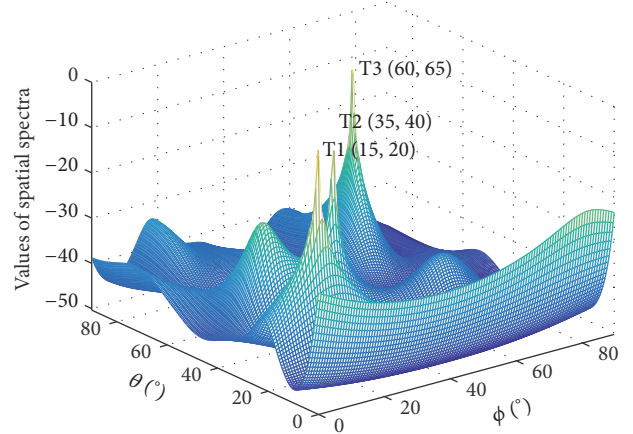


FIGURE 2: The spatial spectra of noncircular signals.

noncircular phases are $\pi/7$, $\pi/7$, and $2\pi/7$, respectively. The snapshot, K , is selected as 200 and the SNR is 10 dB. Figure 2 shows the simulation results of the proposed algorithm. The position of the spectra peak represents the corresponding DOA. Intuitively, the estimation accuracy of the proposed algorithm is high.

To better demonstrate the performance of the proposed method, we study the performance with a varying SNR from 0 dB to 30 dB. Without loss of generality, we select the aforementioned three sources as the targets to verify it. Figure 3 shows the RMSE versus SNR with the snapshots being 200. It can be seen that the proposed method outperforms the CAV method since quaternions have stronger orthogonality compared with complex number. And it has been proved that the stronger the orthogonality, the better the performance [6]. In addition, the proposed algorithm largely decreases the computational complexity, as stated in Section 3. It is worthwhile to note that the simulation curves in Figure 3 are not smooth since the statistical data have certain randomness. Compared with the biquaternion noncircular MUSIC (BNC) algorithm developed by Gou et al. [10], we can see that the RMSEs of the BNC method are close to those of the proposed one. The reason is that both quaternions and biquaternions impose the orthogonality constraint. And they only represent different mathematical languages. In [10], the author constructed the biquaternion data model from the standpoint of covariance. Nevertheless, we reconstructed the conjugate augmented output vector using quaternions in this correspondence. Therefore, in this case, both methods exhibit similar performance. However, from [10], we know that the complexity of eigenvalue decomposition using biquaternions is about $O(64N^3)$. And the corresponding value in this paper is about $O(16N^3)$. Then, using quaternions reduces the computational burden.

Figure 4 illustrates the RMSE versus the number of snapshots with the SNR fixed at 10 dB. Compared with Figure 3, we can draw similar conclusions. In particular, if we pick the points with snapshots being 400 and 800, respectively, we may find that the corresponding RMSEs

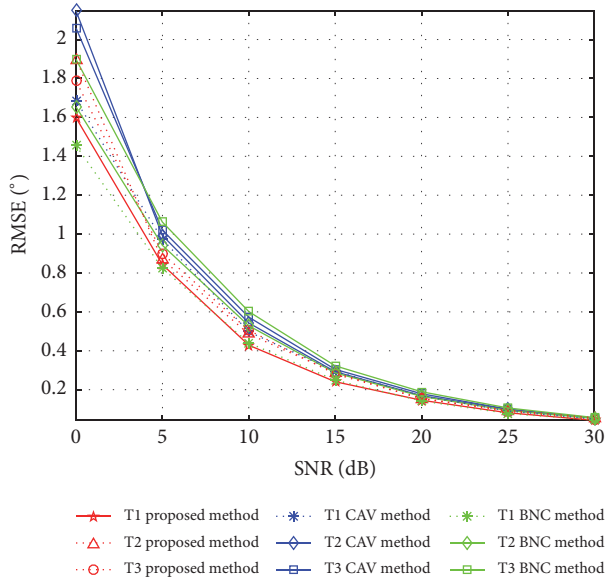


FIGURE 3: RMSE versus SNR with the snapshots being 200.

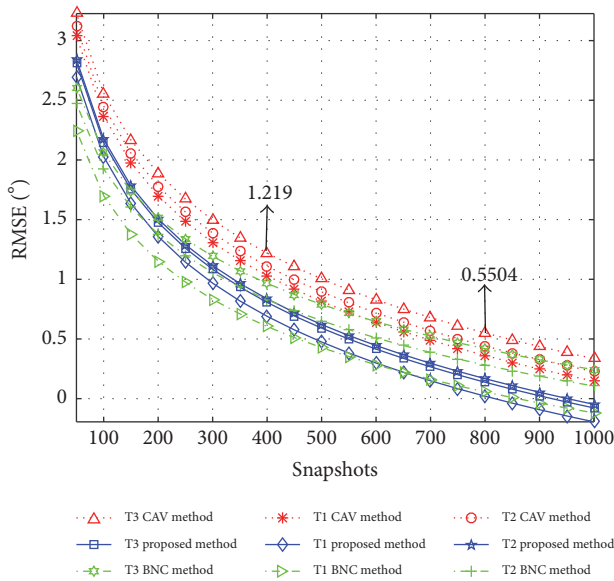


FIGURE 4: RMSE versus snapshots with the SNR fixed at 10 dB.

are 1.219 and 0.5504. This means that the former value is nearly twice as much as the latter one. In fact, these improvements can be predicted from the derivation of CRB. For the specific derivation process, one can refer to literature [16]. The number of snapshots can be extracted from the Fisher information matrix. Moreover, the CRB is found as the element of the inverse of that matrix. So, we can conclude that the RMSE is inversely proportional to K .

5. Conclusion

In this paper, we combine the quaternions with the conjugate augmented vector and present a DOA estimation algorithm

for noncircular signals. Compared with existing methods, the proposed one has two main advantages. Firstly, it can give a more accurate estimation since quaternions have stronger orthogonality. Secondly, the dimension of the covariance matrix is reduced by half and, therefore, has a much lower computational complexity. In addition, the proposed method breaks the platform limitations of vector sensors and extend quaternions to a wider usage. The simulation results verify the effectiveness of the proposed method.

Conflicts of Interest

The authors declare that they have no conflicts of interest.

Acknowledgments

This project was supported by the National Natural Science Foundation of China (Grant no. 61302017).

References

- [1] Y. Xu and Z. Liu, "Noncircularity-exploitation in direction estimation of noncircular signals with an acoustic vector-sensor," *Digital Signal Processing: A Review Journal*, vol. 18, no. 5, pp. 777–796, 2008.
- [2] P. Chargé, Y. Wang, and J. Saillard, "A non-circular sources direction finding method using polynomial rooting," *Signal Processing*, vol. 81, no. 8, pp. 1765–1770, 2001.
- [3] L. Gan, J.-F. Gu, and P. Wei, "Estimation of 2-D DOA for noncircular sources using simultaneous SVD technique," *IEEE Antennas and Wireless Propagation Letters*, vol. 7, pp. 385–388, 2008.
- [4] J. Liu, Z. Huang, and Y. Zhou, "Extended 2q-MUSIC algorithm for noncircular signals," *Signal Processing*, vol. 88, no. 6, pp. 1327–1339, 2008.
- [5] H. Chen, C. Hou, W. Liu, W.-P. Zhu, and M. N. S. Swamy, "Efficient two-dimensional direction-of-arrival estimation for a mixture of circular and noncircular sources," *IEEE Sensors Journal*, vol. 16, no. 8, pp. 2527–2536, 2016.
- [6] S. Miron, N. le Bihan, and J. I. Mars, "Quaternion-music for vector-sensor array processing," *IEEE Transactions on Signal Processing*, vol. 54, no. 4, pp. 1218–1229, 2006.
- [7] N. Le Bihan, S. Miron, and J. I. Mars, "MUSIC algorithm for vector-sensors array using biquaternions," *IEEE Transactions on Signal Processing*, vol. 55, no. 9, pp. 4523–4533, 2007.
- [8] Y. Xu, X. Gong, and Z. Liu, "Quad-quaternion MUSIC for DOA estimation using electromagnetic vector sensors," *Eurasip Journal on Advances in Signal Processing*, vol. 2008, Article ID 213293, 2008.
- [9] X. Gou, Z. Liu, and Y. Xu, "Biquaternion cumulant-MUSIC for DOA estimation of noncircular signals," *Signal Processing*, vol. 93, no. 4, pp. 874–881, 2013.
- [10] X. Gou, Z. Liu, and Y. Xu, "Biquaternion noncircular MUSIC, Multidimensional Systems and Signal Processing," *An International Journal*, vol. 26, no. 1, pp. 95–111, 2015.
- [11] T. A. Ell, N. Le Bihan, and S. J. Sangwine, *Quaternion Fourier Transforms for Signal and Image Processing*, Focus Series in Digital Signal and Image Processing, John Wiley and Sons, UK, London, 2014.

- [12] R. O. Schmidt, "Multiple emitter location and signal parameter estimation," *IEEE Transactions on Antennas and Propagation*, vol. 34, no. 3, pp. 276–280, 1986.
- [13] M. Wu and N. Yuan, "DOA estimation in solving mixed non-circular and circular incident signals based on the circular array," *Progress In Electromagnetics Research M*, vol. 53, pp. 141–151, 2017.
- [14] J. Li and R. T. Compton Jr., "Angle estimation using a polarization sensitive array," *IEEE Transactions on Antennas and Propagation*, vol. 39, no. 10, pp. 1539–1543, 1991.
- [15] M. Wu, T. Meng, and N. Yuan, "DOA estimation of partially polarized signals," *Progress In Electromagnetics Research M*, vol. 56, pp. 111–120, 2017.
- [16] P. Stoica and A. Nehorai, "MUSIC, maximum likelihood, and Cramer-Rao bound," *Institute of Electrical and Electronics Engineers. Transactions on Acoustics, Speech, and Signal Processing*, vol. 37, no. 5, pp. 720–741, 1989.